Properties of bimetallic AuAg nanoparticles for H_2 production

Anna L. Gould

Department of Chemistry, University College London (UCL)

Supervisor: Professor C. R. A. Catlow

Second Supervisor: Dr A. J. Logsdail

Thesis submitted for the degree of Doctor of Engineering

2017

Declaration

I, Anna Louise Gould, confirm that the work presented in this thesis is my own. Where information has been derived from other sources, I confirm that this has been indicated in the thesis.

Abstract

Nanoparticles exhibit distinctly different properties from those of bulk matter, as a result of their large surface area to volume ratio. They have been shown to be catalytically active for a number of reactions, and therefore hold great interest for use in industry, where a fine balance of turnover and cost must be achieved. This thesis focuses on bimetallic gold/silver nanoparticles, where the introduction of a secondary metallic species can be used to not only control nanoparticle properties, but also reduce scale up costs.

For gold/silver bimetallic nanoparticles (nanoalloys), it is unclear as to how the two metals will mix: based on thermodynamic arguments alone, it is unclear whether similarities in atomic size and number of valence electrons lead to the formation of an alloy or a segregated core@shell arrangement. In this work, we investigate the most energetically favourable and stable chemical arrangements based on interatomic potential basin-hopping algorithms, re-optimised using density functional theory (DFT), evaluating their potential as co-catalysts for hydrogen production.

Diffusion is particularly important in catalyst stability, and therefore we examine both Au-Ag interdiffusion and the interaction of Ag nanoparticles and amorphous Si (a-Si). We examine the influence of calcination processes, often used in experimental synthesis, on differing AuAg nanoparticle chemical arrangements using classical molecular dynamics simulations. Our calculations show Ag@Au nanoparticles are the most promising in terms of achieving a higher catalytic turnover; however, we also find that Ag@Au nanoparticles are particularly unstable due to the energetically favourable formation of a ‘rosette-like’ icosahedral geometry, which exposes core Ag atoms. In addition, diffusion of Ag nanoparticles into a-Si is studied for parallel comparison with experiment, performed at the University of Utrecht. Experimental observations suggest the diffusion of Ag atoms into the a-Si matrix, however, we do not observe the same computationally, suggesting that experimental voids in a-Si may facilitate this diffusion. Finally, we investigate the applicability of CO as a probe molecule for determining changes in surface composition through vibrational stretching frequencies, both experimentally and theoretically, using diffuse reflectance infrared Fourier transform spectroscopy and DFT modelling.

Acknowledgements

The work presented here could not have been possible without support and advice from esteemed colleagues, friends and family. First and foremost, I would like to thank my supervisor Professor C. Richard A. Catlow for presenting me with such an interesting project, the opportunity to make it my own, and his overall guidance. I am also very thankful for the support of my second supervisor and mentor, Dr Andrew J. Logsdail, for always being available for scientific discussion, and making my project so prolific. I will always be grateful for his dedication to the various paths certain investigations have led us down, producing even more interesting results.

This EngD was funded by the Engineering and Physical Sciences Research Council and Diamond Light Source, for which I am extremely grateful. I would like to acknowledge the HPC facilities ARCHER, and UCL clusters, Legion and Faraday; I am indebted to those who maintain these facilities; special mentions are required for Owain Kenway, Ilian Todorov, Alin Marin Elena, David Wales, Francesca Baletto and Kevin Rossi for their efforts in unravelling software peculiarities. My first collaboration outside of UCL is due to the hard work of Marcel Di Vece, Shima Kadkhodazadeh, and Jakob Wagner. Finally, I must also thank my industrial support: Diego Gianolis, Peter Wells and Nikos Dimitratos have all provided life advice, enthusiasm, and a home within the UK Catalysis Hub.

I would also like to thank those who kept me sane in the office for the entirety of my EngD, namely Catherine Brookes, Scott Rogers, Wilm Jones, Antonios Vamvakeros, and Alexander O'Malley; Kathryn Bradley and John Sharp, for providing a Liverpudlian haven. Finally, I am extremely grateful to my parents and my brother for their unconditional love, encouragement, and constant cups of tea.

Publications from this work

Gould, A. L., Heard, C. J., Logsdail, A. J., & Catlow, C. R. A. Segregation effects on the properties of $(AuAg)_{147}$. *Physical Chemistry Chemical Physics*, 2014, *16*, 21049-21061.

Gould, A. L., Logsdail, A. J., & Catlow, C. R. A. Influence of Composition and Chemical Arrangement on the Kinetic Stability of 147-Atom Au–Ag Bimetallic Nanoclusters. *The Journal of Physical Chemistry C*, 2015, *19*, 23685-23697.

Gould, A. L., Kadkhodazadeh, S., Wagner, J. B., Catlow, C. R. A., Logsdail, A. J., & Di Vece, M. Understanding the Thermal Stability of Silver Nanoparticles Embedded in a-Si. *The Journal of Physical Chemistry C*, 2015, *119*, 23767-23773.

Rogers, S. M., Catlow, C. R. A., Chan-Thaw, C. E., Gianolio, D., Gibson, E. K., Gould, A. L., Jian, N., Logsdail, A. J., Palmer, R. E., Prati, L. and Dimitratos, N. Tailoring Gold Nanoparticle Characteristics and the Impact on Aqueous-Phase Oxidation of Glycerol. *ACS Catalysis*, 2015, *5*, 4377-4384.

Gould, A. L., Rossi, K., Catlow, C. R. A., Baletto. F., & Logsdail, A. J. Controlling Structural Transitions in AuAg Nanoparticles through Precise Compositional Design. *The Journal of Physical Chemistry Letters*, 2016, *7*, 4414-4419.

Table of Contents

1 Introduction

Nanoparticles are clusters or aggregates of atoms, routinely defined as particles with sizes in the region of 1-100 nm. Clusters towards the lower end of the nanoscale regime may be termed ‘nanoclusters’, usually considered to have nuclearities of less than 50 atoms. Most notably, the unique properties that are observed for nanoclusters and nanoparticles differ considerably in comparison to those associated with bulk matter or isolated atoms and thus have extensive application in catalysis, engineering, magnetism, and electronics.[1-4]

Due to the small size of nanoparticles, experimental studies are non-trivial, requiring the employment of many techniques such as high-resolution transmission electron microscopy (HRTEM), x-ray absorption fine spectroscopy (XAS), scanning tunnelling microscopy (STM) and atomic force microscopy (AFM) (Fig. 1.1).[5-11] However, their implicit size allows the use of computational modelling to complement experiment: theoretical studies using density functional theory tend to focus mainly on nanoparticles towards the lower end of this regime (<200 atoms), as these are much more computationally feasible. Modelling nanoparticles on a scale similar to experiment (≥3 nm) can be performed using interatomic potentials for computational efficiency, optimised according to experimentally measurable parameters, and should therefore replicate experimental behaviour.

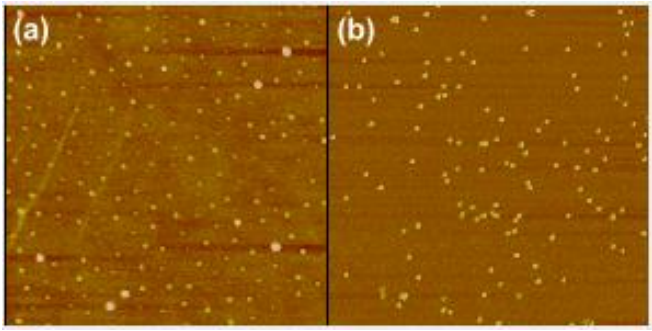

Fig. 1.1 AFM images of 25 nm diameter gold nanoparticles deposited onto a silicon wafer. (a) Ordered organisation, (b) random distribution. Frame sizes: 3 µm and 1 µm, respectively.[11]

Precious metal nanoparticles are of great interest, as they have been shown to be catalytically active for a variety of reactions such as CO and H_2 oxidation,

NO reduction, CO_2 hydrogenation, the water gas shift reaction and the catalytic combustion of methanol.[12-16] Given that these metals are inert as bulk materials, the high reactivity of these small particles is particularly intriguing. Since the first discovery of catalytically active gold nanoparticles by Haruta and Hutchings,[17-18] gold nanoparticle/nanocluster reactivity has been extensively studied to understand the mechanism behind its unusual behaviour, providing a substantial data set for effect comparison. Catalysis is structurally sensitive, and thus catalytic turnover for a particular reaction is heavily influenced by (a) the chosen metal element, (b) the support and (c) the deposition method; all of which influence not only nanoparticle size, but their adopted geometry and the resulting availability of active sites for catalytic processes to occur. The extent of the influence of the above factors is still subject to debate, and thus we will begin by discussing generally the influencing factors in nanoparticle reactivity.

1.1 Size and shape effects

Nanoparticles have a very large surface area to volume ratio and thus surface reactivity is highly dependent on the size of the nanoparticle in question. The electron energy levels in bulk metals are in continuous energy bands. However, if the size of the system is substantially decreased into the finite realm, intrinsic quantum size effects occur, where the band structure begins to disappear and discrete energy levels become dominant (Fig. 1.2).

It was first suggested by Goodman *et al.* that the introduction of a band gap is what makes gold nanoparticles catalytically active; scanning tunnelling spectroscopy (STS) of Au nanoparticles supported on TiO_2 surfaces ($Au/TiO_2(110)$) showed a metal to non-metal transition as the size of the nanoparticles decreases below 3.5 x 1.3 nm^2 (diameter x height), as summarised in Table 1.1.[19] For nanoparticle sizes below this threshold, the Au/TiO_2 interaction dominates, resulting in a catalytically active system.

Table 1.1 STS of 'model' Au/TiO_2 nanoparticles: dependence of band gap and type on cluster size.

Diameter / nm	Height / nm	Layers	No. of atoms	Band gap / eV
1.5	0.6	~ 2	~ 35	> 1.5
2.5	1.0	~ 3	~ 170	0.6
3.0	1.3	~ 4	~ 340	0.3
4.0	1.5	~ 5	~ 600	0

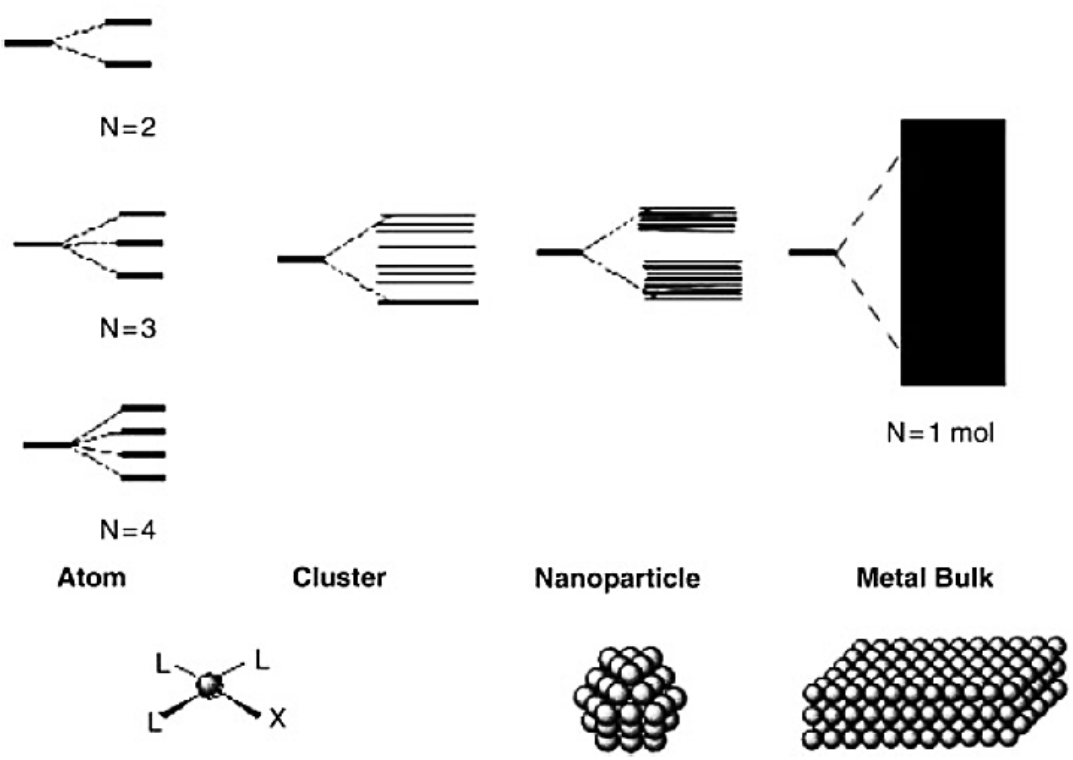

Fig. 1.2 Electron levels of atoms, clusters, nanoparticles and bulk metals.[20]

Despite the findings of Goodman *et al.* in regards to the emergence of a band gap, density functional theory calculations by Mills *et al.* found that the presence of a band gap is not essential for nanoparticle reactivity, as O_2 did not bind to flat, planar Au_n nanoparticles (n = 1-6 atoms).[21] However, O_2 binding did occur when these nanoparticles were deposited on an Au (111) surface, resulting in an Au_n/Au(111) system – a metallic system with no band gap. Similar calculations undertaken by Mavrikakis, Stolze and Nørskov[22] also found that flat bulk Au surfaces were not active for O_2 adsorption, with O_2

binding only occurring for kinked/stepped surfaces. Wu observed a preferential binding of CO at edge and vertex sites for Au nanoparticle DFT studies, whereas the flat nanoparticle surfaces were inactive.[23] Small nanoparticles are known to be intrinsically 'rough' – i.e. there will be a greater number of kinked sites available as nanoparticle size decreases. The fraction of step sites at the perimeter interface around the Au nanoparticle also increases significantly with decreasing particle size, as shown in Fig. 1.3. Therefore it is possible that these effects result in improved catalytic activity: kinks localise the Au nanoparticle HOMO, creating focused regions of HOMO electron density to which O_2 can readily bind, thus increasing charge transfer to the π^* oxygen orbital and catalytic activity.[24]

The mechanism behind catalytic activity is not clear and still open to debate. Another aspect of interest is the ability to control the reactivity or selectivity of the nanoparticle, by fine-tuning its shape. Different preparation methods yield different particle geometries, thus influencing the availability of step sites at which reactions can occur. Hemi-spherical particles have shown greater reactivity than spherical nanoparticles, and a number of different geometries have been identified and studied.[25-26] There is a strong experimental drive to achieve a monodispersed system, such that catalytic activity will be maintained under operating conditions. Favoured geometries occur at specific nuclearities, termed 'magic numbers' – these are nanoparticles that exhibit a particularly high stability as a result of geometric shell and/or electronic shell closure. Structural shell closure is attained when the number of atoms is sufficient to form a high-symmetry structural motif, such as icosahedral, decahedral and cuboctahedral (Ih, Dh and CO, respectively). Electronic closure occurs when the total number of electrons results in a complete valence shell, and a substantial energy gap (~1-2 eV) occurs between the HOMO and LUMO. Experimentally, these magic clusters are of interest as their high stability will favour fully monodispersed systems. They can also be identified through mass spectra – a particularly strong peak is exhibited, indicative of the greater stability with respect to dissociation in comparison to neighbouring atomic sizes, as shown in Fig (1.3).[27]

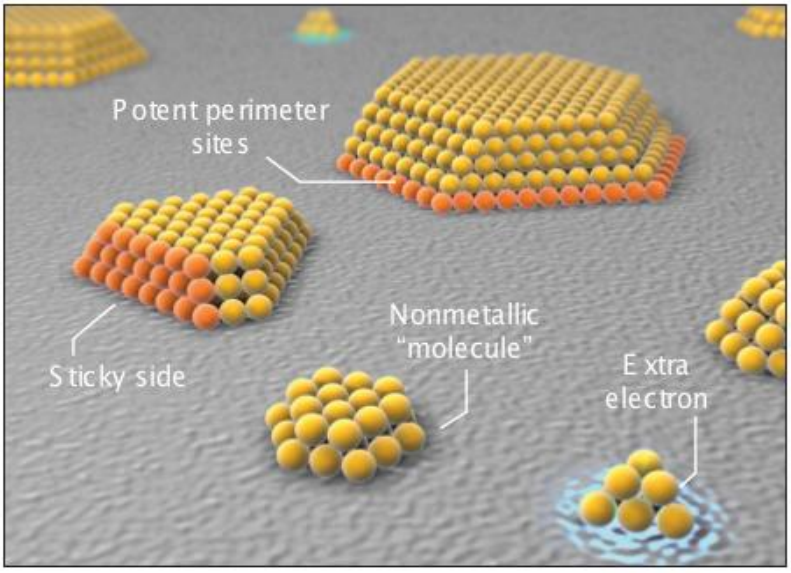

Fig. 1.3 Schematic diagram depicting possible reasons as to why Au nanoparticles are catalytically active.[28]

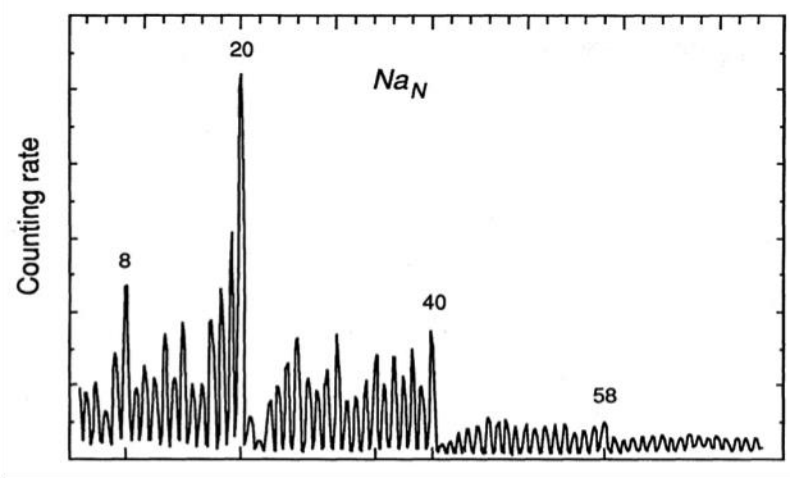

Fig. 1.4 Mass spectrum of sodium nanoparticles, showing jellium magic numbers at cluster sizes of 8, 20, 40 and 58 atoms. Larger peaks indicate greater stability with respect to dissociation.[27]

1.2 Nanoparticle-support interactions

Practical implementation of nanoparticles in catalysis requires the use of a support material, but these supports also affect nanoparticle nucleation and growth. It is hard to determine which properties of the nanoparticle/support system are related to quantum size effects and which are related to metal-support interactions. The smaller the nanoparticle, the greater the number of

surface atoms available for catalysis. However, the fraction of surface atoms interacting with the support is also increased, which changes the properties of the whole nanoparticle. Furthermore, the atomic arrangement on a surface dramatically affects coordination and active site availability. Adsorbate molecules have a particular affinity for a certain active site, and therefore an increase or decrease in the number of these particular active sites can strongly influence catalytic activity.[29]

The role of the support is also still currently under discussion. Hakkinen *et al.*[26,30] attributed the catalytic activity of small Au nanoparticles to the charge-transfer effect from the support, and later studies by Yoon *et al.*[31] and Yan *et al.*[32] highlighted the importance of oxygen vacancies (F-centres) for CO oxidation when using supported Au nanoparticles. The CO oxidation reaction has been used throughout past literature as a standard for measuring the activity of supported nanoparticles. Schubert and co-workers studied CO oxidation for gold nanoparticles on varying supports, showing that irreducible oxide supports (having the ability to store or adsorb oxygen at low temperature e.g. Al_2O_3 and MgO) had a lower, but still considerable turnover frequency in regards to CO oxidation, whereas reducible transition metal oxides (e.g. Fe_2O_3, TiO_2) exhibited far superior activity, of up to an order of magnitude greater.[33] This increased activity for TiO_2 was also observed by Grundwalt *et al.* and Bollinger and Vannice.[34-35] It is thought that in the case of reducible supports, the influence of oxygen vacancies improves O_2 trapping or changes the charge state of the Au nanoparticle.[36-40] Thus it is suggested that for 'inert supports', CO oxidation occurs on the gold nanoparticle, whereas for 'active' metal oxides, the role of the support is essential, as the CO molecule adsorbs and binds to oxygen atoms within the support. In the latter instance, the size of the gold nanoparticle plays a secondary role.

When Comotti *et al.* studied the same reaction comparing supports for Au nanoparticles, both Au/TiO_2 and $Au/\gamma\text{-}Al_2O_3$ were highly active, despite $\gamma\text{-}Al_2O_3$ having a low ability to absorb or store oxygen.[41] All nanoparticles were deemed to have the same size distribution, thereby suggesting that the support affected the adopted geometry of the nanoparticle, resulting in different activity rates. A similar study performed by Lopez and co-workers,[42] contrary

to the work of Schubert *et al.*, found that the differences in the conversion for reducible and irreducible supports were of a factor of 2-4, thus indicating that the reducibility of the support was not an essential consideration. Lopez *et al.* analysed a large amount of data comparing supports, as shown in Fig. 1.5, surmising that a property directly related to the nanoparticle size dominates, and any contributions from the support material, whilst possibly important, are a secondary, smaller influence. This conclusion is also supported by the work of Okumura *et al.*, who found catalytic activity of the nanoparticle to be independent of the 'reducible' support as long as the nanoparticles were sufficiently small.[43] Finally, enhanced CO oxidation is also observed for metal carbide supports, such as TiC.[44-46] Au−C interactions induce a significant charge polarisation around the Au nanoparticle, facilitating the bonding of electron acceptor molecules (such as CO and SO_2).

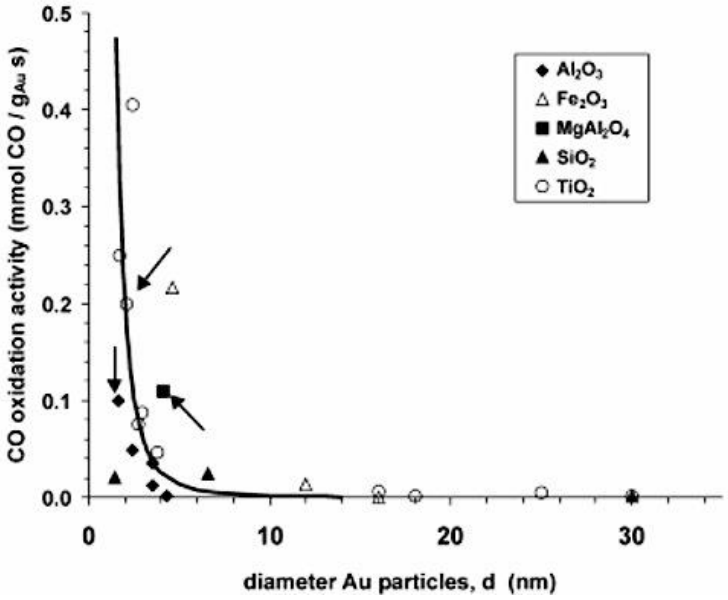

Fig. 1.5 Measured activities (in mmol CO/(gAus)) for CO oxidation at 273 K over different Au-based catalysts as a function of the average particle size (d, in nm). Supports are indicated by the symbol shape. Open symbols are used for reducible supports; solid symbols for irreducible supports. The curve shows a $1/d^3$ guide to the eye, showing that the activity of gold catalysts is approximately proportional to the number of low-coordinated atoms at the corners of the gold particles. Arrows indicate the measurements undertaken by Lopez *et al.*.[42] Full accounts of data and references can be found at http://www.fysik.dtu.dk/CooxidationGoldNano.pdf

As shown in this brief discussion, the elucidation of Au nanoparticle activity is complex, with much room for debate and interpretation of the aforementioned influences. Whilst we may not understand the operating mechanism, nanoparticles can be optimised for specific catalytic reactions, through choice of support, deposition method and reaction conditions. However, to scale these reactions to industrial proportions, the high cost of precious metals is not appealing even on the nanoscale. Therefore, we look at reducing the molar weight of Au that is used in these catalytic reactions, through the combinatory use of a second material. The second element of choice is typically another metal that is more abundant and cheaper, resulting in a synergistic effect for the bimetallic nanoparticle: a reduction in scale-up costs and little compromise in activity; indeed, in some cases, activity can be tuned and enhanced in bimetallic nanoparticles.

1.3 Bimetallic nanoparticles: composition and mixing effects

The ability to fine-tune the nanoparticle structure and properties through the creation of nanoalloys is of great interest in materials science: not only do bimetallic nanoparticles display magic numbers in terms of atomic size, but 'magic compositions' have also been predicted, in which the nanoparticles exhibit a particularly high stability or reactivity at a certain composition.[47-48] XPS studies showed the thermal stability of $Au_{0.8}Fe_{0.2}$ to be particularly high, in comparison to other Au/Fe compositions.[49] Similarly, Mottet *et al.* found a considerable shift to higher melting points of Ag nanoparticles when combined with Ni and Cu impurities.[50] These 'super stabilities' arise as a result of a synergistic effect from the combination of the two metallic species, and thus bimetallic nanoparticles hold promise for attaining the 'best of both worlds' from each respective element.

The chemical composition of a bimetallic nanoparticle can dictate the resultant mixing pattern (chemical arrangement) and, in turn, the properties of the nanoalloy. Four main types of mixing patterns are identified for bimetallic AB systems:

1. *Alloy* [ordered and random, as illustrated in Fig. 1.6 (a) and (b), respectively], involving a high degree of intermixing and a high number of interactions between the two metallic species.

2. *Core-shell*, illustrated in Fig. 1.6(c), where a core of one metallic species is surrounded by an outer shell of the second metallic species. The interactions between the two metallic species are at the interface between the core and shell regions. In this work, the core@shell notation is used throughout (although shell[core] and $A_{core}B_{shell}$ notations are also used in other works).

3. *Segregated subclusters*, illustrated in Fig. 1.6(d) and (e), involving two separate regions, each consisting of one metal type, sharing a common interface with few A−B bonds. Whilst in theory this is a possible structure, it is not actually known for any specific bimetallic combination.

4. *Layered multishell structures* (onion-like), as shown in Fig. 1.6(f), in which there is an alternating A−B−A type arrangement of shells, which has been found to be favoured by Ag-Pd and Co-Rh nanoparticles,[51-52] and most recently, 3-layer Pd-Au clusters were found to favour a tri-layer structure experimentally: AuPd@Au@Pd.[53]

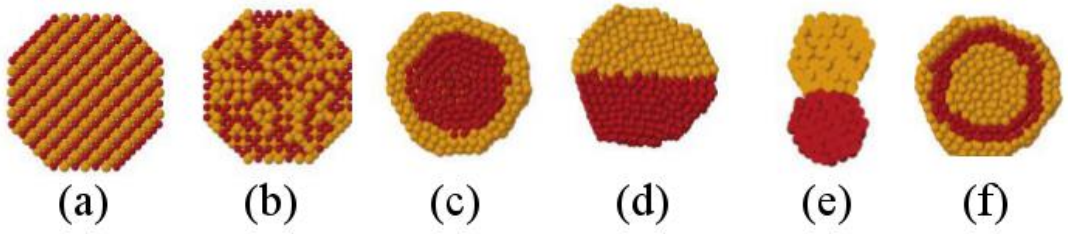

Fig. 1.6 Schematic representation of varying chemical arrangements, left to right: (a)/(b) mixed, (c) core@shell, (d)/(e) segregated subclusters, and (f) onion-like three-shell. The pictures show cross-sections of the specified nanoparticles.[7]

Prediction of the final preferred chemical arrangement of bimetallic nanoparticles is not an easy task, as ordering and segregation are dependent on several key factors, in particular the following:

a) The relative strengths of the A−B bonds, in comparison to A−A and B−B bonds. If the A−B bond is stronger than the monometallic bonds,

an alloy which maximises the number of these mixed interactions will be favoured more than a segregated system. Conversely, if the monometallic bonds are stronger, a segregated system is more favourable.

b) The relative electronegativities of the two metallic species. If one element is more electronegative than the other, the extent of charge transfer to this particular species will be greater, and thus to maximise charge transfer, mixing is favoured.

c) Relative atomic sizes – the smaller the atomic mismatch between two metallic species, the easier intermixing will be.[54-55]

d) The surface energies of the two metallic species. The element with the lowest surface energy will naturally migrate to the surface, as the creation of surfaces is easier for this metallic substituent.

e) Specific electronic/magnetic effects. Electron spin and/or electronic shell structure may stabilise particular chemical ordering.

f) Binding strength to ligands (e.g. CO, micelle): the species that binds most strongly to the surface ligand will favour surface segregation.

Therefore, there are many considerations when predicting chemical ordering within a nanoparticle. Nonetheless, despite the numerous thermodynamic arguments, it is possible experimentally to synthesise nanoparticles of a desired chemical arrangement, through kinetic trapping. These chemical routes usually follow a specific synthetic route, such as a sequential deposition/reduction technique to create a core@shell arrangement.[56]

1.4 Supported Au/Ag nanoparticles for photocatalytic hydrogen production

Thus far, we have highlighted the high catalytic activity of Au nanoparticles and the advantages of the introduction of a secondary metallic species. We now turn our attention to a specific catalytic process, namely photocatalytic hydrogen production, allowing consideration of properties that make Au and Ag nanoparticles suitable for this reaction. Photocatalytic hydrogen production is usually performed using nanoparticles supported on TiO_2, and therefore measurement of electronic properties can be performed with reference to the TiO_2 substrate.

TiO_2 is a highly promising semiconductor for use in photocatalysis, primarily due to its good surface stability and cost-effectiveness. Photocatalytic hydrogen production ideally uses water as its feedstock, although sacrificial agents are required experimentally (e.g. methanol, ethanol or glycols).[57] In principle, the TiO_2 semiconductor absorbs an incoming UV photon, resulting in the production of an electron-hole pair (charge carriers), of which the positive holes can interact with ethanol/water, and the electrons reduce any produced H^+ ions to H_2 gas, as illustrated in Fig. 1.7. However, TiO_2 alone is not efficient for photocatalysis, due to the fast recombination rates of the electron-hole pairs. The introduction of metal nanoparticles has been found to increase reaction efficiency by acting as an 'electron trap', extending the photocatalytic lifetime and reducing the overpotentials for H_2 production.

Electron transfer to Au nanoparticles is straightforward, given that the Au Fermi level (−5.1 eV for bulk Au[58]) (E_f) lies lower in energy than that for TiO_2 (−4.5 eV[59]). Subramanian observed a shift in the Fermi energy for Au/TiO_2 nanocomposites, from 230 mV for nano-TiO_2 to 290 mV for 3 nm Au/TiO_2 particles. Photo-excited electrons migrate to the nanoparticle until E_f is aligned in both systems: this electron storage in the Au nanoparticles allows a greater number of the remaining positive holes in TiO_2 to migrate to the surface for oxidation reactions. The electron depletion at the interface between the nanoparticle/semiconductor, known as a Schottky barrier, reduces recombination rates and facilitates charge separation.[60]

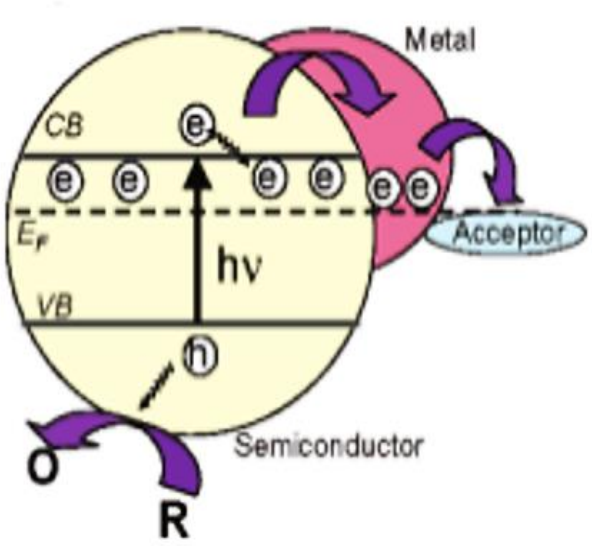

Fig. 1.7 Schematic diagram of Fermi-level equilibration between semiconductor and metallic nanoparticle.[60]

A comparative study of Au/TiO_2 and Pt/TiO_2 nanoparticles by Haruta *et al.* found that hydrogen production from ethylene glycol (or ethanol) aqueous solutions showed Au/TiO_2 to have a catalytic activity of ~70% of that observed for Pt/TiO_2, with an equivalent metal loading. However, the mean particle diameter of Au was larger than Pt (4.6 nm and 2.4 nm, respectively), which may also have been an influencing factor.[61] The effect of particle size and Au loading for the above reaction for Au/TiO_2 nanoparticles was studied by Murdoch *et al.*, showing that nanoparticle sizes in the range 3-30 nm were observed to be very active in the hydrogen production, although the particle size had little effect on the photoreaction in the 3-12 nm range.[62] The highest activity was observed for a 4 wt.% Au/TiO_2(anatase), whereas 8 wt.% Au/TiO_2(rutile) exhibited the highest rate of hydrogen production for the rutile TiO_2 phase. Wahab and co-workers found that Au/TiO_2(P25), which is a combination of the two TiO_2 phases (anatase:rutile ~3:~1[63]), had the highest activity rate of the three TiO_2 supports.[64]

In the complete photocatalytic decomposition of water, the recombination of H_2 and O_2 should be avoided. Thus, whilst Pt is also observed to be highly catalytically active, Au is deemed to be more of a suitable metal choice due to its lesser ability to oxidise hydrogen. Nonetheless, in terms of scaling this reaction towards industrial proportions, Au is still a very expensive metal

choice. As mentioned previously, Ag is a promising candidate as its partner in bimetallic nanoparticles, due to its similar activity and reduced material cost.

The electron storage potential of Ag is greater than that of Au and Pt, making it a very appealing candidate for use in photocatalytic hydrogen production.[65] However, electron transfer to Ag nanoparticles is not as straightforward as in the case of Au, as the E_f of Ag lies at a higher energy than TiO_2 (−4.26 eV for bulk Ag[58]). For electron transfer to Ag to occur, an overpotential is required and it is therefore unclear why this metal is active for photocatalytic hydrogen production when deposited on TiO_2. Suggestions of band bending at the Ag/TiO_2 interface (which have not been measured experimentally) have been raised, which could reduce (or even completely remove) the required overpotential (Fig. 1.8).

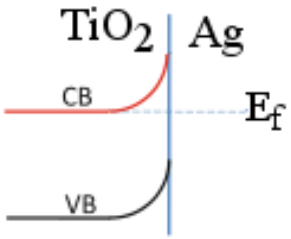

Fig. 1.8 Schematic representation of band bending at the TiO_2 surface / Ag nanoparticle interface.

Sclafani and Herrmann found that for photocatalytic dehydrogenation of 2-propanol, Ag/TiO_2 nanoparticles improved light absorption and subsequent creation of electron-hole pairs, with slightly better activity observed for the rutile phase.[66] Zhang *et al*. investigated both $Ag(0)/TiO_2$ and $Ag(I)/TiO_2$, determining that Ag(I) played a more dominant role in promoting electron-hole separation, thus facilitating photocatalytic degradation through promotion of charge transfer. Ag(0), on the other hand, was suggested to be responsible for the photo-stability of Ag/TiO_2 under visible light irradiation.[67]

Recently, Kennedy *et al*. compared photocatalytic hydrogen production activity for Au/TiO_2, Ag/TiO_2 and $AuAg/TiO_2$ for methanol reformation. The bimetallic nanoparticles were synthesised as alloys and core@shell arrangements, with both Ag@Au and Au@Ag. Au@Ag nanoparticles deposited on the TiO_2 surface were observed to have the highest hydrogen production rate, exceeding that of both the alloy and pure nanoparticles.[68]

1.5 Thesis aims

The work presented here focuses on 147-atom bimetallic AuAg nanoparticles, in particular determining how the chemical arrangement affects their associated properties, and how in turn they respond to experimental conditions, such as the presence of adsorbing molecular species and temperature. 147-atom clusters are chosen not only on the basis it is a magic number for the CO and Ih geometries, but also that the size is sufficient that any observed trends may be extrapolated to experiment, as quantum effects no longer affect any associated properties, as in some cases where 'every atom counts' (typically N < 100 atoms). We examine not only alloys but core@shell arrangements too, as we know that both are possible from experiment.[69]

Our first investigation (Ch. 3) concerns the most thermodynamically viable chemical orderings for these bimetallic nanoparticles, in terms of energetics and stability. These two factors are calculated as a function of the composition of the nanoparticle in question, to ensure that a bias towards Au is not favoured, given its naturally higher binding energy. Given the extremely large number of chemical arrangements that are possible for a 147-atom nanoparticle, the alloy arrangements are analysed using both interatomic potentials and the lowest-lying energy structures re-optimised using a higher-level density functional theory (DFT).

In Ch. 4, we establish the consequences of experimental calcination processes on the chemical arrangements of bimetallic AuAg nanoparticles. In experiment, it is common for high temperature heat treatments to remove long-chain protecting polymers, which are required to control nanoparticle size. Therefore, to replicate this experimental process, we subject the nanoparticles (using the arrangements as from Ch. 3) to an annealing procedure using ensemble MD simulations, to determine if there are any ill-effects.

Chapter 5 moves the focus to Ag nanoparticles and addresses the stability of Ag nanoparticles in a-Si, a popular supporting substrate used in photovoltaics. This chapter is in collaboration with Marcel Di Vece *et al*. (University of Utrecht), who provided interesting experimental data concerning the inter-diffusion of Ag atoms into a-Si. A particular directionality to this diffusion

was observed and thus we aim to re-create this theoretically, using ensemble MD calculations, and determine whether defects stimulate this diffusion.

Finally, the influence of adsorbing molecular species is explored in chapter 6. The possibility of using CO as a probe molecule is examined for detecting changes in surface species, with the aim to pair data with that obtained at Diamond Light Source using the *in situ* EXAFS/DRIFTS facility. Final conclusions are given in the final chapter 7.

1.6 References

1. Liu, J. P.; Fullerton, E.; Gutfleisch, O.; Sellmyer, D. J., *Nanoscale Magnetic Materials and Applications*; Springer, 2009.
2. Chuan-Jian, Z.; Jin, L.; Bin, F.; Bridgid, N. W.; Peter, N. N.; Rameshwori, L.; Jun, Y., Nanostructured Catalysts in Fuel Cells. *Nanotechnology* **2010**, *21*, 062001.
3. Hsieh, C.-T.; Lin, J.-Y., Fabrication of Bimetallic Pt–M (M = Fe, Co, and Ni) Nanoparticle/Carbon Nanotube Electrocatalysts for Direct Methanol Fuel Cells. *Journal of Power Sources* **2009**, *188*, 347-352.
4. Matsui, I., Nanoparticles for Electronic Device Applications: A Brief Review. *Journal of chemical engineering of Japan* **2005**, *38*, 535-546.
5. Antunez-Flores, W.; Miki-Yoshida, M.; Garcia-Gutierrez, D.; Zhou, J.; Jose-Yacaman, M., Hrtem and Haadf Analysis of Au Nanoparticles Supported on Tio2 Thin Films. *Microscopy and Microanalysis* **2003**, *9*, 414-415.
6. Chan, S. C.; Barteau, M. A., Preparation of Highly Uniform Ag/Tio2 and Au/Tio2 Supported Nanoparticle Catalysts by Photodeposition. *Langmuir* **2005**, *21*, 5588-5595.
7. Russell, A. E.; Rose, A., X-Ray Absorption Spectroscopy of Low Temperature Fuel Cell Catalysts. *Chemical Reviews* **2004**, *104*, 4613-4636.
8. Fedlheim, D. L.; Foss, C. A., *Metal Nanoparticles: Synthesis, Characterization, and Applications*; CRC press, 2001.
9. Jimenez, V.; Caballero, A.; Fernandez, A.; Espinós, J.; Ocana, M.; Gonzalez-Elipe, A., Structural Characterization of Partially Amorphous Sno 2 Nanoparticles by Factor Analysis of Xas and Ft-Ir Spectra. *Solid State Ionics* **1999**, *116*, 117-127.
10. Samorì, P., Scanning Probe Microscopies Beyond Imaging. *Journal of Materials Chemistry* **2004**, *14*, 1353-1366.
11. Darwich, S.; Mougin, K.; Rao, A.; Gnecco, E.; Jayaraman, S.; Haidara, H., Manipulation of Gold Colloidal Nanoparticles with Atomic Force Microscopy in Dynamic Mode: Influence of Particle–Substrate Chemistry and Morphology, and of Operating Conditions. *Beilstein journal of nanotechnology* **2011**, *2*, 85-98.
12. Zhou, S.; Varughese, B.; Eichhorn, B.; Jackson, G.; McIlwrath, K., Pt–Cu Core–Shell and Alloy Nanoparticles for Heterogeneous Nox Reduction: Anomalous Stability and Reactivity of a Core–Shell Nanostructure. *Angewandte Chemie* **2005**, *117*, 4615-4619.
13. Knudsen, J.; Nilekar, A. U.; Vang, R. T.; Schnadt, J.; Kunkes, E. L.; Dumesic, J. A.; Mavrikakis, M.; Besenbacher, F., A Cu/Pt near-Surface Alloy for Water-Gas Shift Catalysis. *Journal of the American Chemical Society* **2007**, *129*, 6485-6490.
14. Wieckowski, A.; Savinova, E. R.; Vayenas, C. G., *Catalysis and Electrocatalysis at Nanoparticle Surfaces*; CRC Press, 2003.
15. Molenbroek, A.; Haukka, S.; Clausen, B., Alloying in Cu/Pd Nanoparticle Catalysts. *The Journal of Physical Chemistry B* **1998**, *102*, 10680-10689.
16. Liu, Z.; Ling, X., Su Xd and Lee Jy. *J. Phys. Chem. B* **2004**, *2004*, 108.
17. Haruta, M.; Kobayashi, T.; Sano, H.; Yamada, N., Novel Gold Catalysts for the Oxidation of Carbon Monoxide at a Temperature Far Below 0. Deg. C. *Chemistry Letters* **1987**, 405-408.
18. Hutchings, G. J., Vapor Phase Hydrochlorination of Acetylene: Correlation of Catalytic Activity of Supported Metal Chloride Catalysts. *Journal of Catalysis* **1985**, *96*, 292-295.
19. Valden, M.; Lai, X.; Goodman, D. W., Onset of Catalytic Activity of Gold Clusters on Titania with the Appearance of Nonmetallic Properties. *science* **1998**, *281*, 1647-1650.

20. Philippot, K.; Serp, P., Concepts in Nanocatalysis. *Nanomaterials in Catalysis, First Edition* **2013**, 1-54.
21. Mills, G.; Gordon, M. S.; Metiu, H., Oxygen Adsorption on Au Clusters and a Rough Au (111) Surface: The Role of Surface Flatness, Electron Confinement, Excess Electrons, and Band Gap. *The Journal of chemical physics* **2003**, *118*, 4198-4205.
22. Mavrikakis, M.; Stoltze, P.; Nørskov, J. K., Making Gold Less Noble. *Catalysis Letters* **2000**, *64*, 101-106.
23. Wu, X.; Senapati, L.; Nayak, S.; Selloni, A.; Hajaligol, M., A Density Functional Study of Carbon Monoxide Adsorption on Small Cationic, Neutral, and Anionic Gold Clusters. *The Journal of chemical physics* **2002**, *117*, 4010-4015.
24. Cuenya, B. R., Synthesis and Catalytic Properties of Metal Nanoparticles: Size, Shape, Support, Composition, and Oxidation State Effects. *Thin Solid Films* **2010**, *518*, 3127-3150.
25. Haruta, M., Nanoparticulate Gold Catalysts for Low-Temperature Co Oxidation. *Journal of New Materials for Electrochemical Systems* **2004**, *7*, 163-172.
26. Häkkinen, H.; Abbet, S.; Sanchez, A.; Heiz, U.; Landman, U., Structural, Electronic, and Impurity-Doping Effects in Nanoscale Chemistry: Supported Gold Nanoclusters. *Angewandte Chemie International Edition* **2003**, *42*, 1297-1300.
27. Knight, W.-D.; Clemenger, K.; de Heer, W. A.; Saunders, W. A.; Chou, M.; Cohen, M. L., Electronic Shell Structure and Abundances of Sodium Clusters. *Physical review letters* **1984**, *52*, 2141.
28. Cho, A., Connecting the Dots to Custom Catalysts. *Science* **2003**, *299*, 1684-1685.
29. Bond, G. C.; Louis, C.; Thompson, D. T., *Catalysis by Gold*; World Scientific, 2006; Vol. 6.
30. Sanchez, A.; Abbet, S.; Heiz, U.; Schneider, W.-D.; Häkkinen, H.; Barnett, R.; Landman, U., When Gold Is Not Noble: Nanoscale Gold Catalysts. *The Journal of Physical Chemistry A* **1999**, *103*, 9573-9578.
31. Yoon, B.; Häkkinen, H.; Landman, U.; Wörz, A. S.; Antonietti, J.-M.; Abbet, S.; Judai, K.; Heiz, U., Charging Effects on Bonding and Catalyzed Oxidation of Co on Au8 Clusters on Mgo. *Science* **2005**, *307*, 403-407.
32. Yan, Z.; Chinta, S.; Mohamed, A. A.; Fackler, J. P.; Goodman, D. W., The Role of F-Centers in Catalysis by Au Supported on Mgo. *Journal of the American Chemical Society* **2005**, *127*, 1604-1605.
33. Schubert, M. M.; Hackenberg, S.; Van Veen, A. C.; Muhler, M.; Plzak, V.; Behm, R. J., Co Oxidation over Supported Gold Catalysts—"Inert" and "Active" Support Materials and Their Role for the Oxygen Supply During Reaction. *Journal of Catalysis* **2001**, *197*, 113-122.
34. Grunwaldt, J.-D.; Maciejewski, M.; Becker, O. S.; Fabrizioli, P.; Baiker, A., Comparative Study of Au/Tio 2 and Au/Zro 2 Catalysts for Low-Temperature Co Oxidation. *Journal of Catalysis* **1999**, *186*, 458-469.
35. Lin, S. D.; Bollinger, M.; Vannice, M. A., Low Temperature Co Oxidation over Au/Tio2 and Au/Sio2 Catalysts. *Catalysis Letters* **1993**, *17*, 245-262.
36. Boccuzzi, F.; Chiorino, A.; Manzoli, M.; Lu, P.; Akita, T.; Ichikawa, S.; Haruta, M., Au/Tio 2 Nanosized Samples: A Catalytic, Tem, and Ftir Study of the Effect of Calcination Temperature on the Co Oxidation. *Journal of Catalysis* **2001**, *202*, 256-267.
37. Manzoli, M.; Chiorino, A.; Boccuzzi, F., Ftir Study of Nanosized Gold on Zro 2 and Tio 2. *Surface science* **2003**, *532*, 377-382.
38. Schaub, R.; Wahlström, E.; Rønnau, A.; Lægsgaard, E.; Stensgaard, I.; Besenbacher, F., Oxygen-Mediated Diffusion of Oxygen Vacancies on the Tio2 (110) Surface. *Science* **2003**, *299*, 377-379.

39. Wu, X.; Selloni, A.; Lazzeri, M.; Nayak, S. K., Oxygen Vacancy Mediated Adsorption and Reactions of Molecular Oxygen on the Tio 2 (110) Surface. *Physical Review B* **2003**, *68*, 241402.
40. Wahlström, E.; Lopez, N.; Schaub, R.; Thostrup, P.; Rønnau, A.; Africh, C.; Lægsgaard, E.; Nørskov, J. K.; Besenbacher, F., Bonding of Gold Nanoclusters to Oxygen Vacancies on Rutile T I O 2 (110). *Physical review letters* **2003**, *90*, 026101.
41. Comotti, M.; Li, W.-C.; Spliethoff, B.; Schüth, F., Support Effect in High Activity Gold Catalysts for Co Oxidation. *Journal of the American Chemical Society* **2006**, *128*, 917-924.
42. Lopez, N.; Janssens, T.; Clausen, B.; Xu, Y.; Mavrikakis, M.; Bligaard, T.; Nørskov, J. K., On the Origin of the Catalytic Activity of Gold Nanoparticles for Low-Temperature Co Oxidation. *Journal of Catalysis* **2004**, *223*, 232-235.
43. Okumura, M.; Nakamura, S.; Tsubota, S.; Nakamura, T.; Azuma, M.; Haruta, M., Chemical Vapor Deposition of Gold on Al2o3, Sio2, and Tio2 for the Oxidation of Co and of H2. *Catalysis Letters* **1998**, *51*, 53-58.
44. Ono, L.; Sudfeld, D.; Cuenya, B. R., In Situ Gas-Phase Catalytic Properties of Tic-Supported Size-Selected Gold Nanoparticles Synthesized by Diblock Copolymer Encapsulation. *Surface science* **2006**, *600*, 5041-5050.
45. Ono, L. K.; Roldán-Cuenya, B., Effect of Interparticle Interaction on the Low Temperature Oxidation of Co over Size-Selected Au Nanocatalysts Supported on Ultrathin Tic Films. *Catalysis letters* **2007**, *113*, 86-94.
46. Rodriguez, J. A.; Ramírez, P. J.; Asara, G. G.; Viñes, F.; Evans, J.; Liu, P.; Ricart, J. M.; Illas, F., Charge Polarization at a Au–Tic Interface and the Generation of Highly Active and Selective Catalysts for the Low-Temperature Water–Gas Shift Reaction. *Angewandte Chemie* **2014**, *126*, 11452-11456.
47. Hu, G.; Nitze, F.; Gracia-Espino, E.; Ma, J.; Barzegar, H. R.; Sharifi, T.; Jia, X.; Shchukarev, A.; Lu, L.; Ma, C., Small Palladium Islands Embedded in Palladium–Tungsten Bimetallic Nanoparticles Form Catalytic Hotspots for Oxygen Reduction. *Nature communications* **2014**, *5*.
48. Greeley, J.; Stephens, I.; Bondarenko, A.; Johansson, T. P.; Hansen, H. A.; Jaramillo, T.; Rossmeisl, J.; Chorkendorff, I.; Nørskov, J. K., Alloys of Platinum and Early Transition Metals as Oxygen Reduction Electrocatalysts. *Nature chemistry* **2009**, *1*, 552-556.
49. Naitabdi, A.; Ono, L.; Behafarid, F.; Cuenya, B. R., Thermal Stability and Segregation Processes in Self-Assembled Size-Selected Au X Fe1-X Nanoparticles Deposited on Tio2 (110): Composition Effects. *The Journal of Physical Chemistry C* **2009**, *113*, 1433-1446.
50. Mottet, C.; Rossi, G.; Baletto, F.; Ferrando, R., Single Impurity Effect on the Melting of Nanoclusters. *Physical review letters* **2005**, *95*, 035501.
51. Baletto, F.; Mottet, C.; Ferrando, R., Growth of Three-Shell Onionlike Bimetallic Nanoparticles. *Physical review letters* **2003**, *90*, 135504.
52. Fromen, M.; Morillo, J.; Casanove, M.; Lecante, P., Structure and Chemical Order in Co–Rh Nanoparticles. *EPL (Europhysics Letters)* **2006**, *73*, 885.
53. Ferrer, D.; Torres-Castro, A.; Gao, X.; Sepulveda-Guzman, S.; Ortiz-Mendez, U.; Jose-Yacaman, M., Three-Layer Core/Shell Structure in Au-Pd Bimetallic Nanoparticles. *Nano letters* **2007**, *7*, 1701-1705.
54. Rapallo, A.; Rossi, G.; Ferrando, R.; Fortunelli, A.; Curley, B. C.; Lloyd, L. D.; Tarbuck, G. M.; Johnston, R. L., Global Optimization of Bimetallic Cluster Structures. I. Size-Mismatched Ag–Cu, Ag–Ni, and Au–Cu Systems. *The Journal of chemical physics* **2005**, *122*, 194308.
55. Rossi, G.; Ferrando, R.; Rapallo, A.; Fortunelli, A.; Curley, B. C.; Lloyd, L. D.; Johnston, R. L., Global Optimization of Bimetallic Cluster Structures. Ii. Size-Matched Ag-Pd, Ag-Au, and Pd-Pt Systems. *The Journal of chemical physics* **2005**, *122*, 194309.

56. Jiang, H.-L.; Akita, T.; Ishida, T.; Haruta, M.; Xu, Q., Synergistic Catalysis of Au@ Ag Core− Shell Nanoparticles Stabilized on Metal− Organic Framework. *Journal of the American Chemical Society* **2011**, *133*, 1304-1306.
57. Bahruji, H.; Bowker, M.; Davies, P. R.; Al-Mazroai, L. S.; Dickinson, A.; Greaves, J.; James, D.; Millard, L.; Pedrono, F., Sustainable H 2 Gas Production by Photocatalysis. *Journal of Photochemistry and Photobiology A: Chemistry* **2010**, *216*, 115-118.
58. Hölzl, J.; Schulte, F. K.; Wagner, H., *Springer Tracts in Modern Physics*; Springer-Verlag, 1979; Vol. 85.
59. Fang, X.; Wu, L., *Handbook of Innovative Nanomaterials: From Syntheses to Applications*; CRC Press, 2012.
60. Connelly, K.; Wahab, A.; Idriss, H., Photoreaction of Au/Tio2 for Hydrogen Production from Renewables: A Review on the Synergistic Effect between Anatase and Rutile Phases of Tio2. *Materials for renewable and sustainable energy* **2012**, *1*, 1-12.
61. Haruta, M., Size-and Support-Dependency in the Catalysis of Gold. *Catalysis today* **1997**, *36*, 153-166.
62. Murdoch, M.; Waterhouse, G.; Nadeem, M.; Metson, J.; Keane, M.; Howe, R.; Llorca, J.; Idriss, H., The Effect of Gold Loading and Particle Size on Photocatalytic Hydrogen Production from Ethanol over Au/Tio2 Nanoparticles. *Nature Chemistry* **2011**, *3*, 489-492.
63. Ohno, T.; Sarukawa, K.; Tokieda, K.; Matsumura, M., Morphology of a Tio 2 Photocatalyst (Degussa, P-25) Consisting of Anatase and Rutile Crystalline Phases. *Journal of Catalysis* **2001**, *203*, 82-86.
64. Wahab, K.; Hedhili, M.; Anjum, D.; Al Hazza, A.; Llorca, J., Hydrogen Production from Water over Semiconductor Materials: The Role of Synergism between Different Phases. *Abstracts of papers - American Chemical Society* **2012**, *244*.
65. Takai, A.; Kamat, P. V., Capture, Store, and Discharge. Shuttling Photogenerated Electrons across Tio2–Silver Interface. *Acs Nano* **2011**, *5*, 7369-7376.
66. Sclafani, A.; Herrmann, J.-M., Influence of Metallic Silver and of Platinum-Silver Bimetallic Deposits on the Photocatalytic Activity of Titania (Anatase and Rutile) in Organic and Aqueous Media. *Journal of Photochemistry and Photobiology A: Chemistry* **1998**, *113*, 181-188.
67. Zhang, H.; Wang, G.; Chen, D.; Lv, X.; Li, J., Tuning Photoelectrochemical Performances of Ag− Tio2 Nanocomposites Via Reduction/Oxidation of Ag. *Chemistry of Materials* **2008**, *20*, 6543-6549.
68. Kennedy, J.; Jones, W.; Morgan, D. J.; Bowker, M.; Lu, L.; Kiely, C. J.; Wells, P. P.; Dimitratos, N., Photocatalytic Hydrogen Production by Reforming of Methanol Using Au/Tio2, Ag/Tio2 and Au-Ag/Tio2 Catalysts. *Catalysis, Structure & Reactivity* **2015**, *1*, 35-43.
69. Li, Y.; Shi, Q.; Zhang, P.; Xiahou, Y.; Li, S.; Wang, D.; Xia, H., Empirical Structural Design of Core@Shell Au@Ag Nanoparticles for Sers Applications. *Journal of Materials Chemistry C* **2016**, *4*, 6649-6656.

2 Theoretical Methods

2.1 Energy Minimisation

Attainment of the most energetically favourable configuration of atoms in a system is achieved through a total energy minimisation, from a particular point on the potential energy surface (PES). The energy is minimised by moving the atoms until the forces on the atoms are zero, also known as a structural relaxation or geometry optimisation, and is almost always the starting point in an atomistic simulation. The total energy can be used to analytically calculate the forces on a system of *n* atoms:

$$\boldsymbol{F}_i = -\nabla_{\boldsymbol{r}_i} U(\boldsymbol{r}_1, \boldsymbol{r}_2, \ldots, \boldsymbol{r}_n) \qquad \textbf{(2-1)}$$

where $\nabla_{\boldsymbol{r}_i}$ indicates the gradient, and is dependent on coordinates of the atoms ($\boldsymbol{r}_1$, $\boldsymbol{r}_2$, …, $\boldsymbol{r}_n$). On the PES, several local minima exist, as indicated in Fig. 2.1, and thus it is not always possible to determine whether the lowest energy configuration possible (global minimum, GM) has been found. Stationary points correspond to regions where the slope of the PES is zero with respect to position ***r***:

$$\nabla_{r_i} U(\boldsymbol{r}_1, \boldsymbol{r}_2, \ldots, \boldsymbol{r}_n) = 0 \quad . \qquad \textbf{(2-2)}$$

There are two types of stationary points, corresponding to minima and saddle points. The gradient of the PES slope is downhill in all directions for saddle points; at a minimum, any movement away from the point increases in potential energy, i.e. the second derivative of the energy will be positive:

$$\frac{\partial^2 U}{\partial \boldsymbol{r}^2} > 0 \qquad . \qquad \textbf{(2-3)}$$

The forces on the atoms give the direction in which energy will decrease the fastest, although gradient-following alone is not sufficient for finding the lowest energy structure, and hence there are many different algorithms. Calculation of the total energy, however, is independent of the strategies employed for successful geometry optimisation. The most common methods for finding a minimum are based on derivatives, using the gradient of the potential energy slope to find the minimum, and can be done so in a direct manner (steepest descent, conjugate gradient) or iteratively (residual minimization method direct inversion in iterative subspace (RMM-DIIS),

Davidson). The algorithms employed in Ch. 3 and Ch.5 are iterative (RMM-DIIS and the Davidson scheme), which converge well for parallelisation over bands.

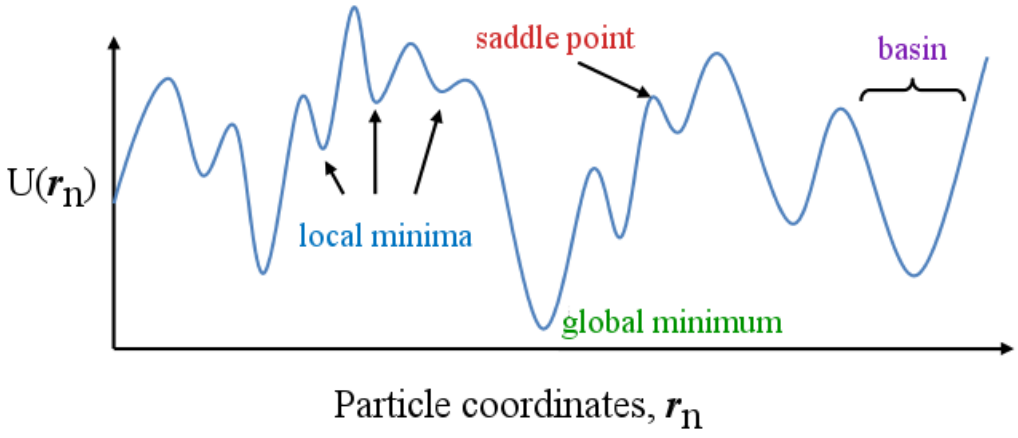

Fig. 2.1 Example PES identifying the different possible transition states for a configuration.

2.2 Force-fields

Force-fields, or potentials, are used to represent interactions between atoms, replicating experimental behaviour. They are computationally efficient and inexpensive, but the degree of transferability is very low, and as such, many interatomic potentials must be parameterised to replicate the same material properties obtained from experiment. Potentials that are fitted solely to experimental data are termed empirical, those with some properties calculated are termed semi-empirical, and quantum mechanical potentials ('ab-initio') are obtained in a purely theoretical manner. The total energy of a system with *n* atoms described by an empirical potential can be expanded in a many-body expansion:

$$U(\boldsymbol{r}_1, \ldots, \boldsymbol{r}_n) = \sum_i U_1(\boldsymbol{r}_i) + \sum_i \sum_{j>i} U_2(\boldsymbol{r}_i, \boldsymbol{r}_j) + \sum_i \sum_{j>i} \sum_{k>j} U_3(\boldsymbol{r}_i, \boldsymbol{r}_j, \boldsymbol{r}_k) + \cdots \quad \textbf{(2-4)}$$

U_1 is a one-body term, due to an external field or boundary conditions (such as the walls of a container). U_2 is a pair potential, or two-body term, which considers the interaction of a pair of atoms dependent on their spacing, and do not interact with anything else. U_3 is a third body term, which arises when the effect of a third atom influences the U_2 interaction. Potentials may therefore be loosely classed as pair-

potentials or many-body potentials, depending on the presence of the U_3 (and higher) terms.

2.2.1 Pair potentials

One of the simplest pairwise potentials is the Lennard-Jones potential, consisting of an attractive and repulsive term to describe van der Waals interactions in inert gases and molecular systems. It has the form:

$$U(\boldsymbol{r}_{ij}) = 4\varepsilon\left[\left(\frac{\sigma}{\boldsymbol{r}_{ij}}\right)^{12} - \left(\frac{\sigma}{\boldsymbol{r}_{ij}}\right)^{6}\right] \quad \textbf{(2-5)}$$

where ε is the potential well-depth, as shown in Fig. 2.2, σ is the separation distance, and $U(\mathrm{r}_{ij})$ is the energy of the system as a whole. The $\left({}^{1}/_{\boldsymbol{r}_{ij}}\right)^{12}$ term represents the repulsion when atoms are brought within close proximity of one another: in close proximity, atomic electronic clouds overlap, increasing the energy of the system abruptly. At large distances, the $\left({}^{1}/_{\boldsymbol{r}_{ij}}\right)^{6}$ term dominates, describing the weakly attractive van der Waals dispersion forces.

Many studies on Lennard-Jones solids, liquids, surfaces, clusters have been performed, being the potential of choice when the focus of the investigation is on fundamental issues, rather than on properties of a specific material. However, pair potentials do not address the directionality of bonds, nor the environment dependence: in reality, bond strength should decrease as the local environment becomes too crowded due to Pauli's principle, and this is not reflected in the pair potential. Therefore, as the electronic structure of the material becomes more delocalised, higher terms are required, such that metal-metal interactions must be described using many-body potentials.

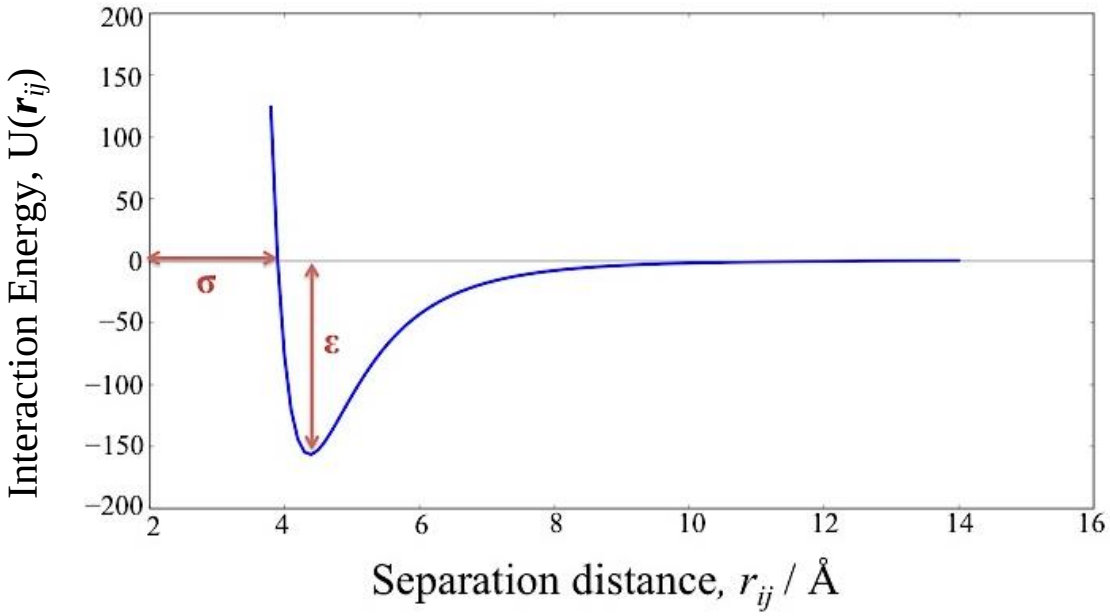

Fig. 2.2 Lennard-Jones potential for Kr, σ and ε are indicated.

2.2.2 Many-body potentials

Metal-metal interactions are frequently described using empirical potentials, of which the most popular are the embedded atom model, glue-model and those based on the second-moment approximation to the tight-binding energy (SMATB), and their variants.

The Gupta potential

The Gupta potential[1] is derived from the SMATB, consisting of an attractive many body (V_i^{m}) and a repulsive pair (V_i^{r}) term, obtained by summing over all *n* atoms, to give a total energy:

$$V_{\mathrm{clus}} = \sum_{i=0}^{n} \left(V_i^{\mathrm{r}} - V_i^{\mathrm{m}} \right) \quad . \tag{2-6}$$

V_i^{r} and V_i^{m} are defined as:

$$V_i^{\mathrm{r}}(\boldsymbol{r}_{ij}) = \sum_{j \neq i}^{n} A\, e^{-p\left(\frac{\boldsymbol{r}_{ij}}{r_0} - 1\right)} \tag{2-7}$$

and:

$$V_i^{\mathrm{m}}(\boldsymbol{r}_{ij}) = \left[\sum_{j\neq i}^{n} \xi^2 e^{-2q\left(\frac{r_{ij}}{r_0}-1\right)}\right]^{\frac{1}{2}} \quad \textbf{(2-8)}$$

where $\boldsymbol{r}_{ij}$ is the interatomic distance between atoms i and j, and r_0 is the equilibrium bond length. All other potential parameters (A, p, ξ and q) are fitted to reproduce experimental values for the cohesive energy, lattice parameters and independent elastic constants for the bulk crystal at 0 K. After fitting to bulk properties, the only independent parameters left (p and q) determine the range of the repulsive and attractive terms, respectively. A, p, ξ and q are assumed to only depend on the interacting species, and thus the Gupta potential naturally describes bond strength and atomic mismatch. Through the many-body (non-linear) term, it also reproduces the bond order/bond length correlations typical of metallic systems and leading, in particular, to a contraction of bond lengths at the metal surface.

The Gupta potential is known to reproduce kinetics in AuAg systems, having been used previously by Chen *et al*. and Calvo *et al*.,[2-4] and are thus used to represent any classical interactions throughout this work, with the exception of Ch.5. The parameters used in this study are taken from the work of Cleri and Rosato,[5] presented in Table 2.1.

Table 2.1 Gupta potential parameters as given by Cleri & Rosato. Bimetallic Au−Ag parameters are taken as the arithmetic mean of the pure parameters.

Parameter	A / eV	r_0 / Å	q	p	ξ / eV
Au−Au	0.2061	2.8843	4.036	10.229	1.790
Au−Ag	0.15445	2.8864	3.5875	10.5785	1.484
Ag−Ag	0.1028	2.8885	3.139	10.928	1.178

Embedded atom model

The embedded atom model (EAM) is an alternative but rather realistic approach to the description of bonding in metallic systems. It has a similar expression for the total energy of the system of n atoms to that of the SMATB, based on a different physical theory: the energy of the atom i is determined by the local electron density at the site of the atom i from all atoms j.

$$U = F_i(p_i) + \frac{1}{2}\sum_{j \neq i} \varphi_{ij}(\boldsymbol{r}_{ij}) \quad \textbf{(2-9)}$$

$$\rho_i = \sum_{j \neq i} f_j(\boldsymbol{r}_{ij}) \quad \textbf{(2-10)}$$

The energy of atom *i* is determined by the local electron density at the position of the atom and the function *f* describes the contribution to the electronic density at the site of the atom *i* from all atoms *j*. The sum over function *f* is therefore a measure of local electron density, ρ_i and the embedding energy *F* is the energy associated with placing an atom in the electron environment described by ρ. The pair-potential term, φ, describes electrostatic contributions.

Tersoff potential

Covalently bounded systems require different treatment as they must account for the potential energy coming from stretching, bending, and torsion deformations of bonds and their angles. The Tersoff potential is a three-body potential, making it simpler than the Gupta potential but more suitable for open structures than simple pair potentials, such as found in the Si diamond lattice. The Tersoff potential incorporates bond order into the atom-atom interactions, directly reflecting the strength of the bond; single, double and triple bonds will have bond orders of 1, 2, and 3, respectively. The bond order is defined as:

$$\Theta_{ij} = \frac{1}{2}(N_{ij}^{(\mathrm{b})} - N_{ij}^{(\mathrm{ab})}) \quad \textbf{(2-11)}$$

where *i* and *j* are the atoms forming the bond, N_{ij} is the number of electrons in the bonding (b) or antibonding (ab) orbital.

The bond order is assumed to depend on the coordination of an atom. Its form has a repulsive exponential and an attractive exponential scaled by a functional that is dependent on the number of neighbours, written as

$$V_{ij} = f_R(\boldsymbol{r}_{ij}) + b_{ij} f_A(\boldsymbol{r}_{ij}) \quad \textbf{(2-12)}$$

$$b_{ij} = (1 + \beta^n \zeta_{ij}^n)^{-1/2n} \quad \textbf{(2-13)}$$

$$\zeta_{ij} = \sum_{k \neq i,j} g(\theta_{ijk}) exp[\lambda(\boldsymbol{r}_{ij} - \boldsymbol{r}_{ik})^3] \quad \textbf{(2-14)}$$

where the subscript *R* and *A* refer to repulsive and attractive terms, respectively. The Tersoff potential is not a pair potential as b_{ij} is not constant, and refers to the bond order for the bond between atoms i and j. θ_{ijk} is the bond angle between atoms i, j and k, $g(\theta)$ is a function which gives an angular dependence to the potential and n, β and λ are parameters. This potential is fitted to elastic constants and phonon frequencies for group IV materials: silicon, germanium, carbon and their alloys based on a few parameters. In Ch. 5, we look at silver nanoparticles embedded in silicon, employing the use of the Tersoff potential for Si-Si and Ag-Si interactions. As the Ag-Si interactions are parameterised based on the EAM, and readily available, we also employ the EAM formalism for Ag–Ag interactions for this chapter only.

2.3 Electronic Structure Methods

Though the kinetics of metallic systems are well represented by the Gupta potential, it does not describe bond directionality and charge transfer effects, missing angular-dependent and coulombic interaction terms, respectively. Furthermore, empirical potentials cannot describe electronic closure effects either, which are explicitly related to the quantum confinement of the electron density and the associated discrete-ness in the spectrum of one-electron energy levels. Therefore, when these effects are included in the search for the groundstate configurations, this can alter the energetic ordering. In chapter 3, we begin by examining the most likely chemical arrangements for 147-atom AuAg nanoparticles, using the Gupta potential to initially represent Au−Ag interactions, due to the high number of electrons in the system (1617 e^-). The nanoparticles are then reoptimised at a higher level of theory, using quantum mechanical methods.

2.3.1 The Schrödinger equation

In order to determine the groundstate energy of a system, the Schrödinger equation must be solved. The time independent Schrödinger equation is of the form

$$\hat{H}\psi = E\psi, \qquad \textbf{(2-15)}$$

where $\hat{H}$ is the Hamiltonian operator, ψ is the wavefunction of the system, and E is the energy of the system. Solutions for the Schrödinger equation only exist at certain values of energy, termed eigenstates. For a single electron moving in one dimension, this can be re-written as:

$$-\frac{\hbar}{2m_e}\frac{d^2\psi}{dx^2} + V(x)\psi(x) = E\psi(x) \qquad \textbf{(2-16)}$$

where $\hbar$ is the reduced Planck's constant, m_e is the mass of the electron, ψ is the wavefunction, and V is the potential energy, dependent on position x. For an N electron, three-dimensional system, with 3N coordinates, equation (2-16) becomes:

$$\left[-\sum_{i=1}^{N}\frac{\hbar}{2m_i}\nabla_i^2 + V(x_1, \dots, z_N)\right]\psi = E\psi \qquad \textbf{(2-17)}$$

where particle i has mass m_i and coordinates (x_i, y_i, z_i), where $i = 1, 2, 3, \dots, N$. The kinetic energy is the sum of the kinetic energies of the individual electrons. The time independent wavefunction is a function of the 3N coordinates of the N electrons:

$$\psi = \psi(x_1, y_1, z_1, \dots, x_N, y_N, z_N) \quad . \qquad \textbf{(2-18)}$$

For a molecular system of N electrons and M nuclei, the wavefunction is dependent on both the positions of the electrons ($\boldsymbol{r}_i$) and the nuclei ($\boldsymbol{R}_i$). The molecular Hamiltonian can be broken down into the following contributions:

$$\hat{H} = \hat{T}_e + \hat{V}_{ee} + \hat{V}_{en} + \hat{V}_{nuc-nuc} \qquad \textbf{(2-19)}$$

where $\hat{T}_e$ and $\hat{T}_n$ is the kinetic energy of the electrons and nuclei, respectively:

$$\hat{T}_e = -\sum_i^N \frac{\hbar}{2m_e} \nabla^2(\boldsymbol{r}_i) \quad \textbf{(2-20)}$$

$$\hat{T}_n = -\sum_i^M \frac{\hbar}{2M_i} \nabla^2(\boldsymbol{R}_i) \quad \textbf{(2-21)}$$

where m_e is the mass of an electron and M_i is the mass of nucleus i. The three latter parts of the Hamiltonian, are the potential energy terms concerning the electron-electron ($\hat{V}_{ee}$), nucleus-nucleus ($\hat{V}_{nuc-nuc}$) interactions and the attractive Coulombic electron-nucleus ($\hat{V}_{en}$) interaction:

$$\hat{V}_{ee} = \sum_i^N \sum_{j>i}^N \frac{e^2}{4\pi\varepsilon_0 |\boldsymbol{r}_i - \boldsymbol{r}_j|} \quad \textbf{(2-22)}$$

$$\hat{V}_{nuc-nuc} = \sum_i^M \sum_{j>i}^M \frac{Z_i Z_j e^2}{4\pi\varepsilon_0 |\boldsymbol{R}_i - \boldsymbol{R}_j|} \quad \textbf{(2-23)}$$

$$\hat{V}_{e-nuc} = -\sum_i^M \sum_j^N \frac{Z_i e^2}{4\pi\varepsilon_0 |\boldsymbol{R}_i - \boldsymbol{r}_j|} \quad \textbf{(2-24)}$$

where Z_i is the atomic number of the nucleus i, e is the elementary charge of an electron and ε_0 is the permittivity of free space. Considering the extremely large differences in mass between nuclei and electrons, the nuclei are so slow moving that the electrons are approximated to be moving in a field of fixed nuclei. Fixed nuclei will have zero kinetic energy and the potential energy from nucleus-nucleus repulsion will be constant, which is known as the Born-Oppenheimer approximation. Thus the Schrödinger equation may be simplified to the electronic Hamiltonian:

$$\hat{H}_{elec} = \hat{T}_e + \hat{V}_{ee} + \hat{V}_{e-nuc} + \hat{V}_{nuc-nuc} \,. \quad \textbf{(2-25)}$$

Nonetheless, determination of eigenstates using the wavefunction is time consuming, due to the dependence of the wavefunction on 3N spatial and N spin coordinates. Thus electronic structure methods that require fewer variables are appealing in the calculation of energetic states and properties.

2.3.2 Density functional theory (DFT)

Density functional theory (DFT) attempts to calculate the ground state energy (E_0) and other ground-state molecular properties from the ground-state electron density, ρ_0, where the zero indicates the ground state.

The Hohenberg-Kohn theorems

The first Hohenberg-Kohn (HK1) theorem, established in 1964,[6] proved that for molecules with a nondegenerate ground state, the ground state energy, wavefunction and all other molecular electronic properties may be determined from the ground state electron probability density, ρ_0. The ground state energy is therefore written as a functional of ρ_0, such that $E_0 = E_0[\rho_0]$. $\rho_0(\boldsymbol{r})$ determines the external potential, $v(\boldsymbol{r}_i)$, and once specified, the electronic wavefunction and allowed energies of the molecule are determined as the solutions of the electronic Schrödinger equation. Hence the ground-state wavefunction and energy are also determined by ρ_0. This theorem implies that the ground state energy can be written as:

$$E_0 = E_v[\rho_0] = \int d\boldsymbol{r}\, v(\boldsymbol{r})\rho_0(\boldsymbol{r}) + F[\rho_0] \qquad \textbf{(2-26)}$$

where the functional $F[\rho_0]$, is independent of the external potential.[7-8] The functional $F[\rho_0]$ in equation (2-26) is unknown, and therefore is an impractical way of calculating E_0 from ρ_0. To transform this equation, a second theorem proven by Hohenberg and Kohn (HK2) is required, as well as an approach developed by Kohn and Sham. This second theorem is also known as the Hohenberg-Kohn variational theorem, who proved that for every trial density $\rho_{tr}(\boldsymbol{r})$ that satisfies $\int \rho_{tr}(\boldsymbol{r})\, d(\boldsymbol{r}) = N$ and $\rho_{tr}(\boldsymbol{r}) \geq 0$ for all $\boldsymbol{r}$, the following inequality holds true: $E_0 \leq E_v[\rho_{tr}]$, where E_v is the energy functional. Since $E_0 = E_v[\rho_0]$, we can say that the true ground state electron density minimises the energy functional $E_v[\rho_{tr}]$. Equation (2-26) becomes:

$$E_0 \leq E_v[\rho_{tr}] = \int d\boldsymbol{r}\, v(\boldsymbol{r})\rho_{tr}(\boldsymbol{r}) + F[\rho_{tr}] \qquad \textbf{(2-27)}$$

The Kohn-Sham method

HK1 tells us that in principle, it is possible to calculate the ground state molecular properties from ρ_0, without determining the molecular wavefunction. Nonetheless, it does not tell us how to calculate E_0 from ρ_0, nor how to determine ρ_0 without the wavefunction. From the HK theorems, Kohn and Sham derived a set of equations for a non-interacting system of N electrons, such that the ground state electron probability density of the reference system is equal to that of the molecule we are interested in.[9] In Kohn-Sham (KS) theory, this can be formulated as a simple expression for the ground state energy:

$$E_0 = E_v[\rho] = T_s[\rho] + V_{e-nuc}[\rho] + J[\rho] + E_{xc}[\rho] \qquad \textbf{(2-28)}$$

where V_{e-nuc} is the electron-nucleus potential energy, expressed in terms of an external potential due to the nuclei, V_{ext}. $T_s[\rho]$ is the KS kinetic energy of one electron orbitals (ϕ_i), for the non-interacting electrons, written as:

$$T_s[\rho] = \sum_i^N d\boldsymbol{r}\, \phi_i^*(\boldsymbol{r}) \left(-\frac{\hbar}{2m}\nabla^2\right) \phi_i(\boldsymbol{r}). \qquad \textbf{(2-29)}$$

$J[\rho]$ is the Coulomb energy:

$$J[\rho] = \frac{e^2}{2} \iint \frac{\rho(\boldsymbol{r})\rho(\boldsymbol{r}')}{|\boldsymbol{r}-\boldsymbol{r}'|} d\boldsymbol{r} d\boldsymbol{r}' , \qquad \textbf{(2-30)}$$

where E_{xc} is the exchange-correlation functional. $T_s[\rho]$ and $J[\rho]$ are analogous to T_e and $\hat{V}_{ee}$ [equation (2-25)], respectively. This is a non-classical electron-electron interaction, and is an unknown term. It is therefore approximated, and it is these approximations that define the accuracy with which the properties of the ground state are calculated. The exchange-correlation functional that is used in this work is the generalised gradient approximation (GGA),[10] which takes into account both the electron density and its gradient:

$$E_{xc} = E_{xc}^{GGA}[\rho(\boldsymbol{r}), \nabla\rho(\boldsymbol{r})] = E_x^{GGA}[\rho(\boldsymbol{r}), \nabla\rho(\boldsymbol{r})] + E_c^{GGA}[\rho(\boldsymbol{r}), \nabla\rho(\boldsymbol{r})] \qquad \textbf{(2-31)}$$

2.3.3 The projector augmented wave method

In order to calculate the ground-state energy of a system, the Kohn-Sham orbitals are expanded using basis set functions. Plane-wave basis sets have many advantages over atomic basis sets, in that they are orthogonal, not subject to Pulay forces, or basis set superposition error (BSSE). The accuracy of plane-wave basis sets is dependent on the energy cut-off chosen, but this must also be compromised with computational efficiency. The chemical properties of the element in question are dependent on the valence electrons, and with increasing atomic number, computational treatment to accurately represent all the electrons becomes increasingly complicated, requiring a large number of basis sets. Furthermore, close to the nucleus, valence wavefunctions are more oscillatory and require high energy plane-waves for accurate representation.

One solution is to consider the core electrons and the valence electrons separately, replacing the strong Coulomb potential between the nucleus and valence electrons with a weaker, modified 'pseudopotential', which also reproduce the screening effect as induced by core electrons. The wavefunction is considerably smoother, reducing computational cost.

The projector augmented wave method works in a similar manner, by transforming the oscillatory behaviour of the valence wavefunction at the nucleus by a linear transformation operator, $\hat{T}$, into a smooth pseudo-wavefunction, while conserving the true wavefunction. The linear transformation $[T]$ consists of a complete basis of partial waves for the valence electrons, a set of pseudo partial waves, and a set of projector functions. The projector augmented wave method (PAW)[11] is a generalisation of the pseudopotential and linear augmented plane wave methods; around each nucleus, *a*, with position $\boldsymbol{R}^a$, a cutoff r_c^a is defined, beyond which the valence wavefunction is smooth. Localised within the augmentation spheres ($|\boldsymbol{r} - \boldsymbol{R}^a| < r_c^a$), it is necessary to expand the wavefunction into a complete basis of *i* partial waves, $\phi(\boldsymbol{r})$. The smooth projector functions join (or augment) the partial and pseudo partial waves at a certain radius. The all-electron and pseudo wavefunctions differ within the core augmentation sphere but match exactly in the valence region. As the partial waves and projection operators do not depend on the

system being studied, they only need be calculated once for each element. Grid-based PAW is used in Ch. 3 and Ch. 6.

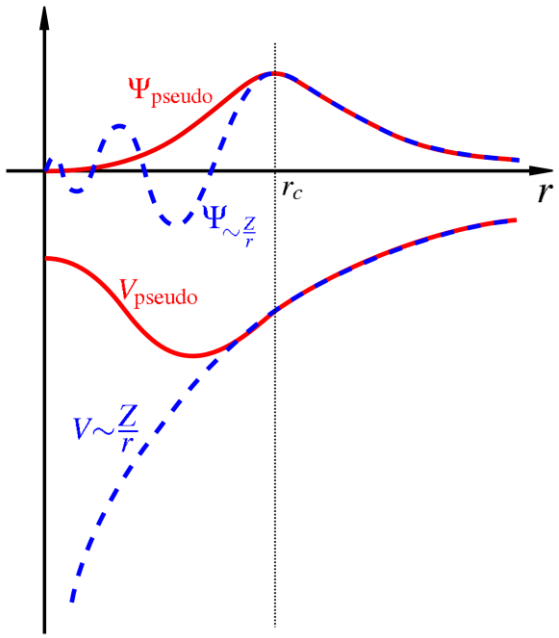

Fig. 2.3 Comparison of a wavefunction in the Coulomb potential of the nucleus (blue) to the one in the pseudopotential (red). The real and the pseudo wavefunction and potentials match above a certain cutoff radius, r_c.

2.4 Molecular Dynamics

Molecular dynamics (MD) is a computer simulation technique where the real-time evolution of a set of interacting molecules/atoms is predicted by numerically integrating Newton's equations of motion.[12] The trajectory is obtained by solving Newton's second law:[13]

$$md^2x(t) = \mathrm{F}\big(x(t)\big) \quad , \tag{2-32}$$

which describes the motion of a particle, where *m* is the mass of the particle, moving along coordinate *x*, *t* is time, and *F* is the force acting on the particle in that direction. For a more realistic system that contains *n* interacting particles, the force acting on a particle will change with position, or upon interaction with another particle, resulting in a set of *n*-coupled Newton's equations:

$$m\frac{d^2\boldsymbol{r_i}}{dt^2} = F_i(\boldsymbol{r}_1, \boldsymbol{r}_2, \ldots, \boldsymbol{r}_n), \;\; i = 1, 2, \ldots, n \tag{2-33}$$

where $\mathbf{r}_i$ are the position vectors, and F_i are the forces acting upon the *n* particles in the system (subscript *i* denotes one particle). The equations of motion for each particle are:

$$\frac{d\boldsymbol{r}_i}{dt} = \frac{p_i}{m} \tag{2-34}$$

$$\frac{dp_i}{dt} = F_i \tag{2-35}$$

where p_i is the momentum.

MD is a deterministic technique – given an initial set of positions and velocities, the real (time-dependent) motion of the particles can theoretically be determined. To find the trajectories, the equations of motion (Equations (2-34) and (2-35)) must be solved, but this cannot be done analytically due to the complicated functional form F_i. MD breaks down the integration into many small stages or timesteps (Δt), known as the finite difference approach. The total force on each particle in the configuration at a time, *t*, is the vector sum of its interactions with other particles. From the force, the acceleration of the particles can be determined, which is then combined with the current positions and velocities to generate new positions and velocities a short time ahead.[14] In this way, a dynamical trajectory is produced to describe the time

evolution of positions and momenta on a time grid. It is noted that the force is constant during the Δt. There are several MD software packages available, such as DL_POLY,[15] GROMACS[16] and AMBER.[17] The many-body Gupta potential, which is suitable for our nanoclusters, is readily available in DL_POLY. However, we have identified a book-keeping error in DL_POLY_Classic when using this particular potential, and thus perform our calculations using DL_POLY_4. DL_POLY_4 is newer and better supported, and should therefore have fewer issues. Additionally, it should be more suitable when looking to scale our calculations to larger nanocluster sizes.[18]

2.4.1 Integration algorithms

Time integration algorithms are used to solve the equations of motion, where time is 'discretized' on a finite grid, with Δt being the distance between consecutive points on the time grid. The most popular integration methods are based on the Verlet algorithm (Verlet,[12] leap-frog,[19] velocity Verlet,[20] Beeman[21]) and the predictor-corrector algorithms.[22] Here only the Verlet and velocity Verlet algorithms are discussed, as they probably the most commonly used integration methods, and are used in this project.

The Verlet algorithm assumes that the positions and dynamics of the system can be approximated using two third-order Taylor expansions; one forward and one backward in time.[23] Calling *v* the velocities (first time derivative of the position with respect to time), *a* the accelerations (second time derivative of the position with respect to time), and *b* the third derivative of the position with respect to time, we have:

$$\boldsymbol{r}(t+\Delta t) = \boldsymbol{r}(t) + \boldsymbol{v}(t)\Delta t + (1/2)a(t)\Delta t^2 + (1/6)b(t)\Delta t^3 + O(\Delta t^4) \quad \textbf{(2-36)}$$

$$\boldsymbol{r}(t-\Delta t) = \boldsymbol{r}(t) - \boldsymbol{v}(t)\Delta t + (1/2)a(t)\Delta t^2 - (1/6)b(t)\Delta t^3 + O(\Delta t^4) \quad \textbf{(2-37)}$$

Combining equations (2-36) and (2-37) gives

$$\boldsymbol{r}(t+\Delta t) = 2\boldsymbol{r}(t) - \boldsymbol{r}(t-\Delta t) + a(t)\Delta t^2 + O(\Delta t^4) \quad \textbf{(2-38)}$$

which can be re-written as

$$a(t) = -(1/m)F = -(1/m)\boldsymbol{\nabla}_{\boldsymbol{r}} V(\boldsymbol{r}_1, \boldsymbol{r}_2, \dots, \boldsymbol{r}_n). \quad \textbf{(2-39)}$$

The Verlet algorithm is simple to implement, accurate and stable. However, the velocities are not directly generated, though their knowledge is sometimes required to compute the kinetic energy. Therefore an improvement to obtain these is the velocity Verlet scheme,[20] which computes positions, velocities and accelerations at the time $(t + \Delta t)$:

$$\boldsymbol{r}(t + \Delta t) = \boldsymbol{r}(t) + \boldsymbol{v}(t)\Delta t + (1/2)a(t)\Delta t^2 \quad \textbf{(2-40)}$$

$$\boldsymbol{v}(t + \Delta t/2) = \boldsymbol{v}(t) + (1/2)a(t)\Delta t \quad \textbf{(2-41)}$$

$$a(t + \Delta t) = -(1/m)\nabla_r V(\boldsymbol{r}(t + \Delta t)) \quad \textbf{(2-42)}$$

$$\boldsymbol{v}(t + \Delta t) = \boldsymbol{v}(t + \Delta t/2) + (1/2)a(t + \Delta t)\Delta t \quad \textbf{(2-43)}$$

MD simulations solve the equations of motion in an iterative process, as outlined below in Fig. 2.4.

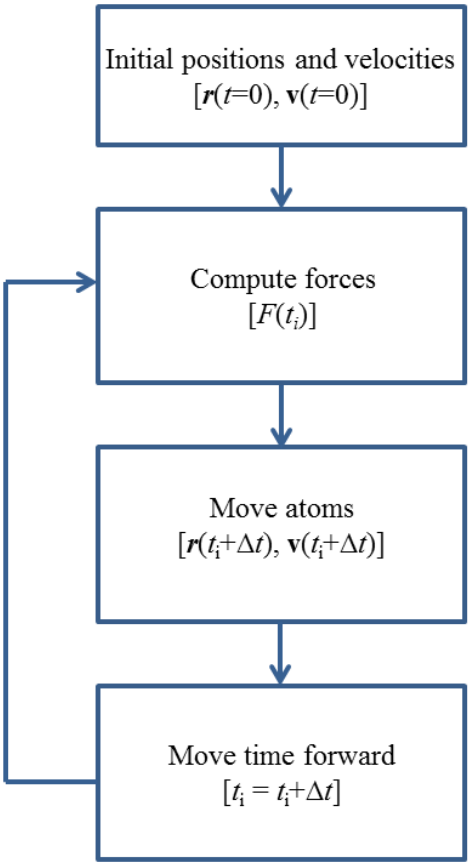

Fig. 2.4 Schematic flow chart of the process used to calculated new atomic positions and forces at a given time, *t*.

2.4.2 Ensembles

Integration of Newton's equations of motion allows for exploration of the constant-energy surface of a system. However, to mimic experimental conditions, state variables such as temperature and pressure are kept fixed. Depending on the chosen constraints, different statistical ensembles can be generated, which are briefly outlined in this section.

Microcanonical Ensemble (NVE)

The microcanonical ensemble isolates the system from changes in moles (N), volume (V) and energy (E) and thus is also referred to as an *NVE* ensemble. There is no heat exchange with the surrounding environment i.e. it is an adiabatic process. An MD trajectory of this form allows for the exchange of potential and kinetic energy, but the total energy is conserved. For every Δt, the position of each particle and its velocity are integration, using an integration scheme such as Verlet. Given the total energy is constant, all microstates have the same energy and equal probability. The microcanonical ensemble has little utility for simulation of real systems since experimental measurements are typically performed under constant temperature and/or pressure conditions. Therefore particularly important is the canonical ensemble, which describes the system at constant temperature, and is a distribution over microcanonical ensembles.

Canonical Ensemble (NVT)

The canonical ensemble conserves moles (N), volume (V) and temperature (T). Here, the energy of endothermic and exothermic processes is exchanged with an external heat bath, controlled by a thermostat. In this project, we have used the *NVT* ensemble, as the heat exchange from an external source is akin to the heat source used for experimental annealing at a specific temperature. As the system is no longer isolated, its total energy is no longer conserved. In the canonical ensemble, the average energy is fixed, thus allowing for fluctuations in the total energy and correspondingly in the temperature. Therefore, the total energy distribution is described by the Maxwell-Boltzmann distribution, as are the probability of the microstates. The thermostat gently drives the course of dynamics to the specific total

energy range that we are interested in, avoiding energy drifts in the system that may occur as a result of numerical noise.

Isothermal/Isobaric Ensemble (NPT)

This ensemble preserves *N*, pressure (*P*) and *T*. Both a barostat and thermostat are required to conserve pressure and temperature, respectively, corresponding to laboratory conditions of an open flask in ambient temperature and pressure. Although the synthesis of Au-Ag nanoclusters occurs at room pressure, we have used the *NVT* ensemble. We have not included periodic boundary conditions for our calculations due to the gas-phase nature of the isolated nanocluster; *NPT* only allows the volume of the unit cell to change, rendering the ensemble unsuitable.

2.4.3 Thermostats

As previously stated, the *NVT* (canonical) ensemble is the most appropriate, allowing specification of the temperature a priori and performing the simulation in the canonical ensemble. Care must be taken to preserve the correct thermodynamics as well as realistic dynamics – velocity rescaling does not generate the correct thermodynamic properties of the canonical ensemble nor the correct energy fluctuations in the system. Generation of the correct canonical ensemble is important to obtain a realistic (and comparable to experiment) Boltzmann distribution of the different microstates. Therefore, the use of a thermostat is necessary for the *NVT* ensemble to control the temperature fluctuations.[24]

Berendsen thermostat

The Berendsen thermostat is similar to a velocity rescaling approach, but rather than assuming that the velocities are completely scaled to the target temperature of each Δt, assigns a timescale for updating the velocities.[25] It is assumed that the system is weakly coupled to a heat bath, where the timescale of heat transfer (coupling constant) is τ (usually 0.1-0.4 ps).[26] The updating of velocities is written as follows:

$$\lambda^2 = 1 + \frac{\Delta t}{\tau}\left(\frac{T_0}{T} - 1\right) \qquad \textbf{(2-44)}$$

where λ is the velocity rescaling factor and T_0 is the initial temperature. Though the Berendsen thermostat does not generate a correct canonical ensemble, the properties derived for large systems (of the order of hundreds/thousands of atoms) are approximately correct. Additionally, it benefits from the efficiency with which it relaxes a system to some target (bath) temperature.

Nosé thermostat

Nosé reformulated the equations of motion to maintain a system at constant temperature by adding two additional degrees of freedom to the Hamiltonian for a Cartesian system:

1) s – the 'position' of an imaginary heat reservoir to which the system is coupled

2) p_s – the conjugate 'momentum' of the imaginary heat reservoir.[27]

Additionally, the parameter Q is introduced: an effective 'mass' that is associated with s, such that $p_s = Q\dot{s}$.

The system Hamiltonian is thus transformed:

$$H = K(p^N) + U(r^N) \quad \textbf{(2-45)}$$

$$= \frac{1}{2}\sum m_i|p_i|^2 + U(r^N) \quad \textbf{(2-46)}$$

$$= \frac{1}{2}\sum m_i|p_i|^2 + U(r^N) + \frac{p_s^2}{2Q} + k_B T(3N+1)\ln s \quad , \quad \textbf{(2-47)}$$

where the additional terms on the right hand side give the kinetic and potential energies of the added degrees of freedom for the heat bath, and k_B is the Boltzmann constant. The microcanonical partition function then follows:

$$\Omega \sim \frac{1}{N!}\int \delta[H-E]s^{3N}dp^N dr^N dp_s ds \quad \textbf{(2-48)}$$

$$\Omega = \frac{1}{N!}\frac{e^{E/k_B T}}{3N+1}\left[\int dp_s e^{\frac{-p_s^2/2Q}{k_B T}}\right]\left[\int e^{-\frac{K(p^N)+U(r^N)}{k_B T}} dr^N dp^N\right] \quad \textbf{(2-49)}$$

$$= \text{const} \times Q(T,V,N) \quad \textbf{(2-50)}$$

where E is the energy of the system and $Q(T,V,N)$ is the canonical partition function for the original N particles. For a detailed derivation, the reader is directed to Frenkel and Smit.[13] Therefore, a microcanonical simulation in the extended system (including heat bath degrees of freedom) returns a canonical ensemble for the original system. The trajectory will be solved for both the atomic coordinates as well as the heat bath degrees of freedom. The time evolution of the particles is deterministic rather than stochastic, resulting in the true dynamics of the system.

Nosé-Hoover thermostat

The above equations of Nosé are not convenient to implement – the scaling of the particle momenta by *s* implies that 'real' time is also variable.[28-29] Hoover developed an alternate formulation of the Nosé approach, where the Hamiltonian is rewritten as:

$$H = \frac{1}{2}\sum m_{\mathrm{i}}|p_i|^2 + U(r^N) + \frac{\xi^2 Q}{2} + 3Nk_B T \ln s \qquad \textbf{(2-51)}$$

where ξ is a friction coefficient that replaces p_s.

$$\frac{d \ln s}{dt} = \xi \qquad \textbf{(2-52)}$$

The Nosé-Hoover (NH) equations are frequently used due to their ability to generate a canonical ensemble; however, as it drives the system much more softly than Berendsen, very long thermalization is necessary. Therefore, the NH thermostat must be started close to equilibrium and it is common for systems to be initially equilibrated using the Berendsen scheme, followed by calculation of properties with the NH thermostat, which does generate trajectories that are consistent with a canonical ensemble. Due to the limitations outlined, we began our calculations by equilibrating our system using the Berendsen thermostat, and then switched to the NH thermostat for the subsequent production runs. Q was chosen following rigorous tests and based on previous literature values,[30-32] using relaxation constants of 0.1 ps and 0.01 ps for Berendsen and NH thermostats, respectively.

2.5 Experimental Methods

2.5.1 Transmission electron microscopy (TEM)

Transmission electron microscopy (TEM) is used to observe sample features, such as crystal structure, dislocations and grain boundaries. High-resolution TEM can be used to assess the geometry, composition, defects and size of nanoparticles. A beam of electrons is transmitted through the sample, interacting with the specimen as it passes through. As a consequence of this interaction, an image is formed and focused onto a fluorescent screen or photographic film. The TEM image produced has a significantly higher resolution than from traditional light microscopes, due to the smaller de Broglie wavelength of electrons, with optimal resolution able to see down to a few angstroms.

Imaging and Diffraction

The electron gun emits a beam of monochromatic electrons, which are focused into a thin coherent beam by electromagnetic condenser lenses. High angle electrons are excluded by the condenser aperture. The beam passes through the sample, where the degree of transmittance is dependent on the thickness and electron transparency of the specimen. Non-scattered electrons hit a fluorescent screen at the bottom of the microscope, creating an image of the specimen. The setup of a typical TEM is shown below in Fig. 2.5. TEM is frequently used to determine nanoparticle size distribution experimentally, and was used in the synthesis performed in Ch. 6.

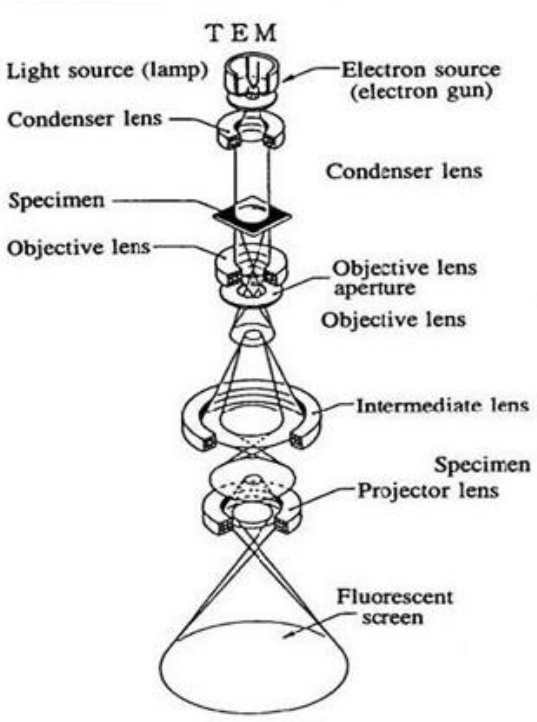

Fig. 2.5 Transmission electron microscope, taken from showing the electron path beam. Taken from JEOL 2000FX Handbook.

2.5.2 Diffuse Reflectance Infrared Fourier Transform Spectroscopy (DRIFTS)

The optical phenomena that occur in DRIFTS are different to that in transmittance IR spectroscopy. In traditional IR spectroscopy, the absorbance of infrared radiation that passes through the sample is measured. However, infrared radiation can also be reflected, or penetrate the sample before being scattered. If the particles are randomly orientated, penetration is isotropic, which is what constitutes the diffuse reflectance phenomenon. This back-reflected, diffusely scattered light is collected by the accessory, and directed to the detector optics. The light that leaves the surface has passed through a thin layer of the reflecting material, which modifies its wavelength content: the wavelength and intensity distribution of the reflected light will contain structural information on the substrate.

DRIFTS is advantageous as a fast and non-destructive local surface characterisation technique, which may be coupled to other techniques, such as XAS.[33] It is much more surface sensitive than a traditional transmission experiment; the relative contribution of the surface to the overall spectrum is far greater than in FTIR due to the grazing angle of the incoming radiation.[34]

2.5.3 Synchrotron Techniques

A synchrotron is a cyclic particle accelerator, which produces highly intense X-rays: electrons are accelerated at high speed close to that of light and undertake a forced change to their direction due to an applied magnetic field. The electromagnetic radiation that is emitted as a consequence (synchrotron light) is extremely intense and highly collimated, allowing for samples to be characterised in real-time.

There are five main components that make up the synchrotron: (i) the electron gun, (ii) the linear accelerator, (iii) booster ring, (iv) storage ring and (v) the beamline, as depicted in Fig. 2.6. Beginning at the electron gun, electrons are fired into the linear accelerator (linac) and packed into 'bunches', and pre-accelerated for injection into the booster ring, to 99.9997% of the speed of light. At the booster ring, the electrons are further accelerated, gaining energy of up to 6 GeV. Dipole bending magnets are used to curve the electrons around the trajectory and an RF voltage source accelerates the electrons along straight sections. Once the electrons have enough energy to produce light, they enter the storage ring at a rate of once per second, where they will have a lifetime of four to twelve hours.

The storage ring is maintained at a very low pressure (~10^9 mbar) and consists of dipole bending magnets and focusing magnets, which ensure that the electrons remain close to their ideal orbital path. As the electrons pass through each magnet, the direction of their flow is altered, causing them to give up their energy in the form of light. In addition to the magnets, insertion devices (wigglers and undulators) are also present within the storage ring: these smaller magnetic structures force the electrons to undertake an undulating/wavy trajectory, resulting in a much more focused and brilliant beam than that produced by a single magnet. It is here the intense X-ray beams are produced, emitted as dozens of thin beams, each directed toward a beamline next to the accelerator, for use in quick measurement experiments.

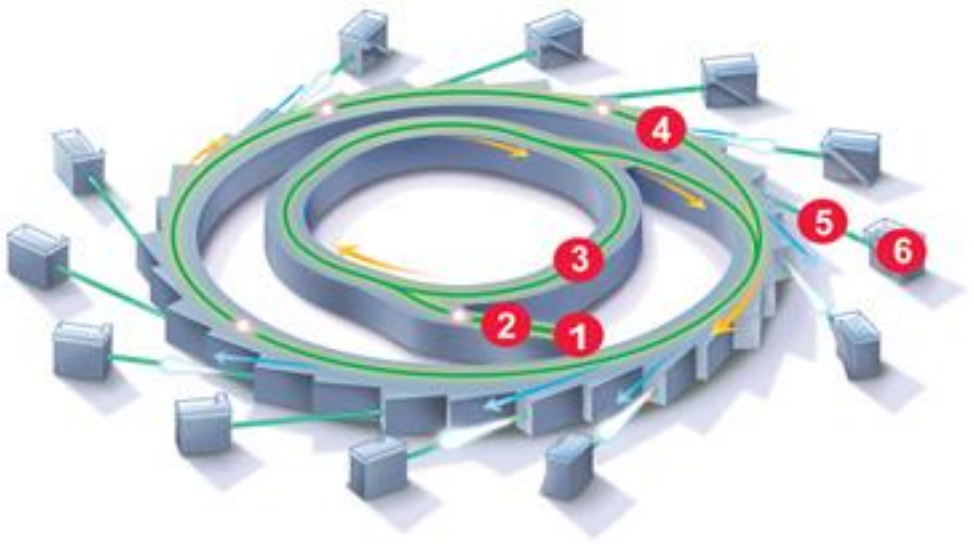

Fig. 2.6 Schematic diagram of a synchrotron: (1) Electron gun, (2) Linac, (3) Booster ring, (4) Storage ring, (5) Beamline, (6) End station (experimental hutch, control rooms). Taken from aerotech.com

2.5.4 X-ray Absorption Spectroscopy

X-ray absorption spectroscopy (XAS) is the measurement of the x-ray absorption coefficient ($\mu(E)$) of a material as a function of energy. XAS experiments require intense and tunable synchrotron X-ray beams to determine the local geometric and/or electronic structure of matter. n XAS spectrum consists of two main regions: (a) the X-ray absorption near edge structure (XANES), the region around an absorption edge, approximately 50 eV below, and above and (b) the extended X-ray absorption fine structure (EXAFS), the region of oscillatory structure above, extending up to approximately 1000 eV. Both XANES and EXAFS are related, but provide different insight into the local environment and chemical state of the sample.[35]

In XAS, an X-ray photon is absorbed by a core level of an atom, resulting in the subsequent emission of a photoelectron from the core shell. The ionised atom is left in an excited state, and the resultant core hole is then filled via either of the two following processes:

1) Auger emission: an electron falls from a higher level to fill the core hole. The transition energy liberated in this process is simultaneously transferred to a second outer electron, the Auger electron, which is then emitted.

2) X-ray fluorescence: the core hole is filled by an electron from another level, accompanied by the emission of an X-ray with energy equal to the difference in the energy of the core-levels.

These decay processes compete with each other, although fluorescence will dominate for elements with a high atomic number, whereas Auger electron emission is more probable for elements with a low atomic number.

XAS may be measured in three modes: transmission, fluorescence and electron yield. Transmission is the most straightforward, and used for measuring concentrated homogeneous samples. The X-ray flux transmittance through the sample is measured, with the X-ray beam intensity measured before and after the sample using ionisation detectors. Fluorescence mode is more appropriate for dilute (down to ppm levels), however, data quality is reduced in comparison to that obtained in transmission mode. Finally, electron yield collects emitted Auger electrons and is useful when fluorescence yield is low. However, this is much more time-consuming.

XANES provides a quick 'fingerprint' analysis that is element specific, arising mainly due to electronic transitions from the core level to higher unfilled or partially filled orbitals. It can be separated into three main features: (i) the absorption edge, E_0, dependent on the oxidation state and local geometry of the absorber, (ii) the pre-edge, resulting from electronic transition to empty bound states near the Fermi energy (usually seen for tetrahedral and distorted octahedral complexes) and (iii) post-edge, which is reliant on multiple scattering features.

For EXAFS, the focus is on the electron wave, propagating out of an atom. The wave is backscattered due to its surrounding neighbours, which causes interference effects to appear in its absorption pattern, and as a result, the local structural geometry can be determined. Bond distances are found easily and accurately through this technique. Coordination numbers may also be determined as the greater the number of surrounding neighbours, the greater the amplitude of the EXAFS oscillations. Both EXAFS and XANES experiments may be measured at any given temperature or pressure, and during reactions and indeed an experiment will normally measure the full spectrum including both near edge and EXAFS regions.

2.6 List of Reference Texts

Parr, R. G., Yang, W., *Density-Functional Theory of Atoms and Molecules*. Oxford University Press, (1989).

Koch, W., Holthausen, M. C., *A Chemist's Guide to Density Functional Theory*. Wiley-VCH Verlag GmbH, (2001).

Frenkel, D., Smit, B., Tobochnik, J., McKay, S. R. and Christian, W. Understanding Molecular Simulation. *Computers in Physics*, 11(4), pp.351-354, (1997).

Hubbard, A. T. *The Handbook of surface imaging and visualization*. CRC Press, (1995).

Schafer, R. and Schmidt, P. C. *Methods in Physical Chemistry, Volume 1*. Weinheim, Germany: Wiley‐VCH Verlag GmbH & Co. KGaA (2012).

2.7 References

1. Gupta, R. P., Lattice Relaxation at a Metal Surface. *Phys. Rev. B* **1981**, *23*, 6265-6270.
2. Chen, F.; Johnston, R. L., Martensitic Transformations in Ag-Au Bimetallic Core-Shell Nanoalloys. *Appl. Phys. Lett.* **2008**, *92*, 023112.
3. Logsdail, A. J.; Johnston, R. L., Interdependence of Structure and Chemical Order in High Symmetry $(Pdau)_N$ Nanoclusters. *RSC Advances* **2012**, *2*, 5863-5869.
4. Calvo, F.; Cottancin, E.; Broyer, M., Segregation, Core Alloying, and Shape Transitions in Bimetallic Nanoclusters: Monte Carlo Simulations. *Phys. Rev. B* **2008**, *77*, 121406.
5. Cleri, F.; Rosato, V., Tight-Binding Potentials for Transition Metals and Alloys. *Physical Review B* **1993**, *48*, 22.
6. Hohenberg, P.; Kohn, W., Inhomogeneous Electron Gas. *Physical review* **1964**, *136*, B864.
7. Levy, M., Universal Variational Functionals of Electron Densities, First-Order Density Matrices, and Natural Spin-Orbitals and Solution of the V-Representability Problem. *Proceedings of the National Academy of Sciences* **1979**, *76*, 6062-6065.
8. Levy, M., Electron Densities in Search of Hamiltonians. *Physical Review A* **1982**, *26*, 1200.
9. Kohn, W.; Sham, L. J., Self-Consistent Equations Including Exchange and Correlation Effects. *Physical Review* **1965**, *140*, A1133-A1138.
10. Perdew, J. P.; Burke, K.; Ernzerhof, M., Generalized Gradient Approximation Made Simple. *Physical review letters* **1996**, *77*, 3865.
11. Blöchl, P. E., Projector Augmented-Wave Method. *Physical Review B* **1994**, *50*, 17953.

12. Allen, M. P.; Tildesley, D. J., *Computer Simulation of Liquids*; Oxford university press, 1989.
13. Frenkel, D.; Smit, B., Understanding Molecular Simulations: From Algorithms to Applications. *Academic, San Diego* **1996**.
14. Leach, A. R., *Molecular Modelling: Principles and Applications*; Pearson education, 2001.
15. Smith, W.; Forester, T., Dl_Poly_2. 0: A General-Purpose Parallel Molecular Dynamics Simulation Package. *Journal of molecular graphics* **1996**, *14*, 136-141.
16. Hess, B.; Kutzner, C.; Van Der Spoel, D.; Lindahl, E., Gromacs 4: Algorithms for Highly Efficient, Load-Balanced, and Scalable Molecular Simulation. *Journal of chemical theory and computation* **2008**, *4*, 435-447.
17. Case, D. A.; Cheatham, T. E.; Darden, T.; Gohlke, H.; Luo, R.; Merz, K. M.; Onufriev, A.; Simmerling, C.; Wang, B.; Woods, R. J., The Amber Biomolecular Simulation Programs. *Journal of computational chemistry* **2005**, *26*, 1668-1688.
18. Todorov, I.; Smith, W.; Cheshire, U., The Dl Poly 4 User Manual. *STFC, STFC Daresbury Laboratory, Daresbury, Warrington, Cheshire, WA4 4AD, United Kingdom, version* **2011**, *4*.
19. Fincham, D., Leapfrog Rotational Algorithms. *Molecular Simulation* **1992**, *8*, 165-178.
20. Swope, W. C.; Andersen, H. C.; Berens, P. H.; Wilson, K. R., A Computer Simulation Method for the Calculation of Equilibrium Constants for the Formation of Physical Clusters of Molecules: Application to Small Water Clusters. *The Journal of Chemical Physics* **1982**, *76*, 637-649.
21. Beeman, D., Some Multistep Methods for Use in Molecular Dynamics Calculations. *Journal of Computational Physics* **1976**, *20*, 130-139.
22. Kresse, G.; Hafner, J., Ab Initio Molecular Dynamics for Liquid Metals. *Physical Review B* **1993**, *47*, 558.
23. Rapaport, D. C., *The Art of Molecular Dynamics Simulation*; Cambridge university press, 2004.
24. Leszczynski, J., *Handbook of Computational Chemistry*; Springer Science & Business Media, 2012; Vol. 2.
25. Berendsen, H. J.; Postma, J. v.; van Gunsteren, W. F.; DiNola, A.; Haak, J., Molecular Dynamics with Coupling to an External Bath. *The Journal of chemical physics* **1984**, *81*, 3684-3690.
26. Hünenberger, P. H., Thermostat Algorithms for Molecular Dynamics Simulations. In *Advanced Computer Simulation*, Springer: 2005; pp 105-149.
27. Nosé, S., A Unified Formulation of the Constant Temperature Molecular Dynamics Methods. *The Journal of chemical physics* **1984**, *81*, 511-519.
28. Nosé, S., A Molecular Dynamics Method for Simulations in the Canonical Ensemble. *Molecular physics* **1984**, *52*, 255-268.
29. Hoover, W. G., Canonical Dynamics: Equilibrium Phase-Space Distributions. *Physical review A* **1985**, *31*, 1695.
30. Mejía-Rosales, S. J.; Fernández-Navarro, C.; Pérez-Tijerina, E.; Montejano-Carrizales, J. M.; José-Yacamán, M., Two-Stage Melting of Au-Pd Nanoparticles. *The journal of physical chemistry B* **2006**, *110*, 12884-12889.
31. Rodrıguez-López, J.; Montejano-Carrizales, J.; José-Yacamán, M., Molecular Dynamics Study of Bimetallic Nanoparticles: The Case of Au X Cu Y Alloy Clusters. *Applied surface science* **2003**, *219*, 56-63.
32. Rodriguez-Lopez, J.; Montejano-Carrizales, J.; Pal, U.; Sanchez-Ramirez, J. F.; Troiani, H.; Garcia, D.; Miki-Yoshida, M.; Jose-Yacaman, M., Surface

Reconstruction and Decahedral Structure of Bimetallic Nanoparticles. *Physical review letters* **2004**, *92*, 196102.
33. Marinkovic, N. S.; Wang, Q.; Frenkel, A. I., In Situ Diffuse Reflectance Ir Spectroscopy and X-Ray Absorption Spectroscopy for Fast Catalytic Processes. *Journal of synchrotron radiation* **2011**, *18*, 447-455.
34. Smith, B. C., Fourier Transform Infrared Spectroscopy. *CRC, Boca Raton, FL* **1996**.
35. Koningsberger, D. C.; Mojet, B. L.; van Dorssen, G. E.; Ramaker, D. E., Xafs Spectroscopy; Fundamental Principles and Data Analysis. *Topics in Catalysis* **2000**, *10*, 143-155.

3 Segregation effects on the properties of $(AuAg)_{147}$: interatomic potentials and density functional theory

3.1 Introduction

Bimetallic nanoparticles, or nanoalloys, have garnered much recent interest, as the combination of two metallic species is thought to result in a synergistic effect – maintaining high catalytic activity whilst lowering production costs.[1] However, the introduction of a secondary metallic species greatly complicates the atomistic picture, as the chemical composition can dictate the chemical ordering, and in turn, the adopted geometry. Additionally, alloy arrangements can sometimes result in compromised rather than enhanced catalytic abilities, and thus the combination of the two metals does not always produce the desired effect. Thus core@shell arrangements also hold promise, as this particular chemical arrangement can be made using a particular sequential deposition synthesis technique.

As discussed in the Ch. 1, possible mixing patterns include random and mixed alloys, segregated subclusters, core@shell arrangements, and onion-like A-B-A layering.[2-3] The quantity of different chemical arrangements available, or 'homotops', for a particular geometry with composition $A_{n_A}B_{n_B}$ is defined as:

$$n_H = \frac{n!}{n_A!\, n_B!} \equiv \frac{n!}{n_A!\,(n - n_A!)} \qquad \textbf{(3-1)}$$

where n is the number of atoms in the cluster, n_H is the number of homotops and n_A and n_B are the number of atoms of type A and B, respectively.[4-7] As n increases, n_H becomes extremely large for alloy systems with a 1:1 metallic ratio.

3.1.1 High symmetry structures

In general, the geometries adopted by nanoparticles are dependent on the preparation conditions, atomic size, electronegativity and electronic charge of its constituent species.[8] Small nanoparticles tend to adopt compact, non-crystalline structures,

which minimise surface area at the expense of increased internal strain. As strain energy is generally proportional to cluster volume, non-crystalline structures become energetically unfavourable at large *n*, and thus there is a cluster size dependency. In the case of bimetallic nanoparticles, the role of atomic mismatch has been observed to have an important role in defining the most preferential chemical arrangements, with the smaller atomic species accommodated within the nanoparticle, reducing the overall strain energy, as observed for Ag−Ni, Ag−Cu and Au−Cu.[9]

Extensive theoretical studies have been performed to understand the geometric preferences of bimetallic AuAg nanoparticles, which vary with the size of the nanoparticle in question. Three prominent high symmetry structures are highlighted for nanoparticles: the icosahedron (Ih), the Ino-decahedron (I-Dh) and the cuboctahedron (CO), all of which form closed shell geometries at equivalent nuclearities i.e. magic numbers. For these three morphologies, the first magic numbers are 1, 13, 55, 92, 147 and 309.[10] Electronic stability can also occur when the total number of electrons results in a complete valence shell ($1s^2$, $2p^2$, $2p^6$, etc). A combination of both complete valence and closed atomic shells will result in the most stable nanoparticles.

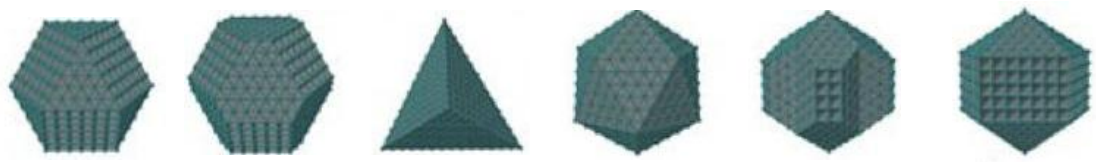

(a) (b) (c) (d) (e) (f)

Fig. 3.1 Common geometries observed in nanoparticles: (a) CO, (b) truncated octahedron, (c) tetrahedron, (d) Ih, (e) Marks decahedron, and (f) I-Dh.[11]

Fig. 3.1 shows examples of geometries observed in nanoparticles, of which the Ih[12-13] is common for noble and transition metals at small cluster sizes. The Ih is almost spherical, comprised solely of (111) faces, maximising nearest neighbour contact whilst minimising the surface area to volume ratio. It may be constructed through the packing of twenty tetrahedra sharing a common central vertex. For this packing to occur, the tetrahedra must be distorted, resulting in high internal strain (Fig. 3.2).

This geometry is typically adopted by small nanoparticles due to its prioritisation of minimising surface energy over strain contributions.

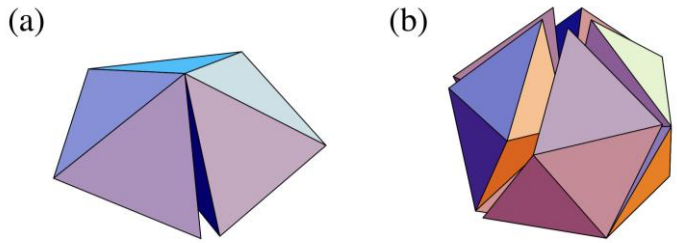

Fig. 3.2 (a) Packing five tetrahedra around a common vertex results in an edge gap of 7.36°, and (b) twenty tetrahedra around a common vertex results in gaps of 1.54 steradians (SI unit of a solid angle, used in 3D geometry; 1.54 steradians = 5055.53 square degrees). To accommodate for these gaps, the tetrahedra must be distorted, resulting in strain.

The I-Dh has 10 (111) faces and 5 (100) faces, whereas the CO has 8 (111) faces and 6 (100) faces. As *n* increases, the elastic strain becomes larger, and the I-Dh is more appealing for medium-sized nanoparticles (*n* ~100-200 atoms). The balance between elastic strain and minimising surface energies depends on the ratio of surface to bulk atoms, which can be approximated as $n^{2/3}$. Both Au and Ag have a bulk FCC structure and, given that the CO is a fragment of the FCC crystal, it is expected that as *n* increases even further the CO is favoured.

3.1.2 Previous theoretical studies on AuAg bimetallics

The preferred geometry and chemical arrangements of AuAg nanoparticles is an interesting debate, as based on traditional thermodynamic arguments, it is not necessarily clear how they would behave. There is minimal size mismatch between the two atomic species, with very similar homogeneous bond lengths: 2.889 and 2.884 Å for Ag and Au, respectively.[14] This suggests that AuAg systems will be highly miscible, with hardly any driving force for strain-induced segregation. However, the surface energy of Ag is less than that of Au (78 and 97 meV $Å^{-2}$, respectively[15]), which would favour surface segregation of Ag atoms. Furthermore, the cohesive energy of Ag is lower than that of Au (2.95 eV $atom^{-1}$ and 3.81 eV

atom^{-1}, respectively[16]), which implies that an Au core would be preferred, where the atoms will have a higher coordination.

Baletto *et al*. studied the variation between the Ih, decahedron (Dh) and truncated octahedron (TO) geometries with atomic size, surmising that the crossover window is highly dependent on the 'stickiness' of the interatomic potential used: the crystal strongly increases its energy for a change in interatomic distances,[17] which can be calculated from the value of *pq*, two of the Gupta potential parameters. Au has a very sticky potential, and thus has much smaller crossover windows in comparison to Ag, and especially more so than Cu, based on the Rosillo, Guillopè and Legrand (RGL) potential (Table 3.1).[14,18]

Table 3.1 Changing crossover sizes between favoured geometries as a result of *pq*, where *pq* is the product of parameters *p* and *q*: $n_{\mathbf{Ih\rightarrow Dh}}$ and $n_{\mathbf{Dh\rightarrow fcc}}$. Adapted from ref. 17.

Metal	*pq*	$n_{\mathbf{Ih\rightarrow Dh}}$	$n_{\mathbf{Dh\rightarrow fcc}}$	$n_{\mathbf{Ih\rightarrow fcc}}$
Cu	25.64	1000	>30000	1500
Ag	34.50	<300	20000	400
Pd	41.69	<100	6500	<100
Pt	41.23	<100	6500	<100
Au	45.28	<100	500	<100

Moving onto slightly larger clusters, Curley *et al.* investigated structure and segregation in 38-atom AuAg nanoclusters using a Gupta many-body potential, in conjunction with a genetic algorithm search technique.[19] These studies showed a clear tendency toward surface segregation of Ag atoms, with cluster stability increasing with the number of Au-Au bonds and decreasing with more Ag-Ag and Au-Ag bonds, as seen in Fig. 3.3. These studies are more in line with the first thermodynamic considerations mentioned. A range of geometries were observed in this work, from complete 6-fold pancakes to truncated octahedra.

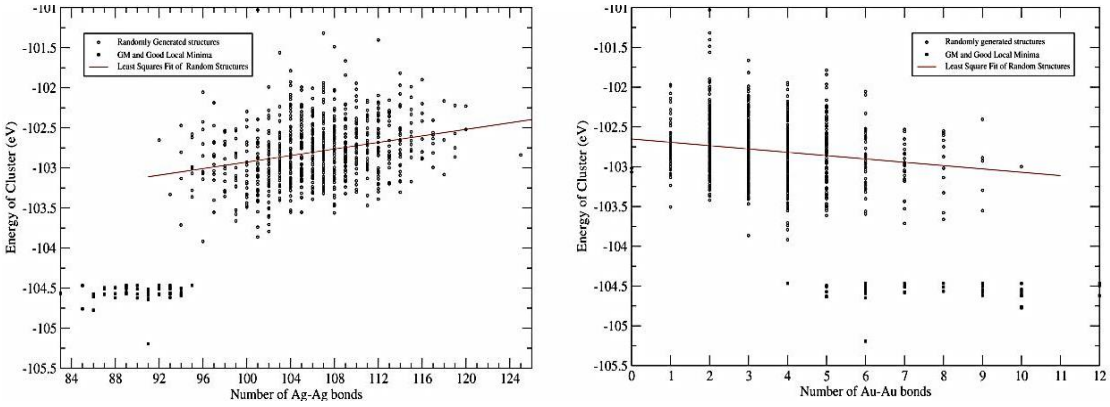

Fig. 3.3 Nanocluster energy becomes more positive with increasing Ag content (left) and more negative with increasing Au content (right).[19]

Moving to slightly large nanoclusters, Zhang and Fournier studied 55-atom AuAg Ih nanoclusters, using pairwise Morse functions, a purely covalent term, modified to include the electrostatic energy of screened atomic charges obtained through the electronegativity equalization (EE) method.[20] It was concluded that mixing metals with substantially different electronegativities (CuAu or AgAu) resulted in slightly higher cohesive energies (by 1%) in comparison to those with very similar electronegativities (CuAg). Relatively, this means that structures with a roughly 50-50% composition of two metallic systems will benefit the most from the stabilising effect of charge transfer, resulting in lower energies for these nanoalloys. For instance, the Mulliken[21] atomic charge in the Ag-Au dimer is −0.22 and +0.22 a.u. for Au and Ag respectively, due to their difference in electronegativity. The hetero-polar (ionic) bonding in Ag-Au nanoalloys favours Au-Ag mixing, as this increases the number of favourable Ag(δ+)-Au(δ-) interactions. For clusters of other compositions, the stabilising effect of charge transfer is found to be more pronounced in the clusters that are richer in the least electronegative element.

The Birmingham cluster genetic algorithm (BCGA)[22] was also used to determine the global minimum of Ih 55-atom AuAg nanoparticles by Chen *et al.*.[15] A single gold dopant was observed to occupy inner icosahedral sites within a silver rich cluster, as shown in Fig. 3.4. As Au content was increased to 13 atoms, it was observed that Au atoms begin to decorate the Ih surfaces, generally occupying positions with high point group symmetries. Further increase to the Au content of the nanocluster

resulted in greatly reduced symmetries for the lowest-energy structures until a 50:50 composition ($Au_{28}Ag_{27}$) was reached.

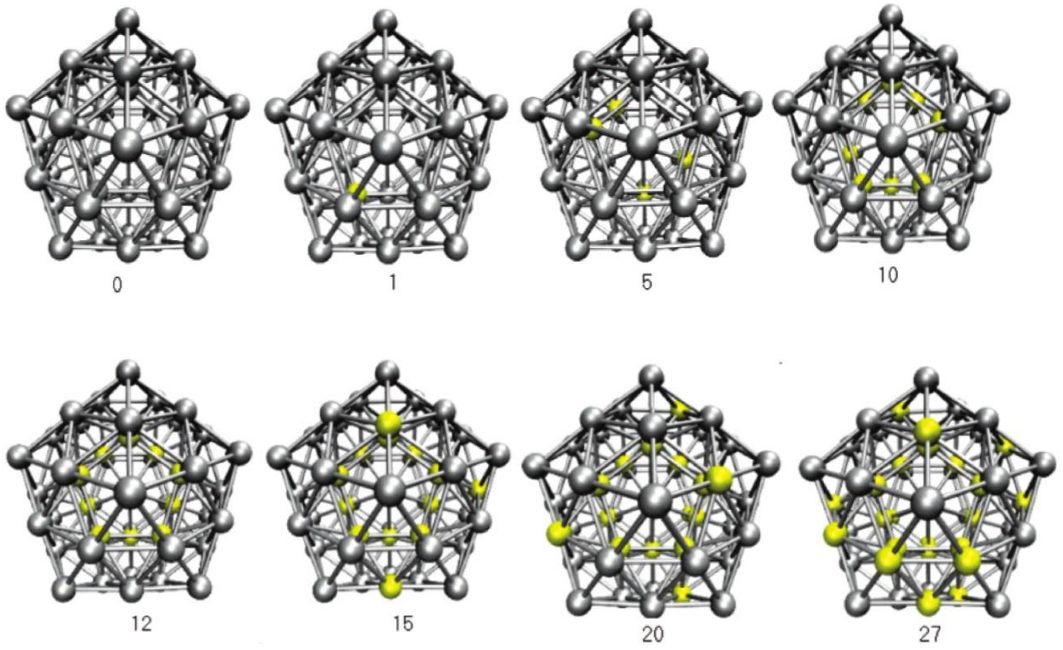

Fig. 3.4 55-atom AuAg nanoalloys of varying composition from Ag_{55} to $Au_{27}Ag_{28}$. Increasing Au content results in a reduction in the symmetry of the cluster. The numbers below indicate the number of gold atoms present; gold spheres represent Au, silver spheres represent Ag.[15]

Due to the size limitations that are placed on calculations from computational cost, previous density functional theory (DFT) studies have mainly focused on small AuAg nanoclusters. Heiles *et al.* produced a genetic algorithm (GA) coupled with DFT study of 8-atom AuAg nanoalloys.[23] The introduction of a single dopant atom into the cluster resulted in only slight distortions, with the structural motif remaining unchanged in the gold and silver rich case. The introduction of a second Ag atom yielded more interesting results, producing two nearly degenerate isomers. Isomer I, the global minimum (GM), was found to be 2D while isomer II was 3D (displayed in Fig. 3.5). Reconfiguration of these two isomers showed a difference of ~19 meV and ~39 meV using PWscf[24] and NWChem[25] respectively.

The above findings are supported by Zhao *et al.*,[26] who also reported the 2D structure to be lower in energy. Nonetheless, this energy difference between the two isomers is not significant enough to clearly identify the GM, due to the inaccuracies associated

with the applied techniques; the accuracy is smaller than the observed energetic separation, and GGA functionals are known to overestimate the stability of 2D structures. However, this study demonstrates that there is a clear transition to 3D structures upon the introduction of a third Ag atom, Au_5Ag_3.

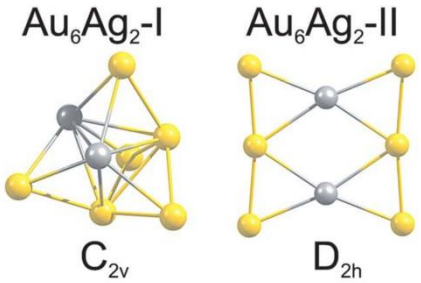

Fig. 3.5 The two isomers obtained as the GM for Au_6Ag_2. Gold spheres represent Au, silver spheres Ag.[23]

Zhao and Zeng studied small bimetallic nanoclusters of Au_xAg_y ($2 \leq x+y \leq 8$), using DFT with relativistic effective core potentials, in which a large amount of charge transfer was seen to occur between Au and Ag atoms.[27] The electronegativity of Au is greater than that of Ag (2.54 and 1.93 respectively[28]), and therefore charge transfer from Ag to Au is expected. Thus the conformations that allowed the largest charge transfer between gold and silver atoms were most favoured, with such topologies placing gold atoms in exposed (surface) positions, forming the most Au–Ag heterobonds.

Chen and Johnston also observed similar findings for Au_3Ag_{10} clusters. The influence of charge transfer plays a significant role in determining the structure adopted by small nanoalloys.[29] From semi-empirical potentials and DFT calculations, 13-atom AuAg nanoalloys were found to be most stable in an Ag@Au arrangement, which is attributed to the Ih (or octahedral) structural order inducing further charge transfer, in addition to that already present from electronegativity differences. This directional charge transfer occurs from the central atom to those at the periphery. As seen in Fig. 3.6, the Mulliken charges[21] are +0.256 *e* for the central Ag atom and −0.022 *e* for the peripheral Ag atom, favouring the less electronegative atom to be positioned at the centre of the nanocluster to maximise charge transfer. Through this reasoning, Chen *et al*. were able to demonstrate that 13-atom Au@Ag structures with high symmetry were energetically stable.

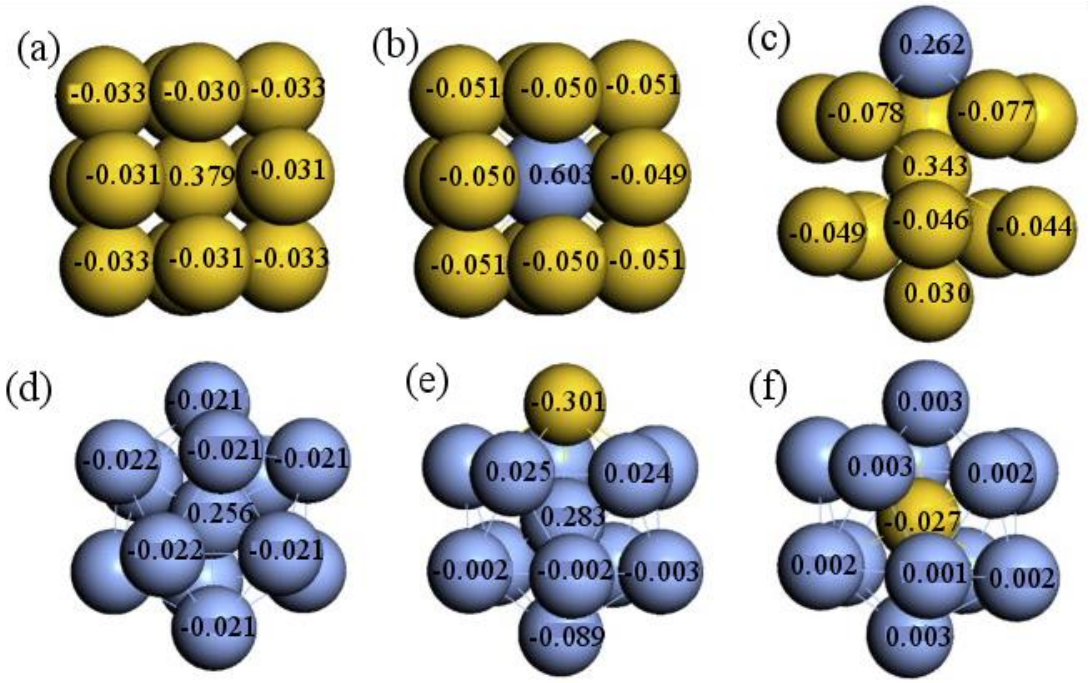

Fig. 3.6 Mulliken charges for 13-atom nanoclusters of (a) pure Au_{13}, (b) and (c) differing geometries for $Au_{12}Ag_1$, (d) pure Ag_{13}, (e) and (f) differing geometries for Au_1Ag_{12}. Additional charge transfer arises from the arrangement of the cluster, affecting stability.[29]

Chen and Johnston also carried out an intensive study of AuAg nanoparticles in a 1:1 ratio, for a range of n = 20-150, using a genetic algorithm global configuration followed by DFT reconfiguration.[30] For n = 20-40, polyicosahedral structures were determined, in an Au@Ag arrangement. From n = 42-66 (with the exception of n=60), a single Ag atom was observed to occupy the core site, while all other Ag atoms segregated to the surface. However, as n increased to 150, the core-shell chemical ordering was not necessary for the larger nanoparticles to maintain their stability. The mixing observed for these sizes is similar to that of a bulk AuAg alloy, an FCC-disordered solution.

3.2 Methodology

In this chapter, our study focuses on 147-atom nanoparticles, so that any results produced may be extrapolated for larger magic numbers and minimise quantum effects. Given that CO geometry is a fragment of the FCC structure, and is experimentally feasible, we focus on this morphology, also allowing for exploration

of both the (100) and (111) faces. These nanoparticles were created using mathematical constructs, and starting from pure Ag_{147}, the Au content was systematically increased until the final composition reached Au_{147}. The optimisation of the chemical ordering was investigated for Au_xAg_{147-x} where x = 1, 13, 55, 73, 92, 134 and 146. Our choices of x are such that the ratios of Au:Ag allow geometric 'magic number' core@shell arrangements to also be formed [x = 13, 55, 92, 134] as well as investigating a 1:1 alloy [x = 74] and the influence of a single atomic dopant [x = 1, 146].

Basin-hopping algorithm

Searches for the optimal chemical ordering of the nanoparticle were performed using the basin-hopping algorithm, as implemented in the software package GMIN.[31-32] More explicitly, the atomic swap functionality is used rather than full basin-hopping, ensuring that the CO arrangement is maintained throughout.

For each chemical composition investigated, a 500,000 iteration search was performed, with 0-147 atomic random swaps at each step, and the new chemical arrangement then energetically reminimised. The geometry and energies of the lowest energy structures were stored throughout. Convergence was deemed to have been achieved for the number of swaps and iterations when there was no variation in the lowest energy arrangements near to the end of the search.

DFT energy calculations

The lowest energy structures generated by GMIN were reminimised using the real-space grid finite-difference DFT code, GPAW.[33-35] The all-electron density approach in combination with the frozen core approximation results in a highly efficient calculation for transition metals. GPAW has the added benefit that isolated gas-phase nanoparticles can be studied without the need for large vacuum regions. The valence electrons are taken as 11 for both Au and Ag, and converged grid spacings of 0.18 for the numerical representation of the wavefunctions. A vacuum of 6 Å was added around the nanoparticle, ensuring that no spurious energies or cut-off artefacts were encountered. Convergence of the geometry optimisations was achieved when the forces on all atoms were reduced below 0.01 eV $Å^{-1}$.

The exchange correlation functional used is that of Perdew, Burke and Ernzerhof (PBE), with the residual minimisation method, direct inversion in iterative subspace (RMM-DIIS) used to calculate the eigenstates of the system. The number of explicit valence electrons in these calculations (1617 e^- in total) is odd, and thus an initial magnetic moment of μ=1 is assigned to the nanoparticle, to account for the unpaired electron. During geometry optimisation, μ is allowed to relax and tended towards μ=0 in all cases, supported by the spin contamination $\langle S^2 \rangle$, which also tended to 0. The delocalisation of μ is an artefact of the DFT method, and due to the metallic nature of the wavefunction at the Fermi Energy (E_f), the effect of geometry, energy and charge density is negligible. The difference in energy from spin-fixed DFT calculations with μ=1 was found to be less than 0.4 meV per atom, and consistent in sign for each arrangement, verifying the effect of delocalisation of the magnetic moment to be minimal.

Empirical potentials vs. DFT

In Ch. 2, the importance of re-optimisation at a higher level of theory (DFT) was highlighted, although the use of empirical potentials is not without merit. For comparison, the (100) and (111) surface energies of Au and Ag are calculated from the Gupta potential using the General Utility Lattice Program (GULP)[36-37] (examining both the Cleri-Rosato[14] and Mottet[17] parameters) and DFT, with the results summarised below in Table 3.2.

Table 3.2 Comparison of surface energies from different Gupta potential parameters, DFT and experiment. All values are in J m^{-2}.

Surface	Cleri-Rosato	Mottet	DFT	Experiment
Au (110)	0.614	0.561	0.897	1.5
Au (100)	0.578	0.532	0.833	
Au (111)	0.491	0.451	0.678	
Ag (110)	0.764	0.734	0.836	1.25
Ag (100)	0.704	0.666	0.760	
Ag (111)	0.626	0.595	0.688	

As we can see, the empirical potentials obtain the correct energetic ordering of the surfaces: (110) > (100) > (111), but the ordering of Au and Ag is completely different to that found from DFT and experiment – Au should have the higher surface energies. However, despite these findings, these potentials still predict correct kinetic behaviour as from experiment and thus can be used qualitatively to determine nanoparticle properties.

3.3 Energetic Analysis

In order to relate the differing stoichiometric compositions of our fixed−size bimetallic clusters, there are several methods of energetic analysis. The simplest observable is the binding energy, E_b:

$$E_b^{Gupta} = \frac{-E_{tot}^{Gupta}}{n} \quad \textbf{(3-2)}$$

where E_{tot}^{Gupta} represents the total energy of a cluster calculated at the Gupta level. For DFT calculations, E_b^{DFT} is more appropriate, as the free atom (E_{atom}^{DFT}) has kinetic contributions (E_{atom}^{DFT} is calculated as −0.185 and −0.194 eV for Au and Ag, respectively). For a bimetallic cluster with a composition of $A_{n_A}B_{n_B}$:

$$E_b^{DFT} = \frac{-E_{tot}^{DFT} - nE_{atom}^{DFT}}{n}, \quad \textbf{(3-3)}$$

$$= \frac{-E_{tot}^{DFT} - n_A E_{atom}^{A,\,DFT} - n_B E_{atom}^{B,\,DFT}}{n} \quad \textbf{(3-4)}$$

where E_{tot}^{DFT} represents the total energy of a cluster calculated at the DFT level.

The excess energy, E_{exc}, is useful as it highlights the energetic difference between the bulk and nanoparticle of interest, and is defined as a function of composition thus:[38]

$$E_{exc}^{Gupta} = E_{tot}^{Gupta} - N_A(E_{coh,\,A}^{Gupta}) - N_B(E_{coh,\,B}^{Gupta}) \quad \textbf{(3-5)}$$

at the Gupta level, where E_{coh} is the cohesive energy per atom in the bulk of metals A and B, respectively. Similarly, for DFT calculations:

$$E_{exc}^{DFT} = E_{tot}^{DFT} - N_A(E_{coh,\,A}^{DFT}) - N_B((E_{coh,\,B}^{DFT}) \quad \textbf{(3-6)}$$

For Gupta calculations (E_{exc}^{Gupta}), the parameterised values of E_{coh} are used: 3.779 eV and 2.96 eV for Au and Ag, respectively. For E_{exc}^{DFT} we have calculated the values for Au and Ag as 3.25 and 2.75 eV, respectively, using the PBE functional. For comparison, the experimental values for E_{coh} are 3.81 eV for Au and 2.95 eV for Ag.[32]

E_{exc} can be related to the number of surface atoms within a structure, inferring the excess energy of the nanoparticle is related to the energy required to create the nanoparticle surfaces. The ratio of E_{exc} to the number of surface atoms, approximated as $n^{2/3}$, is written as:[39-40]

$$\Delta^{Gupta} = \frac{E_{exc}^{Gupta}}{n^{2/3}} \quad , \text{ or} \qquad \textbf{(3-7)}$$

$$\Delta^{DFT} = \frac{E_{exc}^{DFT}}{n^{2/3}} \quad . \qquad \textbf{(3-8)}$$

However, when comparing clusters of the same size but of differing compositions, Δ^{Gupta} and Δ^{DFT} can become biased as metals with larger cohesive energies result in clusters with larger excess energies. Thus, an unbiased alternative is Δ_{147}^{Gupta}, where E_b^{Gupta} is subtracted instead of the bulk cohesive energies:[41-42]

$$\Delta_{147}^{Gupta} = E_{tot}^{Gupta} - n_A \frac{E_{tot}^{Gupta}(A_{147})}{147} - n_B \frac{E_{tot}^{Gupta}(B_{147})}{147} \qquad \textbf{(3-9)}$$

where n_A and n_B are the number of atoms of each metallic elements A and B. Δ_{147}^{Gupta} is zero for pure clusters, and negative values of E_{exc} indicate improved stability. The corresponding quantity at the DFT level is:

$$\Delta_{147}^{DFT} = E_{total}^{DFT} - n_A \frac{E_{total}^{DFT}(A_{147})}{147} - n_B \frac{E_{total}^{DFT}(B_{147})}{147} \qquad \textbf{(3-10)}$$

Chemical Ordering

The extent of mixing (chemical order parameter), σ, may be defined as:[43]

$$\sigma = \frac{n_{AA} + n_{BB} - n_{AB}}{n_{AA} + n_{BB} + n_{AB}} \quad , \qquad \textbf{(3-11)}$$

where n_{AA} and n_{BB} refer to the number of AA and BB nearest neighbour bonds within the binary cluster, and n_{AB} is the number of nearest−neighbour A−B bonds. The nearest neighbour cut-off is defined as the midpoint between the first and second neighbours, which for an FCC structure is: $(r_0 + \sqrt{2}r_0)/2$ (3.484 Å for Au). σ = 1 indicates complete separation, $\sigma \approx 0$ for disordered mixing, and $\sigma < 0$ indicates more ordered mixing, such as layering and onion−like configurations.

3.4 Results and Discussion

3.4.1 Chemical ordering of pure and atomically doped systems

Pure Au_{147} and Ag_{147} CO nanoparticles were created using mathematical constructs, and the geometries minimised with respect to energy. E_b^{Gupta} and E_b^{DFT} were calculated as 3.547 and 2.993 eV for Au, respectively, and 2.670 and 2.526 eV for Ag, respectively. As expected, Au has a higher binding energy than Ag, due to the stronger Au−Au bonds. We also highlight the reduction in the binding energy for DFT in comparison to that from interatomic Gupta potentials, which demonstrates the need for re-optimisation at the DFT level.

The most fundamental combination of the two elements is to introduce a single dopant atom from a secondary species, and substitute an atom within the monometallic cluster. Nine possible non-equivalent dopant sites were identified and trialled for Au_{147} and Ag_{147}, resulting in compositions of Au_1Ag_{146} and $Au_{146}Ag_1$, respectively.

Beginning with the Gupta potential results, the lowest energy (E_{min}) structure for Au_1Ag_{146}, places the dopant Au atom at a subsurface vertex site. The next lowest energy arrangement, $E_{min\text{-}1}$, is also subsurface, but at an edge site. Both are shown in Fig. 3.7. As the Au atom migrates to the surface, the energy of the cluster increases further, implying reduced stability. Given traditional thermodynamic arguments, namely the lower surface energy and cohesive energy of Ag in comparison to that of Au, the preference of Au to occupy a highly coordinated site is understandable.

For each dopant site, *i*, the local atomic energy at that dopant site (E_i) is calculated for both the pure cluster and Au_1Ag_{146}. Table 3.3 shows the change in E_i (ΔE_i) as a result of doping. A decrease in energy is observed for almost all dopant sites, indicating that the incorporation of a single Au atom in Ag_{147} is favourable, due to the increased strength of the Au−Ag interactions, with the exception of Au positioned at a surface edge site (ΔE_i = 0.028 eV).

Conversely, when substituting a single Ag atom into Au_{147}, to give $Au_{146}Ag_1$, surface placement is favoured by the Ag atom. E_{min} positions Ag on a (100) surface and ΔE_i > 0 for all arrangements but one [Table 3.3(r)], indicating that it is generally unfavourable to incorporate the dopant Ag atom.

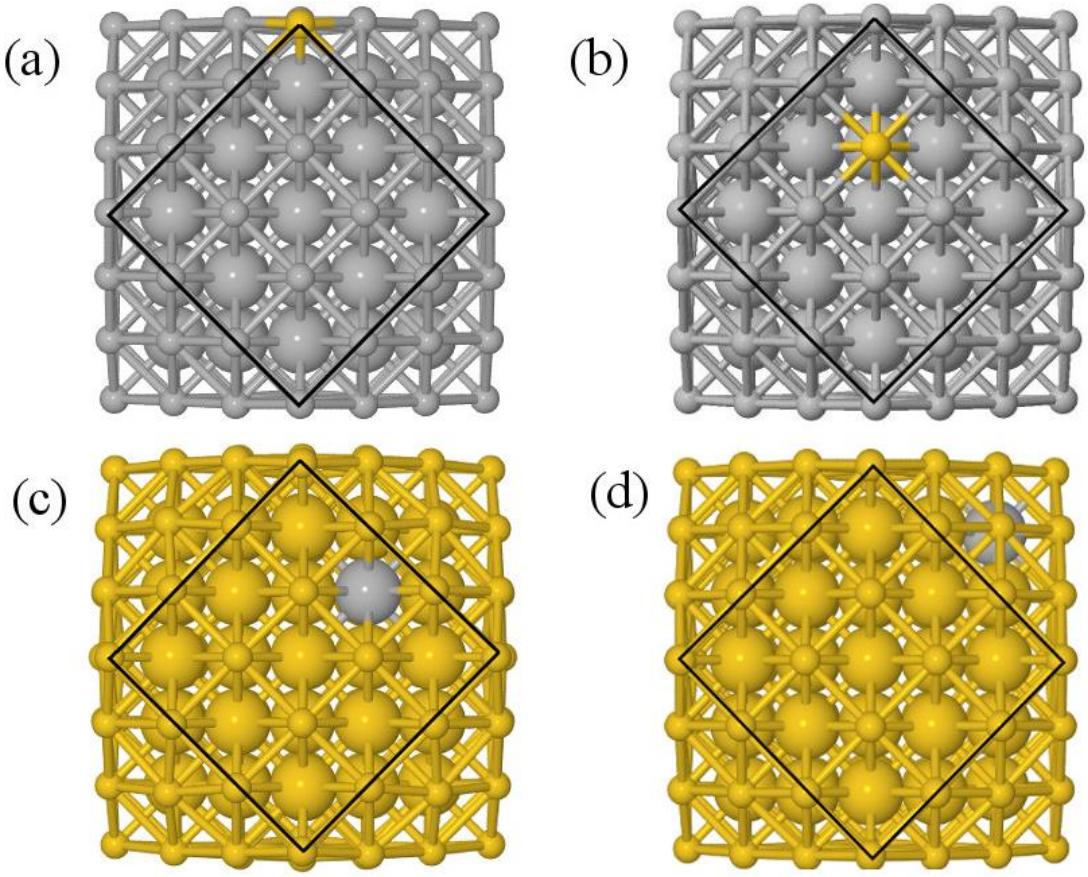

Fig. 3.7 Lowest energy arrangements for atomically doped structures: (a) $E_{min}^{Gupta}(Au_1Ag_{146})$; (b)$E_{min-1}^{Gupta}(Au_1Ag_{146})$; (c) $E_{min}^{Gupta}(Au_{146}Ag_1)$; (d)$E_{min-1}^{Gupta}(Au_{146}Ag_1)$. The outer geometric shell, or surface layer, is represented as ball−and−stick to emphasise the positioning of the dopant atom, with the atomic radius of the sub-surface atoms increased to highlight their depth. Both (a) and (b) have Au in a surface position, whilst

(c) and (d) show Ag subsurface. Au and Ag atoms are represented by yellow and grey spheres, respectively.

In order to ascertain possible reasoning for the adopted dopant position sites, the local atomic pressure (P_i) at each dopant site was also examined. P_i is defined as:

$$P_i = \frac{\partial E_i}{\partial V_i} \quad \textbf{(3-12)}$$

where V_i is the atomic bulk volume, calculated using r_0. $P_i < 0$ indicates tensile strain, whereas if $P_i > 0$, compressive strain exists. The change in P_i (ΔP_i) as a result of doping is also given in Table 3.3 and Table 3.4. For $E_{min}(Au_1Ag_{146})$, ΔP_i = 0.060 GPa, but for the next lowest energy arrangement, $E_{min\text{-}1}(Au_1Ag_{146})$, ΔP_i = −7.573 GPa. As a result of doping, bond lengths between surface Ag atoms and the dopant Au atom are shortened by 0.02−0.03Å, whereas interactions with subsurface Ag atoms are lengthened by the same amount in compensation. ΔP_i also varies dramatically for $Au_{146}Ag_1$; $\Delta P_i < 0$ for E_{min}, whereas for $E_{min\text{-}1}$, $\Delta P_i > 0$. Overall, we can generalise that ΔP_i decreases for doping of Ag_{147} with Au, and increases when doping Au_{147} with Ag. However, there is a large variation in values, and thus it is difficult to correlate preferred positioning of the dopant atoms with the partial pressure encountered at the dopant site.

Each atomically-doped system was reminimised using DFT, resulting in considerable reordering of the nanoparticle energetics when compared to those obtained from Gupta potentials. The lowest DFT arrangement, E_{min}^{DFT}, for Au_1Ag_{146} positions the Au atom on the surface, at a vertex site. For the next lowest energy arrangement of the same nanoparticle, $E_{min\text{-}1}^{DFT}$, we find the Au atom remains at the surface but positioned on the (100) face. $E_{min\text{-}1}^{DFT}$ is higher in energy than E_{min}^{DFT} by 0.036 eV. The positioning of the Au atom at the surface is in stark contrast to that observed for empirical potentials, where sub-surface positioning of the Au atom is most beneficial in terms of energetic ordering.

Reordering of energetics also occurs for $Au_{146}Ag_1$ upon reminimisation with DFT (Table 3.4, column IX). E_{min}^{DFT} positions the single Ag atom in a subsurface edge site, and $E_{min\text{-}1}^{DFT}$ also favours Ag to be subsurface, below a (100) face. There is an energy

difference of 0.031 eV between the two arrangements. The contrast in energetics between those obtained using semi-empirical potentials and DFT may therefore be attributed to the impact of charge transfer when included in our calculations.

Table 3.3 Local atomic pressure (P_i) and energy (E_i) as a result of dopant atom position, i, for Au_1Ag_{146}, calculated using the Gupta potential. Structures (a)-(i) are given in order of decreasing relative total energy, ΔE_{tot}^{Gupta}, with the relative DFT energy given as ΔE_{tot}^{DFT}. $P_i > 0$ indicates compressive strain for the cluster, whilst $P_i < 0$ indicates tensile strain. For comparison, P_i and E_i are given for the same site, i, in Ag_{147}, denoted as $E_i^{Ag_{147}}$ and $P_i^{Ag_{147}}$, respectively. The change in pressure and energy are given as ΔP_i and ΔE_i, respectively. For the site descriptions the notation surf. and subsurf. are used for surface and subsurface sites, respectively.

	ΔE_{tot}^{Gupta} / eV	Site Description	$E_i^{Ag_{147}}$ / eV	$P_i^{Ag_{147}}$ / GPa	$E_i^{Au_1Ag_{146}}$ / eV	$P_i^{Au_1Ag_{146}}$ / GPa	ΔE_i / eV	ΔP_i / GPa	ΔE_{tot}^{DFT} / eV	Δq_i / e
(a)	**0.000**	*Vertex, subsurf.*	−2.255	−1.596	−3.268	−1.536	−1.013	0.060	0.089	0.203
(b)	**0.124**	*Edge, subsurf.*	−2.927	4.815	−3.316	−2.759	−0.388	−7.573	0.111	0.198
(c)	**0.161**	*Centre of (111), surf.*	−2.927	4.841	−3.112	−7.807	−0.184	−12.648	0.055	0.256
(d)	**0.167**	*Centre of (100), subsurf.*	−2.628	−4.759	3.333	−3.856	−0.705	0.902	0.069	0.210
(e)	**0.228**	*Edge, surf.*	−2.961	3.985	−2.932	−4.710	0.028	−8.695	0.042	0.311
(f)	**0.250**	*Centre of cluster*	−2.866	9.768	−3.338	2.121	−0.471	−7.647	0.083	0.259
(g)	**0.262**	*Edge, two-layers subsurf.*	−2.866	9.655	−3.349	0.141	−0.482	−9.515	0.038	0.269
(h)	**0.269**	*Centre of (100), surf.*	−2.960	4.062	−3.056	−7.177	−0.096	−11.239	0.036	0.294
(i)	**0.309**	*Vertex, surf.*	−2.208	−1.589	−2.710	−3.185	−0.502	−1.596	0.000	0.341

Table 3.4 Same as Table 3.3, for $Au_{146}Ag_1$, calculated using the Gupta potential. Structures (j)-(r) are given in order of decreasing relative total energy, ΔE_{tot}^{Gupta}, with the relative DFT energy given as ΔE_{tot}^{DFT}. $P_i > 0$ indicates compressive strain for the cluster, whilst $P_i < 0$ indicates tensile strain. For comparison, P_i and E_i are given for the same site, i, in Au_{147}, denoted as $E_i^{Au_{147}}$ and $P_i^{Au_{147}}$, respectively.

	ΔE_{tot}^{Gupta} / eV	Site Description	$E_i^{Au_{147}}$ / eV	$P_i^{Au_{147}}$ / GPa	$E_i^{Au_{146}Ag_1}$ / eV	$P_i^{Au_{146}Ag_1}$ / GPa	ΔE_i / eV	ΔP_i / GPa	ΔE_{tot}^{DFT} / eV	Δq_i / *e*
(j)	**0.000**	*Centre of (100), surf.*	−3.778	5.521	−3.031	−5.297	0.747	−10.818	0.137	−0.243
(k)	**0.020**	*Edge,two-layers subsurf.*	−3.709	5.730	−3.373	16.749	0.336	11.019	0.113	−0.218
(l)	**0.067**	*Edge, surf.*	−3.778	5.427	−2.911	−3.546	0.867	−8.973	2.592	−0.077
(m)	**0.067**	*Vertex, surf.*	−3.181	−12.140	−2.670	−2.716	0.512	9.424	2.258	−0.075
(n)	**0.078**	*Centre of cluster*	−3.709	5.895	−3.349	21.960	0.360	16.065	0.148	−0.141
(o)	**0.114**	*Centre of (111), surf.*	−3.759	3.280	−3.105	0.305	0.654	−2.975	0.095	−0.278
(p)	**0.118**	*Centre of (100), subsurf.*	−3.501	−11.874	−3.358	15.527	0.143	27.401	0.031	−0.275
(q)	**0.149**	*Edge, subsurf.*	−3.759	3.244	−3.345	19.194	0.414	15.950	0.000	−0.284
(r)	**0.298**	*Vertex, subsurf.*	−3.181	−12.147	−3.277	27.914	−0.096	40.060	0.017	−0.234

In nanoparticles, electrons tend to migrate towards the surface, resulting in partial negative charges being located on the edge, vertex and face atomic sites. However, when dealing with bimetallic systems, the differing electronegativities and resultant charge transfer between the two metallic species can influence the final properties of the nanoalloy. Therefore, we have also investigated the extent of charge transfer that the nanoparticles undergo, using Bader analysis,[44] with particular focus on the partial charging on the dopant atom. The 147-atomic sites are analysed according to their structural position: vertex, edge, face or core, with their accumulated charges denoted as Δq_{vertex}, Δq_{edge}, Δq_{face}, and Δq_{core}, respectively. For pure systems, charge accumulation occurs at the surface as expected ($\Delta q > 0$ *e*) and the core atoms undergo charge depletion ($\Delta q < 0$ *e*), indicating charge migration to surface sites. The order of partial atomic charges for Ag_{147} is: $\Delta q_{\text{vertex}} > \Delta q_{\text{edge}} > \Delta q_{\text{face}}$, whereas for Au_{147} they are: $\Delta q_{\text{vertex}} > \Delta q_{\text{face}} > \Delta q_{\text{edge}}$.

The nine non-equivalent arrangements for the atomically doped Au_1Ag_{146}system exhibit charge accumulation on Au atoms universally, with the lowest energy structures also having the highest Δq_i, for dopant atom *i* (0.341 and 0.294 *e* for $E_{\text{min}}^{\text{DFT}}$ and $E_{\text{min-1}}^{\text{DFT}}$, respectively). The lowest energy Au_1Ag_{146} systems position the dopant Au atom at the surface, and thus we can conclude that there is a relationship between dopant coordination and the maximisation of Δq_i.

In comparison, for $Au_{146}Ag_1$, the dopant Ag atoms from all nine arrangements undergo charge depletion (−0.284 and −0.275 *e* for $E_{\text{min}}^{\text{DFT}}$ and $E_{\text{min-1}}^{\text{DFT}}$, respectively), whilst the majority of Au atoms accumulate charge. We find there is a correlation between the nanoparticle's energy when Ag is subsurface and Δq_i, with the exception of arrangement (o), in Table 3.4.

In general, the addition of a single dopant atom makes E_{exc} of the cluster more negative, with minor distortions to bonds immediately surrounding the dopant atom (< 1%). Structurally, the Gupta potentials favour occupation of subsurface sites by Au atoms in Au_1Ag_{146}, whereas DFT favour Au to be in a surface position. No clear trend was observed for Ag atoms in $Au_{146}Ag_1$ using the Gupta potentials, but the occupation of subsurface positions for Ag atoms are favoured by DFT methods. The

dominating factor for the DFT relative total energy E_{tot}^{DFT} appears to be Δq_i; the preferential positioning of Au at the surface and Ag subsurface by DFT suggests a correlation between both the atomic coordination and the extent of charge transfer. We were unable to establish a clear connection between the energetic ordering and ΔP_i, but it is not completely unexpected given the very similar atomic radii of Au and Ag. Finally, we note that charge accumulation and depletion occur for Au and Ag, respectively, as is perhaps expected given their differing electronegativities.

3.4.2 Chemical ordering of alloys and core@shell arrangements

As the number of Au atoms (x) increases the ordering landscape increases in complexity, with the lowest energy structures preferring an alloy arrangement. maximising Au−Ag interactions. However, as core@shell arrangements are also obtainable experimentally, core@shell arrangements were also analysed for the 147-atom CO geometry, with varying shell thickness, allowing a direct comparison of the properties of alloy and core@shell chemical arrangements.

The lowest energy alloy nanoparticles, obtained from basin-hopping searches, preferentially position Au atoms in sub-vertex positions within the CO geometry (Fig. 3.8). Recently, Bochicchio *et al.* found a preference for subsurface positions to be favoured for size mismatched systems, due to the strain relief that is provided by the accommodation of the smaller atomic species at these sites.[45] This suggests that there is a correlation, however, as highlighted in section 2.4.1, we do not observe a direct relation between atomic pressure and Au−Ag intermixing. As x is increased beyond 13 atoms, the subsurface positions are fully occupied, leading to an onion-like Ag@Au@Ag chemical arrangement; this is particularly apparent for $Au_{55}Ag_{92}$ (Fig. 3.9). Once x is increased beyond 55 atoms, gold atoms begin to occupy surface positions. σ is above 0 for all cases, indicating that disordered mixing is preferred to ordered mixing.

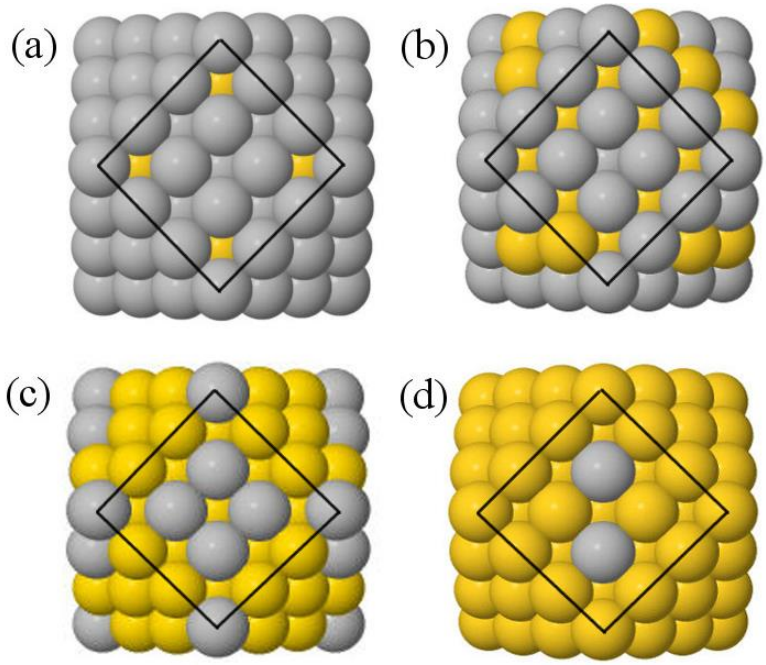

Fig. 3.8 Minimum energy alloy arrangements as calculated using atomic-swap basin-hopping with the Gupta potentials: (a) $Au_{13}Ag_{134}$, (b) $Au_{55}Ag_{92}$, (c) $Au_{92}Ag_{55}$ and (d) $Au_{134}Ag_{13}$. Yellow spheres represent Au, grey spheres Ag. The (100) face is highlighted.

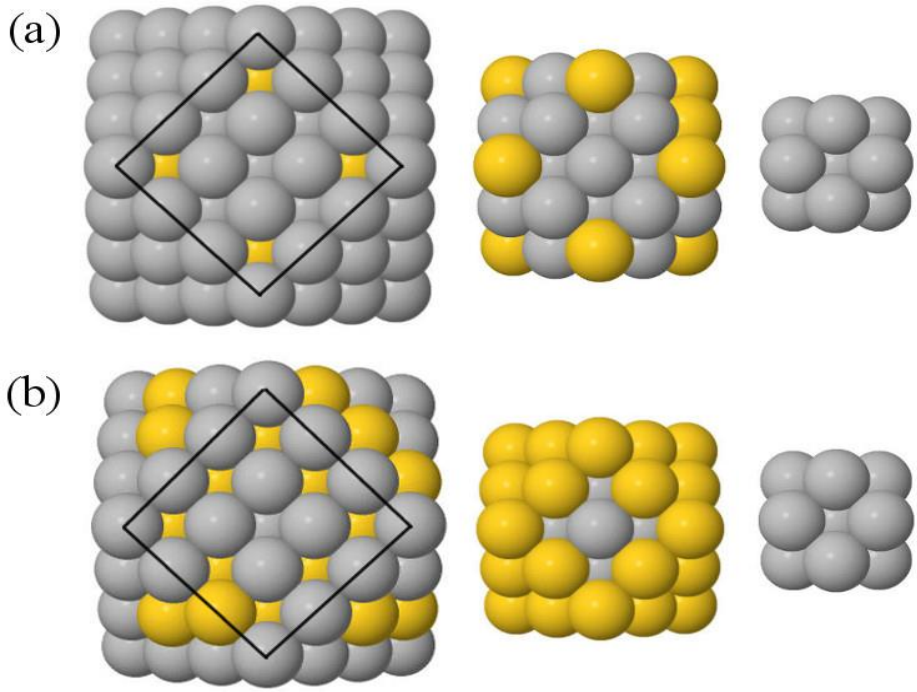

Fig. 3.9 Minimum energy alloy structures of cuboctahedral as calculated using atomic-swap basin-hopping with the Gupta potentials: (a) $Au_{13}Ag_{134}$, (b) $Au_{55}Ag_{92}$. One layer is removed as one moves left to right: 147 atoms; 55 atoms, 13 atoms showing the preference for an Ag@Au@Ag arrangement. Yellow spheres represent Au, grey spheres Ag. The (100) face is highlighted.

Overall, E_b^{Gupta} increases linearly with increasing Au content, from 2.669 eV (Ag_{147}, Au content = 0%) up to 3.541 (Au_{147}), in line with Vegard's law (Fig. 3.10),[46-47] which is as expected, given the bond strengths at the Gupta level are: Au−Au (2.82 eV) > Au−Ag (1.81 eV) > Ag−Ag (1.36 eV); values given in parentheses are for dimer pairs. The core@shell arrangements are energetically similar to alloys when using semi-empirical potentials, as shown in Table 3.5. Upon recalculation of energies using DFT, the same linear trend is obtained for E_b^{DFT}, as shown in Fig. 3.10. At the DFT level, bond order remains the same, but the dimer pair values differ: Au−Au (2.68 eV) > Au−Ag (2.57 eV) > Ag−Ag (2.16 eV). We note that $Ag_{55}@Au_{92}$ has a lower DFT energy than its stoichiometric alloy equivalent, whereas all other core@shell arrangements are higher in energy than their equivalent alloys. In general, the energy difference between the core@shell and alloy structures is not large (≤ 0.05 eV and ≤ 0.02 eV for Gupta and DFT calculations, respectively). Therefore, as restructuring from core@shell geometries requires a great deal of energy (> 2 eV), it is safe to assume that once formed, the chemical ordering would be relatively stable under ambient conditions and in the absence of surface reactions.

Table 3.5 Differences in E_b (ΔE_b) between alloy and core@shell structures for Gupta and DFT calculations. Positive values indicate the alloy is lower in energy than the core@shell arrangement.

Structure	ΔE_b^{Gupta} / eV	ΔE_b^{DFT} / eV
$Au_{13}Ag_{134}$	0.027	0.001
$Au_{55}Ag_{92}$	0.015	0.016
$Au_{92}Ag_{55}$	0.003	−0.019
$Au_{134}Ag_{13}$	0.050	0.002

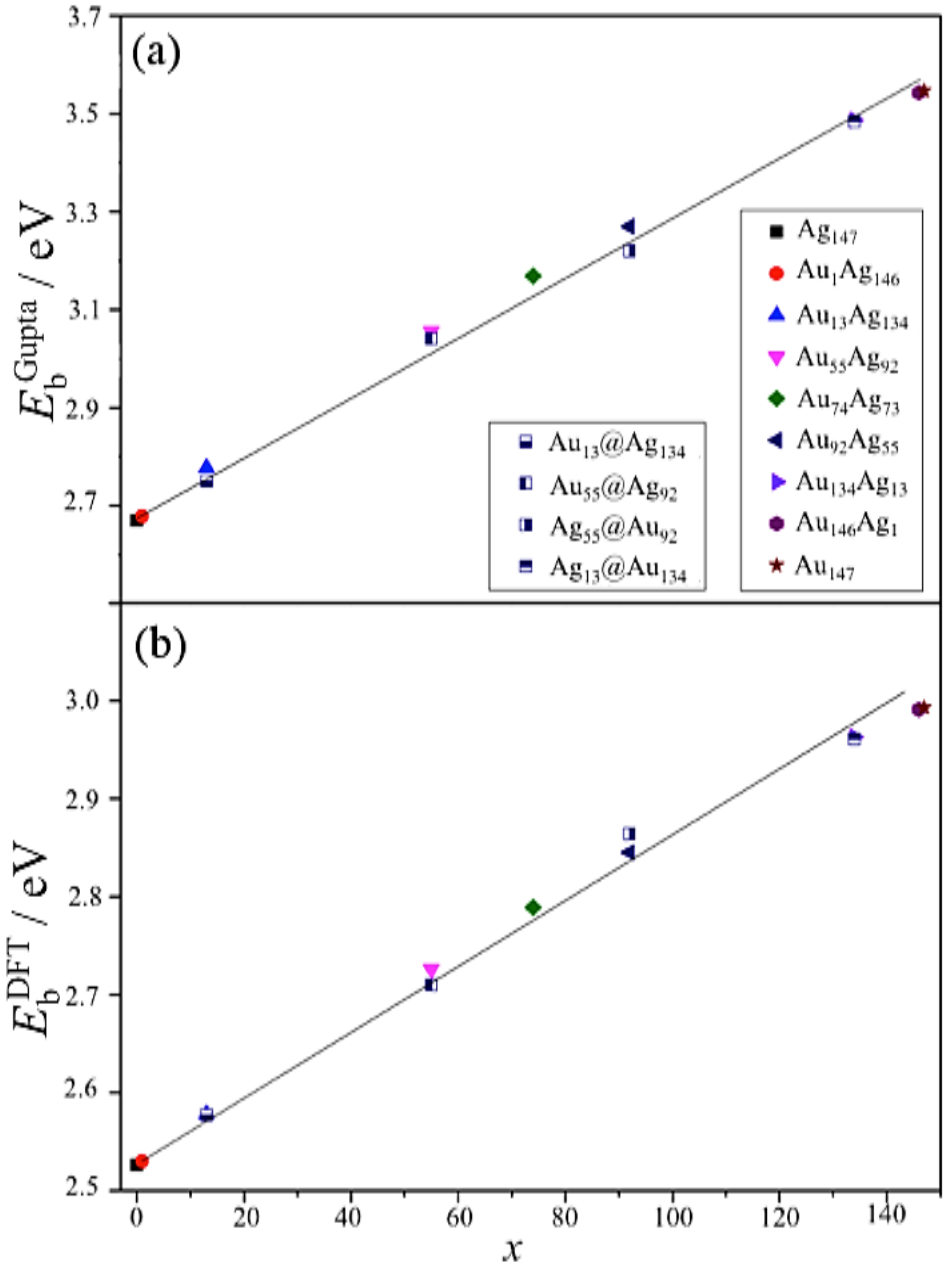

Fig. 3.10 (a) E_b^{Gupta} and (b) E_b^{DFT} as a function of Au content, *x*. The lines are given as a guide to the eye. A key to the symbols is also provided in (a).

3.4.3 Chemical ordering of alloys and core@shell arrangements

The propensity of Au_xAg_{147-x} to preferentially form an alloy at the Gupta level is further confirmed when comparing E_b^{Gupta} with the extent of mixing, σ. Core@shell arrangements for the 55:92 ratio ($Au_{55}@Ag_{92}$ and $Ag_{55}@Au_{92}$) have a noticeably higher σ than their corresponding equivalent alloy arrangements, as is expected for

more segregated systems. At the DFT level, this trend remains consistent for $Au_{55}@Ag_{92}$, but $Ag_{55}@Au_{92}$ is more energetically favourable than the alloy (E_b^{DFT} is greater for $Ag_{55}@Au_{92}$ than $Au_{92}Ag_{55}$ alloy) despite its greater level of segregation. DFT favours the Ag@Au arrangement, but the same generalisations for the 13:134 metallic ratios cannot be made as the energetic differences are too small (Fig. 3.11).

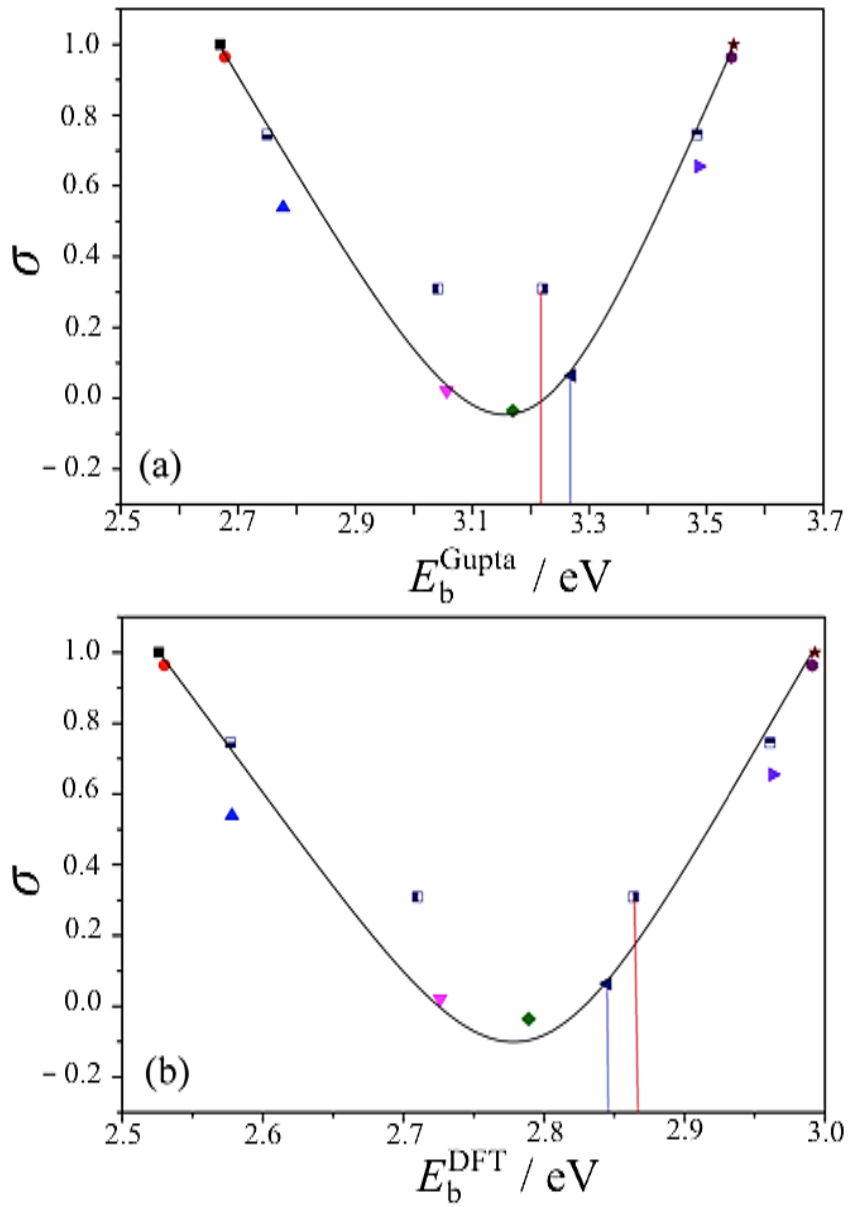

Fig. 3.11 (a) E_b^{Gupta} and (b) E_b^{DFT} against the extent of mixing within the nanocluster, σ. The line is only given as a guide to the eye; symbols are the same as in Fig. 3.10. The red and blue lines are to emphasise the difference in E_b^{Gupta} and E_b^{DFT} between the alloy and its corresponding core@shell arrangement.

3.4.4 Charge Transfer

The DFT energetic preference of an Au shell may occur as a result of improved charge transfer to Au atoms when their coordination is decreased. Consequently, the charge transfer that occurs within the alloy and core@shell nanoparticles was also examined, using Bader analysis.

Alloy arrangements exhibit disordered mixing ($\sigma \approx 0$, Fig. 3.11), yet have the greatest changes in charge (Δq) when Ag is the dominant element in the composition: for instance, Δq_{face} is greater for both $Au_{13}Ag_{134}$ (0.012 *e*) and $Au_{55}Ag_{92}$ (0.087 *e*) in comparison to the core@shell equivalents, $Au_{13}@Ag_{134}$ (0.007 *e*) and $Au_{55}@Ag_{92}$ (0.070 *e*), as a greater number of surface Au−Ag interactions exist between the surface Ag and subsurface Au atoms (Table 3.5). Further analysis of the onion-like $Au_{55}Ag_{92}$ structure shows there is a combination of both charge depletion and charge accumulation at the surface: the subsurface Au shell (42 atoms) accumulates charge, and the inner Ag core (13 atoms) is charge depleted, as shown in Fig. 3.12. There is a trade-off between the additional electronic degrees of freedom at the surface and the contrasting electronegativities of Au and Ag: $Au_{13}Ag_{134}$ also exhibits this compromise, with surface charge accumulation only occurring at the Ag vertices, with any remaining Ag atoms undergoing charge depletion; within the sub−surface Au there is charge accumulation.

Most of the core@shell structures favour charge accumulation at the surface but the degree of charge transfer is determined by whether Au or Ag occupies the surface layer of the nanoparticle. All core@shell arrangements exhibit charge accumulation at the vertices. $Au_{55}@Ag_{92}$ undergoes charge depletion on faces and edges (Δq_{face} = −0.070 *e*, Δq_{edge} = −0.055 *e*), whilst the inverse structure, $Ag_{55}@Au_{92}$, has considerable charge accumulation at the surface (Δq_{face} = 0.062 *e*, Δq_{edge} = 0.079 *e*). $Au_{13}@Ag_{134}$ and $Ag_{13}@Au_{134}$ also exhibit similar behaviour to a lesser extent, with charge accumulation only on the vertices for the Ag shell, whereas Δq_{edge} and Δq_{vertex} > 0 *e* for the Au shelled nanoparticles. This variation is perhaps due to the differing electronegativities of Ag (1.93 *e*) and Au (2.54 *e*), and thus charge transfer occurs from Ag to Au.

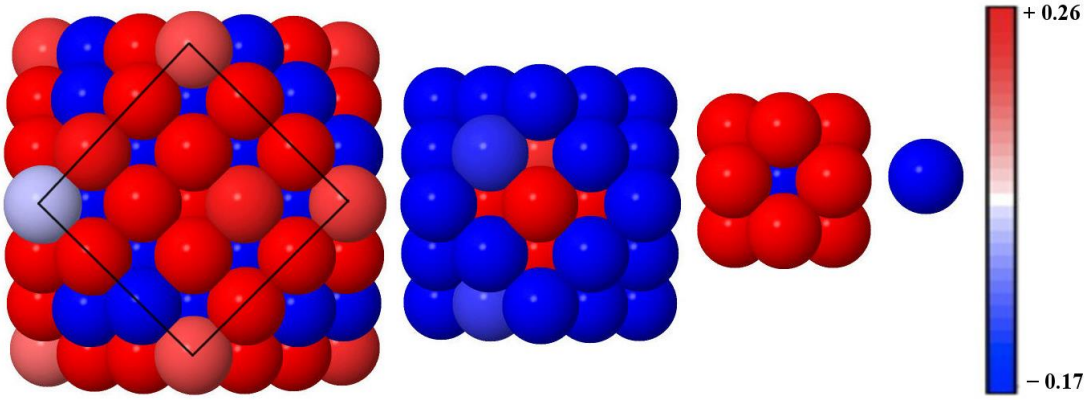

Fig. 3.12 Alloy structure of $Au_{55}Ag_{92}$ showing charge accumulation and depletion. As one moves left to right: 147 atoms; 55 atoms; 13 atoms and 1 atom for Ag@Au@Ag system. Red spheres represent charge depletion (Δq_i > 0 *e*), whilst blue spheres represent atoms with charge accumulation (Δq_i < 0 *e*). A charge colour scale is also provided.

In summary, all nanoparticles experience charge accumulation at the lowest coordination sites in the nanoparticle, irrespective of chemical ordering. Core@shell systems illustrate a greater change in atomic partial charges, as shown when comparing 55:92 systems to the 13:134 systems, due to the segregation of chemical species. In general, charge accumulates on Au, whereas charge depletes from Ag, in the alloys and core@shell arrangements, similar to our observations for single dopants.

Table 3.6 Δq for the lowest energy structures. Units are electrons, with negative values indicating charge depletion and positive values accumulation. σ is also provided.

Structure	σ	Δq_{core} / *e*	Δq_{face} / *e*	Δq_{edge} / *e*	Δq_{vertex} / *e*
Ag_{147}	1.000	−0.030	0.014	0.007	0.072
Au_1Ag_{146}	0.964	−0.018	0.004	0.001	0.067
$Au_{13}Ag_{134}$	0.539	0.035	−0.012	−0.026	−0.025
$Au_{13}@Ag_{134}$	0.745	−0.015	−0.007	0.009	0.052
$Au_{55}Ag_{92}$	0.021	0.143	−0.087	−0.091	−0.064
$Au_{55}@Ag_{92}$	0.309	0.077	−0.070	−0.055	0.046
$Au_{74}Ag_{73}$	−0.036	0.117	−0.119	−0.090	0.143
$Au_{92}Ag_{55}$	0.064	0.088	0.154	−0.019	0.083
$Ag_{55}@Au_{92}$	0.309	−0.129	0.062	0.079	0.110
$Au_{134}Ag_{13}$	0.655	0.013	−0.080	0.030	0.034
$Ag_{13}@Au_{134}$	0.745	−0.043	0.014	0.018	0.085
$Au_{146}Ag_1$	0.964	−0.045	0.003	0.028	0.086
Au_{147}	1.000	−0.050	0.017	0.022	0.089

3.4.5 Stability of Au_xAg_{147-x} alloy and core@shell arrangements

So far, the properties of alloy and core@shell arrangements have been discussed in terms of their relative energies. However, the relative stabilities of these differing compositions and chemical arrangements is also of importance, especially when considering that the true chemical environment of these nanoparticles would be undergoing surface reactions with adsorbate gases, prompting alterations in the intended composition. Therefore, $\Delta_{147}^{\text{Gupta}}$ and $\Delta_{147}^{\text{DFT}}$ have been calculated (where the superscript Gupta and DFT indicate the level of theory), which considers the energy relative to the number of surface atoms; these are plotted as a function of *x* in Fig. 3.13.

In general, a 'U-shaped' trend is observed with increasing *x*; $Au_{55}Ag_{92}$ has the lowest $\Delta_{147}^{\text{Gupta}}$, and may therefore be considered the most stable structure with respect to the formation of surfaces. The stability of this alloy may be attributed to the Ag@Au@Ag arrangement that the alloy takes: Au−Ag interactions are maximised, and there is a corresponding reduction in the (weaker) Ag−Ag bonds. Nonetheless, the stability is not entirely dependent on the number of Au−Ag bonds, as $Au_{74}Ag_{73}$ is less stable despite having more Au−Ag interactions [$\sigma(Au_{92}Ag_{55}) = 0.064$, $\sigma(Au_{74}Ag_{73}) = -0.036$]. The key structural difference between the two is that $Au_{55}Ag_{92}$ has more surface Ag atoms, and thus there must be an overall balance at the Gupta level between reducing surface energies and increasing binding energies. Of the core@shell systems, $Au_{55}@Ag_{92}$ has the lowest $\Delta_{147}^{\text{Gupta}}$ as it maximises the number of Au−Ag interactions, and has a thermodynamically favourable Au core. $Au_{13}@Ag_{134}$ has fewer Au−Ag interactions, thus lowering the stability of this arrangement.

Finally, we note that core@shells are generally less stable than their alloy counterparts. A large difference in $\Delta_{147}^{\text{Gupta}}$ is observed in particular for $Au_{92}Ag_{55}$ and $Ag_{55}@Au_{92}$. This is attributed to the fact that an Ag core is not thermodynamically favourable, due to the low Ag−Ag bond strength and high Au surface energies, resulting in a lower stability for $Ag_{55}@Au_{92}$. Contrastingly, $Ag_{55}@Au_{92}$ has the lowest $\Delta_{147}^{\text{DFT}}$ as calculated at the DFT-level, by an energy of ~2.5 eV, which is

surprising given that thermodynamic considerations would favour an Ag shell. The next most stable structure, $Au_{92}Ag_{55}$, has the same stoichiometry but more Au−Ag bonds, adopting an Ag@Au@AuAg configuration, where the outermost shell is an alloyed layer of both Au and Ag atoms [$\sigma(Ag_{55}@Au_{92}) = 0.309$, $\sigma(Au_{92}Ag_{55}) = 0.064$]. The energetic preference of $Ag_{55}@Au_{92}$ for DFT may be attributed to the Au surface being able to draw electron density from the Ag atoms more readily than if Au atoms were positioned internally; we have seen from the single dopant calculations for DFT methods in Section 3.4.1 that an Au atom prefers to be at the surface. Thus, as electrons migrate to the surface of the cluster due to the increased degrees of electronic freedom available, it also follows that Au would benefit from greater charge transfer when positioned at the surface. We find, therefore, that overall stability is not only a case of maximisation of Au−Ag bonds and minimising surface energies of the nanoparticle through specific chemical ordering, but a compromise of the ease at which Au can gain electrons. For DFT, the latter observable is prevalent in determining Δ_{147}^{DFT}.

Overall, we find that the stability of a nanoalloy at the Gupta-level is determined through a balance of maximising Au−Ag interactions and minimising the surface energy; it is more favourable to have a greater proportion of the surface atoms as Ag rather than Au. However, when reminimised using DFT, the additional factor of maximising charge transfer from Ag to Au must be taken into account. Thus, an Au shell is more favourable than initially thought as a result of the increased degrees of electronic freedom at the surface.

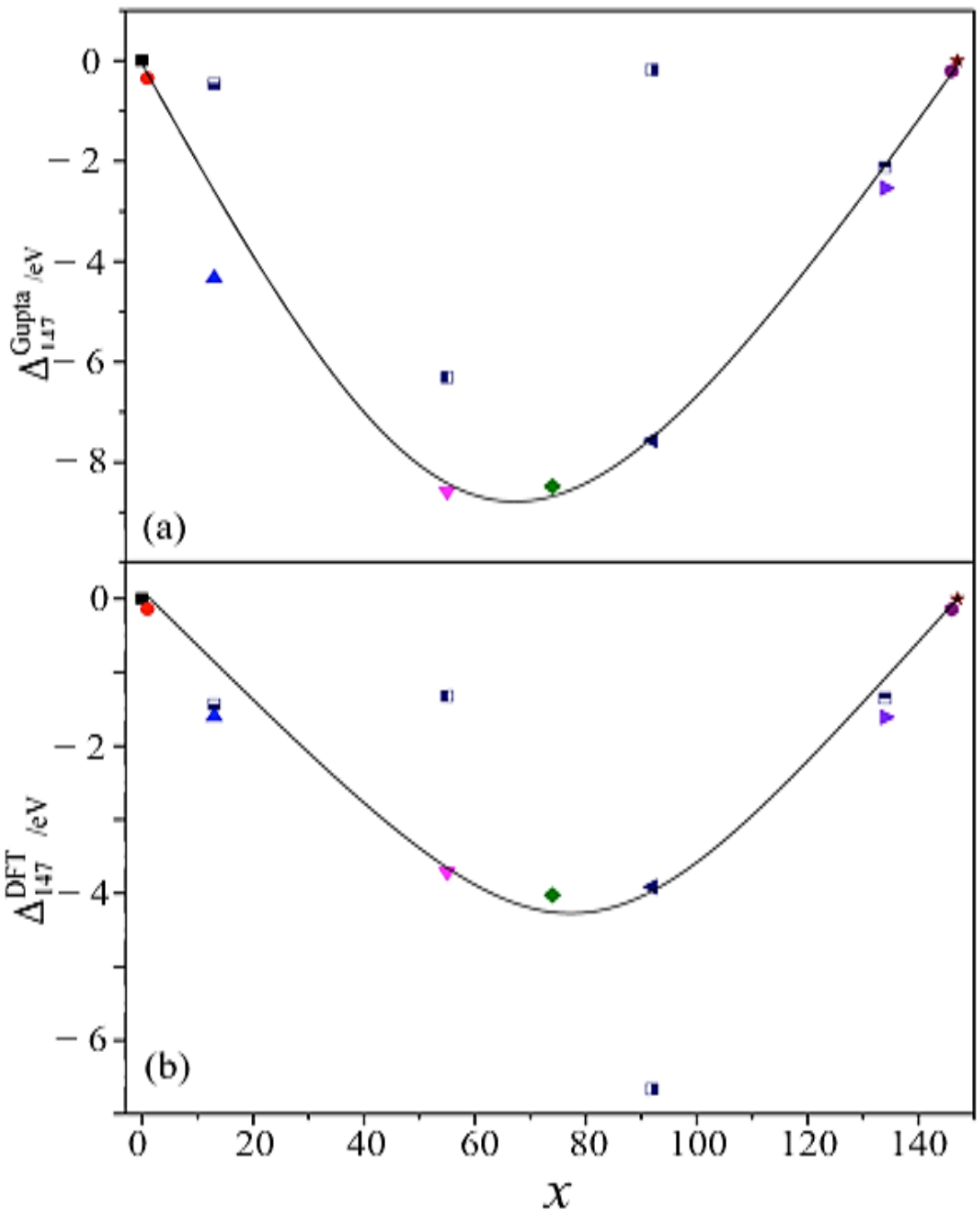

Fig. 3.13 (a) Δ_{147}^{Gupta} and (b) Δ_{147}^{DFT} as a function of Au content, *x*. The black line is given as a guide to the eye; symbols are the same as given in Fig. 3.10.

3.4.6 Electronic properties

DFT also allows insight into the electronic properties, which can provide detailed information on potential catalytic applications. AuAg nanoparticles may be used as semiconducting supported co-catalysts for hydrogen production (Ch. 1), whereby

they act as an 'electron trap' for excited electrons that are transferred from the support, extending the photocatalytic lifetime. It is known that a shift in the Fermi Energy (E_f) for the nanoparticle/support composite towards the conduction band (in comparison to the bare semiconducting support) indicates a greater reductive ability for the material as a whole. Therefore, screening of suitable nanoparticles is possible by comparing the density of states (DOS) of the nanoparticle with the band structure of the support, known as a band alignment procedure.[48-49] As shown in Fig. 3.14, using the work functions of bulk Au and Ag, it appears that Au may exhibit greater catalytic activity in comparison to Ag, due to its greater work function of ~5.4 eV compared to ~4.6 eV, respectively.[50] E_f of Au is below the conduction band minimum of bulk TiO_2 (rutile), which would allow an electron to 'drop' in energy should it transfer from the support conduction band to the unoccupied states of the nanoparticle. However, as the E_f of Ag is greater than that of bulk TiO_2 (rutile), this indicates a need for an overpotential for the electron transfer to occur, making the Ag less likely to accumulate photo-excited electrons which can partake in the hydrogen production.

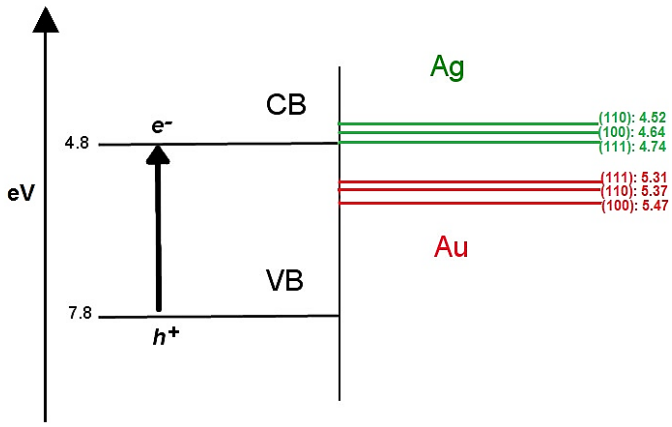

Fig. 3.14 The differing work functions of Au and Ag surfaces in comparison to bulk TiO_2 (rutile), showing that Au is more likely to accept an electron than Ag. Differing surfaces are noted in parentheses, all other values are given in eV.

Empty electronic states must be available close to E_f to allow for electron acceptance from the semiconductor – in our specific case, we use TiO_2 as our example. Additionally, these unoccupied *d*-states must also be lower in energy than the photo-excited electrons in the conduction band of the support. The absence of these empty *d*-states means that any catalytic activity will be reliant upon electron tunnelling to

occupy core atom states, although the probability of this occurring decays exponentially with depth from the surface. Therefore, the most favourable (and idealistic) situation is for the surface atoms to possess a positive partial charge, and not be dependent on electron tunnelling.

According to the *d*-band model, the strength of the bond between molecule and surface is given by the energy of the antibonding states relative to E_f. Antibonding states always lie above the *d*-states, and hence the energy of the *d*-states relative to E_f is a good indicator of bond strength. The higher the *d*-states are in energy relative to E_f, the higher in energy the antibonding states are, and thus the stronger the bond is. Following on from the above reasoning, our observations in section 3.4.3 imply that an Au@Ag system would be the most favourable, as its surface would be charge depleted. Nonetheless, given the work function alignment (Fig. 3.14), one would expect Ag@Au to be more suitable, due to the lowering of E_f, and more energetically accessible states for an additional electron. Therefore, we examine the total density of states (DOS) profiles in comparison to the decomposed projected contributions for core and shell electrons.

Fig. 3.15 shows the DOS profiles for Ag_{147}, Au_{147} and a 1:1 composition, $Au_{74}Ag_{73}$. The number of available *d*-states (core and shell) in Au_{147} is higher than that of Ag_{147}, and $Au_{74}Ag_{73}$ has a profile representative of its composition, i.e. somewhere between that of Ag_{147} and Au_{147}. Core@shell arrangements ($Au_{55}@Ag_{92}$, $Ag_{55}@Au_{92}$) DOS profiles are compared with their stoichiometrically equivalent alloys in Fig. 3.16. These core@shell arrangements are specifically highlighted due to their aforementioned characteristics which show promise for catalytic activity, such as surface charges and energetic stability. However, none of the bimetallic nanoparticles show better promise for catalytic activity than pure Au_{147}, which itself has few available *d*-states. The $Ag_{55}@Au_{92}$ chemical arrangement is the best of these four candidates but is still far-removed from what one would expect for a catalytically active nanoparticle. [E_f values are given in Appendix A, as are DOS plots for 13:134 systems.] Previous studies by Su *et al.*[51] showed a large shift in the number of *d*-states for Au@Pd nanoparticles, which also exhibit high catalytic activity experimentally. The same expectation of AuAg nanoparticles did not hold

true, and thus we suggest that the role of the support may be much more influencing for these particular nanoalloys.

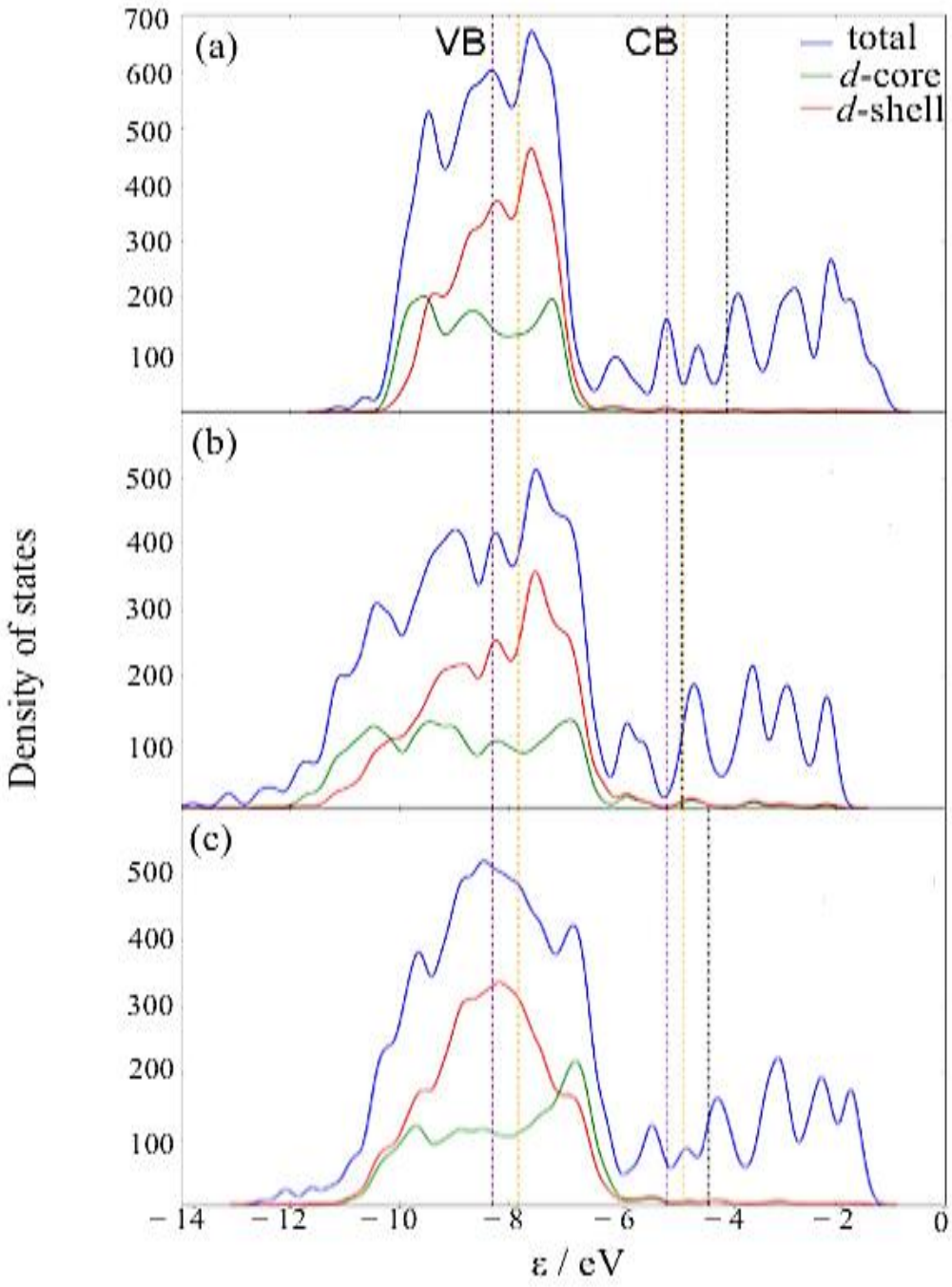

Fig. 3.15 Density of states (DOS) profiles for (a) Ag_{147}, (b) Au_{147} and (c) $Au_{74}Ag_{73}$. A key is provided. E_f is given as a black dotted line, with the valence band maximum (VBM) and conduction band minimum (CBM) in purple and orange for anatase and rutile TiO_2, respectively.[48] A Gaussian broadening of 0.05 eV has been used.

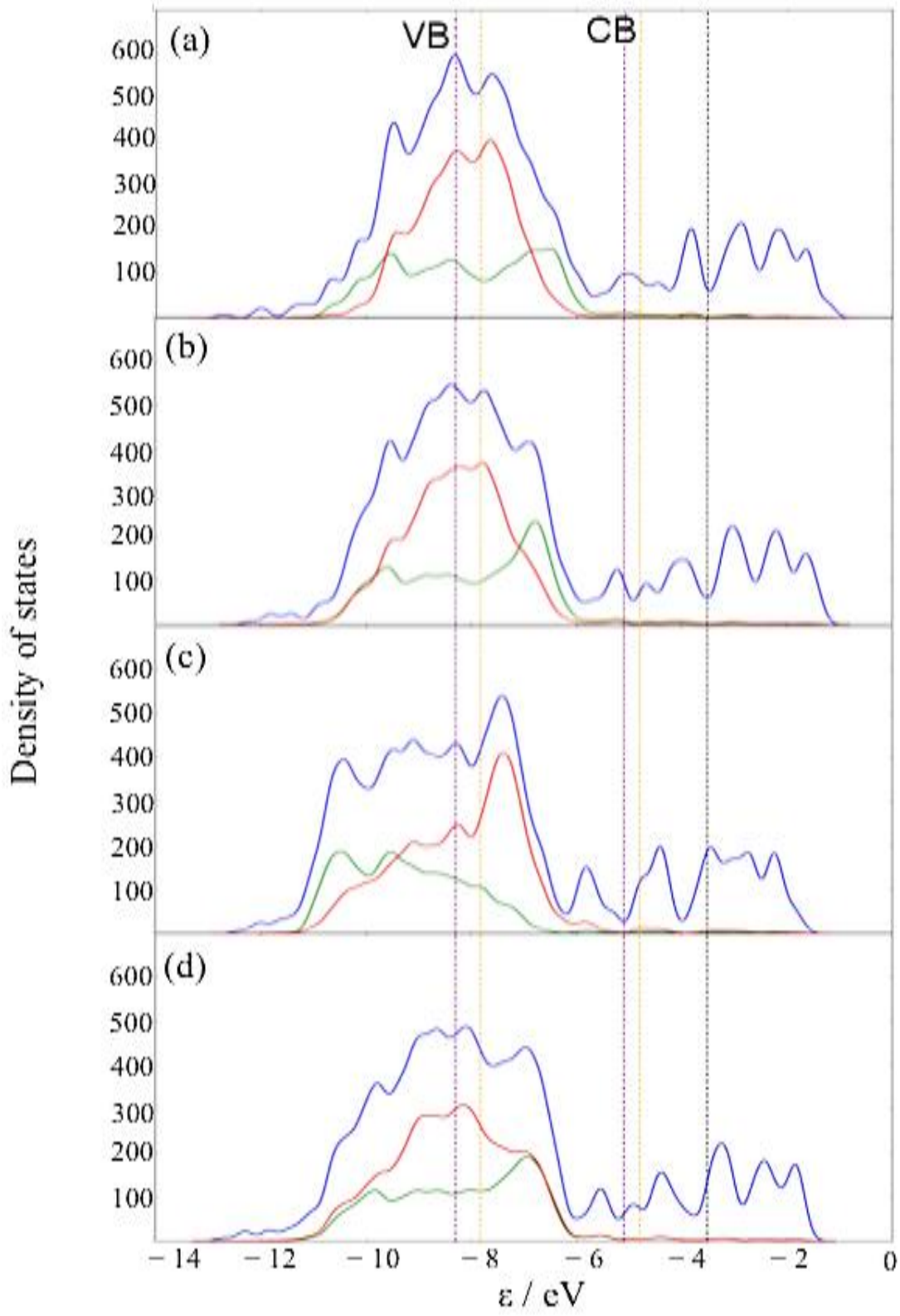

Fig. 3.16 Density of states (DOS) profiles for (a)$Au_{55}@Ag_{92}$, (b)$Au_{55}Ag_{92}$, (c)$Ag_{55}@Au_{92}$ and (d)$Au_{92}Ag_{55}$. Colours and broadening are the same as in Fig. 3.15.

3.5 Conclusions

Both BH algorithms and DFT were used in order to investigate the optimal chemical ordering of 147-atom CO AuAg nanoparticles. As Au content increases, the binding energy of the nanoparticle also increases, which may be attributed to the extra energy of Au−Au bonds, in comparison to Au−Ag and Ag−Ag bonds. The difference in binding energies between alloy and core@shell structures at equivalent stoichiometries is small, and thus both structures can be assumed to be energetically stable. The most stable arrangement for the Gupta potentials was a 1:1 alloy combination, and thus this super stability arises from the maximisation of Au−Ag interactions. A noticeable difference in the energetic stability was observed for $Ag_{55}@Au_{92}$: Gupta potentials predicted the Au shell to be particularly energetically unfavourable, as one would expect given traditional thermodynamic arguments, whereas DFT found this arrangement to be the most energetically stable. We can therefore confirm the extent of charge transfer is a huge factor in determining optimal chemical arrangements, as DFT prefers to position Au in such a way that it can draw electron density away from Ag most easily. Charge transfer between core@shell arrangements is of an interfacial nature, and thus influences from the core are more pronounced for thin shells, allowing for co-catalyst design.

The electronic properties of the optimal chemical arrangements from DFT were also examined, to determine their likelihood to partake in chemical reactions. Firstly, the level of charge accumulation or depletion at the surface; a charge depleted surface is much more likely to accept an incoming electron from a photo-excited semiconducting support (such as TiO_2), and secondly, the density of states profile, which is a good indicator of catalytic activity. The nanoparticle most likely to accept an incoming electron was $Au_{55}@Ag_{92}$, as the Ag surface undergoes the greatest amount of charge depletion. $Ag_{55}@Au_{92}$ is the least likely to accept an incoming electron from the support, as it has a great deal of charge accumulation at the surface, which is unfortunate given its reported energetic stability from DFT. However, this particular nanoparticle is still viable if electron tunnelling occurs, although its chances of accepting an incoming electron are considerably less.

The density of states profiles reveals the number of unoccupied *d*-orbitals close to E_f, which indicates catalytic ability. Nonetheless, minimal improvement was observed as a consequence of combining the two metallic species. Given, from experiment, that Au supported nanoparticles are known to be catalytically active,[52] this result suggests that there are possible surface reactions that aid the catalytic evolution of H_2, which are not considered in our nanoparticle profiles. Therefore, the presence of the support and adsorbing species are also essential factors when considering catalytic activity, and suitable for future investigation. The work in this chapter has been published: Gould, A. L., Heard, C. J., Logsdail, A. J., & Catlow, C. R. A. Segregation effects on the properties of $(AuAg)_{147}$. *Physical Chemistry Chemical Physics*, **2014,** *16*, 21049-21061.

3.6 References

1. Ferrando, R.; Jellinek, J.; Johnston, R. L., Nanoalloys: From Theory to Applications of Alloy Clusters and Nanoparticles. *Chemical reviews* 2008, *108*, 845-910.
2. Mott, D.; Thuy, N. T.; Aoki, Y.; Maenosono, S., Aqueous Synthesis and Characterization of Ag and Ag–Au Nanoparticles: Addressing Challenges in Size, Monodispersity and Structure. *Philosophical Transactions of the Royal Society of London A: Mathematical, Physical and Engineering Sciences* 2010, *368*, 4275-4292.
3. Nishimura, S.; Dao, A. T. N.; Mott, D.; Ebitani, K.; Maenosono, S., X-Ray Absorption near-Edge Structure and X-Ray Photoelectron Spectroscopy Studies of Interfacial Charge Transfer in Gold–Silver–Gold Double-Shell Nanoparticles. *The Journal of Physical Chemistry C* 2012, *116*, 4511-4516.
4. Jellinek, J., *Theory of Atomic and Molecular Clusters: With a Glimpse at Experiments*; Springer Science & Business Media, 2012.
5. Jellinek, J.; Krissinel, E., Ni N Al M Alloy Clusters: Analysis of Structural Forms and Their Energy Ordering. *Chemical physics letters* 1996, *258*, 283-292.
6. Pittaway, F.; Paz-Borbón, L. O.; Johnston, R. L.; Arslan, H.; Ferrando, R.; Mottet, C.; Barcaro, G.; Fortunelli, A., Theoretical Studies of Palladium− Gold Nanoclusters: Pd− Au Clusters with up to 50 Atoms. *The Journal of Physical Chemistry C* 2009, *113*, 9141-9152.
7. Oakley, M. T.; Johnston, R. L.; Wales, D. J., Symmetrisation Schemes for Global Optimisation of Atomic Clusters. *Physical Chemistry Chemical Physics* 2013, *15*, 3965-3976.
8. Moreno, V.; Creuze, J.; Berthier, F.; Mottet, C.; Tréglia, G.; Legrand, B., Site Segregation in Size-Mismatched Nanoalloys: Application to Cu–Ag. *Surface science* 2006, *600*, 5011-5020.
9. Rapallo, A.; Rossi, G.; Ferrando, R.; Fortunelli, A.; Curley, B. C.; Lloyd, L. D.; Tarbuck, G. M.; Johnston, R. L., Global Optimization of Bimetallic Cluster Structures. I. Size-Mismatched Ag–Cu, Ag–Ni, and Au–Cu Systems. *The Journal of chemical physics* 2005, *122*, 194308.
10. Martin, T. P., Shells of Atoms. *Physics Reports* 1996, *273*, 199-241.
11. Somorjai, G. A.; Chaudret, B.; Serp, P.; Philippot, K., *Nanomaterials in Catalysis*; John Wiley & Sons, 2012.
12. Marks, L., Surface Structure and Energetics of Multiply Twinned Particles. *Philosophical Magazine A* 1984, *49*, 81-93.
13. Marks, L.; Smith, D. J., High Resolution Studies of Small Particles of Gold and Silver: I. Multiply-Twinned Particles. *Journal of Crystal Growth* 1981, *54*, 425-432.
14. Cleri, F.; Rosato, V., Tight-Binding Potentials for Transition Metals and Alloys. *Physical Review B* 1993, *48*, 22.
15. Chen, F.; Curley, B. C.; Rossi, G.; Johnston, R. L., Structure, Melting, and Thermal Stability of 55 Atom Ag-Au Nanoalloys. *J. Phys. Chem. C* 2007, *111*, 9157-9165.
16. Kittel, C.; Holcomb, D. F., Introduction to Solid State Physics. *American Journal of Physics* 1967, *35*, 547-548.

17. Baletto, F.; Ferrando, R.; Fortunelli, A.; Montalenti, F.; Mottet, C., Crossover among Structural Motifs in Transition and Noble-Metal Clusters. *The Journal of chemical physics* 2002, *116*, 3856-3863.
18. Rosato, V.; Guillope, M.; Legrand, B., Thermodynamical and Structural Properties of Fcc Transition Metals Using a Simple Tight-Binding Model. *Philosophical Magazine A* 1989, *59*, 321-336.
19. Curley, B.; Rossi, G.; Ferrando, R.; Johnston, R., Theoretical Study of Structure and Segregation in 38-Atom Ag-Au Nanoalloys. *The European Physical Journal D* 2007, *43*, 53-56.
20. Zhang, M.; Fournier, R., Structure of 55-Atom Bimetallic Clusters. *Journal of Molecular Structure: THEOCHEM* 2006, *762*, 49-56.
21. Mulliken, R. S., Electronic Population Analysis on Lcao–Mo Molecular Wave Functions. I. *The Journal of Chemical Physics* 1955, *23*, 1833-1840.
22. Johnston, R.; Roberts, C., Soft Computing Approaches in Chemistry. *Studies in Fuzziness and Soft Computing* 2003, 120.
23. Heiles, S.; Logsdail, A. J.; Schäfer, R.; Johnston, R. L., Dopant-Induced 2d–3d Transition in Small Au-Containing Clusters: Dft-Global Optimisation of 8-Atom Au–Ag Nanoalloys. *Nanoscale* 2012, *4*, 1109-1115.
24. Paolo, G., et al., Quantum Espresso: A Modular and Open-Source Software Project for Quantum Simulations of Materials. *Journal of Physics: Condensed Matter* 2009, *21*, 395502.
25. Valiev, M., et al., Nwchem: A Comprehensive and Scalable Open-Source Solution for Large Scale Molecular Simulations. *Computer Physics Communications* 2010, *181*, 1477-1489.
26. Wang, J.; Wang, G.; Zhao, J., Density-Functional Study of Au N (N= 2–2 0) Clusters: Lowest-Energy Structures and Electronic Properties. *Physical Review B* 2002, *66*, 035418.
27. Zhao, G.; Zeng, Z., Geometrical and Electronic Structures of Aumagn (2⩽ M+ N⩽ 8). *The Journal of chemical physics* 2006, *125*, 014303.
28. Haynes, W. M., *Crc Handbook of Chemistry and Physics*; CRC press, 2014.
29. Chen, F.; Johnston, R. L., Charge Transfer Driven Surface Segregation of Gold Atoms in 13-Atom Au–Ag Nanoalloys and Its Relevance to Their Structural, Optical and Electronic Properties. *Acta Materialia* 2008, *56*, 2374-2380.
30. Chen, F.; Johnston, R. L., Energetic, Electronic, and Thermal Effects on Structural Properties of Ag− Au Nanoalloys. *ACS nano* 2007, *2*, 165-175.
31. Doye, J. P.; Wales, D. J., Global Minima for Transition Metal Clusters Described by Sutton–Chen Potentials. *New journal of chemistry* 1998, *22*, 733-744.
32. Wales, D. J.; Doye, J. P. K., Global Optimization by Basin-Hopping and the Lowest Energy Structures of Lennard-Jones Clusters Containing up to 110 Atoms. *J. Phys. Chem. A* 1997, *101*, 5111-5116.
33. Mortensen, J. J.; Hansen, L. B.; Jacobsen, K. W., Real-Space Grid Implementation of the Projector Augmented Wave Method. *Physical Review B* 2005, *71*, 035109.
34. Enkovaara, J., et al., Electronic Structure Calculations with Gpaw: A Real-Space Implementation of the Projector Augmented-Wave Method. *Journal of Physics: Condensed Matter* 2010, *22*, 253202.
35. Bahn, S. R.; Jacobsen, K. W., An Object-Oriented Scripting Interface to a Legacy Electronic Structure Code. *Computing in Science & Engineering* 2002, *4*, 56-66.

36. Gale, J. D., Gulp: A Computer Program for the Symmetry-Adapted Simulation of Solids. *Journal of the Chemical Society, Faraday Transactions* 1997, *93*, 629-637.
37. Gale, J. D.; Rohl, A. L., The General Utility Lattice Program (Gulp). *Molecular Simulation* 2003, *29*, 291-341.
38. Ismail, R.; Johnston, R. L., Investigation of the Structures and Chemical Ordering of Small Pd–Au Clusters as a Function of Composition and Potential Parameterisation. *Phys. Chem. Chem. Phys.* 2010, *12*, 8607-8619.
39. Cleveland, C. L.; Luedtke, W. D.; Landman, U., Melting of Gold Clusters. *Phys. Rev. B* 1999, *60*, 5065-5077.
40. Uppenbrink, J.; Wales, D. J., Structure and Energetics of Model Metal Clusters. *The Journal of chemical physics* 1992, *96*, 8520-8534.
41. Rossi, G.; Ferrando, R., Searching for Low-Energy Structures of Nanoparticles: A Comparison of Different Methods and Algorithms. *Journal of Physics: Condensed Matter* 2009, *21*, 084208.
42. Paz-Borbón, L. O.; Johnston, R. L.; Barcaro, G.; Fortunelli, A., A Mixed Structural Motif in 34-Atom Pd-Pt Clusters. *The Journal of Physical Chemistry C* 2007, *111*, 2936-2941.
43. Aguilera-Granja, F.; Vega, A.; Rogan, J.; Andrade, X.; García, G., Theoretical Investigation of Free-Standing Copd Nanoclusters as a Function of Cluster Size and Stoichiometry in the Pd-Rich Phase: Geometry, Chemical Order, Magnetism, and Metallic Behavior. *Physical Review B* 2006, *74*, 224405.
44. Henkelman, G.; Arnaldsson, A.; Jónsson, H., A Fast and Robust Algorithm for Bader Decomposition of Charge Density. *Computational Materials Science* 2006, *36*, 354-360.
45. Bochicchio, D.; Negro, F.; Ferrando, R., Competition between Structural Motifs in Gold–Platinum Nanoalloys. *Computational and Theoretical Chemistry* 2013, *1021*, 177-182.
46. Vegard, L., The Constitution of Mixed Crystals and the Space Occupied by Atoms. *Z. Phys* 1921, *5*, 17-26.
47. Vegard, L., X-Rays in the Service of Research on Matter. *Z Krist* 1928, *67*, 239-259.
48. Scanlon, D. O.; Dunnill, C. W.; Buckeridge, J.; Shevlin, S. A.; Logsdail, A. J.; Woodley, S. M.; Catlow, C. R. A.; Powell, M. J.; Palgrave, R. G.; Parkin, I. P., Band Alignment of Rutile and Anatase Tio2. *Nature materials* 2013, *12*, 798-801.
49. Pfeifer, V., et al., Energy Band Alignment between Anatase and Rutile Tio2. *The Journal of Physical Chemistry Letters* 2013, *4*, 4182-4187.
50. Hölzl, J.; Schulte, F. K.; Wagner, H., Solid Surface Physics. *Springer Tracts in Modern Physics* 1979, *84*.
51. Su, R.; Tiruvalam, R.; Logsdail, A. J.; He, Q.; Downing, C. A.; Jensen, M. T.; Dimitratos, N.; Kesavan, L.; Wells, P. P.; Bechstein, R., Designer Titania-Supported Au–Pd Nanoparticles for Efficient Photocatalytic Hydrogen Production. *ACS nano* 2014, *8*, 3490-3497.
52. Kennedy, J.; Jones, W.; Morgan, D. J.; Bowker, M.; Lu, L.; Kiely, C. J.; Wells, P. P.; Dimitratos, N., Photocatalytic Hydrogen Production by Reforming of Methanol Using Au/Tio2, Ag/Tio2 and Au-Ag/Tio2 Catalysts. *Catalysis, Structure & Reactivity* 2015, *1*, 35-43.

Appendix A

Table A1. Change in E_b and E_{exc} for all systems (lowest energy alloy arrangements) investigated (ΔE_{exc} and ΔE_b, respectively) with values given relative to the structure with the lowest ΔE_{exc} or ΔE_b. [All cases given relative to the lowest value]. The Fermi Energy (E_f) is given in the final column. All values are given in eV.

Structure	ΔE_b^{Gupta}	ΔE_{exc}^{Gupta}	ΔE_b^{DFT}	ΔE_{exc}^{DFT}	E_f
Ag_{147}	0.000	12.959	0.000	4.499	−3.996
Au_1Ag_{146}	0.008	12.549	0.004	4.384	−4.013
$Au_{13}Ag_{134}$	0.108	7.864	0.052	3.204	−4.067
$Au_{13}@Ag_{134}$	0.082	11.738	0.051	3.364	−3.964
$Au_{55}Ag_{92}$	0.388	1.150	0.200	2.080	−4.227
$Au_{55}@Ag_{92}$	0.372	3.420	0.184	4.470	−4.039
$Au_{74}Ag_{73}$	0.500	0.135	0.263	2.212	−4.335
$Au_{92}Ag_{55}$	0.602	0.000	0.319	2.746	−4.515
$Ag_{55}@Au_{92}$	0.551	7.379	0.338	0.000	−4.802
$Au_{134}Ag_{13}$	0.818	2.561	0.437	6.040	−4.808
$Ag_{13}@Au_{134}$	0.815	2.971	0.436	6.296	−4.873
$Au_{146}Ag_1$	0.873	4.190	0.466	7.789	−4.839
Au_{147}	0.879	4.336	0.468	7.956	−4.830

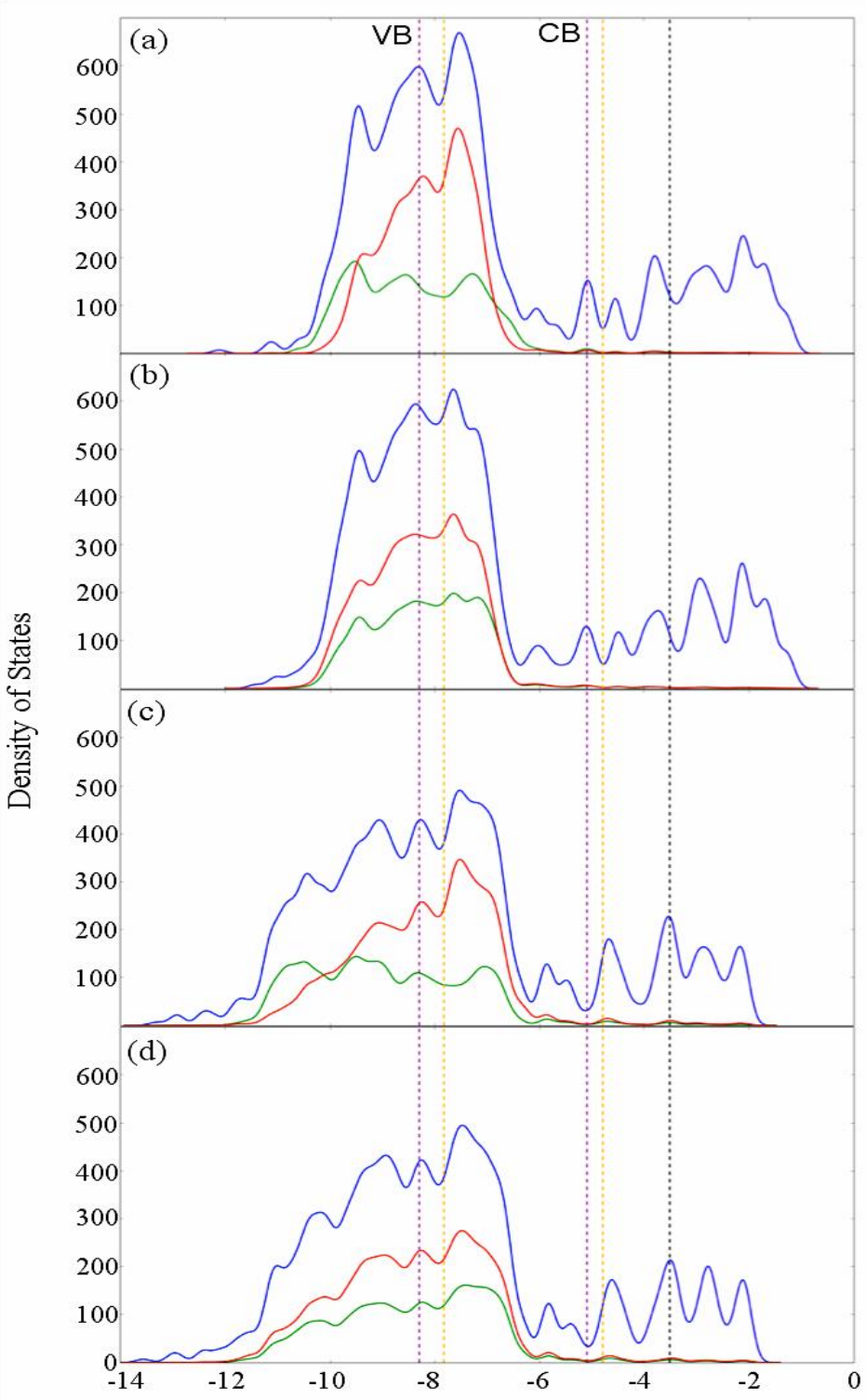

Fig. A1 DOS profiles for both alloys and core@shell compositions: (a) $Au_{13}@Ag_{134}$, (b) $Au_{13}Ag_{134}$, (c) $Ag_{13}@Au_{134}$, (d) $Au_{134}Ag_{13}$. A key is provided. E_f is given as a black dotted line, with the valence band maximum (VBM) and conduction band minimum (CBM), in purple and orange, for anatase and rutile TiO_2, respectively. A Gaussian broadening of 0.05 eV has been used for the electronic states.

4 Kinetic stabilities of $(AuAg)_{147}$ nanoparticles: the influence of calcination processes on chemical ordering

4.1 Introduction

Core@shell nanoparticles can be advantageous when compared to the same mixed nanoalloy. For instance, the optical properties usually associated with gold and silver are maintained in an Au@Ag or Ag@Au structure, but when mixed as an alloy, the resultant properties are somewhere in between the two.[1] Not only do core@shell nanoparticles potentially result in the manifestation of more ideal properties, but they can also benefit from the interactions between the core and shell. Electron transfer from the core to shell can lead to enhanced stability, as observed for Au@Ag clusters, thus allowing for a more 'complete' shell coating.[2-3] Experimental synthesis of core@shell nanoparticles may be achieved through a sequential deposition/reduction process, beginning from an initial 'seed' core nanocluster. However, synthesis is not always straightforward due to the competing formation of alloys, and experimental reports of spontaneous interdiffusion at the core@shell boundary are rather troublesome.[4-5]

Competing alloy formation is particularly problematic for Au and Ag, due to their similar atomic radii, thus allowing easy mixing of the two metallic species. Jiang *et al.*[6] synthesized Au@Ag nanoparticles by immersing a desolvated metal organic framework (MOF) in an aqueous precursor Au solution, followed by an Ag precursor, with respective reduction and drying at each stage (Fig. 4.1). Nonetheless, the reverse deposition sequence (Fig. 4.1, approach II) resulted in Au@AuAg nanoparticles, with an alloy surface, rather than the intended Ag@Au chemical ordering. Mallin and Murphy also attempted synthesis of sub-10 nm Ag@Au nanoparticles, which, unfortunately proved to be alloys rather than core@shell arrangements, evidenced by direct dependence of the metal-to-salt ratio to the shift of the absorbance peak, and TEM imaging.[7] Finally, colloidal nanoparticles created by Srnová-Šloufová *et al.*[8] were found to have an Ag@AuAg chemical arrangement, rather than the intended Ag@Au.

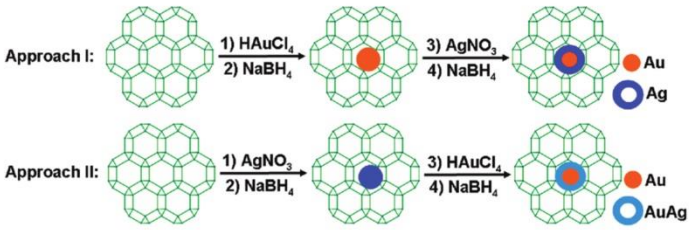

Fig. 4.1 The two synthesis methods used by Jiang et al. – approach I yielded Au@Ag structures, whilst approach II resulted in Au@AuAg nanoparticles.[6]

Nonetheless, Ag@Au nanoparticles are not impossible to synthesize: Li *et al.* achieved successful synthesis of 4-5 nm Ag@Au, Au@Ag and alloy nanoparticles using an inverse micelle method:[9] the micelle stabilises the outer layer of Ag@Au nanoparticles. These smaller core-shell particles are harder to characterise, as the shell will dominate the interaction with incident light, and electron plasmon oscillations will be dampened by any interactions between the two metallic constituent species. Using a combination of TEM and high angle annular dark field (HAADF) imaging in a scanning transmission electron microscope (STEM), confirmation of core-shell structures was achieved, even when shell thickness only extended to one or two atomic layers, for both Au@Ag and Ag@Au (Fig. 4.2, denoted as Au/Ag and Ag/Au in the image).[9]

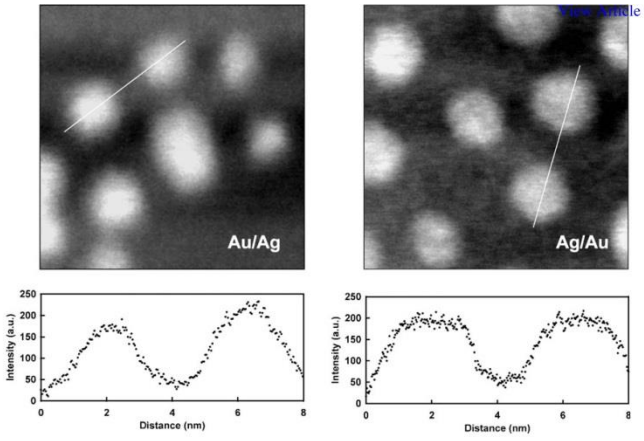

Fig. 4.2 HAADF-STEM images (13 nm x 13 nm) from core@shell nanoparticles, Au@Ag (left) and Ag@Au (right), with atomic composition 1 : 1. The representative line profiles are shown under the corresponding images.[9]

In the quest for uniformity, capping agents such as polyvinylpyrrolidone (PVP) are frequently enlisted to control nanocluster size, resulting in surfaces that are primarily capped by (100) facets.[10-11] The catalytic activity of these nanoparticles is

dramatically enhanced if the capping agents are removed following synthesis, which can be achieved through a calcination treatment. Therefore, an understanding of the stability of these nanoparticles under elevated temperatures is essential, particularly if the reactivity is dependent on a specific chemical ordering. Should chemical structure be vulnerable to operating conditions ('operando'), interatomic diffusion and/or phase segregation can have significant repercussions in regards to reactivity.

A powerful tool for investigating the thermal properties of nanoparticles is provided by molecular dynamics (MD) simulations using interatomic potentials. Simulations that maintain a continuous temperature are appropriate for studying the thermal behaviour of nanoparticles, performed in the canonical ensemble (constant composition, volume and energy (*NVT*)). Previous MD studies of pure Au nanoparticles by Cho *et al.*[12] were performed over a temperature range of 0-1300 K, using the modified embedded atom method (MEAM) potential, with some parameters slightly modified to fit elastic properties at 0 K. The MEAM is a semi-empirical potential with a single formalism for body-centred cubic (BCC), face-centred cubic (FCC), hexagonal close packed (HCP) and diamond-structure materials; its inclusion of angular forces distinguishes it from the original embedded atom method (EAM).

The melting point (T_m) of these spherical nanoparticles was observed to decrease with nanoparticle size (n = 6708 to 140, where n is the number of atoms), and has been verified by other studies as performed by Lewis *et al.* (n = 135-3997)[13] and Zhou *et al.* (n = 675-5425).[14] These studies established that the surface melts initially, followed by the core at a higher temperature (Fig. 4.3). However, surface pre-melting was not observed by Dellago and co-workers, instead finding that the Au nanocluster (n = 2624) melted as one, at T_m.[15] However, increased mobility of the surface atoms does significantly affect the geometry of the nanocluster, particularly the vertex and edge atoms: the increased inter- and intra-diffusion for these atomic positions means that T_m is ultimately measured for an almost-spherical geometry. Kuo *et al.* observed a structural transition from FCC to Ih, was found to occur in gold nanoparticles (n = 333-3055) as a result of heating, followed by a 'quasi-molten' state, in which the nanocluster fluctuated between several structural moieties continuously.[16] This solid-solid transition to the Ih has also been observed previously by Cleveland *et al.* for gold nanoparticles (n = 75-459).[17-18]

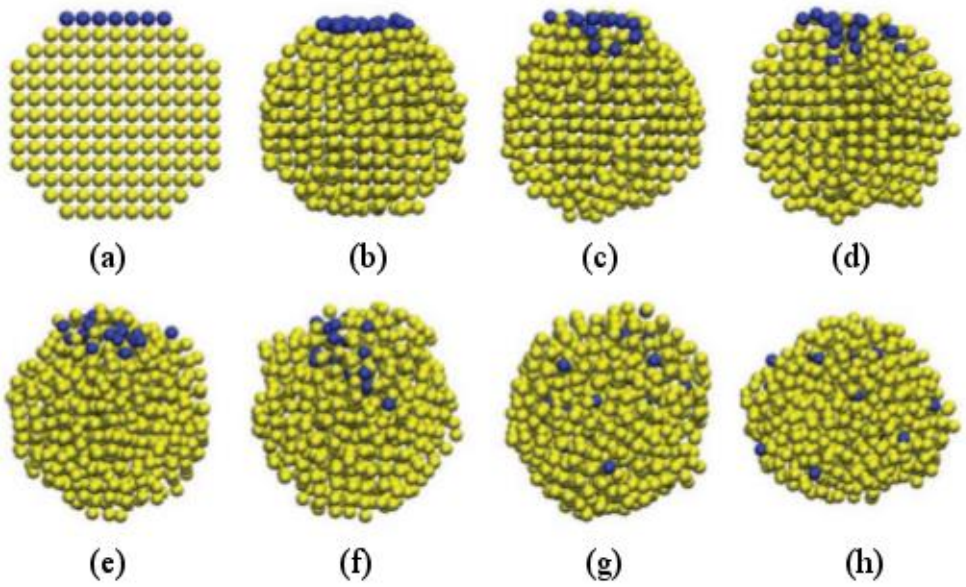

Fig. 4.3 Snapshots of the melting process of Au nanoparticles (*n* = 675) at 690 K, taken from Zhou et al.; (a) 0 ps, (b) 1 ps, (c) 50 ps, (d) 100 ps, (e) 150 ps, (f) 200 ps, (g) 500 ps, (h) 800 ps. The surface atoms have been marked as blue for clarity.

The melting temperature of Ag nanoparticles has also been found to decrease with decreasing nanocluster size.[19-20] On the basis of the calculated Gibbs free energy, Luo *et al*.[21] deduced general trends in the thermodynamic properties of nanoparticles, using MD simulations with the MEAM to establish free energy curves. Comparisons of bulk and surface free energies show that it is the surface atoms that determine the size effect on the thermodynamic properties of nanoparticles. These studies are in good agreement with the liquid drop model,[22] which assumes that T_m of a nanocluster is primarily based on the variation of the cohesive energy and its surface tension, i.e. T_m and molar heat of fusion should decrease with atomic size (Fig. 4.4).

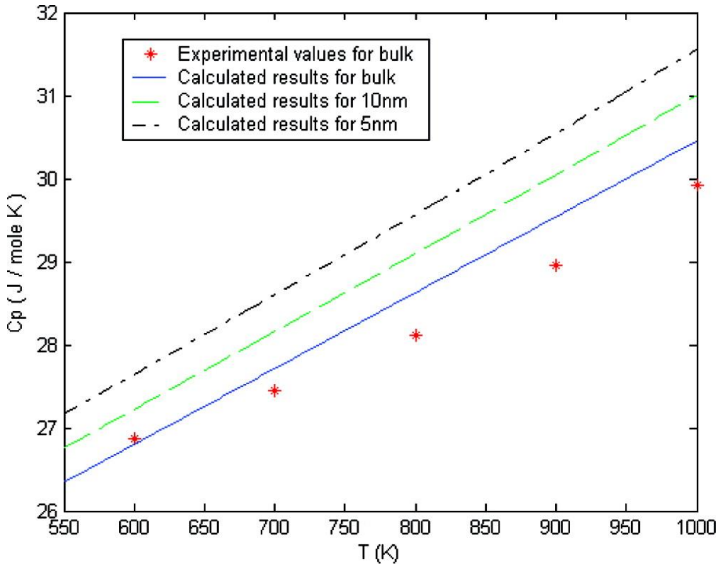

Fig. 4.4 Molar heat capacity as a function of *T* for Ag nanoparticles and bulk, from Luo et al.[21]

Chernyshev determined that surface pre-melting of the nanocluster does not occur if the nanocluster radius (r) is below that of the critical radius (r_c), which differs according to the material in question.[23] If $r < r_c$, there is a transition for the surface layer to a pseudo-crystalline state, before the whole particle melts. MD simulations by Zhou *et al.* found that Ag nanoparticles melted at a single temperature for nanocluster sizes below 8 nm and, above this size range (8-20 nm), formed quasi-liquid pools at a surface pre-melting temperature.[24] These pools expanded to form a quasi-liquid layer before the entirety of the nanocluster melted. Similarly, Zhao and co-workers identified three distinctive melting mechanisms for Ag nanoparticles. Surface pre-melting was observed for nanoparticles n = 258-3871, whereas the melting of $Ag_{13} - Ag_{178}$ may be described as a transition from a low-energy solid-like structure at low temperatures to a higher energy liquid-like structure at high temperatures. Finally, for n = 120-240, a third intermediate melting mechanism was established, in which as n decreases, T_m depresses very slowly and the latent heat of fusion has a great enhancement.

As expected, the thermal properties of bimetallic nanoparticles are more complex than those observed for the monometallic equivalents. Mottet *et al.*[25] found that the introduction of a single impurity dopant can elevate T_m, as shown by the incorporation of a single Ni or Cu atom into Ih Ag clusters of n atoms (n = 55, 147, 309, and 561). However, the incorporation of an Au atom did not elevate T_m,

suggesting that only when the atomic size mismatch is significant, atoms smaller than Ag tend to be incorporated inside the nanocluster. The strained Ih is more relaxed and its thermal stability is enhanced as a result. Likewise, canonical Monte Carlo (MC) simulations showed the addition of a single Cu atom to Au_{55} (Ih) increased T_m by up to 150 K.[26]

MD simulations of Ih Au_xAg_{55-x} nanoparticles by Chen *et al.*[27] identified a correlation between increasing Au content and decreasing T_m, in line with the melting temperatures for the corresponding monometallics [$T_m(Ag_{55})$ = 525–600 K; $T_m(Au_{55})$ = 290–460 K]. Au_{55} has a large melting temperature range, due to the presence of glass transitions during the melting process, also present in Au-rich nanoalloys ($30 \leq x \leq 50$). Chen and Johnston also performed a selective MD simulation of a core@shell $Au_{55}@Ag_{92}$ bimetallic nanocluster, where the spontaneous transformation from CO to Ih was observed.[28] This solid-solid transition has since been termed a martensitic transformation (MT), i.e. a diffusion-less cooperative atomic movement. The MT is not observed for the larger $Au_{147}@Ag_{162}$ nanocluster, which instead forms a solid solution before melting at 632 K. The core@shell ordering is lost during melting.

The influence of size and composition on the phase stability of Au-Ag nanoparticles was studied by Qi and Lee in spherical nanoparticles, (n = 555, 959).[29] The formation energy initially decreased and then increased with increasing Au concentration, with the most negative formation energy occurring at 50% Au, as this has the greatest mixing of the bimetallic clusters. The larger 959-atom nanocluster has lower formation energies than the 555-atom nanocluster, for almost all compositions, indicating that larger nanoparticles are more stable than small ones with the same composition (Fig. 4.5). Alloys were also determined to be more energetically stable than core@shell arrangements. Surface melting was observed to occur before the core, and the melting process resulted in a loss of the core@shell arrangement, resulting in similar T_m for alloy and core@shell arrangements.

Qi and Lee[29] also studied the influence of geometry, with n = 561 for CO and Ih nanoparticles and n = 584 for a decahedral motif (Dh). The shape was found to have little effect on the melting process, however, during a sustained anneal (600 K for 58 ns), shape heavily influenced the stability of core@shell arrangements: the CO

formed an alloy surface quickest, followed by the Ih. The Dh retains its core@shell arrangement during annealing, and thus the alloy rate of formation is CO > Ih > Dh.

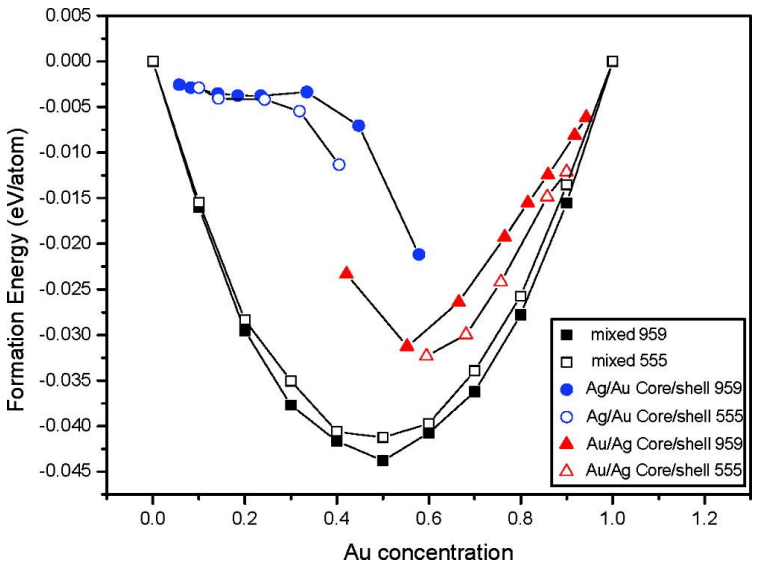

Fig. 4.5 Formation energies of Au−Ag bimetallic spherical nanoparticles with 555 and 959 atoms at 0 K. A key is provided, 'mixed' refers to an alloy chemical arrangement.

As we have seen so far, there is uncertainty regarding whether the shell melts before the core in nanocluster simulations. It is also unclear as to whether the initial geometry is maintained throughout, with MTs to/from the Ih observed at lower nuclearities. This chapter concerns the influence of heating of 147-atom Au_xAg_{147-x} nanoparticles (where x is the number of Au atoms) as a function of composition (x = 0, 1, 13, 55, 92, 134, 146, and 147) and chemical arrangement (alloy vs. core@shell). Our aims are to establish the stability of chemical ordering in these nanoparticles, and determine whether this is lost in pre-melting stages, or only after T_m has been reached. The structures are those as obtained from Ch. 3, and we simulate the annealing process that is performed during nanocluster synthesis in order to remove protecting agents.[30] The stability of kinetically obtained structures is of particular interest, rather than that of equilibrium poly-disperse samples produced in the absence of any stabilizing ligands, as the shape-controlled geometries are experimentally viable and desirable for applications such as heterogeneous catalysis. Both gold and silver have a bulk FCC crystal structure, and thus we use, among other motifs, the CO as an experimentally obtainable fragment of the FCC crystal.

4.2 Methodology

We subject the CO AuAg nanoparticles, with chemical ordering as obtained from the basin-hopping algorithm in Ch. 3, as well as ordered core@shell, to a heating process analogous to experiment, using MD simulations in the *NVT* ensemble, as outlined in Ch. 2. Initial testing of parameters showed an MT from CO to Ih, and thus when comparing melting points, it is essential that we consistently compare the Ih melting point. Therefore, if the nanocluster does not undergo this transition, the heating process is repeated using an Ih starting geometry.

4.2.1 Energetic and Compositional Analysis

Energetic Analysis

Fluctuations in the internal energy of nanoparticles indicate the occurrence of morphological changes; the solid-liquid transition that occurs for the melting of nanoparticles can be identified by a sudden increase in the internal energy. In this chapter, caloric curves are plotted, determining the change in the total internal energy (E) relative to that of the starting arrangement:

$$E_{\mathrm{diff}} = E_t - E_{t=0} \qquad \textbf{(3-1)}$$

where E_t is the total internal energy at time t, $E_{t=0}$ is the energy of the starting structure when t=0. E_{diff} is then averaged over the ten independent simulations (which have different random number seeds) to give $\langle E_{\mathrm{diff}} \rangle$, and thus where applicable, we also provide the $\langle E_{\mathrm{diff}} \rangle$ range. Whilst we cannot establish precise melting points for the nanoparticles, we aim to obtain a qualitative interpretation of how the chemical ordering influences the $\langle E_{\mathrm{diff}} \rangle$ trend. $\langle E_{\mathrm{diff}} \rangle$ allows for energetic transitions, such as the MTs that occur for Ag-rich nanoparticles, to be easily identified, although we acknowledge that the relative energies of different isomers can also be lost in plotting this. Therefore, the total internal energy is also plotted as a function of T in Appendix B.

Chemical and Structural Characterisation

Structure type assignment is performed using the adaptive common neighbour analysis (a-CNA) method, as implemented in the software package Ovito.[31] The a-CNA is advantageous in that it does not rely upon a user-defined cutoff radius for

determining nearest neighbours, working without a fixed cutoff. The a-CNA is given as a percentage, which is averaged over ten independent simulations (with different random number seeds). The percentages provided in this work concern only FCC and HCP characteristics (referred to hereafter as $\langle P_{FCC} \rangle$ and $\langle P_{HCP} \rangle$, respectively); percentages for all 'other' structure types are collectively referred to as $\langle P_{OTH} \rangle$.

The chemical ordering within the nanocluster is more complex, especially where alloy nanoparticles are concerned. The radial distribution function (RDF) is an averaging technique, and thus the data it provides do not allow for proper insight into the chemical arrangement. Instead, we map the radial chemical distribution function (RCDF): working from the nanocluster's centre of mass outwards, the molar ratio of Au is monitored within the volume delimited by two spherical surfaces, with radii r_{RCDF} and $r_{RCDF} + \varepsilon$, respectively (Fig. 4.6), where ε is the thickness.[32] r_{RCDF} is measured relative to the nanocluster's centre of mass and ranges from zero to the maximum pair distance of the cluster in integer multiples of ε, which is fixed at 0.3 Å.

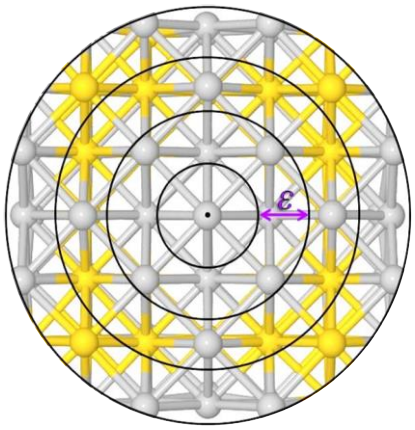

Fig. 4.6 Schematic diagram of the division of the nanocluster into concentric spheres, used to map the RCDF. The distance between spherical surfaces is ε. No atoms are found within the volume delimited between the centre of mass and the first surface, at ε, which would result in a region of white space in the RCDF.

4.3 Results and Discussion

4.3.1 Thermal behaviour of pure and single dopant atom nanoparticles

Pure nanoparticles

Starting from a 147-atom CO arrangement, the thermal behaviour of AuAg nanoparticles was studied over a temperature range of 1-900 K, in increments of 10 K. This temperature range was chosen on the basis that experimental calcination can require temperatures of up to 673 K,[53] and we have extended it further to include the melting behaviour of the nanoparticles. The clusters were initially equilibrated at 1 K, first using the Berendsen thermostat (relaxation constant = 0.1 ps), followed by the NH thermostat (relaxation constant = 0.01 ps), for a total equilibration time of 200 ps and Δt = 0.001 ps. The production runs were then performed in the *NVT* ensemble, Δt = 0.001 ps, for a duration of 1 ns, using the NH thermostat. To ensure that a canonical system is represented correctly, we have performed ten independent simulations (using different random seeds) to determine an ensemble average and unless otherwise discussed, results are presented as these averages. The majority of CO nanoparticles exhibit a transition to the Ih, and thus for direct T_m comparison, the structures that did not undergo the same transformation were also subjected to the same heat treatment from an initial Ih geometry. *Unless otherwise stated, T_m refers to the melting point of the Ih.*

Under heating, Ag_{147} undergoes a solid-solid transformation, or structural MT,[54] from CO to Ih at 226 K (the transition temperature, T_t) (Fig. 4.7), reflected in a reduction of $<E_{diff}>$. An MT refers to a structural change that occurs via cooperative atomic movement with no long range diffusion of atoms, driven by the difference in energy between the parent and product phases. The newly-formed Ih is stable until melting at 688 K (Table 4.1), as indicated by a sudden increase in the energy of the system. We aim to establish the thermal behaviour trends that occur as a result of differing chemical arrangements, rather than to determine exact transition and/or melting points for specific systems. Therefore, in order to verify that the MT does not occur as a result of the chosen heating rate, we also performed sustained annealing for longer periods (100 ns) for Ag_{147} at 150 K and 200 K; no MT was found to occur at these lower temperatures.

Fig. 4.8 shows $<E_{diff}>$ for Au_{147}; there is no MT – at most the formation of facets can be observed at ~340 K (inset), as a result of a step dislocation. Pinpointing of T_m from $<E_{diff}>$ is much more difficult for Au_{147}, due to the smoother energetic profile. Therefore, T_m is indicated by a complete loss of structure in the a-CNA profile.

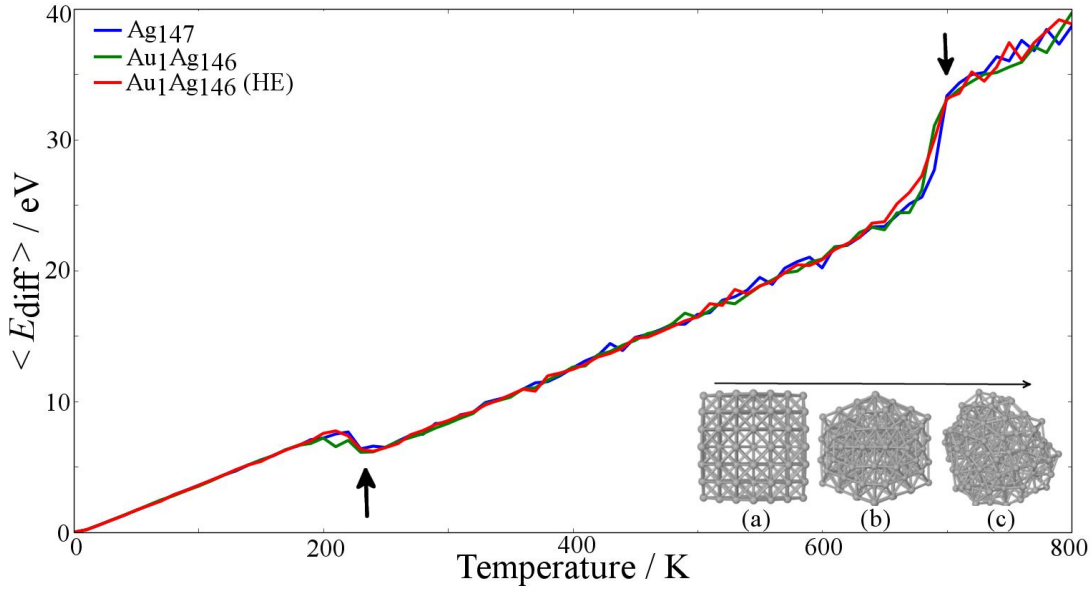

Fig. 4.7 <Ediff> as a function of T for: pure Ag_{147}, and the addition of a single gold dopant atom in (i) a low energy position [Au_1Ag_{146}] and (ii) a high energy (HE) position [Au_1Ag_{146} (HE)]. A key is provided; the transition temperature, T_t, and the melting temperature, T_m, have been highlighted with upward and downward arrows, respectively. Inset: Ag_{147} at (a) 0 K, (b) 230 K, after an MT, and (c) 690 K, after melting.

An a-CNA profile for a 147-atom CO nanocluster has $<P_{FCC}>$ = 37.4%, and no HCP features at 0 K; in contrast, the perfect Ih geometry has $<P_{HCP}>$ = 20.4%. Fig. 4.9 shows the a-CNA profile for Ag_{147} and Au_{147}; initially, the Ag_{147} nanocluster has perfect CO geometry, and when T is increased to 210-230 K, there is a sharp increase in $<P_{HCP}>$ (20.4%) (and decrease in $<P_{FCC}>$), indicative of the sudden MT to the Ih geometry. In contrast, when competing HCP character begins to occur for Au_{147} (300 K), $<P_{FCC}>$ does not immediately go to zero. Instead, the two structure types compete with one another until close to T_m, and thus the perfect Ih geometry is never obtained i.e. there is no MT. The competition between the two crystal structures increases the extent of deformation Au_{147} is able to undergo and allows the maintenance of a facetted crystalline geometry [5- and 6-fold rings at the vertices] during the heat treatment (Fig. 4.8, inset). The FCC and HCP phases are present

until $T \approx$ 420-460 K, about 100 K below $T_m(Au_{147})$, after which only HCP features remain, with the solid-liquid transition occurring at 555 K.

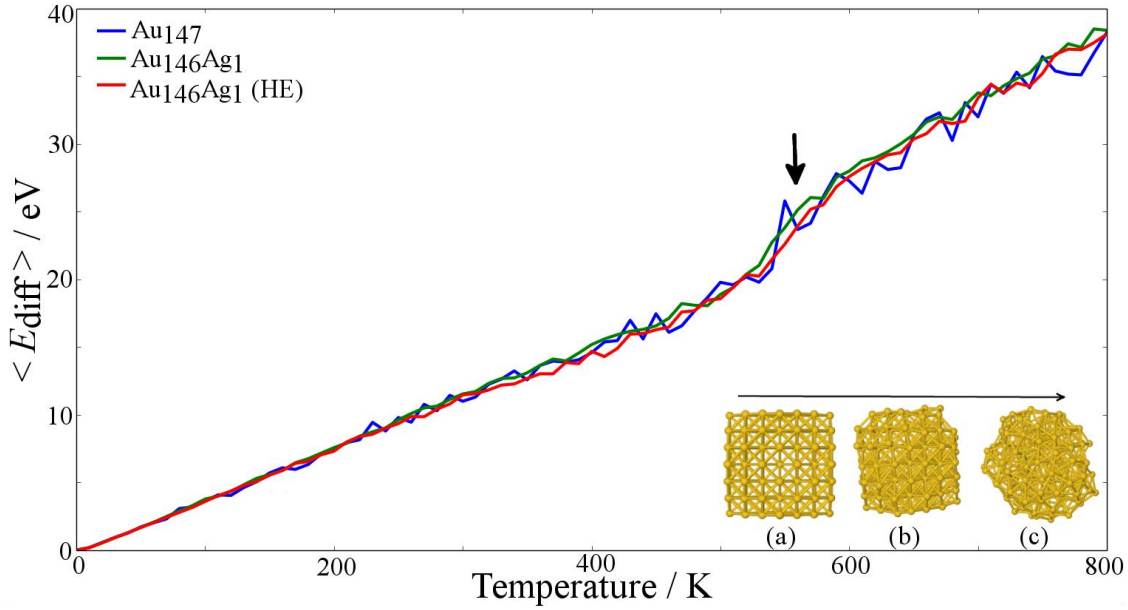

Fig. 4.8 $<E_{diff}>$ as a function of T for Au_{147} and the addition of a single Ag dopant atom in (i) a low energy (thermodynamically favourable at 0 K) position [$Au_{146}Ag_1$] and (ii) a high energy (HE) position (thermodynamically unfavourable at 0 K) [$Au_{146}Ag_1$ (HE)]. A key is provided and T_m is highlighted by a downward arrow. Inset: Au_{147} undergoes a step dislocation as it transitions from (a) CO at 0 K to (b) a facetted arrangement at 340 K. However, no significant energy change is noted before it melts (c), after which there are energy fluctuations.

The observed MT for these nanoparticles is known as Lipscomb's diamond-square-diamond (DSD) mechanism: triangular facets are stretched into a diamond arrangement, followed by a square via a collective screw dislocation of atoms (Fig. 4.10).[33-36] The dislocation corresponds to a rotation of different angles according to the initial and final configuration. Conversely, a square facet can transform into two triangular facets by the same mechanism in reverse. Given the differing behaviour for CO Ag_{147} and Au_{147} nanoparticles, we extended the study to include initial Dh geometries: this time, both Ag_{147}(Dh) and Au_{147}(Dh) exhibit an MT, at 289 and 285 K, respectively. The higher T_t for Ag_{147}(Dh) in comparison to Ag_{147}(CO) indicates that the barriers to transformation are greater for the Dh geometry, which suggests that the kinetic stability of Ag_{147} is CO < Dh < Ih. However, the kinetics for Au_{147} are more complicated due to the lack of structural transitions, e.g. Dh < CO ≈ Ih.

Given the occurrence of the MT, the melting points are equivalent to that of Ag_{147}(Ih) and Au_{147}(Ih), respectively.

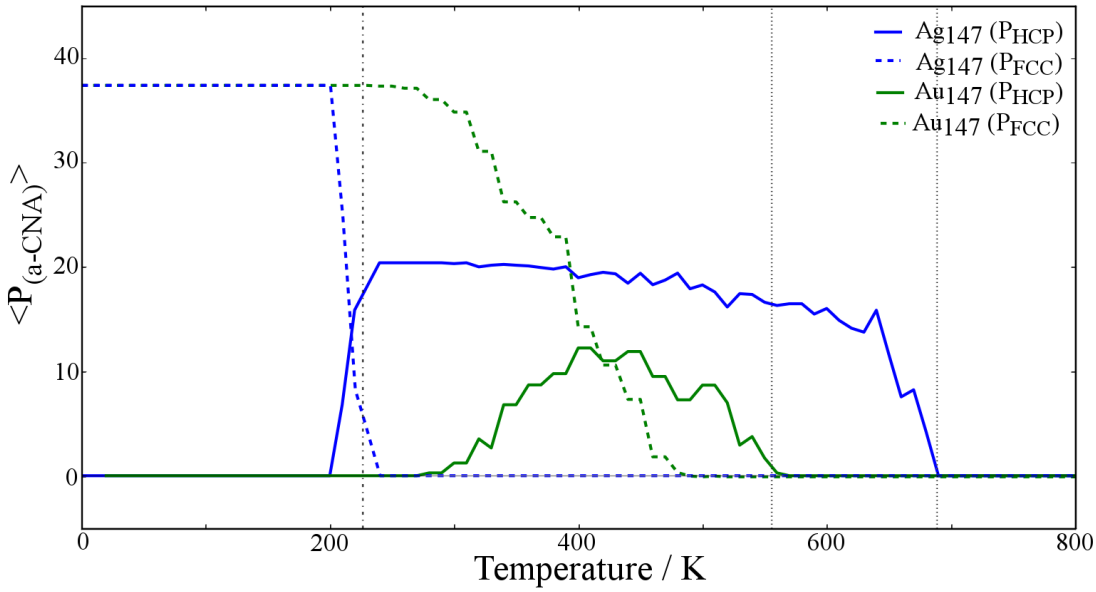

Fig. 4.9 Average a-CNA percentages as a function of *T* for Ag_{147} and Au_{147}. Solid lines represent $<P_{HCP}>$ and dashed lines represent $<P_{FCC}>$; a key is provided. A perfect CO geometry consists of $<P_{FCC}>$ = 37.4%, $<P_{HCP}>$ = 0%, and $<P_{OTH}>$ = 62.6%, whereas a perfect Ih geometry does not contain any FCC features ($<P_{HCP}>$ = 20.4% and $<P_{OTH}>$ = 79.6%). T_t and T_m are indicated by dash-dotted and dotted lines, respectively.

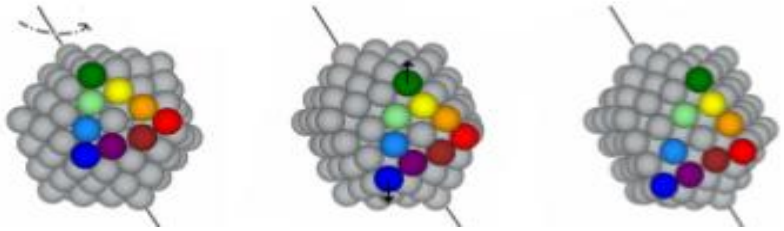

Fig. 4.10 Ih transforming to CO via the DSD mechanism, the central image is the saddle point, from Pavan *et al.*.[33] Multicoloured atoms highlight a facet of the original Ih, which rotate by 60° (in the opposite direction to the other parallel triangular (111) facets) to form a diamond facet, which then transforms to a square (100) facet.

Single dopant atoms

The simplest bimetallic systems involve the addition of a single dopant atom into the pure nanocluster, resulting in Au_1Ag_{146} and $Au_{146}Ag_1$. Several permutations of the dopant atom are possible, and therefore we take both the lowest energy and highest energy (HE) arrangements as found in Ch. 3, to ensure that the results we obtain are not a consequence of the chosen starting arrangement. The single dopant structures we have used are provided in Appendix B.

Au_1Ag_{146}(CO) undergoes an MT, with little difference to T_t and T_m in comparison to Ag_{147}; similarly, a single Ag atom in Au_{147} ($Au_{146}Ag_1$(CO)) has little effect on T_t or T_m [the variance is < 10 K, which is smaller than the heat increments used in the annealing process]. In both instances, the dopant atom remains static until close to melting point. In regards to the Dh geometry, the introduction of dopants has little effect, with the exception of $Au_{146}Ag_1$(Dh): when the dopant atom is in a high energy configuration, T_t is lowered by 30 K, suggesting that the barriers to transformation are dependent on the position of a dopant in this instance.

Of the pure and singly doped systems, all nanoparticles exhibit an MT, with the exception of Au_{147}(CO) and $Au_{146}Ag_1$(CO). Fig. 4.8 shows many fluctuations in $\langle E_{diff} \rangle$, demonstrating the high number of local basins that are available, indicating a lack of preference for a particular structural motif; previous work by Garzon *et al.* has shown small Au clusters can undergo a high degree of deformation, and are just as stable as highly ordered FCC morphologies. Baletto *et al.*[37] demonstrated that the Ih window for small Au nanoparticles is very small, and these high and low facetted symmetries are in close competition with one another energetically. Therefore, a greater understanding of the kinetic influences is warranted, such as an investigation into the energy transition barriers.

Table 4.1 Summary of the transition and melting temperatures for pure and single dopant structures, where (CO) = cuboctahedral, (Ih) = icosahedral, (Dh) = decahedral, and (HE) = high energy. T_m[Ih] is averaged from 10 ensembles and refers to the Ih melting point, although the starting geometry is also provided in square parentheses for clarity, given that not all clusters undergo an MT. Transition/melting ranges over the ensemble are provided in parentheses. For the nanoparticles that do not undergo an MT, the melting point of the CO, T_m[CO], is also available.

Composition & Structure	T_t [CO to Ih] / K	T_m [Ih] / K [*starting geometry*]	T_m [CO] / K
Ag_{147} [CO]	226 (220-230)	688 (660-700) [*CO*]	
Au_1Ag_{146} [CO]	228 (200-230)	696 (690-700) [*CO*]	
Au_1Ag_{146} (HE) [CO]	221 (190-240)	691 (680-700) [*CO*]	
Ag_{147} [Dh]	289 (240-310)	693 (680-710) [*Dh*]	
Au_1Ag_{146} [Dh]	294 (270-310)	693 (680-710) [*Dh*]	
Au_1Ag_{146} (HE) [Dh]	274 (240-300)	688 (680-710) [*Dh*]	
Au_{147} [CO]	-	555 (540-570) [*Ih**]	555 (540-560)
$Au_{146}Ag_1$ [CO]	-	-	551 (540-560)
$Au_{146}Ag_1$ (HE) [CO]	-	-	554 (540-570)
Au_{147} [Dh]	285 (270-300)	550 (540-560) [*Dh*]	
$Au_{146}Ag_1$ [Dh]	286 (250-310)	555 (540-570) [*Dh*]	
$Au_{146}Ag_1$ (HE) [Dh]	256 (210-280)	553 (540-570) [*Dh*]	

*As this cluster does not undergo an MT, a stoichiometrically equivalent Ih is used as the starting arrangement to obtain T_m(Ih).

4.3.2 Alloy nanoparticles for Au_xAg_{147-x} (x = 13, 55, 92, 134)

Low-energy, mixed alloy Au_xAg_{147-x} CO nanoparticles, with x = 13, 55, 92 and 134, were subjected to the same heat treatment. As highlighted in Ch. 3, the Gupta potentials favour Au in a subsurface position and in an arrangement that maximises the number of Au-Ag bonds.[38] As we have found differing kinetic behaviours for Ag_{147} and Au_{147} in regards to the MT, it is reasonable to assume that the route taken will depend on the stoichiometric ratio of the two metallic species. As it is difficult to determine these structural changes from a-CNA alone, any local basins visited pre-

melting have been visualized. Indeed, we find that only certain nanoalloy stoichiometries undergo MTs, and thus direct comparison of T_m is made only for the Ih geometry – this topic is discussed separately below for clarity.

Martensitic transformations (MTs)

$Au_{13}Ag_{134}$ and $Au_{55}Ag_{92}$ undergo MTs from the CO to the Ih, at 254 and 331 K, respectively. The resulting Ih nanoparticles have a pseudo-onion chemical arrangement with an alloy surface: Ag@AuAg, maintaining the chemical ordering as in the CO. These transition temperatures are both higher than for Ag_{147} (T_t = 226 K), and thus we conclude that the incorporation of Au into the nanocluster increases the barrier to transition. Au-rich nanoparticles ($x \geq 92$) do not exhibit a clear-cut structural transformation, instead mimicking the behaviour of Au_{147} with the formation of surface facets (Fig. 4.11).

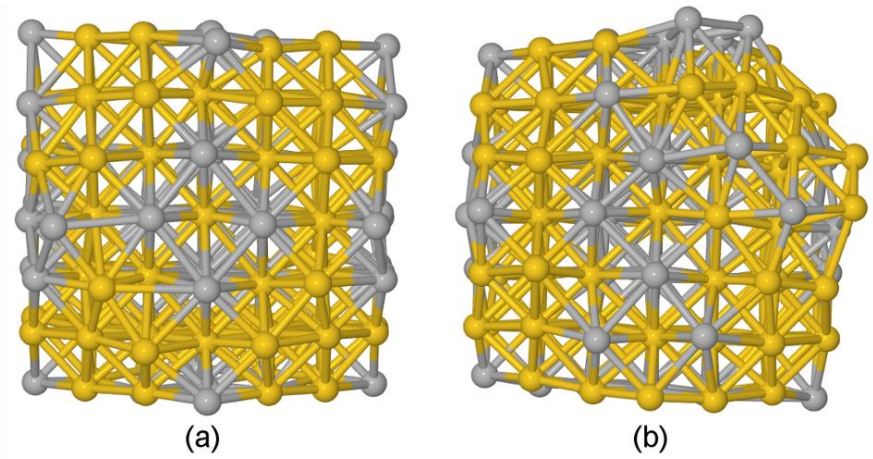

Fig. 4.11 Snapshot images of the alloy $Au_{92}Ag_{55}$(CO) at (a) 350 K and (b) 450 K, illustrating partial transformation of the nanoalloy structure. Grey spheres represent Ag atoms, while yellow spheres represent Au atoms.

Melting of the Ih

Direct T_m comparison can only be performed for Ih geometries, given the occurrence of MTs. Therefore, as neither $Au_{92}Ag_{55}$ nor $Au_{134}Ag_{13}$ undergo an MT, we also perform the same calcination treatments for $Au_{92}Ag_{55}$(Ih) and and $Au_{134}Ag_{13}$(Ih). These Ih alloys are obtained using the same atomic swapping methods as in Ch. 3; their structures are given below in Fig. 4.12.

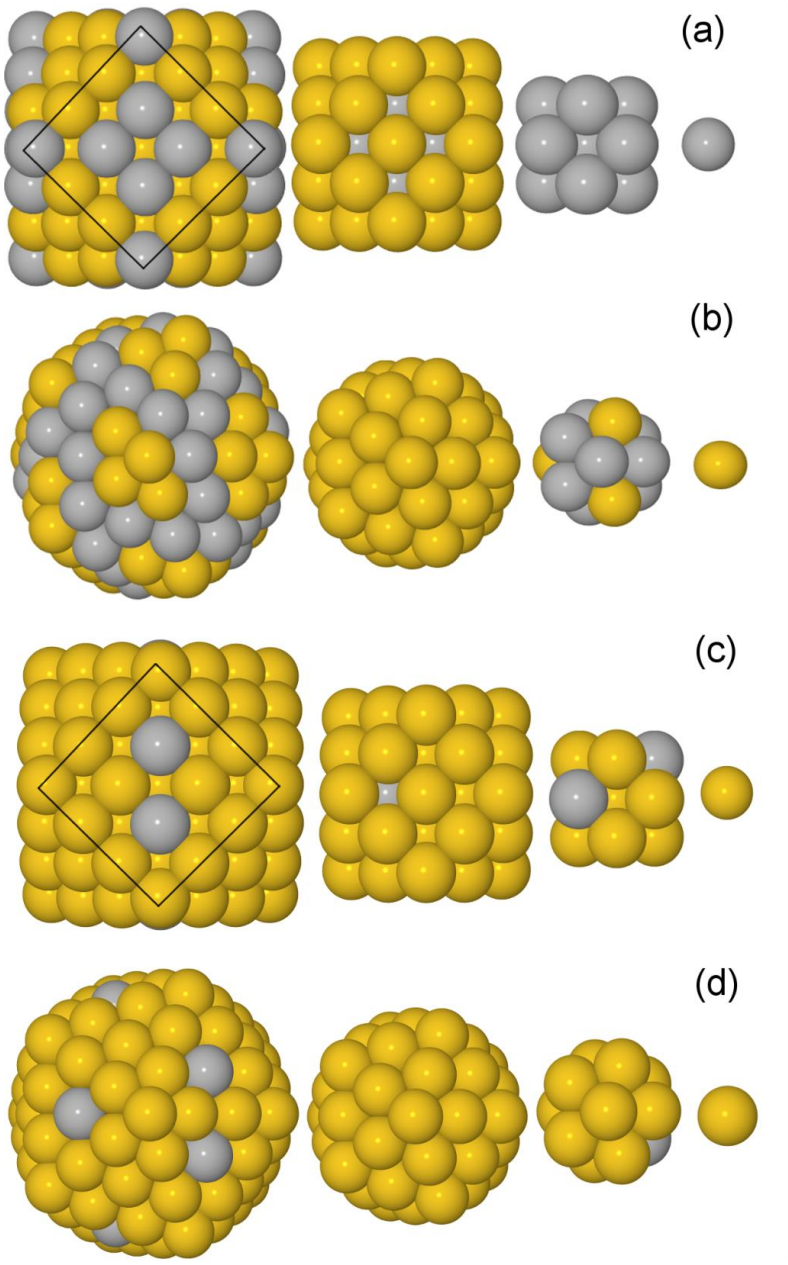

Fig. 4.12 Starting arrangements for alloy nanoparticles (a)-(d) at 0 K, removing one layer at a time: 147 atoms, 55 atoms, 13 atoms and 1 atom (left to right). Clusters depicted: (a) $Au_{92}Ag_{55}$(CO), (b) $Au_{92}Ag_{55}$(Ih), (c) $Au_{134}Ag_{13}$(CO) and (d) $Au_{134}Ag_{13}$(Ih). Grey spheres represent Ag atoms, yellow spheres represent Au atoms. For clarity, the (100) face of the CO has been outlined in black. $Au_{92}Ag_{55}$(CO) and (Ih) have very similar chemical arrangements, as do $Au_{134}Ag_{13}$(CO) and (Ih), with the majority of Ag atoms on the surface positioned centrally on the (100) faces and (111) faces for the CO and Ih geometries, respectively.

Fig. 4.13 and Fig. 4.14 represent the changes that occur in the alloy nanoparticles as a function of T for $\langle E_{diff} \rangle$ and the RCDF, respectively. The plotted nanoparticles are: $Au_{13}Ag_{134}$ and $Au_{55}Ag_{92}$, beginning in a CO arrangement, which undergo an MT, to

give T_m(Ih); $Au_{92}Ag_{55}$ and $Au_{134}Ag_{13}$, beginning from an Ih arrangement (as there is no MT). The RCDF is monitored in 0.3 Å increments, which can result in regions of 'white space' where no atoms are present within a particular radial segment. However, as the nanocluster is heated, the extent of structural disorder increases, and the number of 'white space' regions decreases.

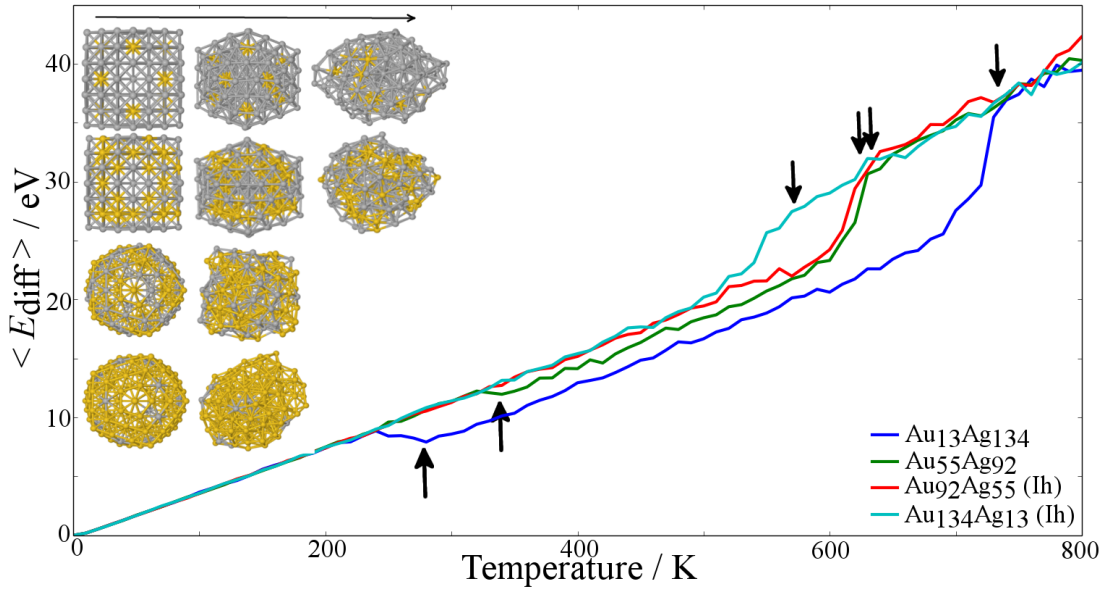

Fig. 4.13 <E_{diff}> as a function of temperature for alloy nanoparticles; a key is provided for the differing chemical arrangements. T_t and T_m are highlighted by upward and downward arrows, respectively. Inset, left to right: Nanoparticles at 0 K, T_t (where applicable), and T_m. Inset, top to bottom: $Au_{13}Ag_{134}$, $Au_{55}Ag_{92}$, $Au_{92}Ag_{55}$, $Au_{134}Ag_{13}$.

$Au_{13}Ag_{134}$ begins in a layered arrangement at 0 K, with Au atoms located at subsurface positions (Fig. 4.14(a)), where green markers represent regions that are Au-rich). The chemical ordering is stable until close to T_m (T_m = 724 K), where a greater degree of mixing between the two metals occurs, as indicated by an increase in the number of red markers (Au/Ag ratio ≈ 0.4 - 0.6). $Au_{55}Ag_{92}$ possesses a certain degree of intermixing initially, due to its chemical composition. All atoms are found to remain stationary until close to T_m for $Au_{55}Ag_{92}$, $Au_{92}Ag_{55}$ and $Au_{134}Ag_{13}$, which melt at 629 K, 624 K and 559 K, respectively. If we compare T_m of alloy nanoparticles with that of Ag_{147} and Au_{147}, we can determine that as x is increased, there is generally a corresponding decrease in T_m: $T_m(Ag_{147})$ = 688 K; $T_m(Au_{13}Ag_{134})$ = 724 K; $T_m(Au_{55}Ag_{92})$ = 629 K, $T_m(Au_{92}Ag_{55})$ = 624 K, $T_m(Au_{134}Ag_{13})$ = 559 K, $T_m(Au_{147})$ = 555 K. T_m for $Au_{13}Ag_{134}$ is higher than expected, suggesting that small

amounts of Au incorporation can actually lead to improved stability. Phase transitions are clear-cut for Ag-rich alloys, which undergo an MT, whereas Au-rich nanoparticles become facetted, making the solid-liquid transition more difficult to pinpoint.

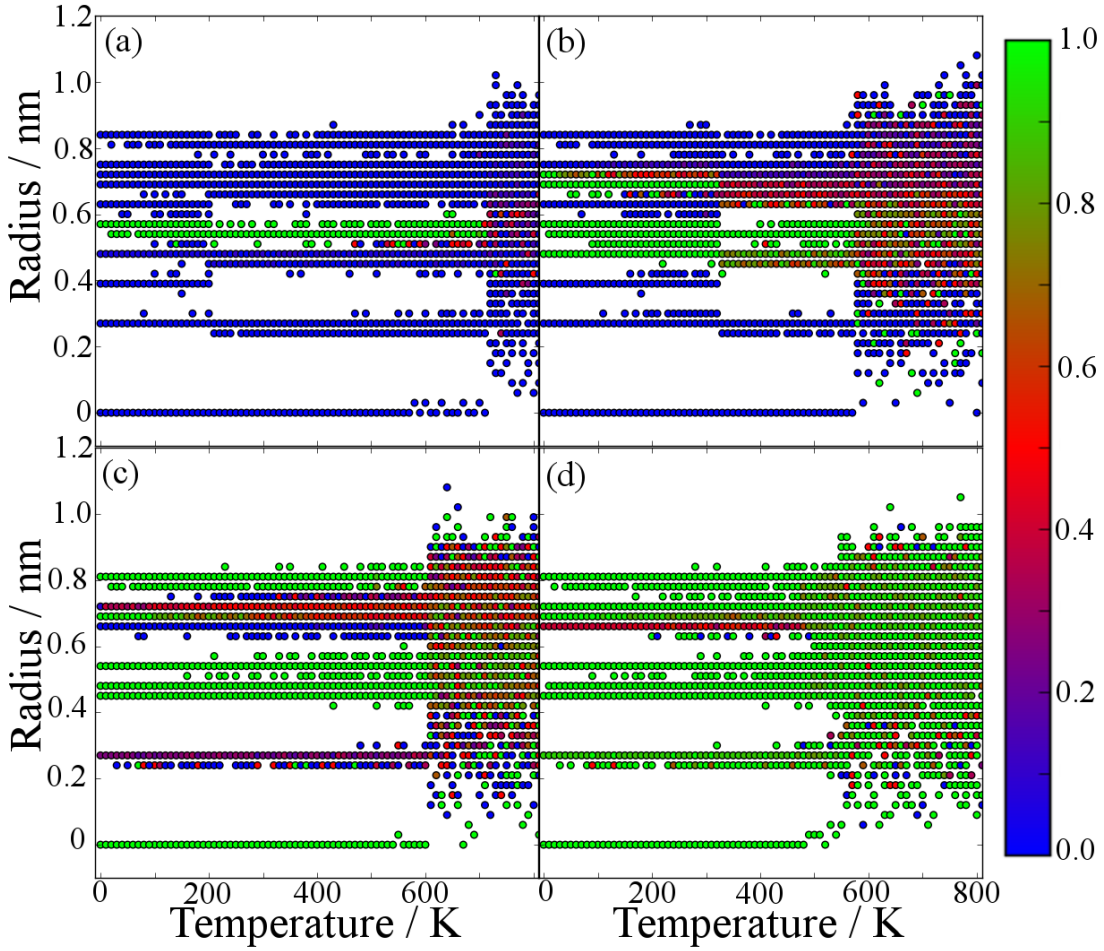

Fig. 4.14 RCDF (for a one simulation) for Au_xAg_{147-x} alloy nanoparticles: (a) $Au_{13}Ag_{134}$, (b) $Au_{55}Ag_{92}$, (c) $Au_{92}Ag_{55}$[Ih] and (d) $Au_{134}Ag_{13}$[Ih]. The colour scale represents the Au ratio, where 1.0 (green) represents an Au-rich radial segment, and 0.0 (blue) represents an Au-poor radial segment. (a) and (b) have undergone an MT from CO to Ih earlier in the heating process.

Overall, two melting-types are observed: Ag-rich nanoparticles exhibit a sharp transition to the melted amorphous structure, whereas Au-rich nanoparticles exhibit smoother transitions, developing defects during the annealing process. These observations support the work of Chen *et al.*, who also observed glass-like transitions to dominate the thermal stability of Au_xAg_{55-x} nanoparticles when $x \geq 30$ i.e. Au-rich.[39] The anomalously higher T_m for $Au_{13}Ag_{134}$ (724 K) in comparison to Ag_{147} (688 K) is perhaps due to improved stability from accommodating a few Au atoms

within the Ag nanocluster. Baletto *et al.* found that improved stability occurred for bimetallic systems when atom size mismatch between the two metallic species was large. However, Au and Ag have very similar atomic radii, and thus this reasoning would not be intuitive in this instance. We also note that $T_m(Au_{55}Ag_{92})$ and $T_m(Au_{92}Ag_{55})$ are very similar, despite the different Au:Ag stoichiometries. This result indicates that the chemical arrangement may influence T_m; $Au_{55}Ag_{92}$ still has Ag-rich regions at the surface and in the very core at its melting point, whereas $Au_{92}Ag_{55}$(Ih) appears to be a completely random alloy (Fig. 4.12). Whilst one could expect the melting point of $Au_{55}Ag_{92}$ to be higher as a result of the Ag core, both nanoparticles have similar AuAg shells and so it is more likely that in fact the chemical arrangement in the shell of the nanocluster dominates the melting properties. $Au_{134}Ag_{13}$(Ih) has the highest Au content of the alloys and exhibits the lowest T_m (559 K), which is very close to the melting point of Au_{147} (T_m = 555 K).

Table 4.2 The transition temperature (T_t) from CO to Ih geometries and averaged melting temperature (T_m) of Au_xAg_{147-x} alloy nanoparticles. T_m[Ih] is averaged from 10 ensembles and refers to the Ih melting point, although the starting geometry is also provided in square parentheses for clarity, given that not all clusters undergo an MT. Transition/melting ranges over the ensemble are provided in parentheses. For the nanoparticles that do not undergo an MT, the melting point of the CO, T_m[CO], is also available.

Composition	T_t [CO to Ih] / K	T_m [Ih] / K [*starting geometry*]	T_m [CO] / K
Ag_{147}	226 (220-230)	688 (660-700) [*CO*]	
$Au_{13}Ag_{134}$	254 (220-270)	724 (710-730) [*CO*]	
$Au_{55}Ag_{92}$	331(300-340)	629 (610-640) [*CO*]	
$Au_{92}Ag_{55}$	-	624 (610-640) [*Ih**]	552 (540-570)
$Au_{134}Ag_{13}$	-	559 (540-580) [*Ih**]	553 (540-570)
Au_{147}	-	555 (540-570) [*Ih**]	555 (540-560)

*As these Au-rich nanoalloys do not undergo an MT, a stoichiometrically equivalent Ih is used as the starting arrangement to obtain T_m(Ih).

4.3.3 Core@shell arrangements

Core@shell chemical arrangements hold considerable potential for nanoparticle applications in catalysis, due to the ability to tailor the chemical ordering, as discussed in Ch. 1. Not only do core@shell nanoparticles potentially result in the manifestation of more ideal properties, but they can also benefit from the synergy between core and shell elements. The core@shell structures that we expose to the heating process are stoichiometrically equivalent with the alloy nanoparticles: $Au_{13}@Ag_{134}$, $Au_{55}@Ag_{92}$, $Ag_{55}@Au_{92}$, and $Ag_{13}@Au_{134}$. As previously, in instances where an MT does not occur, we perform the same calcination process on an equivalent nanocluster with initial Ih geometry.

Au@Ag - Martensitic transformation (MTs) and melting

$Au_{13}@Ag_{134}$ and $Au_{55}@Ag_{92}$ exhibit MTs from CO to Ih at 196 and 221 K, respectively, as shown in Fig. 4.15. Knowing that Au_{147} does not undergo the MT, it is logical that as Au content increases, T_t also increases. $Au_{13}@Ag_{134}$ has a marginally lower T_m than Ag_{147} (682 and 688 K, respectively) and when the Au core is increased to 55 atoms we find that T_m increases to 704 K, i.e. the nanocluster is stabilised.

The RCDFs of Au@Ag systems (Fig. 4.16) show that the nanoparticles remain chemically segregated with no alloying (i.e. no red markers); the first indication of atomic diffusion occurs ~40 K below T_m. After melting, it is noticeable for $Au_{13}@Ag_{134}$ that the Au atoms remain predominantly in the sub-surface layer, forming a pseudo-onion arrangement.

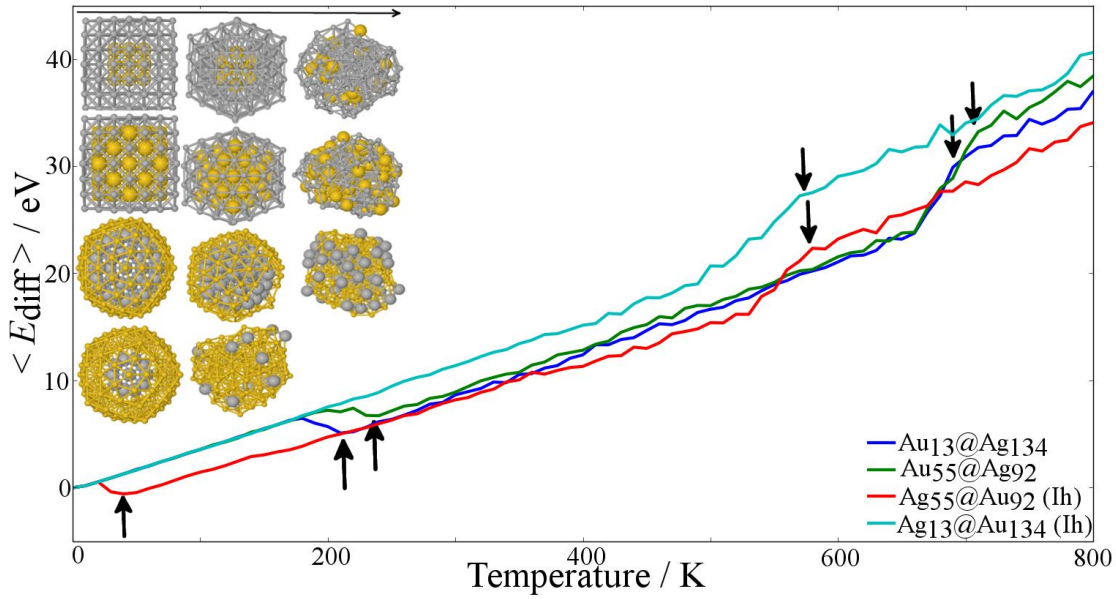

Fig. 4.15 $\langle E_{diff} \rangle$ as a function of T for core@shell nanoparticles; a key is provided for the differing chemical arrangements. T_t and T_m are highlighted by upward and downward arrows, respectively. Inset, left to right: Nanoparticles at 0 K, T_t (where applicable; the pseudo-spherical arrangement is shown for $Ag_{55}@Au_{92}$), and T_m. Inset, top to bottom: $Au_{13}@Ag_{134}$, $Au_{55}@Ag_{92}$, $Ag_{55}@Au_{92}$, $Ag_{13}@Au_{134}$; core atoms have been enlarged for clarity.

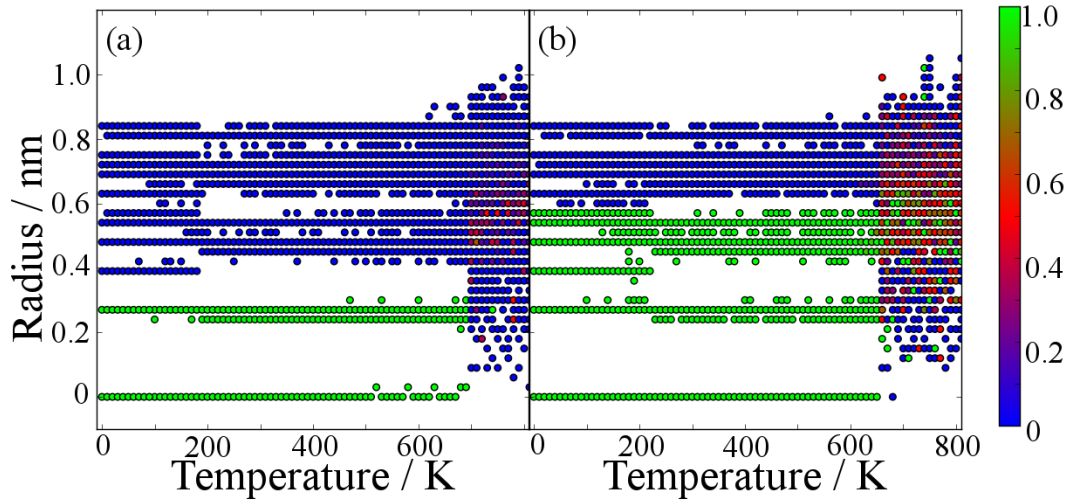

Fig. 4.16 RCDFs (for one simulation) for (a) $Au_{13}@Ag_{134}$ and (b) $Au_{55}@Ag_{92}$; both systems undergo an MT at 196 and 221 K, respectively. The colour scale is the same as in Fig. 4.14.

Ag@Au - Martensitic transformation (MTs) and melting

At 192 K, $Ag_{55}@Au_{92}$ exhibits a structural transition: however, rather than undergoing an MT, it forms a pseudo-spherical geometry. Vertices are lost as a result of the deformation of the Au shell, occurring via a surface step dislocation, similar to that observed for Au_{147} (but less structured). The pseudo-spherical geometry is stimulated by the outward migration of core Ag atoms to the surface at low temperatures. The migration occurs over a temperature range of 140-180 K – more than 350 K below the melting point ($T_m(Ag_{55}@Au_{92})$ = 551 K) and far below room temperature, implying the occurrence of spontaneous diffusion in experiment. By definition, this is a non-MT due to the diffusion of core Ag atoms; no other arrangements exhibit core-atom migration until ~20 K below T_m, implying that in all other cases, migration is associated with melting. $Ag_{13}@Au_{134}$ does exhibit core migration, but much more slowly – the core@shell arrangement is not broken until close to T_m – Ag atoms do not reach the surface, nor does it undergo the MT/form a lower energy geometry, such as the pseudo-spherical arrangement.

As Ag@Au structures do not transform to Ih, the calculations were repeated with $Ag_{13}@Au_{134}$(Ih) and $Ag_{55}@Au_{92}$(Ih), for comparison with other melting points. However, $Ag_{55}@Au_{92}$(Ih) also exhibits the novel non-MT to the pseudo-spherical geometry, with Ag atoms diffusing to the nanocluster surface at even lower temperatures (T = 20-30 K) than for the CO morphology (Fig. 4.17). The difference in kinetic behaviour between the two Ag@Au arrangements can be observed in the RCDF, Fig. 4.18 (we compare nanoparticles with initial Ih geometry, as $Ag_{13}@Au_{134}$(CO) does not undergo the MT). Migration of the central Ag core atom outwards for $Ag_{55}@Au_{92}$(Ih) can be seen to occur at ~30 K for (192 K for the CO starting geometry). The migration of the core atom in $Ag_{13}@Au_{134}$(Ih) does not occur until approximately ~340 K, where the rate of alloying is much slower. Ag atoms do not reach the surface in $Ag_{13}@Au_{134}$(Ih) until melting is achieved.

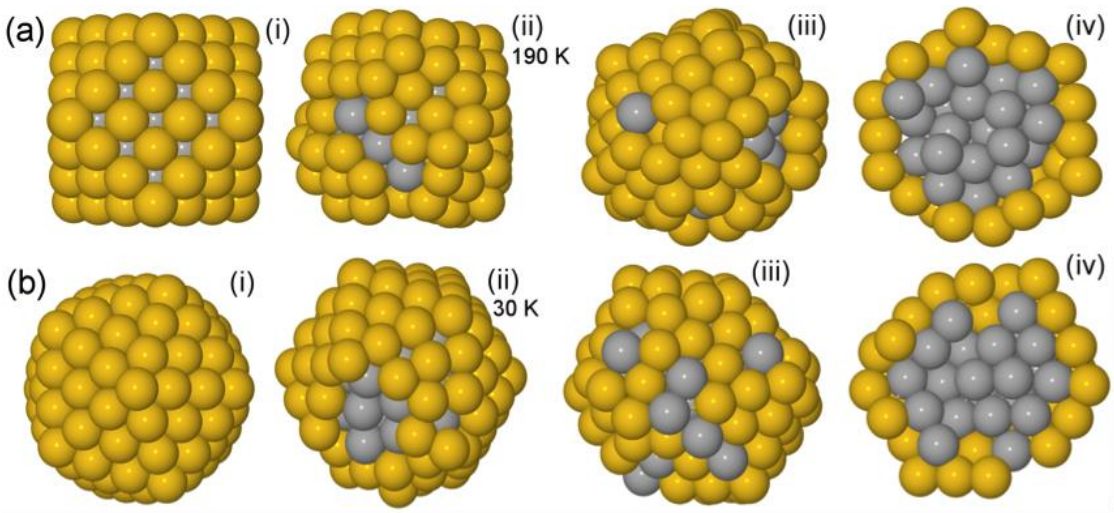

Fig. 4.17 (a) $Ag_{55}@Au_{92}$(CO) and (b) $Ag_{55}@Au_{92}$(Ih) at: (i) 0 K, (ii) the temperature at which diffusion is first observed, as labelled, (iii) 300 K, and (iv) a cross section of the nanoparticles at 300 K. Colours are the same as in Fig. 4.11.

It is particularly interesting that only $Ag_{55}@Au_{92}$ undergoes the non-MT to pseudo-spherical arrangements, irrespective of starting geometry, whereas $Ag_{13}@Au_{134}$ and Au_{147} do not transform geometrically: all three nanoparticles possess a gold shell. The outward migration of Ag for $Ag_{55}@Au_{92}$ can be perhaps rationalized according to shell thickness: $Ag_{55}@Au_{92}$ has a thinner Au shell than $Ag_{13}@Au_{134}$, and so fewer Au−Au bonds need to be broken during the diffusion process, meaning that Ag migrates at low temperature to the surface. Therefore, not only is composition a factor in determining the adopted geometry upon annealing, but also shell thickness. As a consequence of the migration of Ag atoms, any pre-defined starting geometry and core@shell chemical arrangements are compromised very early in the simulation: the Ag migration stimulates the formation of facets in the Au shell and the structure re-stabilises in a pseudo-spherical arrangement once Ag atoms reach the surface.

For $Ag_{55}@Au_{92}$, T_m is very similar to that of Au_{147} ($T_m(Ag_{55}@Au_{92})$ = 551 K and $T_m(Au_{147})$ = 555 K, respectively), which may be due to the lower crystallinity in the morphology following the non-MT. After melting, we again notice that the Au atoms tend to migrate to the sub-surface area to form a pseudo-onion chemical arrangement; this is especially noticeable for $Ag_{55}@Au_{92}$ in Fig. 4.18(a), where we observe an inward migration of Au (green markers). $Ag_{13}@Au_{134}$(Ih) maintains a

core@shell arrangement until close to the T_m of 548 K, which is very similar to $T_m(Au_{147})$. Finally, we note that diffusion of the Ag atoms from the core to the surface occurs for $Ag_{13}@Au_{134}$, as well as $Ag_{55}@Au_{92}$, but closer to T_m in the former case; atomic diffusion of Ag to the surface is slower due to the increased thickness of the Au shell. Therefore, for $Ag_{13}@Au_{134}$, T_m is related to the Au shell, and not the migrating Ag atoms, as the difference in T_m compared to Au_{147} is < 10 K. T_m for all analysed nanoparticles are given in Table 4.3.

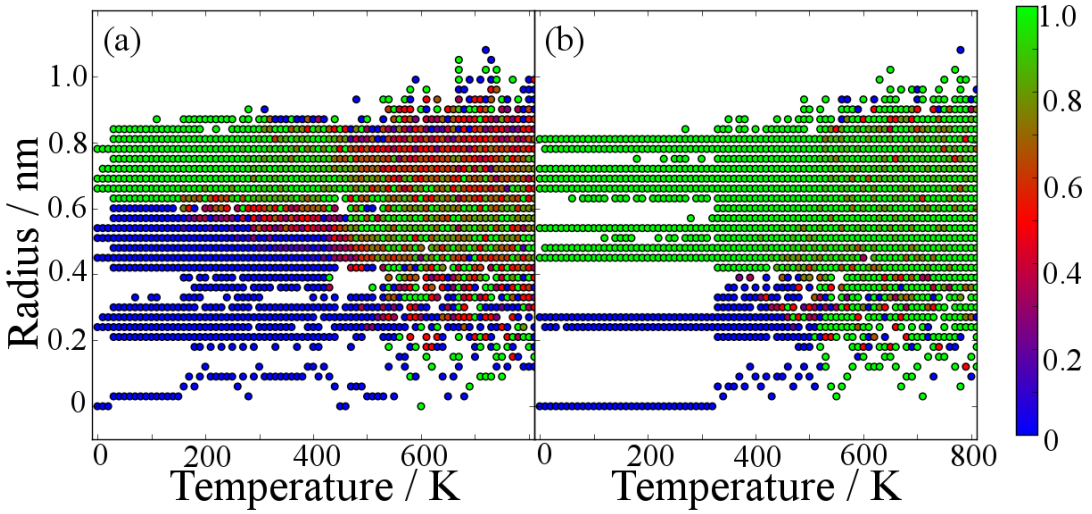

Fig. 4.18 RCDF (for one simulation) for Ag@Au nanoparticles (a) $Ag_{55}@Au_{92}$(Ih) and (b) $Ag_{13}@Au_{134}$(Ih). The colour scale is the same as in Fig. 4.14.

Table 4.3 The transition temperature (T_t) from CO to Ih geometries and melting temperature (T_m) for Au_xAg_{147-x} core@shell nanoparticles. T_m[Ih] is averaged from 10 ensembles and refers to the Ih melting point, although the starting geometry is also provided in square parentheses for clarity, given that not all clusters undergo an MT. Transition/melting ranges over the ensemble are provided in parentheses. For the nanoparticles that do not undergo an MT, the melting point of the CO, T_m[CO], is also available.

Structure & composition	T_t [CO to Ih] / K	T_m [Ih] / K [*starting geometry*]	T_m [CO] / K
Ag_{147}	226 (220-230)	688 (660-700) [*CO*]	
$Au_{13}@Ag_{134}$	196 (180-210)	682 (670-690) [*CO*]	
$Au_{55}@Ag_{92}$	221 (200-240)	704 (700-710) [*CO*]	
$Ag_{55}@Au_{92}$	†192 (170-230)	†551 (530-570) [Ih^*]	†543 (530-570)
$Ag_{13}@Au_{134}$	-	548 (540-570) [Ih^*]	556 (540-570)
Au_{147}	-	555 (540-570) [Ih^*]	555 (540-560)

*As these Au-rich nanoalloys do not undergo an MT, a stoichiometrically equivalent Ih is used as the starting arrangement to obtain T_m(Ih).

†$Ag_{55}@Au_{92}$ transforms to a pseudo-spherical arrangement regardless of the initial geometry.

4.3.4 Comparison of $Ag_{55}@Au_{92}$ and $Au_{92}Ag_{55}$

$\langle P_{HCP} \rangle$ is compared for $Ag_{55}@Au_{92}$ with that of its stoichiometric equivalent alloy, $Au_{92}Ag_{55}$ for both CO and Ih geometries in Fig. 4.19, so that we can compare fully the influence of chemical arrangement for this particular nanocluster, and shed some light on the novel non-MT. For the nanoparticles that begin in a CO arrangement, $\langle P_{FCC} \rangle$ is also provided.

As mentioned previously, a perfect 147-atom CO geometry consists of $\langle P_{FCC} \rangle$ = 37.4%, $\langle P_{HCP} \rangle$ = 0%, and $\langle P_{OTH} \rangle$ = 62.6%, whereas a perfect 147-atom Ih geometry does not contain any FCC features ($\langle P_{HCP} \rangle$ = 20.4% and $\langle P_{OTH} \rangle$ = 79.6%). Let us first consider $Ag_{55}@Au_{92}$(CO): When T = 150-190 K, there is an increase in $\langle P_{HCP} \rangle$ (and decline in $\langle P_{FCC} \rangle$), corresponding to the nanocluster transformation to a pseudo-spherical arrangement as a result of the Ag migration to the surface. Subsequently, $\langle P_{HCP} \rangle$ is approximately constant (4% - 10%), until the nanocluster melts ($\langle P_{HCP} \rangle$ = 0%). This low level of $\langle P_{HCP} \rangle$ is similar to that observed for Au_{147} just below its T_m (Fig. 4.9), suggesting that the pseudo-spherical geometry has a larger degree of structural fluctuation at low temperatures before melting. The same is also true for $Ag_{55}@Au_{92}$(Ih), with the non-MT occurring at ~30 K.

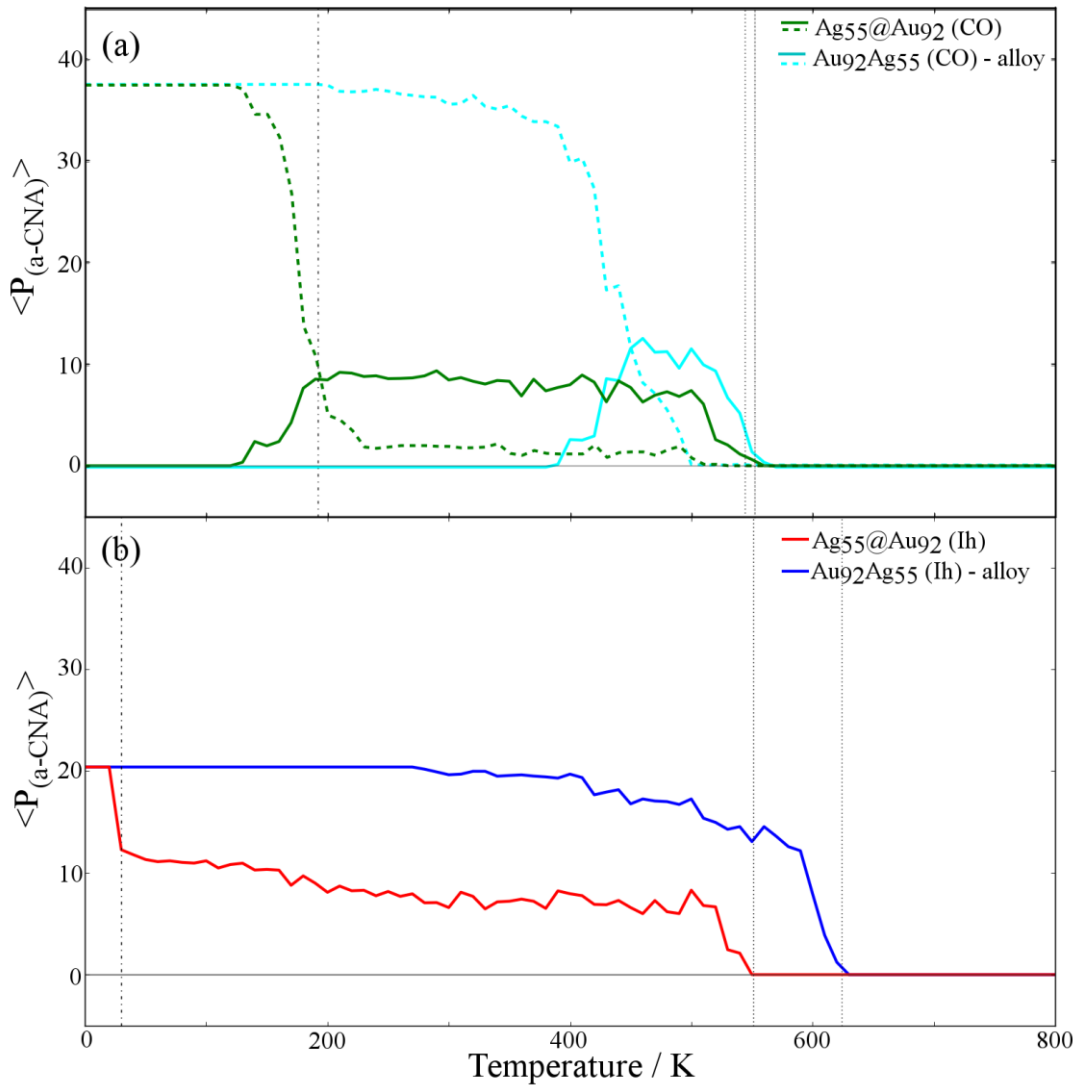

Fig. 4.19 $\langle P_{(a\text{-}CNA)}\rangle$ as a function of temperature for (a) CO $Ag_{55}@Au_{92}$ and alloy $Au_{92}Ag_{55}$; (b) Ih Ag55@Au92 and alloy $Au_{92}Ag_{55}$. A key is provided. $\langle P_{HCP}\rangle$ is represented as solid lines and, for the nanoparticles that begin with a CO geometry, $\langle P_{FCC}\rangle$ is also given, as dashed coloured lines. T_t and T_m are given as dash-dotted and dotted lines, respectively.

$\langle P_{FCC}\rangle$ also seems to influence the rate at which the alloy is formed: $Ag_{55}@Au_{92}$(Ih) does not possess any FCC features, and migration of Ag atoms occurs very readily. Similarly, if we compare $Ag_{55}@Au_{92}$(CO) and $Au_{92}Ag_{55}$(CO), the core@shell arrangement loses its FCC elements much more readily than the alloy. The drive to form a solid solution equilibrium phase is strong for Ag@Au arrangements, and has been shown in the work of Calvo *et al.*.[40] Due to the already mixed nature of the alloy systems (both CO and Ih), there is no similar driving force towards the solid solution as in the core@shell systems. For the RCDFs of these systems, Ag atoms that originate in the core can be observed to migrate to the surface, with full

migration first identifiable at 400 K in Fig. 4.20(a). This process is more difficult within the CO and thus is not observed until T_m has been reached (Fig. 4.20(b)).

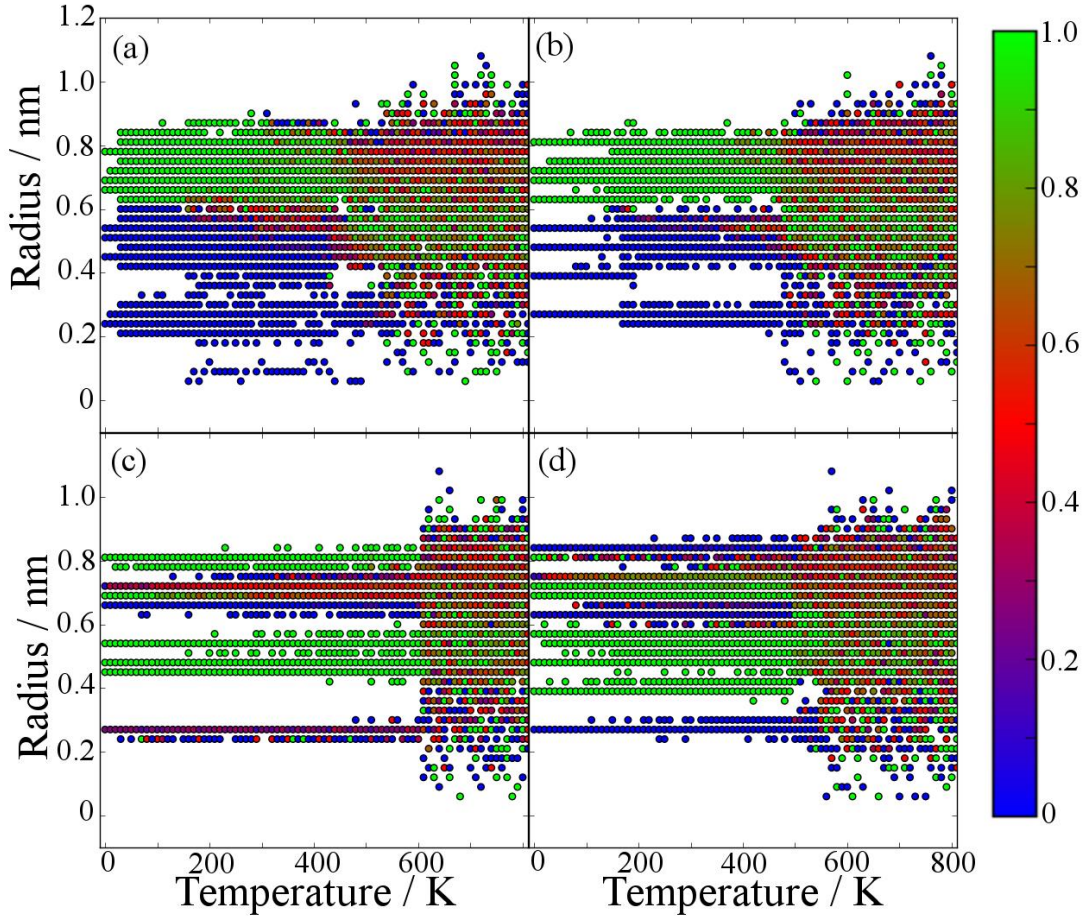

Fig. 4.20 RCDF as a function of *T* for one simulation of the following: core@shell (a) $Ag_{55}@Au_{92}$ [Ih], (b) $Ag_{55}@Au_{92}$ [CO], and alloy (c) $Au_{92}Ag_{55}$ [Ih] and (d) $Au_{92}Ag_{55}$ [CO)]. The colour scale represents the Au ratio, where 1.0 (green) represents an Au-rich radial segment, and 0.0 (blue) represents an Au-poor radial segment.

The energetic drive of Ag@Au arrangements to attain alloy arrangements is further highlighted in Fig. 4.21. $Au_{92}Ag_{55}$(Ih) has a higher melting point than the other three arrangements (T_m = 624 K), and we suggest that this difference is due to the CO comprising of the less stable (100) faces as well as (111) faces: the surface energy of Au (111) and Au (100) are 0.491 and 0.614 Jm^{-2}, respectively, for the Cleri-Rosato parameters. As $Au_{92}Ag_{55}$(Ih) comprises only (111) faces, it melts at a higher temperature – snapshot images for $Au_{92}Ag_{55}$ (CO, Ih) at 550 K are given in Appendix B.

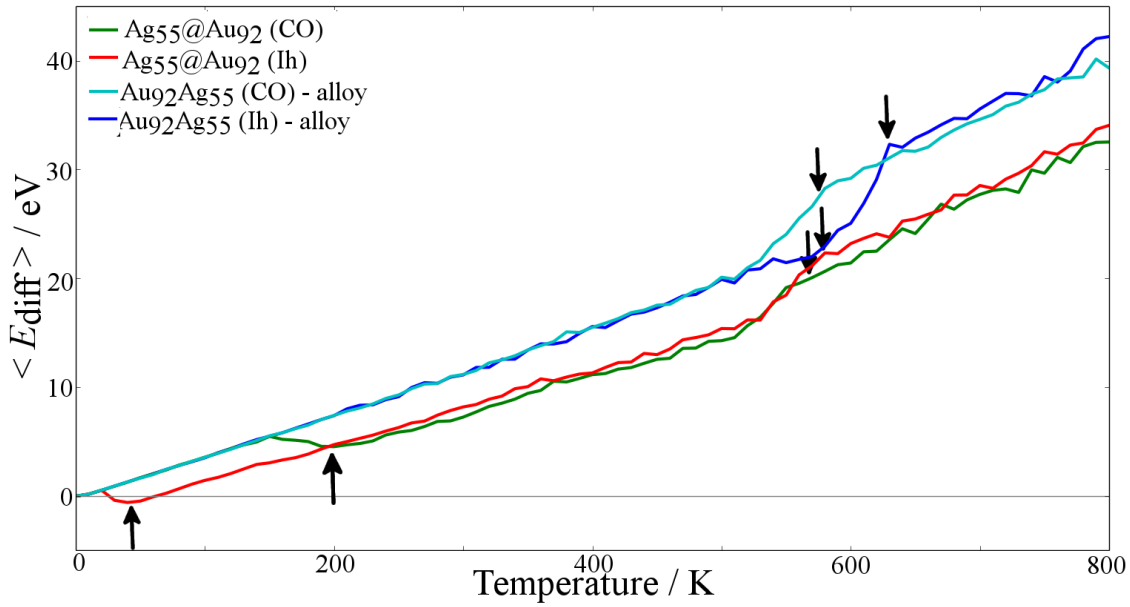

Fig. 4.21 Energetic comparison of $Au_{92}Ag_{55}$ and $Ag_{55}@Au_{92}$; a key is provided. T_t and T_m are highlighted by upward and downward arrows, respectively.

4.4 Discussion and Conclusions

Core@shell arrangements melt at temperatures according to the shell component, with $T_{m\ of}$ Au@Ag nanoparticles similar to Ag_{147}, and T_m for Ag@Au close to that of Au_{147}. The calculated T_m is very similar for $Ag_{55}@Au_{92}$, $Ag_{13}@Au_{134}$ and Au_{147}, despite the pseudo-spherical geometry attained by $Ag_{55}@Au_{92}$. Furthermore, given the difference in T_m of the pure 147-atom nanoparticles, where Au_{147} is less stable than Ag_{147}, one would expect T_m to decrease with increasing Au content; however, $Au_{55}@Ag_{92}$ has a *higher* T_m than $Au_{13}@Ag_{134}$.

The unexpected stability of $Au_{55}@Ag_{92}$ may be attributed to the core atoms, where previous literature has shown that core@shell arrangements can actually improve stability in comparison to pure nanoparticles, depending on the core atom geometry.[41-42] Global optimisation methods have shown Au_{55} to be particularly stable as a heavily distorted and rearranged icosahedron,[43] and thus the core Au atoms in $Au_{55}@Ag_{92}$ may allow the structure to maintain an Au@Ag arrangement to higher temperatures than other systems. The stability of the Au_{55} core may also explain why $Au_{55}@Ag_{92}$ has a higher T_m than its corresponding stoichiometric alloy arrangement, $Au_{55}Ag_{92}$; for all other compositions investigated, the alloy arrangements is more stable than the core@shell chemical ordering.

The experimental synthesis of Ag@Au nanoparticles is not as straightforward as one would expect, and the extended analysis of core@shell structures presented here may help to shed some light on this issue. In addition to the aforementioned reports of competing alloy formation by Jian *et al*, Mallin and Murphy, Srnová-Šloufová *et al*.,[6-8] we highlight computational studies that report spontaneous alloying: Qi and Lee[29] studied sustained annealing (600 K for 58 ns) for Ih nanoparticles; annealing of Ag@Au resulted in the migration of core Ag atoms to the surface, whereas Au@Ag arrangements were stable. The driving force behind alloy formation is greater for Ag@Au than Au@Ag; Calvo *et al.*[40] obtained a solid solution to be the most stable phase (below the melting temperature) from parallel tempering studies, suggesting that alloy formation is highly dependent on the starting arrangement – our study of $Au_{55}@Ag_{92}$ exhibits a 'super stability', whereas diffusion occurs very readily for $Ag_{55}@Au_{92}$.

Our observations regarding the influence of shell thickness on Ag@Au stability also support the work of Chen *et al.*,[44] who found spontaneous surface alloying for colloidal Ag@Au nanoparticles with a thin Au shell (Ag:Au = 0.4:0.1 mol fraction), but no alloying as the Au shell thickness was increased ($\geq$ 0.2 mol fraction). The extended x-ray absorption fine structure spectroscopy (EXAFS) spectra oscillation of Ag:Au = 0.4:0.1 (Au L_{III} edge) was similar to that obtained for alloy samples, indicating the presence of first nearest-neighbour Ag atoms rather than a uniform Au environment, as obtained for the other core@shell arrangements. Chen *et al*. attribute this spontaneous alloying to an increasing diffusion coefficient with decreasing nanocluster size, and ease of alloy formation due to the similar atomic sizes of Au and Ag. However, as neither of these are contending factors in our work, we suggest an alternative explanation: namely that the stability of the Ag@Au arrangement is highly dependent on the Au shell thickness. Only when the stability of the thin Au shell can be secured, e.g. by external ligands, as shown by Li *et al.*, is Ag@Au viable.

In summary, Au-rich nanoparticles did not favour an MT to the Ih, whereas Ag-rich nanoparticles all underwent an MT. This is surprising given their similar atomic radii and electron configuration, and thus further investigation into the energetic barriers to the MT would be of interest to understand the differences. Alloy nanoparticles have been found to have a T_m that is representative of their composition: As %Au

increases, T_m decreases. Two melting-types are observed for alloys: Ag-rich nanoparticles exhibit a sharp transition to the melted amorphous structure, whereas Au-rich nanoparticles exhibit smoother transitions, developing defects during the annealing process. The melting point of core@shell nanoparticles is dependent on the shell component, and will not be dissimilar to that of the pure nanocluster. For Ag@Au arrangements, there is a strong drive to form an alloy at very low temperatures (30 K and 192 K for the Ih and CO starting geometries), and thus this may explain why experimentally it is very difficult to obtain these chemical orderings. Au@Ag, however, is stable in the core@shell arrangement.

4.5 Sensitivity of MD trajectories

Following the investigation into 147-atom nanoparticles, we wanted to determine whether the same trends occur for larger nanoparticles up to experimental sizes (3871 atoms). During this time, the HPC facility and DL_POLY_4 were upgraded, and testing revealed some differences in the results obtained with variation in (a) the number of CPUs used and (b) the HPC facility used, where the occurrence of the MT tended to vary between machine and was found to be dependent on the number of nodes used. This problem clearly needed detailed investigation. The previous results presented on 147-atom nanoparticles are certainly reliable, given that all calculations were performed on the same machine, using 8 CPUs. We have also performed several validation studies to ensure that the transition temperature and/or melting point does not change as a result of noise when performed in a consistent manner, and is known to give reliable and reproducible results (as performed by Alin Marin Elena, a developer of DL_POLY, and UCL Research-Computing support). Table 4.4 shows the differences that were identified. It was suggested that perhaps we revert back to DL_POLY_Classic, and simply comment out the keywords ‘no vdw’, which would remove the book-keeping errors that occurred. However, when testing this, the structures that were obtained (merely following equilibration) were highly disordered, which should not occur at low temperatures, as the CO and the Ih are energetically favourable geometries. In addition to this error, we also note that the formulism for the Gupta potential was incorrect – there is a missing factor of 2 in DL_POLY_ Classic – an error which was reported to the code developers, and it is unclear as to how this would propagate in terms of calculated forces. Therefore, we

remained with DL_POLY_4, and attempted to correct for the differences observed as discussed below.

Table 4.4 Summary of differences between HPC facility, DL_POLY version and number of CPUs used - the occurrence of the MT for Ag_{147} is used to distinguish these differences.

HPC Facility	DL_POLY version	Number of CPUs	Occurrence of MT
Legion (old OS)	4.04	8	Yes
Legion (new OS)	4.07	8	No
Legion (new OS)	4.04	8	No
Legion (new OS)	4.07	1	Yes
Faraday	4.04	8	No
Faraday	4.07	8	Yes

These issues were thoroughly investigated, in collaboration with Alin Marin Elena and Ilian Todorov, who develop the DL_POLY code. The trajectories were found to diverge after 20-22 ps, which was attributed to the different levels of numerical noise from each HPC. This is particularly troublesome when the energetic barrier between two states is small (i.e. between the CO and Ih geometries), and the amount of noise escalates with increasing temperature. New settings were established, that would minimise the amount of numerical noise. The following changes were made to our setup:

1. The Nosé-Hoover thermostat constant was increased to 1.0 to decrease temperature fluctuations
2. The directive 'restart noscale' was added – when a simulation is restarted, rather than beginning anew, DL_POLY will continue the same as previously, without initial rescaling of temperature, taking forward the same velocities as previously.
3. Δt was reduced to 0.1 fs – a smaller Δt allows for more accurate capturing of the forces, as the global error in the friction coefficient and velocities is reduced. Δt tests were performed, and while Δt = 0.4 fs agreed with the data produced from a Δt = 0.1 fs, the data produced from Δt = 0.2 fs did not. Therefore, we were forced to use as small a Δt as possible, and persevered with 0.1 fs.

These changes as listed above help to stabilise the system we are investigating. However, the extremely small Δt requires a much larger amount of CPU time. Additionally, as DL_POLY_4 uses the link cell algorithm for domain decomposition, these simulations are limited to a maximum of 8 processors. Therefore, due to the time requirements of these calculations, and the cautionary approach required to understand the sensitivity of MD trajectories to details of the simulation, this avenue was not further pursued.

4.6 Martensitic transition barriers

The ease of the MT as observed in MD between the CO and the Ih geometry prompt us to question the energetic barrier between these two minima, particularly given that the MT is not always observed. An understanding of the connecting pathway between these two geometries may also help to understand the difficulties that were initially observed following the software upgrades, as propagation of numerical noise will differ according to machine, and may result in different configurations if this numerical noise is sufficient to overcome the MT barrier.

In order to find the connecting pathway between the CO and Ih geometries of our nanoparticles, double-ended transition state searches are performed for 147-atom nanoparticles: pure, core@shell, and doped vertices ($Au_{12}Ag_{135}$; Au_{13}@ $Au_{12}Ag_{122}$; Au_{55}@$Au_{12}Ag_{80}$) chemical orderings. It is not a given that a direct path involving a single transition state will exist; a connection may require intermediate minima and several transition states. The doubly-nudged elastic band (DNEB) approach determines a pathway by considering a series of images at intermediate geometries between starting and finishing points, connected by a spring.

The DNEB method,[45-47] as implemented in the program OPTIM,[48-49] was used to identify transition state candidates between the two minima, using the L-BFGS minimisation algorithm;[50] convergence was achieved when the root mean square DNEB force fell below 0.001 eV for all images. The missing connection Dijkstra-based algorithm[51-52] is used to choose minima for connection cycles, with an energy difference of 10^{-6} eV to identify permutational isomers.

Missing path sections between candidate pairs of minima are found through the repeated application of the missing connection algorithm until a connected sequence of minima and transition states are identified. To characterise complete paths, the minima are considered to be nodes on a graph and, if no connection is known, the algorithm identifies breaks in the path that are short in configuration space, making it more plausible that a connection will be found. Following on from this, the PATHSAMPLE program was used to expand the minima database and see whether a similar energy barrier between the two geometries is obtained. Algorithms for connecting regions of configuration space use discrete path sampling (DPS) to obtain a more complete picture of the potential energy landscape.[53-54]

This section of work on transition barriers forms part of a collaboration with Francesca Baletto and Kevin Rossi (Kings College London), who examined the same MT using metadynamics. The metadynamics algorithm enhances the sampling of conformational space through the use of a history-dependent potential developing in an order parameter space (also known as collective variable space), which acts as a coarse-grained representation of the system. Comparison of the free energy barriers with increasing *T* is also performed, although we note that at low *T*, metadynamics is expected to provide more accurate results than OPTIM, due to the additional anharmonic superposition approximation that is present.

The NEB calculations show a simple single transition state connection between the CO and the Ih for the majority of nanoparticles (Fig. 4.22). The MT from CO to Ih for Ag_{147} has a barrier of 0.496 eV, whereas the barrier for Au_{147} to transform is higher at 1.142 eV, which may explain why it is more difficult for Au nanoparticles to achieve the Ih in our MD simulations (Table 4.5).

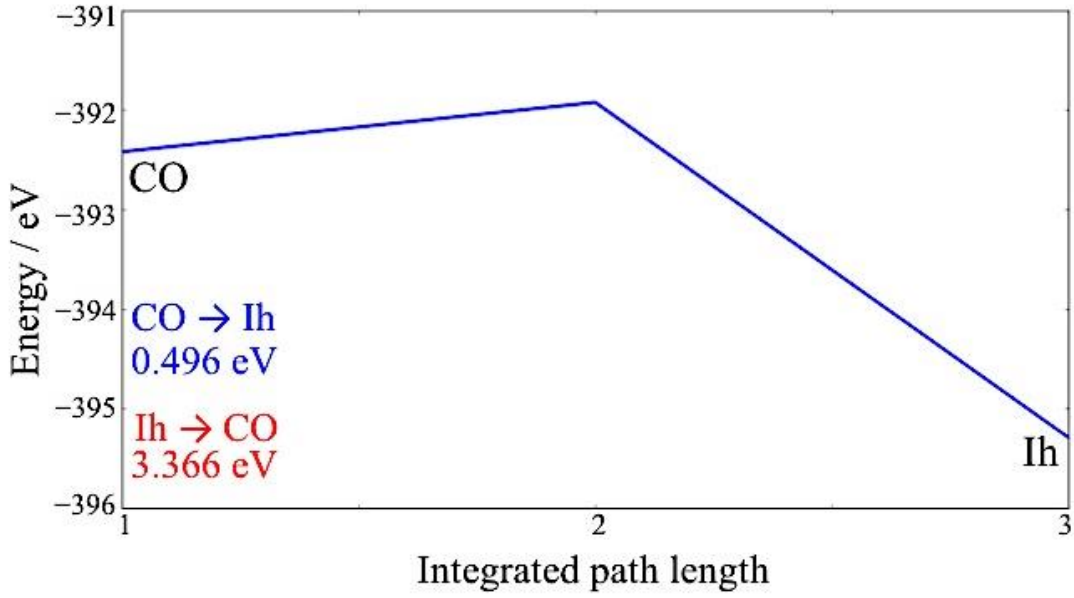

Fig. 4.22 Energetic pathway for Ag_{147}, the CO and Ih are indicated at either end of the pathway.

For Au@Ag systems, increasing the thickness of the Ag shell results in a lowering of the energetic barrier for the transition to the Ih (0.551 eV to 0.396 eV for $Au_{55}@Ag_{92}$ and $Au_{13}@Ag_{134}$, respectively), but an increase in the barrier height for the backward (Ih → CO) pathway. Single-atom core@shell arrangements do not quite follow the

same pattern; $Au_1@Ag_{146}$ has a lower energy barrier for the forward transition (0.487 eV), than $Au_{55}@Ag_{92}$, but it is higher than that of $Au_{13}@Ag_{134}$. The backward barrier, on the other hand, increases with Ag shell thickness (3.378, 3.253, and 2.784 eV for $Au_1@Ag_{146}$, $Au_{13}@Ag_{134}$, and $Au_{55}@Ag_{92}$, respectively). Ag@Au nanoparticles exhibit a far more complicated energetic pathway for the CO → Ih transition, with many intermediate minima between these two particular geometries. In fact, PATHSAMPLE finds two possible connection pathways for $Ag_{1@}Au_{146}$, with barriers of 3.006 and 2.971 eV (Fig. 4.23). The difference between these two pathways is that a low-lying minima is missed by the latter pathway, resulting in a smaller energy barrier. The numerous minima occur because the Ih arrangement is not the lowest energy; a 'rosette-like' geometry is energetically preferable for Ag@Au systems. The rosette formation is the amorphization of the Ih, where a vertex atom is pushed out and inserted between its five neighbours on the surface, to form 5-, 6- or 7-fold rings centred on the original position of the vertex (Fig. 4.24). Thus for Ag@Au nanoparticles, the DSD mechanism is no longer favourable. As a consequence of the many intermediate transition states, the transition barrier for these nanoparticles is considerably higher: 2.030, 1.152, 3.067 eV for $Ag_1@Au_{146}$, $Ag_{13}@Au_{134}$, and $Ag_{55}@Au_{92}$, respectively, for the forward pathway (Fig. 4.26).

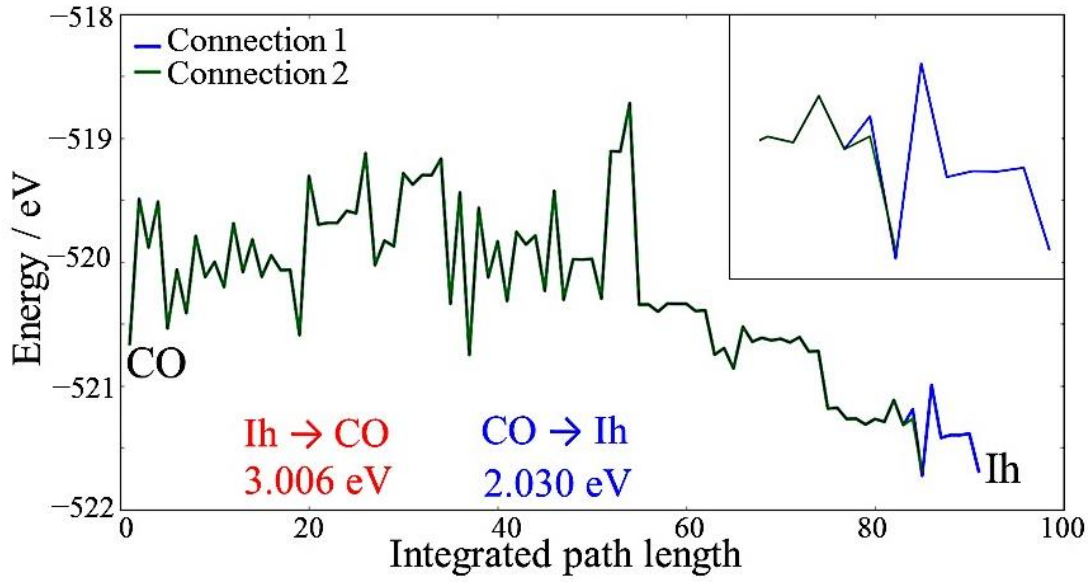

Fig. 4.23 Different connecting paths as observed for $Ag_1@Au_{146}$, a key is provided for the different connecting paths. Inset: Magnification of missed minima by connection 2.

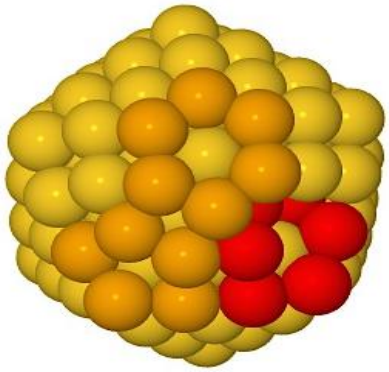

Fig. 4.24 The lowest lying minima as found by OPTIM/PATHSAMPLE for $Ag_1@Au_{146}$; five and six-fold rings formed from pushing out a vertex atom are highlighted in orange, and the beginning of a third six-fold ring is highlighted in red.

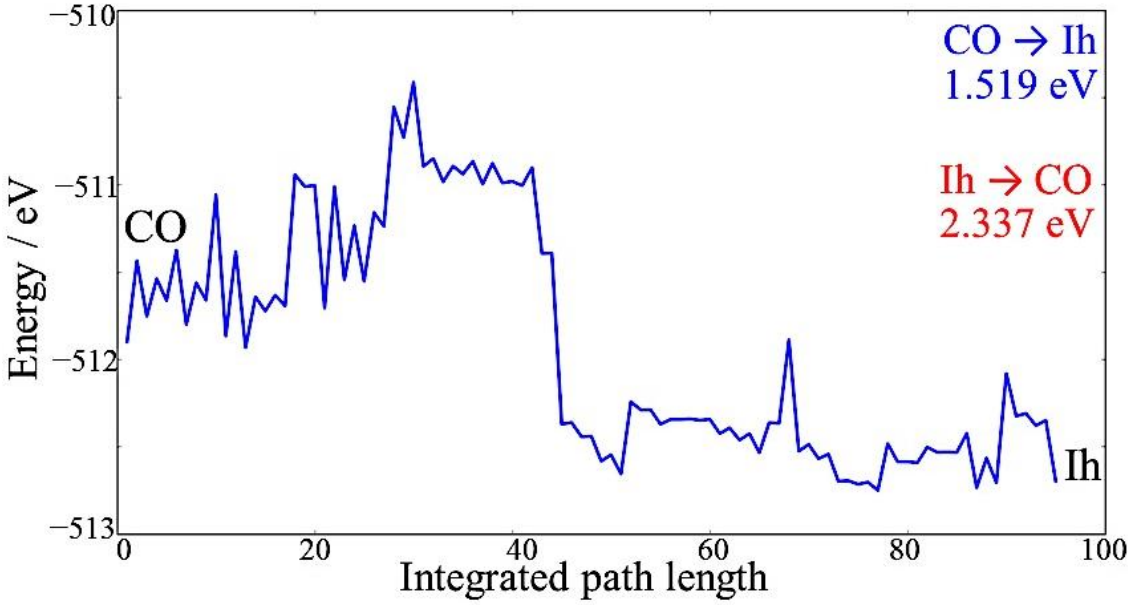

Fig. 4.25 Transition pathway for $Ag_{13}@Au_{134}$.

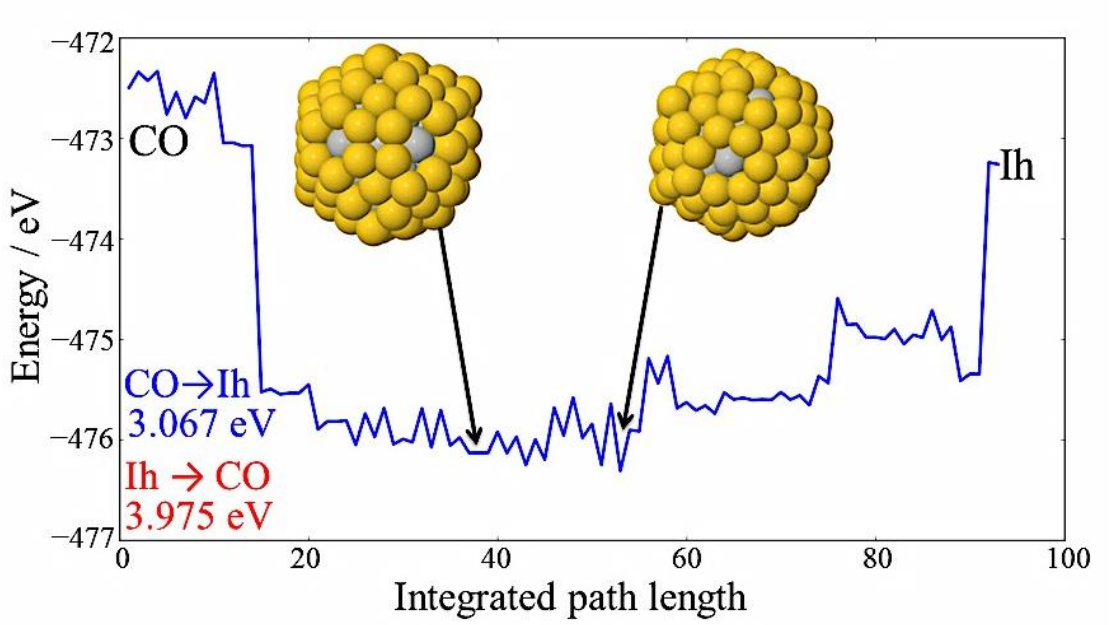

Fig. 4.26 Transition pathway for $Ag_{55}@Au_{92}$. Two snapshots of the lowest lying minima as found by OPTIM/PATHSAMPLE are included, showing the rosette-like arrangement.

The disruption in the DSD mechanisms for Ag@Au systems can be observed in Fig. 4.27, where the transition pathway is no longer smooth, but exhibits many transitions, passing through the rosette-Ih. The $Ag_{55}@Au_{92}$ transition pathway sees a considerable lowering of the intermediate minima in comparison to the CO and Ih, in comparison to $Ag_1@Au_{146}$ and $Ag_{13}@Au_{134}$, which may be attributed to the formation of 5-, 6-, 7-fold rings that bring a greater number of Ag atoms to the surface, as shown in Fig. 4.28, which also demonstrates the local Ih geometry of the 55-atom Ag core.

Due to this departure from the DSD for Ag@Au systems, we also performed static calculations using GULP. These gave E(CO → Ih) as 1.19, 1.28 and 0.90 eV, and E(Ih → CO) as 2.22, 2.08 and 1.66 eV, for $Ag_1@Au_{146}$, $Ag_{13}@Au_{134}$ and $Ag_{55}@Au_{92}$, respectively, which are lower in energy than the pathway via the rosette-Ih motifs. However, the lower overall energy of the rosette-Ih motifs, in combination with the low barriers between minima, mean that the transition from CO to the rosette-Ih is downhill and facile, preventing DNEB from identifying the DSD mechanism as being feasible.

Table 4.5 Transition barriers for the forward (CO → Ih) and backward (Ih → CO) pathway.

System	CO → Ih / eV	Ih → CO / eV
Ag_{147}	0.496	3.366
Au_{147}	1.142	2.331
$Au_1@Ag_{146}$	0.487	3.378
$Au_{13}@Ag_{134}$	0.396	3.253
$Au_{55}@Ag_{92}$	0.551	2.784
$Ag_1@Au_{146}$	2.030	3.006
$Ag_{13}@Au_{134}$	1.519	2.337
$Ag_{55}@Au_{92}$	3.067	3.975

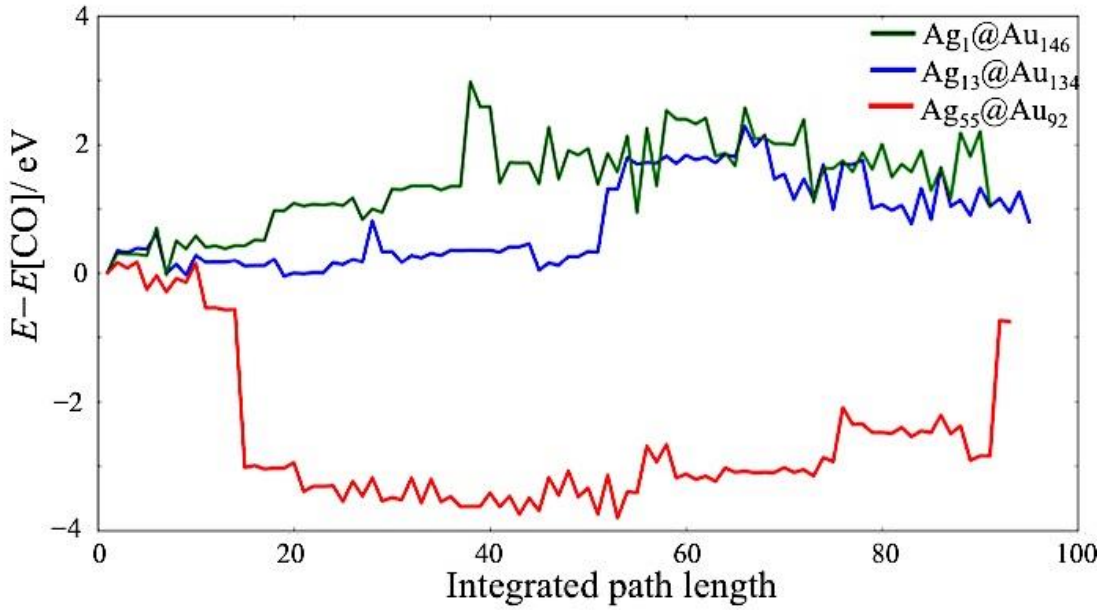

Fig. 4.27 Transition pathways for CO ↔ Ih for $Ag_1@Au_{146}$, $Ag_{13}@Au_{134}$ and $Ag_{55}@Au_{92}$, all of which proceed via the rosette-Ih. A key is provided, with energies given relative to that of the CO motif (E_0).

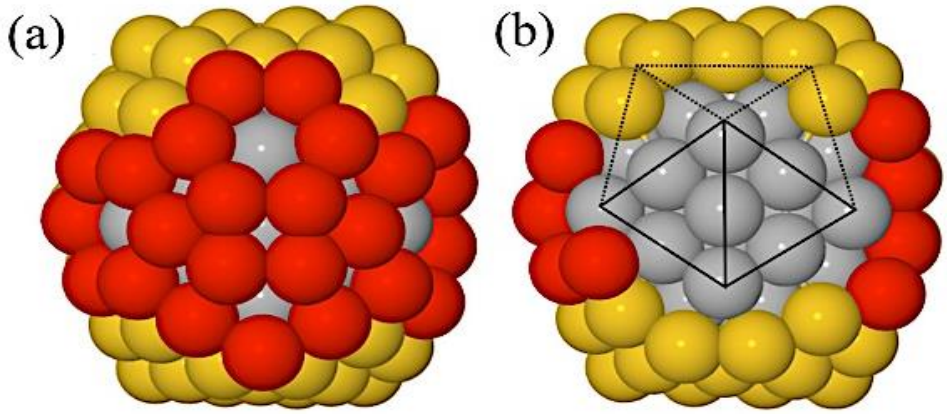

Fig. 4.28 Illustrations of the rosette-Ih local minima identified as the lowest energy arrangement in the transition pathway for $Ag_{55}@Au_{92}$, also pictured in Fig. 4.26. Au and Ag atoms are shown as gold and silver spheres, respectively, while Au atoms that for parts of the 5-, 6- and 7-fold rings have been highlighted in red. Figure (a) shows all atoms, whereas in (b) 16 Au atoms have been removed from the front of the nanoparticle, demonstrating the underlying Ih Ag core.

As shown so far, the substitution of a single atom for Ag at the core of the Au_{147} nanocluster results in a much more complicated energetic pathway, thus prompting the question: is the pathway dependent on the positioning of this single atomic dopant? $Ag_1@Au_{146}$ is not the most thermodynamically favourable arrangement (see Ch. 3), but rather an Ag atom on the (100) face (for the CO). Therefore, we have also examined other dopant positions for the single Ag atom (Table 4.5).

The transition barrier for the forward pathway for Au_{147} is 1.142 eV, which can be lowered or raised according to the positioning of a single Ag dopant atom; for instances where the barrier is lowered, these have been highlighted in bold in Table 3.5. For instances where the transition barrier for the forward pathway is slightly lowered, the Ag atom is practically stationary, and the NEB path to the Ih is simple, with Au atoms migrating around the Ag atom in a DSD manner. The dopant atom has very similar transition barriers for the majority of atomic positions, with the exceptions of the (aforementioned) central core, and both (100) face centre positions (Table 4.6, (h) and (i)). If the dopant atom is heavily involved in the MT, the barrier to the transition is increased, as shown for surface vertex, and (100) face centre atoms, which go on to become either (111) face centre atoms or (111) edge atoms.

The backward barrier for Au_{147} is 2.331 eV; the dopant Ag atom results in the same trends as for the forward reaction (again highlighted in bold), with the exception of (f), when Ag occupies a surface edge, which results in an increased transition barrier. As summarised in Ch. 3, it is energetically unfavourable for a single Ag dopant to be positioned within the nanocluster – there is a strong preference for (100) surface / subsurface positioning. Therefore, this result seems to suggest the involvement of the dopant atom in the MT affects the energetic barrier, and the core atom also has an unforeseen role in the MT.

Table 4.6 Transition barriers for the forward (CO → Ih) and backward (Ih → CO) pathway for $Au_{146}Ag_1$, changing the position of the dopant Ag atom.

$Au_{146}Ag_1$	Position of Ag atom	CO → Ih	Ih → CO
(a)	core	2.030	3.006
(b)	1st layer	**1.122**	**2.286**
(c)	2nd layer, vertex	**1.107**	**2.274**
(d)	2nd layer, edge	**1.100**	**2.301**
(e)	Surface vertex (3rd layer)	1.160	2.346
(f)	Surface edge (3rd layer)	**1.121**	2.347
(g)	(111) face centre	**1.022**	**2.323**
(h)	(100) face centre	1.707	2.745
	[→ becomes (111) edge on Ih]		
(i)	(100) face centre	3.745	3.774
	[→ becomes (111) face on Ih]		

For comparison, we also examined the same single dopant positions in Au_1Ag_{146}, in Table 4.7. Having Au as a core dopant does not have the same effect as a single Ag atom in $Au_{146}Ag_1$: there is minimal difference between the single dopant sites, with the exception of (h) and (i), when the Au atom begins on a (100) face, and is therefore highly involved in the MT.

The barrier for Ag_{147} to undergo the MT is small, at 0.496 eV. The Au dopant positions that result in a lowering of the transition barrier are bolded again in Table 3.6, notably at the core, first layer and surface vertex. However, there is very little difference between all dopant positions (±0.012 eV), with the exceptions of (h) and (i), which is within the degree of error.

The (100) face centre dopant positions for both $Au_{146}Ag_1$ and Au_1Ag_{146} result in unusually high energetic barriers, due to the high degree of restructuring required.

For comparison, the transition barrier for the DSD pathway was calculated using GULP, this time achieving barriers of 1.147 eV and 1.169 eV for $Au_{146}Ag_1$ for the (100) face → (111) face and (100) face → (111) edge, respectively. [The backwards GULP barriers are 2.334 and 2.328 eV, respectively]. For the Ag-rich system, Au_1Ag_{146}, the DSD forward (backward) pathway barriers are 0.498 (3.394) and 0.480 (3.374) eV, respectively. The Ag-rich system prefers to proceed via a (100) face → (111) edge → (111) face, with the barrier being 0.02 eV smaller than the (100) face → (111) face → (111) edge pathway. Alternatively, the Au-rich system prefers to proceed via a (100) face → (111) face → (111) edge, again due to a smaller barrier of 0.02 eV. It is unclear as to why OPTIM does not find the DSD mechanism for these structures.

Table 4.7 Transition barriers for the forward (CO → Ih) and backward (Ih → CO) pathway for Au_1Ag_{146}, changing the position of the dopant Ag atom.

Au_1Ag_{146}	Position of Au atom	CO → Ih	Ih → CO
(a)	core	**0.487**	3.378
(b)	1st layer	**0.494**	3.357
(c)	2nd layer, vertex	0.500	3.358
(d)	2nd layer, edge	0.499	3.339
(e)	Surface vertex (3rd layer)	**0.481**	3.373
(f)	Surface edge (3rd layer)	0.507	3.361
(g)	(111) face centre	0.510	3.299
(h)	(100) face centre [→ becomes (111) edge on Ih]	4.558	4.561
(i)	(100) face centre [→ becomes (111) face on Ih]	4.578	4.581

Influence of vertex decoration

The MT is a cooperative atomic movement, and thus it is also of interest whether the transition barrier can be fine-tuned through the doping of vertex atoms.[55] Au vertex doping for pure Ag and Au@Ag arrangements led to a lowering of the transition barrier (0.352, 0.374 and 0.267 eV for $Au_{12}Ag_{135}$, $Au_{55}@Au_{12}Ag_{80}$, and $Au_{13}@Au_{12}Ag_{122}$, respectively). Most interestingly, substituting Ag atoms at vertex positions for Ag@Au systems ($Ag_1@Au_{134}Ag_{12}$, and $Ag_{13}@Au_{122}Ag_{12}$, respectively) resulted in much smoother transition pathways, but only lowers the transition barrier for $Ag_1@Au_{134}Ag_{12}$ due to the reattainment of the DSD mechanism; the transition barrier for $Ag_{13}@Au_{122}Ag_{12}$ is slightly increased. $Ag_{55}@Au_{80}Ag_{12}$ does not find the

DSD pathway in spite of doping and still exhibits a complicated transition pathway, but much less so than $Ag_{55}@Au_{92}$. The rosette-Ih is too low in energy for the DSD mechanism to be identified for this particularly nanocluster, as demonstrated earlier in Fig. 4.27. For the backward pathway, the transition barrier is only lowered for doped Ag@Au systems (2.196, 2.303, and 3.307 eV for $Ag_1@Au_{134}Ag_{12}$, $Ag_{13}@Au_{122}Ag_{12}$ and $Ag_1@Au_{134}Ag_{12}$, respectively), Ag doping results in a lowering of the transition barrier but increases when Au decorates the vertices. Results for vertex doping are presented in Table 4.8 and

Table 4.9, alongside results from Table 4.5, for the reader's ease – lowered barriers have been highlighted in bold.

Table 4.8 Influence of vertex doping for the forward reaction, columns 1 and 2 are the same as in Table 4.5. For clarity, if a decrease in the transition barrier occurs as a result of doping, the doped barrier is highlighted in bold.

System	CO → Ih / eV	Doped Vertex System	CO → Ih / eV
Ag_{147}	0.496	$Ag_{135}Au_{12}$	**0.352**
Au_{147}	1.142	$Au_{135}Ag_{12}$	1.270
$Au_1@Ag_{146}$	0.487	$Au_1@Ag_{134}Au_{12}$	**0.375**
$Au_{13}@Ag_{134}$	0.396	$Au_{13}@Ag_{122}Au_{12}$	**0.267**
$Au_{55}@Ag_{92}$	0.551	$Au_{55}@Ag_{80}Au_{12}$	**0.374**
$Ag_1@Au_{146}$	2.030	$Ag_1@Au_{134}Ag_{12}$	**1.169**
$Ag_{13}@Au_{134}$	1.519	$Ag_{13}@Au_{122}Ag_{12}$	1.539
$Ag_{55}@Au_{92}$	3.067	$Ag_{55}@Au_{80}Ag_{12}$	**2.368**

Table 4.9 Influence of vertex doping for the backward reaction columns 1 and 2 are the same as in Table 4.5. For clarity, if a decrease in the transition barrier occurs as a result of doping, the doped barrier is highlighted in bold.

System	Ih → CO / eV	Doped Vertex System	Ih → CO / eV
Ag_{147}	3.366	$Ag_{135}Au_{12}$	3.502
Au_{147}	2.331	$Au_{135}Ag_{12}$	2.452
$Au_1@Ag_{146}$	3.378	$Au_1@Ag_{134}Au_{12}$	3.383
$Au_{13}@Ag_{134}$	3.253	$Au_{13}@Ag_{122}Au_{12}$	3.395
$Au_{55}@Ag_{92}$	2.784	$Au_{55}@Ag_{80}Au_{12}$	2.803
$Ag_1@Au_{146}$	3.006	$Ag_1@Au_{134}Ag_{12}$	**2.196**
$Ag_{13}@Au_{134}$	2.337	$Ag_{13}@Au_{122}Ag_{12}$	**2.303**
$Ag_{55}@Au_{92}$	3.975	$Ag_{55}@Au_{80}Ag_{12}$	**3.307**

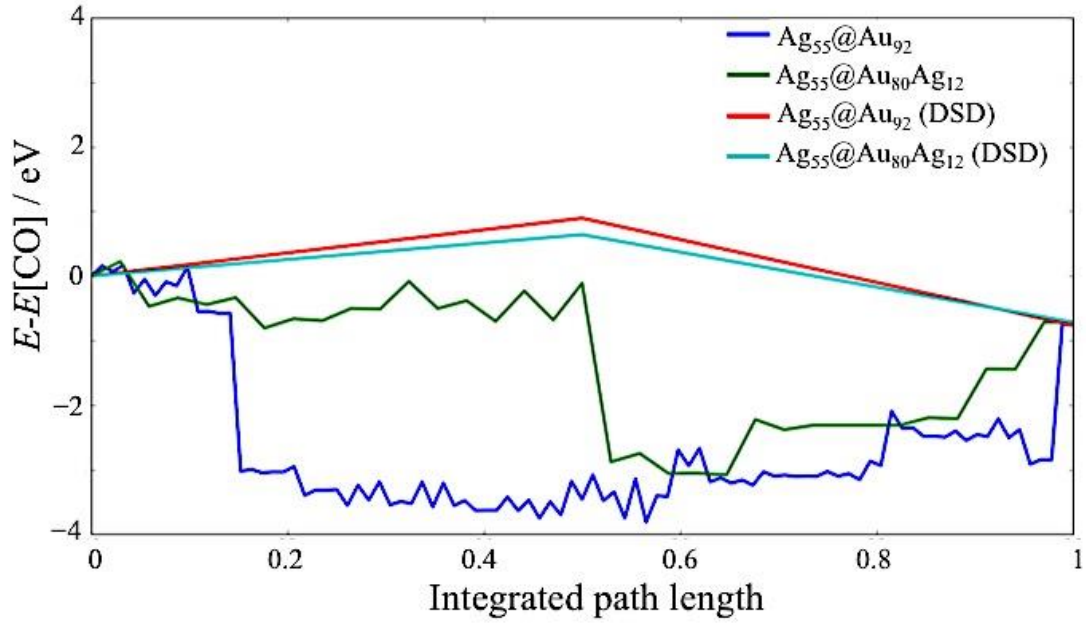

Fig. 4.29 Transition pathways for CO ↔ Ih for $Ag_{55}@Au_{92}$ and $Ag_{55}@Au_{80}Ag_{12}$, via both the DSD mechanism and the rosette-Ih. A key is provided, with energies given relative to that of the CO motif (E_0).

Comparative static calculations of the DSD pathway for $Ag_{55}@Au_{92}$ and its vertex decorated counterpart, $Ag_{55}@Au_{80}Ag_{12}$ give a forward barrier of only 0.897 and 0.642 eV, respectively, showing that the rosette-Ih dominates the DNEB calculations due to its accessibility and energetic competitivity, as demonstrated in Fig. 4.29. The backward transitions from GULP are 1.659 eV and 1.357 eV, and thus these calculations show that vertex decoration of Ag@Au systems with Ag atoms lowers the barrier for the MT.

Free Energy Transition Barriers

In order to provide some experimental context, free energy calculations were also performed, with respect to increasing temperature, using DPS within PATHSAMPLE (keywords TEMPERATURE, REGROUPFREE). As T was increased up to 500 K, in 100 K intervals, up to 500 K, there is an almost universal decrease in the free energy barrier of the forward transition [F(Ih → CO)]: a drop of 0.03-0.04 eV occurs when T = 100 K, whereafter the rate of decrease is reduced to ~0.01 eV per 100 K (Table 4.10, Table 4.11), with the exception of $Ag_{55}@Au_{92}$. In fact, the free energy transition barrier for $Ag_{55}@Au_{92}$ increases steadily with increasing temperature (0.04 eV per 100 K), which is not intuitive at all. The lowest

lying energy minima do not change, with the rosette-Ih motif route consistently identified by PATHSAMPLE as the most facile downhill route. Intermediate motifs close to the CO increase in energy with increased *T*, resulting in an increased transition barrier, as shown in Fig. 4.30. It is also noted that the high entropy of the rosette-Ih, with respect to the CO and Ih, makes this minima more favourable with increasing *T*.

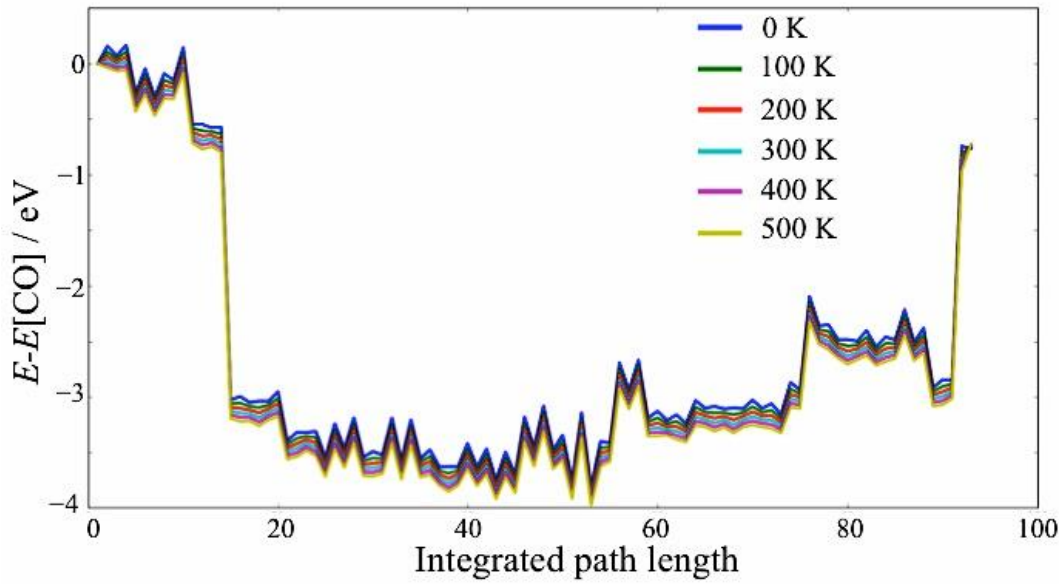

Fig. 4.30 Free energy transition pathway for $Ag_{55}@Au_{92}$, normalised to *E*(CO), with respect to increasing temperature. A key is provided.

For the backward pathway, the transition barrier for all nanoparticles (apart from $Ag_{55}@Au_{92}$) decreases with increasing *T*, although at different rates: Ag_{147} *F*(Ih → CO) decreases by 0.02 eV per 100 K, however for Au_{147}, the barrier decreases by 0.04 eV per 100 K. For $Ag_{55}@Au_{92}$, the transition barrier decreases with increasing *T* when $0 \leq T \leq 300$ K, rising to 3.944 eV and 3.977 eV for $T = 400$ and 500 K, respectively, due to the lowering and raising of energies for intermediate motifs close to the CO starting motif.

Selective comparative metadynamics calculations, as performed by K. Rossi and F. Baletto, give slightly lower free energy barriers. Although this method cannot extend to such high temperatures, we see that Ag-rich systems find *F*(Ih → CO) = 2.85 ±0.15 eV at 50 K, and these barrier heights are maintained at 100 K and 150 K.

Similarly, free energy barriers for Au_1Ag_{146} are steady up to 150 K, with F(Ih → CO) in the range 2.8 - 3.0 eV.

The transition pathway for the MT is characterised by the diamond-square-diamond mechanism, and we performed DNEB calculations in order to determine barrier heights, alongside selective metadynamics calculations for comparison. Both techniques showed that, for Ag@Au systems a rosette-Ih minima, with 5-, 6- and 7-fold rings exposing Ag atoms, between the CO and the Ih was energetically preferable as an intermediate motif, thus preventing exploration of the DSD mechanism via these methods.

In general, the difference in barriers calculated using DPS and metadynamics are not deemed significant, as underestimations in metadynamics may arise due to the effect of reduced dimensionality. Given the identical pathways and similar barrier heights by both methods provides some reassurance as to the existence of the rosette-Ih. Consequently, static calculations for the DSD mechanism were also performed, for which the transition barrier was found to be significantly lower, thereby highlighting the facile downhill preference to the rosette-Ih for DNEB and metadynamics. Fine-tuning of the transition barrier can be obtained through careful chemical ordering and stoichiometry of the nanoparticle; we have shown the barrier for the DSD can be altered by up to 0.15 eV as a result of the decoration of vertices by a secondary element in bimetallic systems. Finally, we also examined the influence of temperature on the free energy barriers for experimental relevance: generally these decrease in accordance with increasing temperature, however, $Ag_{55}@Au_{92}$ does not follow this trend due to its complex potential and free energy landscapes, with many low-lying minima.

Table 4.10 F(CO → Ih) energy barriers (forward pathway). Units are in eV.

System	0 K	100 K	200 K	300 K	400 K	500 K
Ag_{147}	0.496	0.465	0.446	0.431	0.419	0.410
Au_{147}	1.142	1.093	1.056	1.023	0.993	0.966
$Au_1@Ag_{146}$	0.487	0.456	0.437	0.422	0.411	0.401
$Au_{13}@Ag_{134}$	0.396	0.365	0.346	0.331	0.319	0.310
$Au_{55}@Ag_{92}$	0.551	0.520	0.501	0.486	0.475	0.465
$Ag_1@Au_{146}$	2.030	2.005	1.992	1.983	1.977	1.974
$Ag_{13}@Au_{134}$	1.519	1.488	1.469	1.454	1.442	1.433
$Ag_{55}@Au_{92}$	3.067	3.090	3.131	3.172	3.214	3.255
$Au_{55}@Ag_{80}Au_{12}$ (core+vertices)	0.374	0.343	0.324	0.309	0.298	0.288
$Au_{13}@Ag_{122}Au_{12}$ (core+vertices)	0.267	0.236	0.217	0.203	0.191	0.181
$Au_{12}Ag_{135}$ (vertices)	0.352	0.321	0.302	0.287	0.276	0.266

Table 4.11 F(Ih → CO) energy barriers (backward pathway). Units are in eV.

System	0 K	100 K	200 K	300 K	400 K	500 K
Ag_{147}	3.366	3.327	3.300	3.278	3.258	3.241
Au_{147}	2.331	2.274	2.229	2.188	2.151	2.115
$Au_1@Ag_{146}$	3.378	3.339	3.312	3.289	3.270	3.252
$Au_{13}@Ag_{134}$	3.253	3.214	3.187	3.164	3.145	3.127
$Au_{55}@Ag_{92}$	2.784	2.745	2.719	2.696	2.676	2.659
$Ag_1@Au_{146}$	3.006	2.981	2.968	2.959	2.953	2.950
$Ag_{13}@Au_{134}$	2.337	2.312	2.299	2.290	2.285	2.281
$Ag_{55}@Au_{92}$	3.975	3.950	3.941	3.939	3.944	3.977
$Au_{55}@Ag_{80}Au_{12}$ (core+vertices)	2.803	2.764	2.737	2.714	2.694	2.677
$Au_{13}@Ag_{122}Au_{12}$ (core+vertices)	3.395	3.356	3.329	3.307	3.287	3.270
$Au_{12}Ag_{135}$ (vertices)	3.502	3.463	3.436	3.413	3.394	3.376

4.7 Conclusions

We performed MD simulations to understand the kinetic processes that occur when bimetallic AuAg systems are subjected to thermal conditions, analogous to experiment. At low *T*, the existence of a martensitic transition (MT) from the CO to the Ih geometry was identified for Ag-rich nanoparticles, whereas Au-rich nanoparticles did not favour an MT. Alloy nanoparticles have been found to have a melting point, T_m, that is representative of their composition: as %Au increases, T_m decreases. The melting point of core@shell nanoparticles is dependent on the shell component, and not dissimilar to that of the pure nanocluster. For Ag@Au arrangements, there is a strong drive to form an alloy at very low *T*, and thus we observe the formation of the rosette-Ih, an amorphization of the Ih, (at 30 K and 192 K for the Ih and CO starting geometries, respectively), which may explain why it is very difficult to obtain Ag@Au nanoparticles experimentally. Au@Ag, however, is stable in the core@shell arrangement.

Only Ag-rich nanoparticles undergo the MT, prompting further investigation into the transition barriers. We performed DNEB calculations, in conjunction with metadynamics and static GULP calculations to determine these barriers. The transition pathway for the MT is characterised by the diamond-square-diamond (DSD) mechanism for the majority of nanoparticles, with the exception of Ag@Au systems, where a rosette-Ih minima, is energetically preferable as an intermediate motif, thus preventing exploration of the DSD mechanism. Both the potential and free energy landscapes were shown to be highly complex for Ag@Au systems due to the existence of the rosette-Ih. The identification of the rosette-Ih arrangement is reassuring that its observance in MD simulations is not purely as a result of the chosen heating rate. Furthermore, the transition barriers may be manipulated through careful control of the nanoparticle composition and chemical arrangement for bimetallic systems. It would be of interest to extend this study to larger nanoparticle sizes, on a scale similar to experiment. A crossover point may exist, where no MT is observed once a particular nuclearity is reached, due to an increased transition barrier. The work presented here on annealing 147-atom nanoparticles has been published in *The Journal of Physical Chemistry C*[56] and the metadynamics/DNEB study of transition barriers for different morphologies can be found in *The Journal of Physical Chemistry Letters*.[57]

4.8 References

1. Sinzig, J.; Radtke, U.; Quinten, M.; Kreibig, U., Binary Clusters: Homogeneous Alloys and Nucleus-Shell Structures. *Zeitschrift für Physik D Atoms, Molecules and Clusters* **1993**, *26*, 242-245.
2. Nishimura, S.; Dao, A. T. N.; Mott, D.; Ebitani, K.; Maenosono, S., X-Ray Absorption near-Edge Structure and X-Ray Photoelectron Spectroscopy Studies of Interfacial Charge Transfer in Gold–Silver–Gold Double-Shell Nanoparticles. *The Journal of Physical Chemistry C* **2012**, *116*, 4511-4516.
3. Anh, D. T. N.; Singh, P.; Shankar, C.; Mott, D.; Maenosono, S., Charge-Transfer-Induced Suppression of Galvanic Replacement and Synthesis of (Au@ Ag)@ Au Double Shell Nanoparticles for Highly Uniform, Robust and Sensitive Bioprobes. *Applied Physics Letters* **2011**, *99*, 073107.
4. Shibata, T.; Bunker, B. A.; Zhang, Z.; Meisel, D.; Vardeman, C. F.; Gezelter, J. D., Size-Dependent Spontaneous Alloying of Au-Ag Nanoparticles. *Journal of the American Chemical Society* **2002**, *124*, 11989-11996.
5. Chen, H.; Liu, R.; Jang, L.-Y.; Lee, J.-F.; Hu, S.-F., Characterization of Core–Shell Type and Alloy Ag/Au Bimetallic Clusters by Using Extended X-Ray Absorption Fine Structure Spectroscopy. *Chemical Physics Letters* **2006**, *421*, 118-123.
6. Jiang, H.-L.; Akita, T.; Ishida, T.; Haruta, M.; Xu, Q., Synergistic Catalysis of Au@ Ag Core− Shell Nanoparticles Stabilized on Metal− Organic Framework. *Journal of the American Chemical Society* **2011**, *133*, 1304-1306.
7. Mallin, M. P.; Murphy, C. J., Solution-Phase Synthesis of Sub-10 Nm Au-Ag Alloy Nanoparticles. *Nano Letters* **2002**, *2*, 1235-1237.
8. Srnová-Šloufová, I.; Lednický, F.; Gemperle, A.; Gemperlová, J., Core-Shell (Ag)Au Bimetallic Nanoparticles: Analysis of Transmission Electron Microscopy Images. *Langmuir* **2000**, *16*, 9928-9935.
9. Li, Z.; Wilcoxon, J.; Yin, F.; Chen, Y.; Palmer, R.; Johnston, R., Structures and Optical Properties of 4–5 Nm Bimetallic Agau Nanoparticles. *Faraday discussions* **2008**, *138*, 363-373.
10. Rycenga, M.; Cobley, C. M.; Zeng, J.; Li, W.; Moran, C. H.; Zhang, Q.; Qin, D.; Xia, Y., Controlling the Synthesis and Assembly of Silver Nanostructures for Plasmonic Applications. *Chemical reviews* **2011**, *111*, 3669-3712.
11. Pietrobon, B.; Kitaev, V., Photochemical Synthesis of Monodisperse Size-Controlled Silver Decahedral Nanoparticles and Their Remarkable Optical Properties. *Chemistry of Materials* **2008**, *20*, 5186-5190.
12. Shim, J.-H.; Lee, B.-J.; Cho, Y. W., Thermal Stability of Unsupported Gold Nanoparticle: A Molecular Dynamics Study. *Surface science* **2002**, *512*, 262-268.
13. Lewis, L. J.; Jensen, P.; Barrat, J.-L., Melting, Freezing, and Coalescence of Gold Nanoclusters. *Physical Review B* **1997**, *56*, 2248.
14. Qiao, Z.; Feng, H.; Zhou, J., Molecular Dynamics Simulations on the Melting of Gold Nanoparticles. *Phase Transitions* **2014**, *87*, 59-70.
15. Wang, Y.; Teitel, S.; Dellago, C., Melting and Equilibrium Shape of Icosahedral Gold Nanoparticles. *Chemical physics letters* **2004**, *394*, 257-261.
16. Kuo, C.-L.; Clancy, P., Melting and Freezing Characteristics and Structural Properties of Supported and Unsupported Gold Nanoclusters. *The Journal of Physical Chemistry B* **2005**, *109*, 13743-13754.
17. Cleveland, C. L.; Luedtke, W.; Landman, U., Melting of Gold Clusters: Icosahedral Precursors. *Physical review letters* **1998**, *81*, 2036.

18. Cleveland, C.; Luedtke, W.; Landman, U., Melting of Gold Clusters. *Physical Review B* **1999**, *60*, 5065.
19. Patil, S.; Shinde, P.; Takale, M., Size Dependent Cohesive Energy, Melting Temperature and Debye Temperature of Silver Nanoparticles. *Asian Journal of Research in Chemistry* **2014**, *7*, 1013-1015.
20. Cui, J.; Yang, L.; Wang, Y., Molecular Dynamics Simulation Study of the Melting of Silver Nanoparticles. *Integrated Ferroelectrics* **2013**, *145*, 1-9.
21. Luo, W.; Hu, W.; Xiao, S., Size Effect on the Thermodynamic Properties of Silver Nanoparticles. *The Journal of Physical Chemistry C* **2008**, *112*, 2359-2369.
22. Nanda, K.; Sahu, S.; Behera, S., Liquid-Drop Model for the Size-Dependent Melting of Low-Dimensional Systems. *Physical Review A* **2002**, *66*, 013208.
23. Chernyshev, A., Melting of Surface Layers of Nanoparticles: Landau Model. *Materials Chemistry and Physics* **2008**, *112*, 226-229.
24. Alarifi, H. A.; Atis, M.; Ozdogan, C.; Hu, A.; Yavuz, M.; Zhou, Y., Determination of Complete Melting and Surface Premelting Points of Silver Nanoparticles by Molecular Dynamics Simulation. *The Journal of Physical Chemistry C* **2013**, *117*, 12289-12298.
25. Mottet, C.; Rossi, G.; Baletto, F.; Ferrando, R., Single Impurity Effect on the Melting of Nanoclusters. *Physical review letters* **2005**, *95*, 035501.
26. Cheng, D.; Huang, S.; Wang, W., Thermal Behavior of Core-Shell and Three-Shell Layered Clusters: Melting of Cu 1 Au 54 and Cu 12 Au 43. *Physical Review B* **2006**, *74*, 064117.
27. Chen, F.; Curley, B. C.; Rossi, G.; Johnston, R. L., Structure, Melting, and Thermal Stability of 55 Atom Ag-Au Nanoalloys. *The Journal of Physical Chemistry C* **2007**, *111*, 9157-9165.
28. Chen, F.; Johnston, R. L., Martensitic Transformations in Ag-Au Bimetallic Core-Shell Nanoalloys. *Applied Physics Letters* **2008**, *92*, 3112.
29. Qi, W.; Lee, S., Phase Stability, Melting, and Alloy Formation of Au− Ag Bimetallic Nanoparticles. *The Journal of Physical Chemistry C* **2010**, *114*, 9580-9587.
30. Lopez-Sanchez, J. A.; Dimitratos, N.; Hammond, C.; Brett, G. L.; Kesavan, L.; White, S.; Miedziak, P.; Tiruvalam, R.; Jenkins, R. L.; Carley, A. F., Facile Removal of Stabilizer-Ligands from Supported Gold Nanoparticles. *Nature Chemistry* **2011**, *3*, 551-556.
31. Alexander, S., Visualization and Analysis of Atomistic Simulation Data with Ovito–the Open Visualization Tool. *Modelling and Simulation in Materials Science and Engineering* **2010**, *18*, 015012.
32. Pavan, L.; Baletto, F.; Novakovic, R., Multiscale Approach for Studying Melting Transitions in Cupt Nanoparticles. *Physical Chemistry Chemical Physics* **2015**, *17*, 28364-28371.
33. Pavan, L.; Rossi, K.; Baletto, F., Metallic Nanoparticles Meet Metadynamics. *The Journal of chemical physics* **2015**, *143*, 184304.
34. Lipscomb, W. N., Framework Rearrangement in Boranes and Carboranes. *Science* **1966**, *153*, 373-378.
35. Apra, E.; Baletto, F.; Ferrando, R.; Fortunelli, A., Amorphization Mechanism of Icosahedral Metal Nanoclusters. *Physical review letters* **2004**, *93*, 065502.
36. Farrell, J. D.; Lines, C.; Shepherd, J. J.; Chakrabarti, D.; Miller, M. A.; Wales, D. J., Energy Landscapes, Structural Topologies and Rearrangement Mechanisms in Clusters of Dipolar Particles. *Soft Matter* **2013**, *9*, 5407-5416.

37. Baletto, F.; Ferrando, R.; Fortunelli, A.; Montalenti, F.; Mottet, C., Crossover among Structural Motifs in Transition and Noble-Metal Clusters. *The Journal of chemical physics* **2002**, *116*, 3856-3863.
38. Gould, A. L.; Heard, C. J.; Logsdail, A. J.; Catlow, C. R. A., Segregation Effects on the Properties of $(Auag)_{147}$. *Phys. Chem. Chem. Phys.* **2014**, *16*, 21049-21061.
39. Chen, F.; Curley, B. C.; Rossi, G.; Johnston, R. L., Structure, Melting, and Thermal Stability of 55 Atom Ag-Au Nanoalloys. *J. Phys. Chem. C* **2007**, *111*, 9157-9165.
40. Calvo, F.; Cottancin, E.; Broyer, M., Segregation, Core Alloying, and Shape Transitions in Bimetallic Nanoclusters: Monte Carlo Simulations. *Phys. Rev. B* **2008**, *77*, 121406.
41. Logsdail, A. J.; Li, Z.; Johnston, R. L., Faceting Preferences for Au_n and Pd_n Nanoclusters with High-Symmetry Motifs. *Phys. Chem. Chem. Phys.* **2013**, *15*, 8392-8400.
42. Logsdail, A. J.; Johnston, R. L., Interdependence of Structure and Chemical Order in High Symmetry $(Pdau)_N$ Nanoclusters. *RSC Advances* **2012**, *2*, 5863-5869.
43. Baletto, F.; Ferrando, R., Structural Properties of Nanoclusters: Energetic, Thermodynamic, and Kinetic Effects. *Rev. Mod. Phys.* **2005**, *77*, 371-423.
44. Chen, H.; Liu, R.; Jang, L.-Y.; Lee, J.-F.; Hu, S., Characterization of Core–Shell Type and Alloy Ag/Au Bimetallic Clusters by Using Extended X-Ray Absorption Fine Structure Spectroscopy. *Chem. Phys. Lett.* **2006**, *421*, 118-123.
45. Trygubenko, S. A.; Wales, D. J., A Doubly Nudged Elastic Band Method for Finding Transition States. *The Journal of chemical physics* **2004**, *120*, 2082-2094.
46. Trygubenko, S. A.; Wales, D. J., Erratum: A Doubly Nudged Elastic Band Method for Finding Transition States [J. Chem. Phys. 120, 2082 (2004)]. *The Journal of Chemical Physics* **2004**, *120*, 7820-7820.
47. Sheppard, D.; Terrell, R.; Henkelman, G., Optimisation Methods for Finding Minimum Energy Paths. *The Journal of chemical physics* **2008**, *128*, 134106.
48. Wales, D. J., Decoding the Energy Landscape: Extracting Structure, Dynamics and Thermodynamics. *Philosophical Transactions of the Royal Society of London A: Mathematical, Physical and Engineering Sciences* **2012**, *370*, 2877-2899.
49. Wales, D. J., Energy Landscapes: Some New Horizons. *Current opinion in structural biology* **2010**, *20*, 3-10.
50. Nocedal, J., Updating Quasi-Newton Matrices with Limited Storage. *Mathematics of computation* **1980**, *35*, 773-782.
51. Evans, D. A.; Wales, D. J., Folding of the Gb1 Hairpin Peptide from Discrete Path Sampling. *The Journal of chemical physics* **2004**, *121*, 1080-1090.
52. Dijkstra, E. W., A Note on Two Problems in Connexion with Graphs. *Numerische mathematik* **1959**, *1*, 269-271.
53. Wales, D. J., Discrete Path Sampling. *Molecular physics* **2002**, *100*, 3285-3305.
54. Wales*, D. J., Some Further Applications of Discrete Path Sampling to Cluster Isomerization. *Molecular Physics* **2004**, *102*, 891-908.
55. Zhang, H.; Watanabe, T.; Okumura, M.; Haruta, M.; Toshima, N., Catalytically Highly Active Top Gold Atom on Palladium Nanocluster. *Nat Mater* **2012**, *11*, 49-52.
56. Gould, A. L.; Logsdail, A. J.; Catlow, C. R. A., Influence of Composition and Chemical Arrangement on the Kinetic Stability of 147-Atom Au–Ag Bimetallic Nanoclusters. *The Journal of Physical Chemistry C* **2015**, *119*, 23685-23697.

57. Gould, A. L.; Rossi, K.; Catlow, C. R. A.; Baletto, F.; Logsdail, A. J., Controlling Structural Transitions in Auag Nanoparticles through Precise Compositional Design. *The Journal of Physical Chemistry Letters* **2016**, *7*, 4414-4419.

5 Understanding the thermal stability of Ag nanoclusters embedded in a-Si

5.1 Introduction

In Ch. 4, we observed a strong affinity for Ag migration to the surface from an Ag@Au arrangement. In Au/Ag systems, there is little atomic mismatch and thus diffusion is expected to occur easily. However, nanoparticle stability is a very important issue, particularly when regarding nanoparticle deposition onto a semiconducting substrate. We have previously discussed Au-Ag/TiO_2 nanoparticle/support systems (Ch. 1), where the nanoparticles improve the photocatalytic activity of the composite system: should these nanoparticles penetrate to the sub-surface layers of the support, there can be very different properties for the system as a whole.

One particularly prominent support material used in photovoltaics is amorphous silicon (a-Si); thin film a-Si solar cells are a cheaper (and therefore, more popular) alternative to bulk crystalline silicon solar cells, due to the reduction in the required amount of semiconductor material.[1] Nonetheless, to maintain sufficient light absorption, the influence of metallic nanoparticles on the optoelectronic properties of a-Si is a highly topical area of interest. Ag is often the choice metallic nanoparticle for improving the light-trapping performance of thin film a-Si solar cells, and thus the stability of Ag nanoparticles in a-Si is an important consideration.[2-3]

The collective oscillation of the free electrons in a metallic nanoparticle, known as surface plasmon resonance (SPR), can result in a strong enhancement of the electric field in its surrounding.[4] The strong scattering and increase of the local electric field strength for metallic nanoparticles can contribute to a higher photocurrent, although can only be realised at particular scattering wavelengths, which is in turn dictated by the nanoparticle size and shape.[5-7] Zeman *et al.* demonstrated an improvement in light trapping when self-assembled Ag nanoparticles were embedded into the back contact.[8] Similarly, Gu *et al.* studied the effect of using nucleated Ag nanoparticles to scatter light in a broadband wavelength range, observing a significant enhancement

(23%) in energy conversion efficiency.[9] Therefore, in addition to nanoparticle size and shape, the positioning of Ag nanoparticles within the thin film solar cell matters considerably. However, knowledge concerning the stability of these embedded Ag nanoparticles is limited to studies performed on bulk interfaces, where diffusion of Ag into Si is found to be slow.[10-12]

We received an experimental report from Marcel Di Vece and his co-workers (University of Utrecht), who examined the properties of Ag nanoparticles embedded in amorphous silicon (a-Si) under extended heating, observing unusual experimental phenomena: not only did morphological changes in the Ag nanoparticle occur, but in some cases, some regions of the Ag nanoparticle appeared to diffuse into the a-Si framework, creating voids in the original sample. Understanding why only certain regions of the nanoparticle diffuse at higher temperatures warrants further investigation, as structural changes of this nature indicate that atomic structure plays an important role in determining nanoparticle stability. The observed directionality of this diffusion suggests that the presence of defects at the nanoparticle surface may stimulate the process or perhaps even result in an accelerated rate of inter-diffusion between Ag and a-Si.

We present here a brief overview of the experimental methods and observations, with full detail provided in Appendix C. The composite systems of Ag nanoparticles and a-Si, henceforth referred to as Ag-a-Si, were produced via a three-step protocol: (i) deposition of an a-Si layer (15 nm) on a SiN (10 nm) TEM grid; (ii) Ag nanoparticle deposition; (iii) deposition of another a-Si layer (15 nm), effectively encapsulating the Ag nanoparticles. Sample 1 (S1) was created using 15 nm a-Si layers surrounding the nanoparticle, and sample 2 (S2) had 35 nm thick a-Si layers encapsulating the Ag nanoparticle. A schematic diagram of the embedded Ag nanoparticles is given in Fig. 5.1. *In situ*, pre and post-heating high resolution transmission electron microscopy (HRTEM) images of the samples were acquired, as well as high-angle annular dark field scanning TEM (HAADF STEM) images for post-heating (as mentioned in Section 2.5.1). From these, Di Vece and co-workers observed a particular directionality in regards to the loss of Ag atoms, and thus we were approached to determine whether we could corroborate their suggested conclusions, which were

that the presence of defects stimulates the diffusion of Ag atoms into a-Si (Appendix C, Fig. C2). Therefore, computational simulations of the annealing of Ag nanoparticles, embedded in a-Si, were performed.

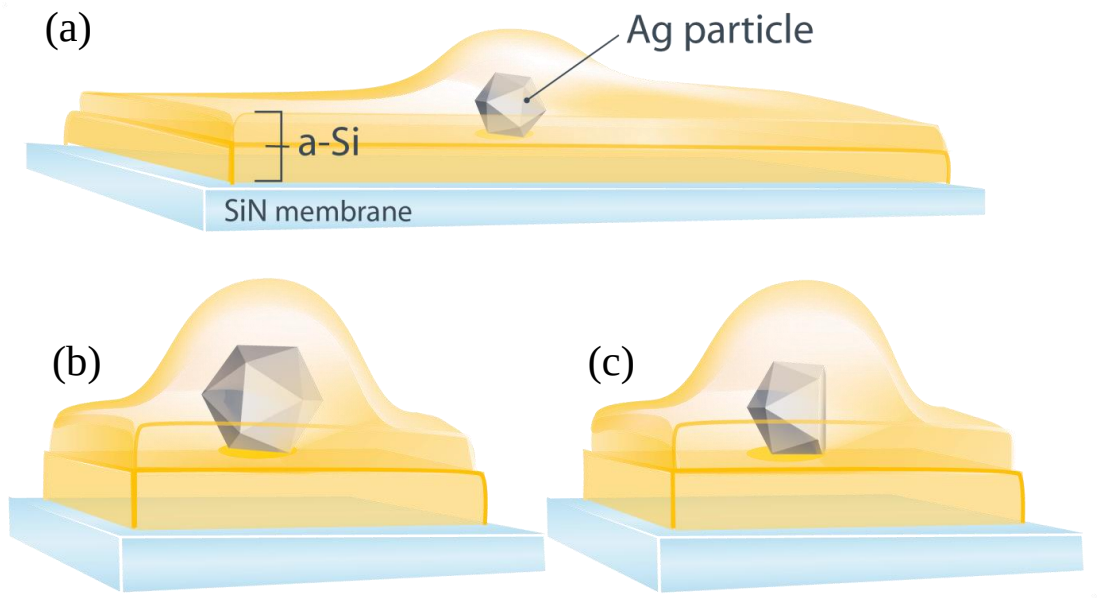

Fig. 5.1 Schematic representation of the Ag nanoparticles embedded in a-Si as created by Di Vece *et al.*: (a) Sample S1, nominally 15 nm a-Si/layer embedding nanoparticles with an average diameter of 9.4 ± 1.2 nm; (b) Sample S2, nominally 35nm a-Si/layer embedding nanoparticles with an average diameter of 31.9 ± 10.0 nm; (c) Sample S2 after partial atomic detachment during annealing.

Explicit theoretical studies of atomic Ag migration into Si are limited to computational first-principles analysis of the Ag adsorption onto c-Si surfaces:[13-14] Julg and Allouche reported that 'valley' sites (i.e. voids on the c-Si surface) on the Si (111) face were the most stable position for the adsorption of small Ag clusters (1-7 atoms), with an adsorption energy of 3.3±0.1 eV/atom, in agreement with experiment. It was originally suggested by Saitoh *et al*. that upon adsorption, Ag atoms may become embedded within the Si lattice.[15] However, based on estimated van der Waals radii, the penetration of Ag atoms into the c-Si matrix was determined to be impossible without considerable distortion energy,[13] due to the limited interspatial region between Si atoms. This finding was confirmed by Chou *et al.*, who reported a penetration barrier for an Ag atom into an Si (111) surface of 2.30 eV, which is very large when compared to the 0.17 eV barrier calculated similarly for Cu atoms, which are observed to diffuse into the lattice.[14]

For static calculations of interfacial energetics, Butler *et al*.[16] developed a Tersoff[17] type interatomic potential for modelling the interaction of Si with Ag. This potential is parameterized using ab-initio calculations of model Si-Ag systems, and validated against experimental data and further ab-initio calculations of Ag-Si interfaces and nanoparticles. The parameters include the bond length and binding energy of the Ag-Si dimer, the geometry obtained after replacing an Ag atom in the unit cell by a Si atom and geometry optimising, as well as the geometries and work of separation for the following interfaces: Si(111)//Ag(111), Si(110)//Ag(110), Si(100)//Ag(100) and Si(100)//Ag(110). This interatomic potential provides a much quicker route to calculating optimised geometries in comparison to DFT methods.

5.2 Methodology

We performed ensemble MD simulations of the embedded Ag-a-Si systems to investigate and reproduce the experimental observations. In order for the calculations to represent the experimental conditions as closely as possible, a bulk a-Si system needed to be created initially. A crystalline unit cell consisting of 8000 Si atoms was equilibrated at 3500 K and cooled to 1K, at a rate of 5 K / ps, as outlined in previous studies.[18-20] A 147-atom Ag nanoparticle was then inserted into the bulk a-Si, and any Si atoms close to the Ag nanoparticle were removed (hereafter the composite system is referred to as Ag-a-Si, Fig. 5.2). The bond cut-off distance was set to 1.7 Å, as this particular distance still allows for Ag-Si interactions at Ag nanoparticle. The embedded Ag nanoparticle was modelled as both a cuboctahedral (CO) and icosahedral (Ih) structure [the two systems are hereafter referred to as Ag(CO)-a-Si and Ag(Ih)-a-Si, respectively], as these geometries can be constructed with concentric complete shells around a central atom, when the number of atoms (N) is 13, 55, 147, 309, etc..[21] Whilst for smaller sizes the properties of these nanoparticles are governed by quantum effects, by performing the calculations for slightly larger sizes we hope that any identifiable trends may be reasonably related to the experimental observations for larger nanoparticles.

The combined Ag-a-Si system was annealed to 1000 K in 10 K intervals, at a rate of 10 K / 10 ps, using a timestep (Δt) of 1 fs (i.e. 10,000 steps at each temperature level), with *NPT* conditions (1 atm) enforced. An ensemble of results was achieved

by repeating the above process 10 times, thus providing different starting structures in each case for the a-Si, and the final results were then averaged over the entire ensemble. Thus, all numerical values discussed from hereon in are an average result from these ten simulations. All calculations were performed using DL_POLY_4[22] and the velocity Verlet algorithm to integrate Newton's equations of motion. The Nosé–Hoover[23-24] thermostat is used with a relaxation time of 1 fs. Si-Si interactions were represented throughout using the Tersoff potential;[17] the Tersoff potential was also used for Ag-Si interactions, and Ag-Ag interactions were represented using the embedded atom model (EAM) as modified by Butler *et al*. (Table 5.1).[16]

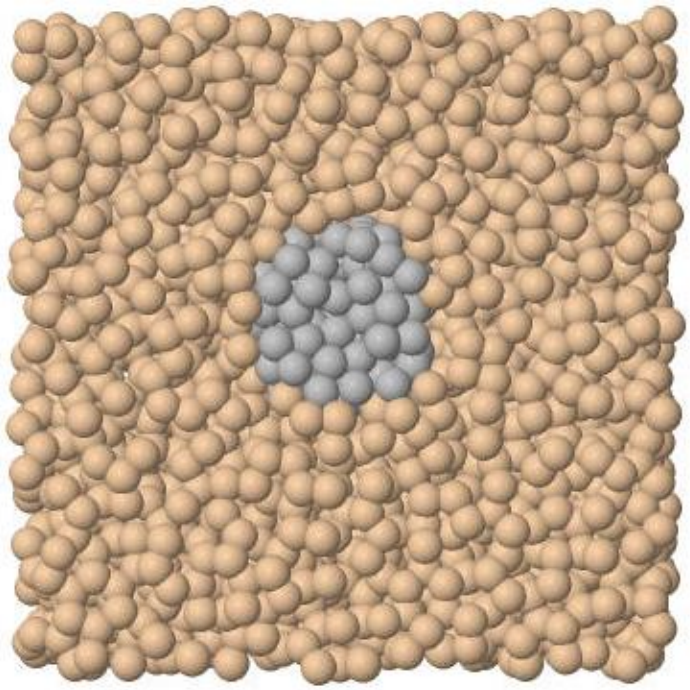

Fig. 5.2 Cross-section of an Ag(CO)-a-Si system after equilibration. Grey atoms represent Ag, beige atoms represent Si.

Table 5.1 Potential parameters as derived by Butler *et al.*.[16] A number of constraints have been applied to the parameters used for the Si-Ag potential to ensure that Ag atoms do not interact through the Tersoff potential.

Tersoff Ag-Si parameters		EAM Ag parameters	
A (eV)	99.93	α	7.689628
a ($Å^{-1}$)	1.016	r_{eq}	2.959130
B (eV)	99.93		
b ($Å^{-1}$)	1.016		
R (Å)	4.50		
S (Å)	4.50		
β	0		
η	0.5		

5.3 Structural Analysis

Radial Distribution Function

After the MD simulation has been performed, the trajectory can be used to compute the radial distribution function (RDF). The RDF describes the distribution of distances between any two atoms in the material, representing the relative probability to find a pair of atoms separated by distance r. The RDF $g(r)$ is given as

$$g(r) = \left\langle \frac{n(r+\Delta r) - n(r)}{4\pi r^2 \Delta r} \frac{V}{N} \right\rangle$$

where $n(r)$ is the number of atoms within a distance r from a certain atom, Δr is the distance step, V is the total volume and N is the total number of atoms.[25] By looking at the RDF plots, we will be able to determine changes in the coordination of the Ag atoms.

Dimer calculations

In order to relate our findings to the strength of the Ag−Si and Ag−Ag interactions, we have also performed calculations on these dimers, finding that the Ag−Si bond is 0.75 eV/atom stronger than the Ag−Ag interaction, as is to be expected from the experimental cohesive energies of Ag (2.95 eV) and Si (4.63 eV).[26]

5.4 Results and Discussion

5.4.1 Testing of Ag parameters

Butler *et al*. altered the parameters for the Ag EAM from their original form[27] in order to reproduce the energy vs. volume results from Ag−Si DFT calculations, and thus to ensure the validity of any subsequent results, we tested these differences by performing comparative simulated heating calculations for gas-phase Ag nanoparticles.

Parameters

The original Ag EAM parameters as specified by Zhang *et al.*[27] were tested for the annealing of an isolated 147-atom Ag nanoparticle, averaging over an ensemble of ten simulations. The nanoparticle was observed to undergo an MT from CO to Ih at 250-260 K and melts at 690 K.

The updated parameters, as provided by Butler *et al.*,[16] reproduce the energy vs. volume results from DFT calculations for Ag−Si systems, and should therefore be correctly parameterized for our investigation. The potential is parameterized through ab-initio calculations of model Ag−Si systems and tested against both experimental data and larger ab-initio calculations of Ag−Si interfaces and clusters. Using the same test as for the original parameters, the MT was observed to occur at 230 K, and melt at 890-900 K (Fig. 5.3).

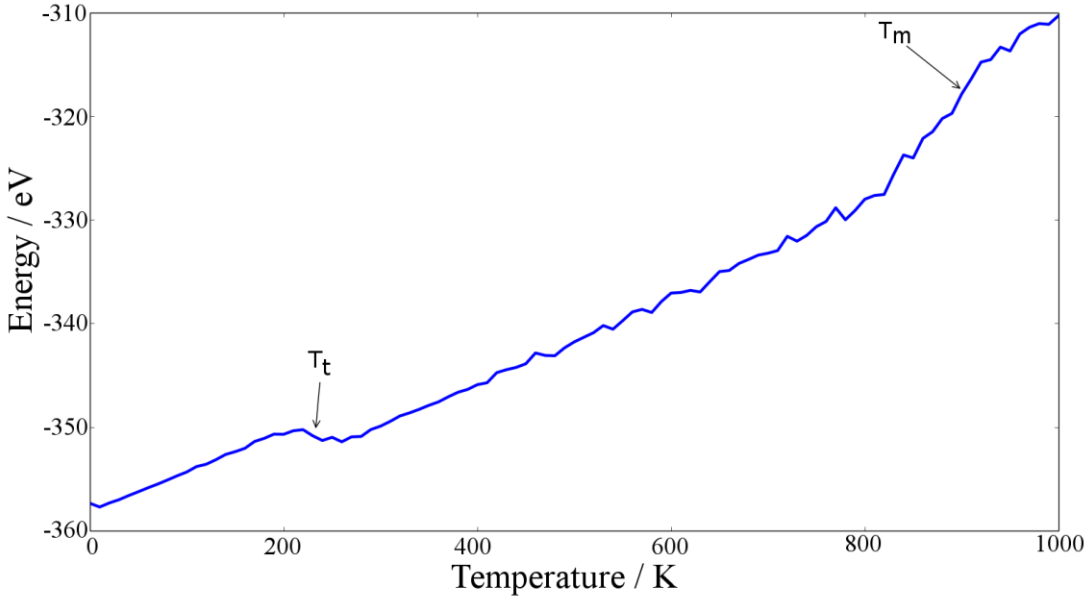

Fig. 5.3 *E* as a function of *T* for an isolated Ag_{147} nanoparticle, highlighting T_t and T_m.

When the same simulation was performed beginning from an Ag nanoparticle with Ih geometry, no structural transition was observed (as expected, given that the Ih is the lowest energy arrangement for a 147-atom Ag nanoparticle).

5.4.2 Ag(CO)-a-Si

Following equilibration at 1 K, the embedded Ag nanoparticle loses its well-defined structure, but still exhibits CO characteristics (Fig. 5.4). The Ag(CO)-a-Si system is then annealed in 10 K steps up to 1000 K. At 100 K, the Ag-Ag interactions for Ag(CO)-a-Si still represent a CO arrangement, with the same oscillations in $g(r)$, although the peak at 6.3 Å is no longer present. When 100 K < T < 400 K, there is a loss of order in the RDF plot for Ag-Ag interactions (Fig. 5.5), with the number of distinct peaks decreasing from 6 to 3, alongside broadening: the Ag nanoparticle begins to change its morphology. Additionally, a peak that was previously identifiable at ~4 Å is no longer present, indicating a transition towards an arrangement more of an Ih nature, the RDF peaks are consistent with that of the Ag(Ih)-a-Si system.

The structural transformation from CO to Ih is due to the lower energy, and thus higher stability, of the Ih at small sizes. The transition is observed at 120 K, which is

a much lower transition temperature (T_t) than that of an isolated Ag nanoparticle (230 K, see Section 5.4.1), attributed to destabilisation by the strong Ag−Si interactions: the Ag-Si interactions are 0.75 eV/atom stronger than the Ag−Ag interactions in our test calculations. More Ag-Si interactions occur at the nanoparticle surface, although Si atoms do not penetrate the nanoparticle until ~500 K. At 500 K, there are (on average) 3 Si atoms embedded within the Ag nanoparticle, but the Ag−Ag RDF remains approximately unchanged.

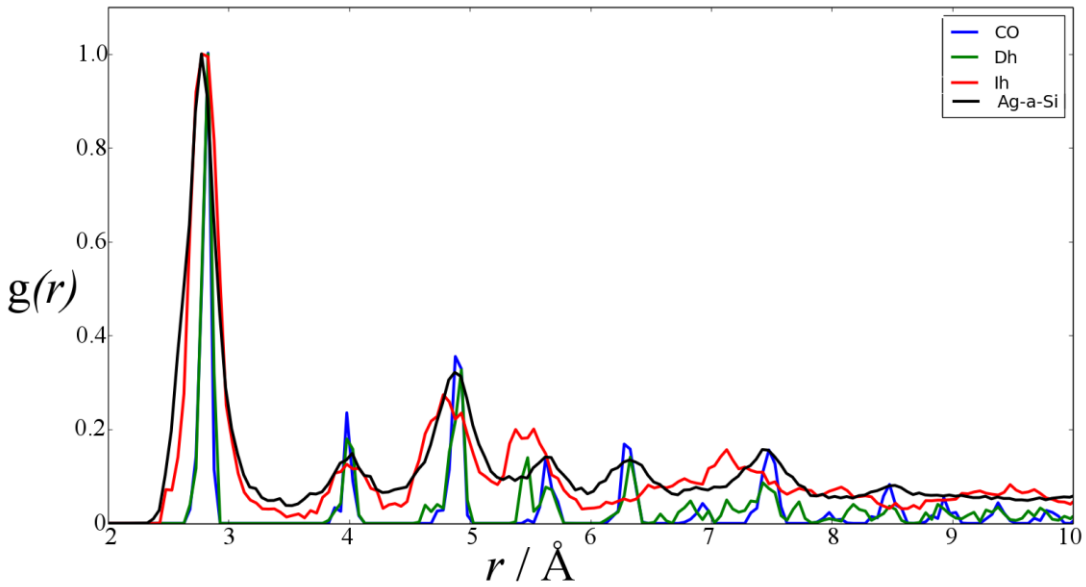

Fig. 5.4 RDF comparison of Ag−Ag interactions within Ag(CO)-a-Si system, following equilibration, with 147-atom Ag nanoparticles of CO, Dh (Decahedral) and Ih geometries at 1 K, all normalised to unity. A key is provided.

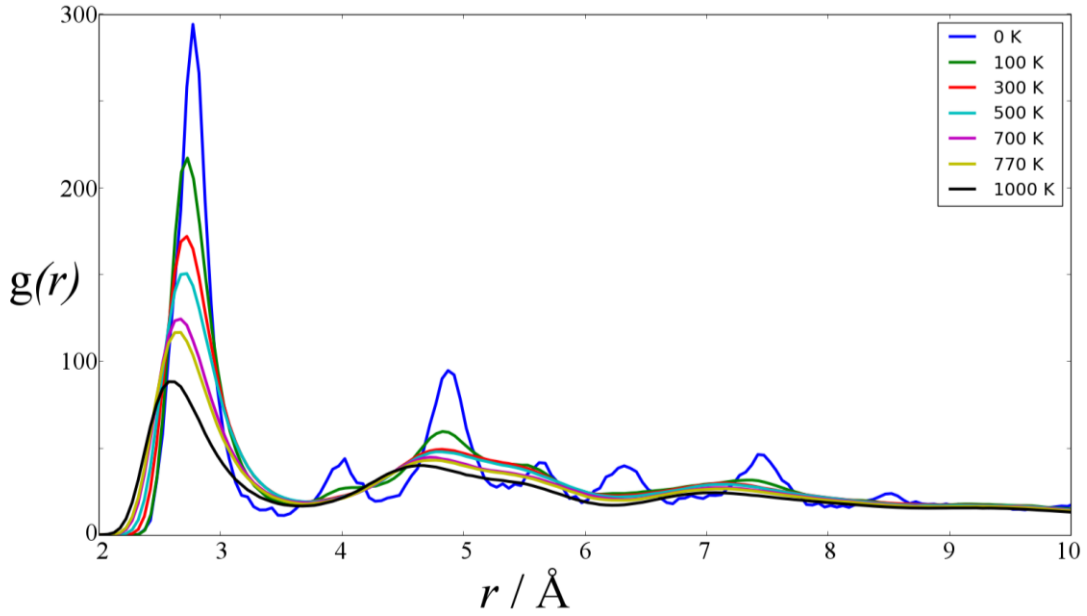

Fig. 5.5 RDF of ensemble averaged Ag−Ag interactions within Ag(CO)-a-Si system at 1, 100, 300, 500, 700, 770 and 1000 K. A key is provided. The 770 K (500°C) plot is included due to its experimental significance, when morphological changes are initially observed in the NP surface.

As *T* is increased further, the extent of Si diffusion into the Ag nanoparticle also increases. The re-emergence of a 'shoulder' in the RDF at 5.4 Å at 700 K indicates that the system has regained some structural ordering, and thus at some point the inclusion of Si atoms in the Ag nanoparticle actually results in improved stability. At 700 K, 12 Si atoms are accommodated within the Ag framework, and this increases to 31 atoms at 1000 K (Fig. 5.6). This is far above the melting temperature of an isolated 147-atom gas-phase Ag nanoparticle, occurring at 900 K. The first peak in the RDF corresponds to the first coordination shell, for which we observe a consistent decrease with increasing temperature at 2.8 Å. Therefore, we can say with certainty that the number of nearest-neighbour Ag-Ag interactions decreases as a result of increased temperature and Si diffusion.

The RDF of Ag-Si interactions are provided in Fig. 5.7. Upon raising the temperature of the system, the first peak in the RDF (2.8 Å) increases in intensity, corresponding to a greater number of Ag-Si interactions in the first coordination shell. A summary of the different configurations (starting from CO Ag nanoparticle) is given in Table 5.2 and Table 5.3. The results for Ag(Ih)-a-Si have not been tabulated as they should be consistent with Ag(CO)-a-Si once $T > 120$ K, given the

pseudo-Ih transformation that is observed. As *T* is increased beyond 400 K, there is a significant decrease in the number of distinct peaks in the RDFs, from six to three, with the remaining peaks shifted now to align with those of the Ih. At *T* = 500 K, we begin to see inter-diffusion of Si and Ag atoms, with on average 3 Si atoms diffusing in to the Ag nanoparticles, as documented in Table 5.2, which increases up to 12 (31) Si atoms within the Ag nanoparticle at *T* = 700 (1000) K, resulting in an increased amplitude for the Ag-Si RDF (Fig. 5.7).

Table 5.2 Summary of the number of internal Si atoms within the Ag_{147} nanoparticle, as a function of *T*. A mean is provided, illustrating the increase in Si atoms within the Ag nanoparticle, with increasing *T*. The bond distance cutoff is 2.7 Å.

Configuration	100 K	500 K	700 K	1000 K
1	0	3	11	31
2	0	3	10	32
3	0	3	13	32
4	0	2	5	28
5	0	1	14	32
6	0	4	13	31
7	0	3	9	27
8	0	3	15	31
9	0	3	8	28
10	0	8	18	37
Mean	**0**	**3**	**12**	**31**

Table 5.3 Summary of the number of Ag-Si bonds for Ag_{147} embedded in a-Si, as a function of *T*. The bond distance cutoff is 2.7 Å.

Configuration	100 K	500 K	700 K	1000 K
1	16	22	31	95
2	12	20	34	91
3	18	28	35	100
4	8	20	37	71
5	12	18	33	90
6	19	28	30	97
7	26	22	23	77
8	17	22	36	77
9	19	17	31	76
10	8	30	60	125
Mean	**16**	**23**	**35**	**90**

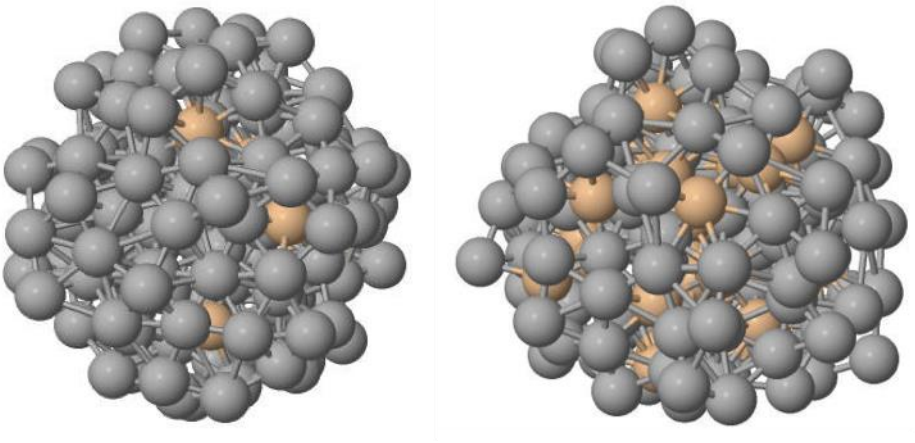

Fig. 5.6 Snapshot of embedded Ag NP at *T* = 700 K (left) and 1000 K (right) for Ag(CO)-a-Si, with surface Si interactions removed. Grey atoms represent Ag, beige atoms represent Si.

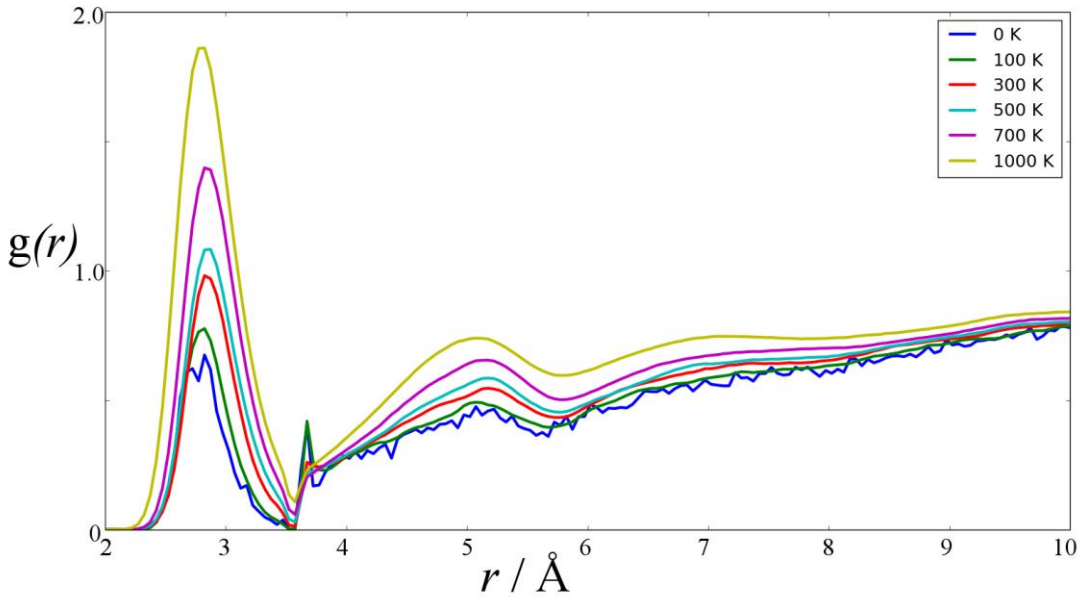

Fig. 5.7 RDF of Ag−Si interactions at 0, 100, 300, 500, 700 and 1000 K for Ag(CO)-a-Si, with a key provided. The increasing amplitude with *T* indicates the increasing number of Ag-Si interactions that are formed.

Analysis shows that the energy of the system increases continually with *T*, as is to be expected, although no discernible discontinuities, which would be indicative of melting behaviour and/or the rapid inter-diffusion of Si and Ag atoms, could be identified. To ensure that we have not overlooked any energy transitions, we plotted the change in energy (ΔE) at each *T* for all configurations:

$$\Delta E = E_T - E_{T-1}$$

where lowercase T is the final structural configuration for temperature step. However, ΔE also emphasises that there is no significant energy discontinuities; instead, only mild fluctuations in ΔE are observed (Fig. 5.8).

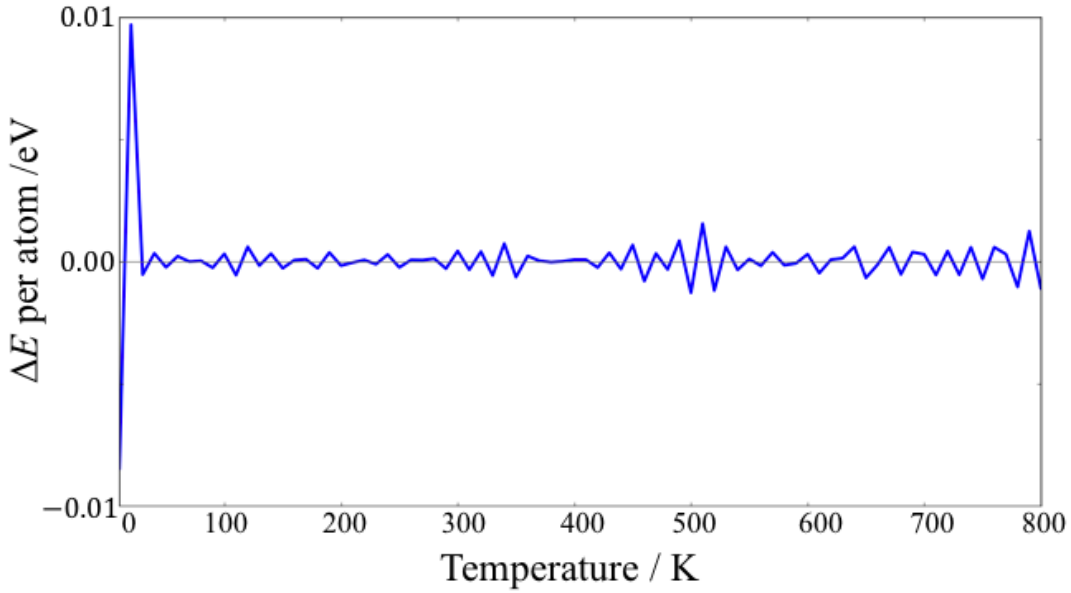

Fig. 5.8 The average ΔE per atom as a function of increasing T for the simulation system.

The changes in the system volume (V) were also correlated with T, as seen in Fig. 5.9. We note that the tenth configuration in Fig. 5.9 exhibits significantly different behaviour to the other systems: rather than V increasing, we see an overall decrease until T = 600 K, before V finally increases, highlighting the need for ensemble MD. Further analysis of the energy and structure show us that the initial a-Si is significantly higher in energy than all other configurations, stabilised via kinetic trapping, which has a smaller unit cell with many more Si−Si interactions than our other simulations (> 850 interactions). This strain leads to rapid inter-diffusion of the Ag and Si atoms during annealing, at temperatures much lower than for the other 9 configurations, most noticeable at 700 K (Table 5.3). Whilst this calculation is anomalous in its behaviour, it highlights the dependence of the results on the structure of the a-Si, something that may also be influential in the understanding of the experiment.

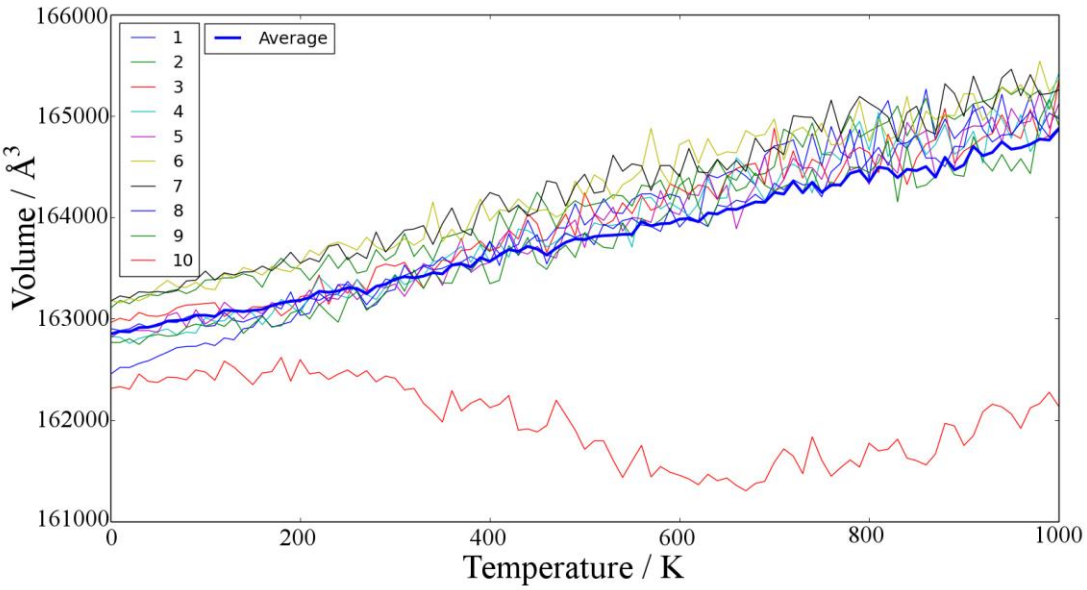

Fig. 5.9 *V* Ag(CO)-a-Si, as a function of *T*, with all configurations numbered 1-10 (thin lines). The average volume of the configurations is represented as a thick blue line, with a key also provided. The anomalous behaviour of simulation 10 is due to the kinetic trapping of a high-energy a-Si structure during the initial construction of the a-Si model.

5.4.3 Defective nanoparticles

Synthesised nanoparticles are not likely to have perfect CO or Ih geometry, and nanoparticle defects may stimulate the diffusion process that is observed experimentally. Thus to improve our theoretical comparisons to experiment, the vertices of the Ih Ag nanoparticle were substituted for Si atoms, creating surface defects, and these 'defective' nanoparticles subjected to the same heat treatment.

An increased rate of diffusion of Si into the Ag nanoparticle as a result of these defects is observed, with Si atoms penetrating the Ag surface at temperatures as low as 180 K. It was noted that Ag-Si inter-diffusion was more prevalent in this case at *T* = 500 K and 700 K, with on average 8 and 15 Si atoms in the Ag nanoparticles, respectively (Table 5.4) [3 and 12 Si atoms when no defects were present]. Such an observation clearly indicates that increased inter-diffusion of Ag and Si atoms can occur at low *T* when surface imperfections, such as defects, are present in the Ag nanoparticle. The observed mobility of Si atoms into the Ag nanoparticles in the calculations is attributed to the Si-Si interactions being stronger than the Ag-Ag

interactions. The large thermodynamic energy barriers prevent distortion of the Si-Si bond, while the weaker Ag-Ag interactions allow the inclusion of Si atoms. However, at 1000 K, the number of Si atoms accommodated within the nanoparticle is approximately the same, suggesting that there is a limit to the number of Si atoms that may be accommodated in the framework.

Table 5.4 Summary of the number of internal Si atoms within the defective Ag nanoparticle, as a function of *T*. A mean is provided, illustrating the increase in Si atoms within the Ag nanoparticle, with increasing *T*. The bond distance cutoff is 2.7 Å.

Configuration	100 K	300 K	500 K	700 K	1000 K
1	0	4	7	12	30
2	0	3	9	15	30
3	0	0	7	15	25
4	0	3	9	14	32
5	0	1	11	16	31
6	0	2	10	14	30
7	0	5	7	17	33
8	0	2	6	14	30
9	0	2	5	13	25
10	0	3	10	17	37
Mean	**0**	**3**	**8**	**15**	**30**

5.4.4 Gas-phase Ag-Si nanoparticles

To determine the influence of Si support on the Ag nanoparticles, our calculations were compared to calculations of gas-phase Ag nanoparticles doped with a small number of Si atoms at the surface at the beginning of the simulations ($Ag_{146}Si_1$ and $Ag_{134}Si_{13}$). These mixed systems were subjected to the same heating process, again using an ensemble of ten independent simulations with different random seeds.

Interestingly, single Si dopant atoms lowered the T_m from 890 K (Ag_{147}) to 599 K ($Ag_{146}Si$), whereas 13 Si dopant atoms caused T_m to rise again to 843 K ($Ag_{134}Si_{13}$), implying that small quantities of Si impurities could actually destabilise the Ag nanoparticles whereas larger quantities could improve stability.

5.5 Relating Simulations with Experiment

In relating these results to the experimental work performed by Di Vece and co-workers, we do not observe complete melting of the embedded Ag nanoparticles, and thus our calculations support the idea of enhanced nanoparticle stability as a result of the surrounding a-Si matrix. The preservation of order in the Ag-Ag RDF up to 1000 K for Ag-a-Si, well above the gas-phase T_m, indicates that the a-Si framework stabilises the embedded Ag nanoparticles.

No significant energy transitions are observed for the composite system, and thus it may be regarded stable as a whole. Morphological rearrangements are observed with increasing *T*, due to the inter-diffusion of Si and Ag atoms. However, the MD simulations suggest the diffusion of Si into the Ag atoms, whereas experiment suggests the dissolution of Ag atoms and their migration into the a-Si matrix. The stability of the a-Si matrix (T_m = 1420 K[28]) suggests that the movement of Ag atoms through the semiconductor would be an energetically unfavourable and slow process, additionally hindered by the size of the Ag atoms. This is also supported by previous theoretical work, where the diffusion of Ag into Si is calculated as requiring a very large distortion energy.[14]

Therefore, the differing outcomes of the MD simulations in comparison to the experiment suggests that there is something missing in our own model, such as atmospheric oxygen, or the formation of cracks and voids, both of which occur naturally in experiment. Experimentally, void formation in the a-Si matrix could possibly be caused by: (a) the diffusion of Ag atoms, detaching at their melting point, through micro-cracks towards the a-Si surface, as seen in Sample S2 [Appendix C, Fig. C5], or (b) that the a-Si layer has some degree of porosity (micro-voids), hosting the Ag atoms in pores. Further computational work could be pursued into the effects of these voids, again using ensemble MD simulations, looking at the influence of void size on the stability of the Ag-a-Si system.

Single Si dopant atoms lowered the T_m of gas-phase Ag-Si nanoparticles, whereas larger quantities of Si atoms increased the T_m, and could therefore improve the stability of the gas-phase nanoparticles. This would have a strong effect on the

dissolution of the larger Ag nanoparticles (detachment of Ag atoms) seen in experiment: Si dopants stimulate localised melting and subsequent detachment of Ag surface atoms when present in low concentrations; in experiment, the sharp angles and planes of the Ag nanoparticles, as well as the remaining complete Ag nanoparticles, indicate that the process of melting and subsequent dissolution stops at a neighbouring defect/dopant free atomic plane.

5.6 Conclusions

Pristine Ag nanoparticles embedded in amorphous silicon upon heat treatment were investigated with *in situ* TEM and *ex situ* HRTEM and HAADF STEM by Di Vece *et al*.. The morphological changes in these embedded Ag nanoparticles during extended heating, highlighted the preferential diffusion of Ag atoms away from nanoparticles of small sizes, especially in the presence of surface plane defects. It was suggested that parts of the Ag nanoparticles remain stable at elevated temperatures due to their 'perfect' atomic planes that resist detachment of atoms. Therefore, we performed complementary ensemble MD simulations of Ag nanoparticles embedded in a-Si, subjected to an annealing process. It was observed that nanoparticle defects accelerated the inter-diffusion of Ag and Si atoms in our simulations, supporting experimental findings.

The inclusion in our model of Si atoms inside the Ag nanoparticle shows both stabilising and de-stabilising effects, depending on the Si dopant concentration, which explains why parts of the Ag nanoparticles preferentially dissolve and other parts remain intact, as observed by the experiment. Regions of the Ag nanoparticle that contain small amounts of Si preferentially melt at the elevated temperatures, with Ag atoms migrating into the a-Si, resulting in the creation of voids. Defect inclusion also led to enhanced inter-diffusion, occurring at lower temperatures, which shows the intricate behaviour of a metal nanoparticle inside a semiconductor matrix as a function of temperature can lead to different degrees of stability. The results are of relevance to optical coatings such as those used in solar cells, where the stability of the system has great influence on its overall properties. The work in this chapter has been published in *The Journal of Physical Chemistry C*.

5.7 References

1. McEvoy, A.; Markvart, T.; Castañer, L.; Markvart, T.; Castaner, L., *Practical Handbook of Photovoltaics: Fundamentals and Applications*; Elsevier, 2003.
2. Atwater, H. A.; Polman, A., Plasmonics for Improved Photovoltaic Devices. *Nature materials* **2010**, *9*, 205-213.
3. Ferry, V. E.; Munday, J. N.; Atwater, H. A., Design Considerations for Plasmonic Photovoltaics. *Advanced materials* **2010**, *22*, 4794-4808.
4. Green, M. A.; Pillai, S., Harnessing Plasmonics for Solar Cells. *Nat Photon* **2012**, *6*, 130-132.
5. Yuan, Z.-h.; Li, X.-n.; Huang, J., Absorption Enhancement of Silicon Solar Cell with Ag Nanoparticles by Surface Plasmons Resonance. *Optoelectronics Letters* **2013**, *9*, 405-409.
6. Park, J.; Park, N.; Varlamov, S., Optimum Surface Condition for Plasmonic Ag Nanoparticles in Polycrystalline Silicon Thin Film Solar Cells. *Applied physics letters* **2014**, *104*, 033903.
7. Lim, S.; Mar, W.; Matheu, P.; Derkacs, D.; Yu, E., Photocurrent Spectroscopy of Optical Absorption Enhancement in Silicon Photodiodes Via Scattering from Surface Plasmon Polaritons in Gold Nanoparticles. *Journal of Applied Physics* **2007**, *101*, 104309.
8. Tan, H.; Santbergen, R.; Smets, A. H. M.; Zeman, M., Plasmonic Light Trapping in Thin-Film Silicon Solar Cells with Improved Self-Assembled Silver Nanoparticles. *Nano Letters* **2012**, *12*, 4070-4076.
9. Chen, X.; Jia, B.; Saha, J. K.; Cai, B.; Stokes, N.; Qiao, Q.; Wang, Y.; Shi, Z.; Gu, M., Broadband Enhancement in Thin-Film Amorphous Silicon Solar Cells Enabled by Nucleated Silver Nanoparticles. *Nano Letters* **2012**, *12*, 2187-2192.
10. Coffa, S.; Poate, J.; Jacobson, D.; Frank, W.; Gustin, W., Determination of Diffusion Mechanisms in Amorphous Silicon. *Physical review B* **1992**, *45*, 8355.
11. Nason, T.; Yang, G. R.; Park, K. H.; Lu, T. M., Study of Silver Diffusion into Si (111) and Sio2 at Moderate Temperatures. *Journal of applied physics* **1991**, *70*, 1392-1396.
12. Chen, L.; Zeng, Y.; Nyugen, P.; Alford, T., Silver Diffusion and Defect Formation in Si (1 1 1) Substrate at Elevated Temperatures. *Materials chemistry and physics* **2002**, *76*, 224-227.
13. Julg, A.; Allouche, A., Theoretical Study of the Adsorption of Silver Atoms on the (111) Face of Silicon. *International Journal of Quantum Chemistry* **1982**, *22*, 739-752.
14. Chou, S. H.; Freeman, A.; Grigoras, S.; Gentle, T.; Delley, B.; Wimmer, E., Bonding of Noble Metals to Semiconductor Surfaces: First-Principles Calculations of Copper and Silver on Silicon (111). *Journal of the American Chemical Society* **1987**, *109*, 1880-1881.
15. Mitsuchika, S.; Fumiya, S.; Kenjiro, O.; Teruo, H., Atomic Arrangement of the Si(111)-$\sqrt{3}\times\sqrt{3}$-Ag Structure Derived from Low-Energy Ion-Scattering Spectroscopy. *Japanese Journal of Applied Physics* **1980**, *19*, L421.
16. Butler, K. T.; Vullum, P. E.; Muggerud, A. M.; Cabrera, E.; Harding, J. H., Structural and Electronic Properties of Silver/Silicon Interfaces and Implications for Solar Cell Performance. *Physical Review B* **2011**, *83*, 235307.
17. Tersoff, J., Empirical Interatomic Potential for Silicon with Improved Elastic Properties. *Physical Review B* **1988**, *38*, 9902.

18. He, Y.; Donadio, D.; Galli, G., Heat Transport in Amorphous Silicon: Interplay between Morphology and Disorder. *Applied physics letters* **2011**, *98*, 144101.
19. Ishimaru, M.; Munetoh, S.; Motooka, T., Generation of Amorphous Silicon Structures by Rapid Quenching: A Molecular-Dynamics Study. *Physical Review B* **1997**, *56*, 15133.
20. Landman, U.; Luedtke, W.; Ribarsky, M. W.; Barnett, R.; Cleveland, C., Molecular-Dynamics Simulations of Epitaxial Crystal Growth from the Melt. I. Si (100). *Physical Review B* **1988**, *37*, 4637.
21. Martin, T. P., Shells of Atoms. *Physics Reports* **1996**, *273*, 199-241.
22. Todorov, I.; Smith, W.; Cheshire, U., The Dl Poly 4 User Manual. *STFC, STFC Daresbury Laboratory, Daresbury, Warrington, Cheshire, WA4 4AD, United Kingdom, version* **2011**, *4*.
23. Hoover, W. G., Canonical Dynamics: Equilibrium Phase-Space Distributions. *Physical Review A* **1985**, *31*, 1695.
24. Nosé, S., A Molecular Dynamics Method for Simulations in the Canonical Ensemble. *Molecular physics* **1984**, *52*, 255-268.
25. Tildesley, D.; Allen, M., Computer Simulation of Liquids. *Clarendon, Oxford* **1987**.
26. Kittel, C., *Introduction to Solid State Physics*; Wiley, 2005.
27. Zhang, P.-F.; Han, J.-G.; Pu, Q.-R., A Density Functional Investigation of Agsi N (N= 1− 5) Clusters. *Journal of Molecular Structure: THEOCHEM* **2003**, *635*, 25-35.
28. Donovan, E.; Spaepen, F.; Turnbull, D.; Poate, J.; Jacobson, D., Heat of Crystallization and Melting Point of Amorphous Silicon. *Applied Physics Letters* **1983**, *42*, 698-700.

Appendix C

Experimental Methods

Ag nanoparticles and a-Si composites were produced in a dedicated vacuum system which contains a NC200U-B cluster source (Oxford Applied Research) and a magnetron sputter source to deposit thin films. The cluster and sputter sources are located in different chambers, connected via a central chamber through which samples are transferred, allowing vacuum conditions to be maintained throughout sample fabrication. The background pressure in the cluster and sputter source was ~10^{-8} mbar. The silver nanoparticles were produced at a DC magnetron power of 30 W in argon plasma using a 99.99 % pure Ag target.

The composite systems of Ag nanoparticles and a-Si, henceforth referred to as Ag-a-Si, were produced via a three-step protocol: (i) deposition of an a-Si layer (15 nm) on a SiN (10 nm) TEM grid (temwindows.com); (ii) Ag nanoparticle deposition; (iii) deposition of another a-Si layer (15 nm), effectively encapsulating the Ag nanoparticles. Sample 1 (S1) was created using 15 nm a-Si layers surrounding the nanoparticle, and sample 2 (S2) had 35 nm thick a-Si layers encapsulating the Ag nanoparticle. The specimens were loaded into a Gatan heating holder and heated *in situ* inside an aberration-corrected FEI Titan microscope from room temperature (RT, 293 K), to a temperature, T, of 1173 K, in incremental temperature steps of 50 K. High resolution transmission electron microscopy (HRTEM) images of the sample were acquired *in situ* during the treatment, as well as at RT pre- and post-heating. High-angle annular dark field scanning TEM (HAADF STEM) images were also obtained post-heating. Following exposure to air, such as during transfer to the microscope, it is expected that a limited thin oxide film will form at the a-Si surface. Electron energy loss spectroscopy (EELS) measurements show that the presence of 4-5% oxygen in the a-Si film is present. The encapsulation of the Ag nanoparticles, however, ensures that they remain ultraclean, with no formation of Ag oxide.

Experimental Results and Discussion

Two samples were studied experimentally, henceforth named S1 and S2, with the Ag nanoparticle in each sample encapsulated by 15 nm and 35 nm thick a-Si layers, respectively. The pre-heating HRTEM examination showed the Ag nanoparticles to have a mean diameter (d) of 9.4 ± 1.2 nm and 31.9 ± 10.0 nm for S1 and S2, respectively, based on an average of 15 nanoparticle measurements per sample. Fig. C1 presents a pre-heating HRTEM image of an Ag nanoparticle in S1 with d ≈ 8 nm. The fast Fourier transform (FFT) pattern of the image [Fig. C1(b)] reveals that the particle is not a single crystal but contains multiple twinning-planes joining (111) faces, as highlighted with white arrows, which was observed consistently for nanoparticles in S1. Comparing these images with simulated HRTEM images of face centred cubic Fe nanoparticles leads us to conclude that the silver nanoparticles in S1 have an Ih structural motif. The predominant observation of Ih structures for the nanoparticles in S1 is in contrast to the gas-phase theoretical predictions, where Ih motifs are favoured for $d < 2$ nm, due to their close to spherical geometry and subsequent low surface area, whereas decahedral and truncated octahedral are more stable when $d > 2$ nm. It was concluded, therefore, that the larger of the observed Ih-structured Ag nanoparticles are likely to be stabilised by the encapsulating a-Si, which will affect the relative energies of competing surfaces. Incomplete rows of atoms along the surface facets, e.g. perpendicular to the red arrow in Fig. C1(a), can also be observed in nanoparticles in S1 prior to heating, and this structure is schematically represented in Fig. 5.1(c).

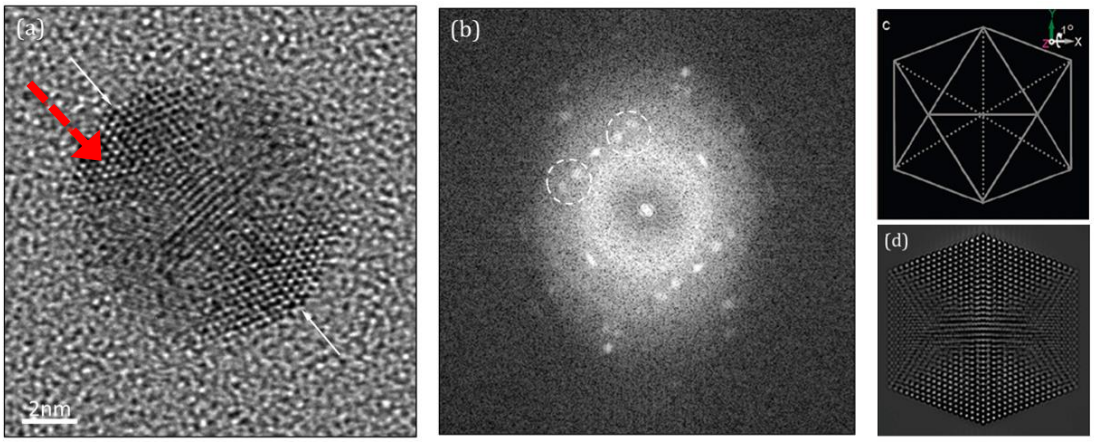

Fig. C1 (a) HRTEM image of a silver nanoparticle embedded in a-Si (Sample S1), acquired at room temperature (293 K), with twinning-planes and incomplete packing of surface atoms identified by white and red arrows, respectively, and (b) the corresponding FFT, where the encircled spots correspond to the twinning of crystal planes. Comparable HRTEM images of an icosahedron are presented: (c) schematic of an icosahedral geometry; (d) corresponding simulated HRTEM image for the icosahedral morphology. Images (c) and (d) are reprinted with permission, Copyright 2009 American Chemical Society.[1]

In contrast to the predominately Ih nanoparticles in S1, a wider variety of nanoparticle shapes is observed in S2 (Fig. C2), in contrast to theoretical predictions that show bulk-crystalline FCC structures are to be expected. The mean nanoparticle diameter in S2 is considerably greater than S1, which will play a dominating role in the stability of the different morphologies. Nonetheless, the encapsulating a-Si layer is also thicker, and it is also possible that this thicker layer exerts an increased constraining force on the particle. Detailed analysis of HRTEM images of the particle structures is extremely challenging, given the thickness of the a-Si layers in S2, but the variation of 2D outlines of the nanoparticles (Fig. C2) clearly indicates that a range of structures are present. For consistency in our present work the focus in our analysis of S2 is only on the morphological changes that occur for the Ih nanoparticles as the result of heating.

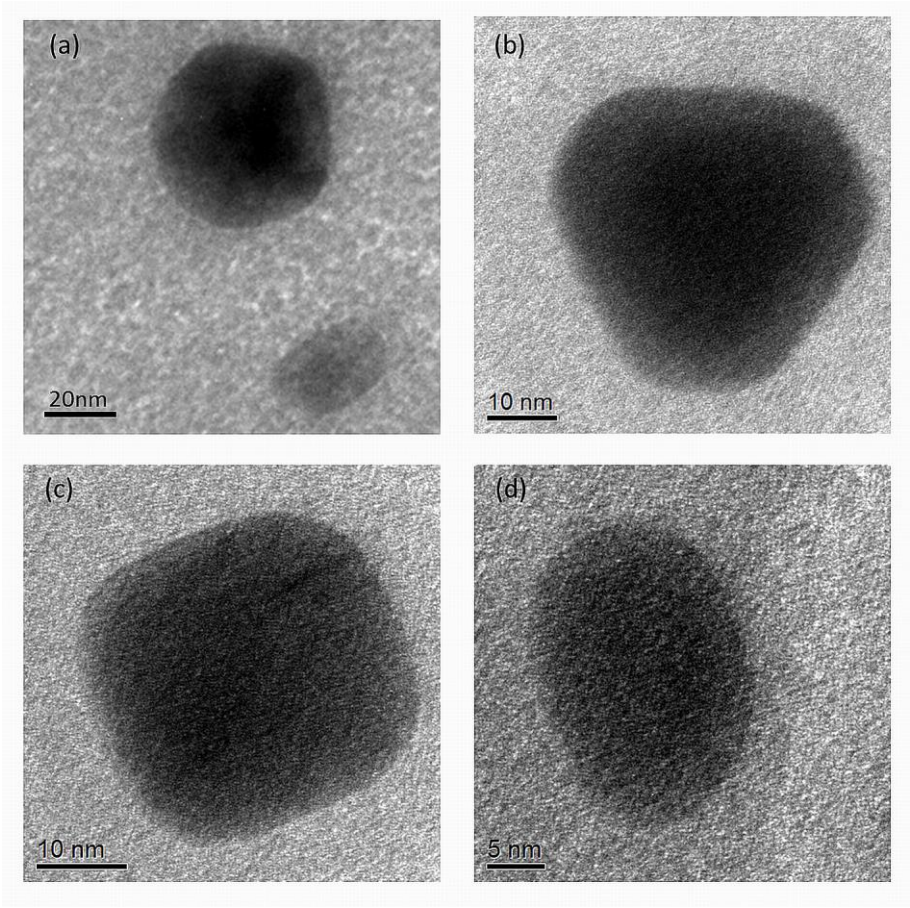

Fig. C2 Bright field TEM images showing examples of the various nanoparticle shapes observed in Sample S2.

Changes in nanoparticle morphologies were observed upon heating: Fig. C3 follows the outline (using TEM) of an Ih Ag nanoparticle in S2, with $d \approx 25$ nm, as it is heated from RT to 1173 K. Minimal change in the nanoparticle structure is seen for $T < 773$ K; however, surface indentations appear at 873 K and with further heating ($T > 923$ K) the sample starts to change shape and lose material, with the direction of loss of Ag atoms highlighted by the white arrows in Fig. C3. The specific directionality of Ag loss from the nanoparticle is of particular interest, highlighting the essential role that atomic structure plays in the detachment of Ag atoms. For instance, surface defects are likely to stimulate this process in hopes of attaining a perfect, uninterrupted atomic plane: the defect makes Ag diffusion or dissolution energetically possible, whereas removal of Ag atoms from a perfect plane requires much more energy. When the same *in situ* characterisation was performed while heating S1 (focusing specifically on an Ih Ag nanoparticle with d = 9.0 nm),

we observed outward migration of material from the Ag nanoparticle for $T > 773$ K, i.e. at lower temperatures than in S2. For both samples, the nanoparticles appear to decrease slightly in size during heating.

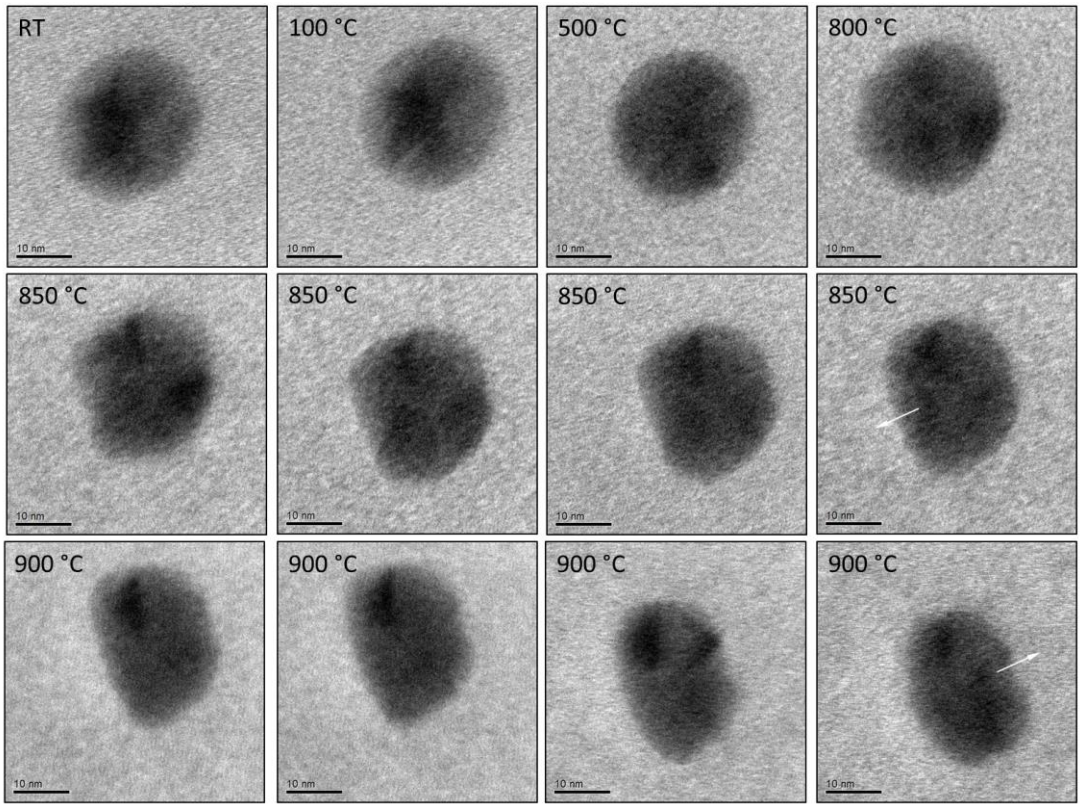

Fig. C3 TEM images of an Ag nanoparticle ($d \approx 25$ nm) embedded in a-Si (Sample S2) as the sample is heated from room temperature (293 K) up to 1173 K. The temperature is provided in the top left of each image, along with a scale in the bottom left.

In order to understand better our observations, the samples were examined post-heating using HAADF STEM, where diffraction contrast is negligible and image intensity is primarily dependent on the atomic number, Z, of an element. Fig. C4 presents HAADF STEM images of different Ag nanoparticles from S1 at RT after annealing to 773 K. The following observations can be made: (i) a greater variety of Ag nanoparticle morphologies are observed post-heating than prior; (ii) parts of the Ag nanoparticles disappear, leaving voids in the a-Si that are not observed pre-heating, as shown in Fig. C4 (b); (iii) Ag atoms remain present in the surrounding a-Si in a random arrangement, as confirmed using energy dispersive spectroscopy (EDS), with the resulting Ag distribution visible as a 'halo' in the

HAADF STEM images [Fig. C4(a)]. Furthermore, the migration of the Ag atoms into or onto the a-Si matrix appears to be specific to certain parts of the nanoparticles. Particularly, the 120° angle between the remaining surface planes of the nanoparticle at the void is important, as it points to a strong relation between the crystal structure and detachment/dissolution of Ag atoms. The majority of voids in the a-Si matrix occurring in S1 for nanoparticles with d < 5 nm, indicating a significant size-dependence for the diffusion of parts of the Ag nanoparticles.

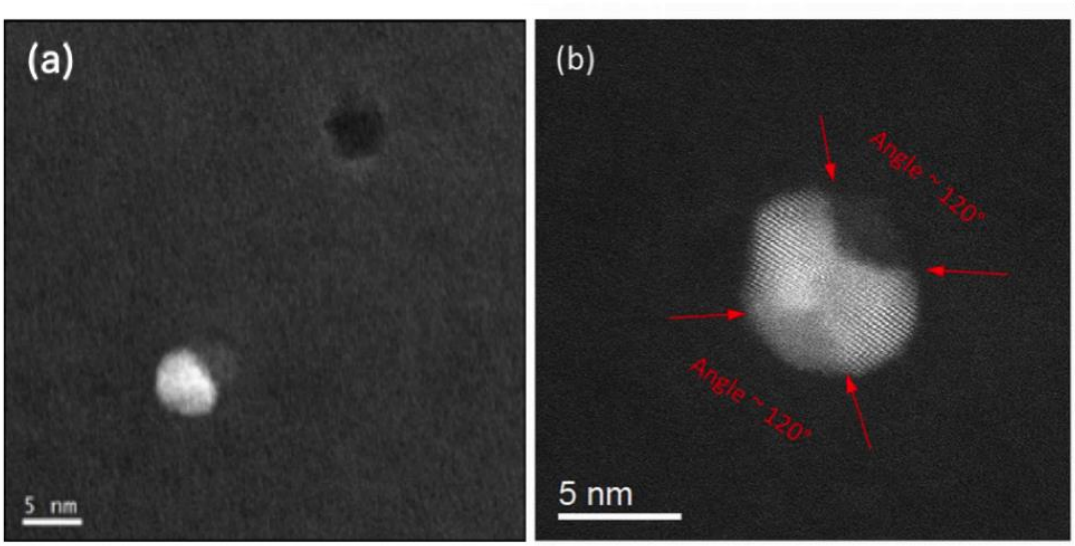

Fig. C4 Post-heating HAADF STEM images of Ag nanoparticles embedded in a-Si (Sample S1) at room temperature; the sample was heated to 773 K. Bright regions represent Ag atoms, grey regions the a-Si framework and dark regions the voids. Areas where the Ag atoms have been removed are clearly visible in all images (a) and (b), with an entire nanoparticle removed in the top right of (a), leaving a dark void and a silver 'halo' effect from the nearby embedded Ag atoms. A scale is provided in the bottom left of each image.

The preferential detachment/diffusion of particular regions of the Ag nanoparticle (in some cases leaving voids in the a-Si structure), leads to several questions regarding the properties of the Ag-a-Si system and, more specifically, the Ag/a-Si interface. The Si-Ag phase diagram indicates that mixtures with high Ag concentrations result in a melting temperature (T_m) of ~1108 K,[2] illustrating the possibility of Ag/Si interfacial inter-diffusion as found in research on solar cell applications;[3-4] though in general the mobility of Ag in Si is much lower than witnessed here.[5-6] A dependence of the thermal stability on the nanoparticle size is to be expected, and although a systematic size investigation was not performed, the

change in T_m as observed for these experiments likely holds true for larger atomic sizes and thus provides a qualitative explanation of the experimental results. For example, T_m and subsequent detachment of Ag atoms could be stimulated by the presence of structural defects, which are indeed visible in some of our samples (Fig. C1).

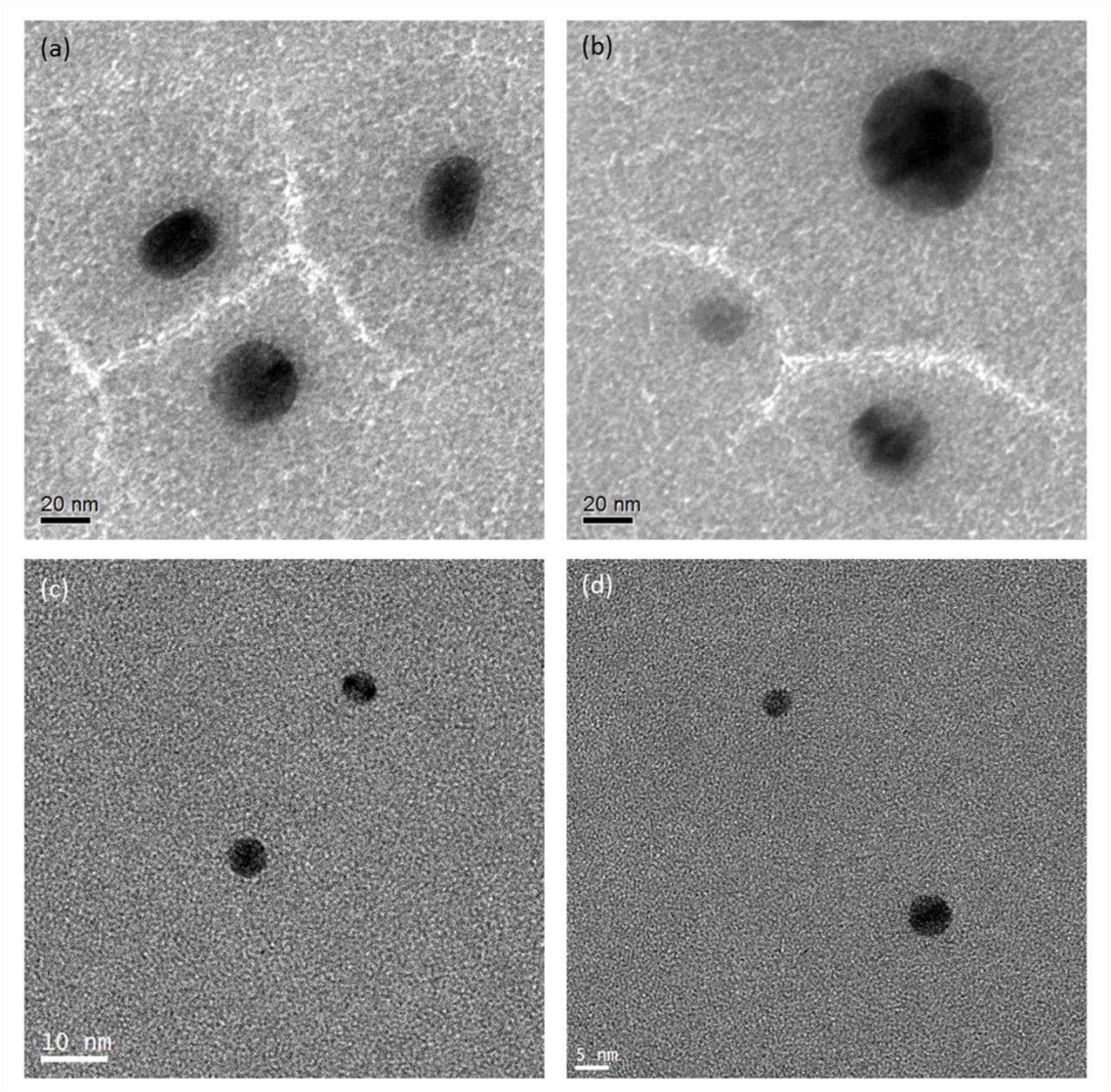

Fig. C5. (a) and (b) bright field TEM images of S2 showing cracks observed in the a-Si matrix in this sample. (c) and (d) bright field TEM images of sample S1 showing no such cracks in the a-Si in this sample.

Experimental References

1. Ling, T.; Xie, L.; Zhu, J.; Yu, H.; Ye, H.; Yu, R.; Cheng, Z.; Liu, L.; Yang, G., Icosahedral Face-Centered Cubic Fe Nanoparticles: Facile Synthesis and Characterization with Aberration-Corrected Tem. *Nano letters* 2009, *9*, 1572-1576.
2. Olesinski, R.; Gokhale, A.; Abbaschian, G., The Ag-Si (Silver-Silicon) System. *Journal of Phase Equilibria* 1989, *10*, 635-640.
3. Rollert, F.; Stolwijk, N.; Mehrer, H., Solubility, Diffusion and Thermodynamic Properties of Silver in Silicon. *Journal of Physics D: Applied Physics* 1987, *20*, 1148.
4. McBrayer, J. D.; Swanson, R.; Sigmon, T., Diffusion of Metals in Silicon Dioxide. *Journal of The Electrochemical Society* 1986, *133*, 1242-1246.
5. Coffa, S.; Poate, J.; Jacobson, D.; Frank, W.; Gustin, W., Determination of Diffusion Mechanisms in Amorphous Silicon. *Physical review B* 1992, *45*, 8355.
6. Nason, T.; Yang, G. R.; Park, K. H.; Lu, T. M., Study of Silver Diffusion into Si (111) and Sio2 at Moderate Temperatures. *Journal of applied physics* 1991, *70*, 1392-1396.

6 Molecular adsorption on AuAg nanoclusters: using CO as a probe molecule to determine chemical ordering changes

6.1 Introduction

Gold nanoclusters (< 5 nm) dispersed on metal oxide surfaces have been shown to exhibit surprisingly high catalytic activity and/or selectivity for low-temperature catalytic combustion, partial oxidation of hydrocarbons, hydrogenation of unsaturated hydrocarbons, and reduction of nitrogen oxides.[1] The catalytic activity of the nanoclusters is dependent on the chosen support, preparation method, and the size of the Au nanoclusters (see also Ch. 1).[2] Furthermore, the presence of atmospheric species can also influence the reactivity of nanoclusters, either by facilitating charge transfer or through the blocking of active sites, and thus it is necessary to include these adsorbates in our atomistic picture.

CO adsorption

The bonding model for CO to a transition metal involves two components: 1) a 2 e^- donation of the lone pair on C from the 5σ orbital to the vacant metal *d* orbital (M←CO), accompanied by π back donation from the (now filled) metal *d*-orbital to the empty anti-bonding $2\pi^*$ molecular orbital (M→CO). This is demonstrated in Fig. 6.1: different components of the bonding interaction have been colour-coded. This bonding is synergistic – the more σ donation by the CO ligand, the more electron rich the metal will become, resulting in stronger the π back-bonding. The CO bond is weakened, resulting in a lengthening of the CO bond and a red shift of the stretching frequency in comparison to gas-phase CO.

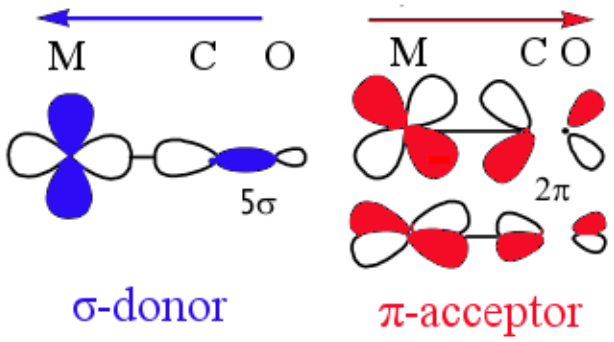

Fig. 6.1 CO is both a σ-donor (blue) and π-acceptor (red) ligand: arrows show the direction of charge transfer.

In the IR, typical stretching frequencies are:

- Uncoordinated or 'free' CO: 2143 cm^{-1}
- Terminal M−CO: 2125-1850 cm^{-1}
- Doubly bridged (μ = 2): 1850-1750 cm^{-1}
- Triply bridged (μ = 3): 1675-1600 cm^{-1} .

With each charge added to the metal centre, the CO stretching frequency decreases by approximately 100 cm^{-1}. Additionally, the better the σ-donating capability (or worse the π-acceptor capability) of the other ligands on the metal, the lower the CO stretching frequency. Therefore the IR spectra of carbonyl complexes shows convenient trends that make CO a useful probe molecule.

Depending on the metal surface, CO may adsorb in an associative or dissociative manner. The reactive metals on the left hand side of the periodic table favour dissociative adsorption, leading to the formation of adsorbed C and O atoms (surface oxide and oxy-carbide compounds), whereas the metals on the right hand side of the *d*-block (e.g. Cu, Ag, Au) interact predominantly in a molecular fashion; the strength of the M−CO bond is much weaker, allowing easy desorption of the CO molecule (without any dissociation) by raising the surface temperature. The (HOMO) 5σ orbital is slightly antibonding and has significant C 2s character, as shown in Fig. 6.2, which is why CO bonds to a metal as a σ-donor through the C atom and not the O atom (better overlap). Fig. 6.3 shows that the 2 x 2π LUMO orbitals (antibonding) are empty. It is these

orbitals that can interact with metal *d*-orbitals accepting electron density. The 5*d* orbitals of Au are filled and below the singly-occupied 6s state, suggesting that their involvement in the Au-CO bond is likely to be weak. The major component of the interaction is electrostatic, involving the small $C^{\delta-}=O^{\delta+}$ dipole, which can be enhanced through interaction with a cationic Au centre. Thus, Au_1 anions or neutral species adsorb CO relatively weakly. Au_1 cations, on the other hand, increase the bond polarisation of the CO molecule, strengthening the C=O bond and resulting in a blue-shift in the stretching frequency.

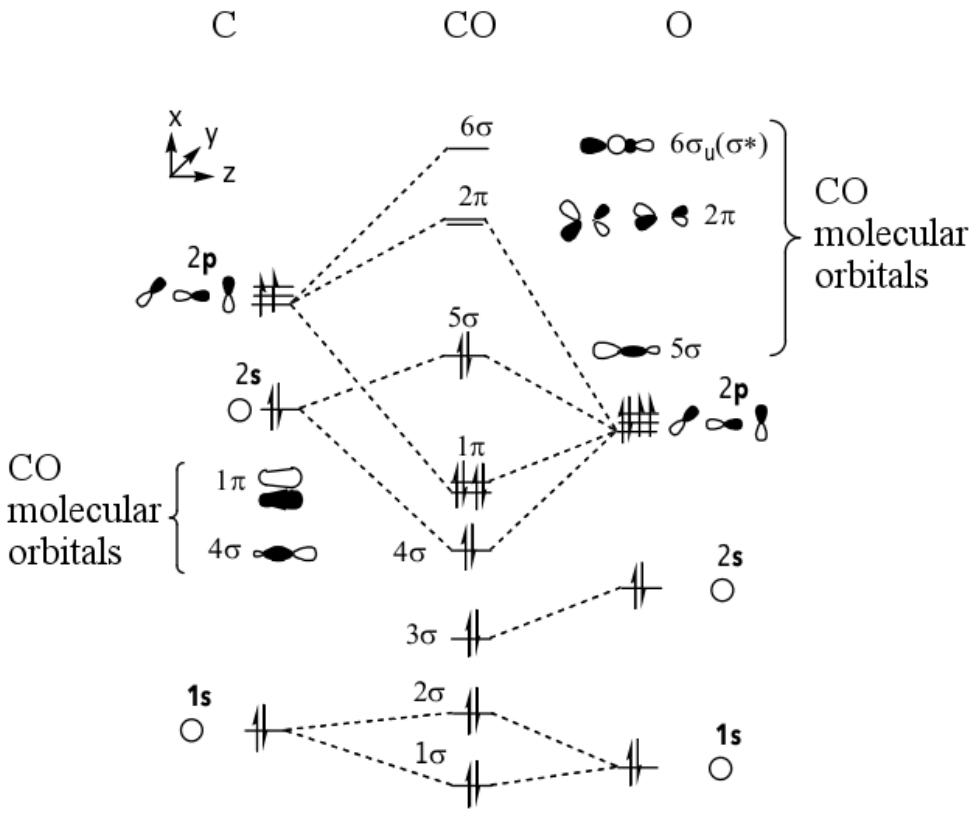

Fig. 6.2 Molecular orbital (MO) diagram of CO.

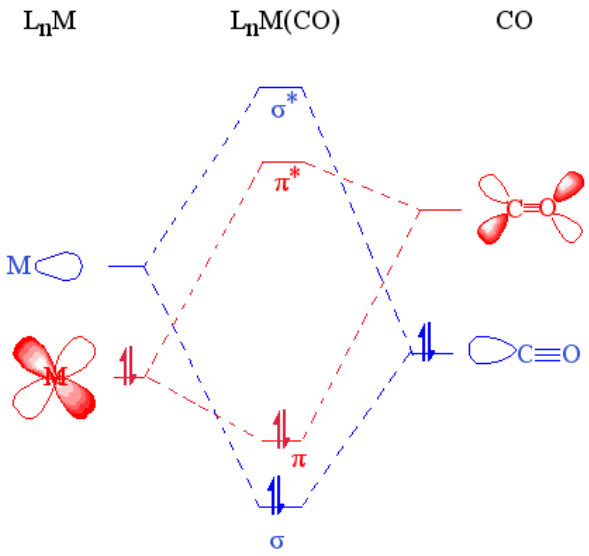

Fig. 6.3 Proposed molecular orbital diagram for CO bonding to *d*-block metals.

Binding of CO to gold clusters as a function of cluster size (n = 1-6 in Au_n) and overall charge was investigated by Wu *et al.*.[3] Using the lowest energy isomers for each system, the most energetically favourable CO adsorption sites positioned CO in an atop fashion, as shown in Fig. 6.4, through a mono-dentate (single Au−CO bond), and positively charged clusters having the strongest CO interaction (up to 2.57 eV). As the size of the cluster is increased, the difference in the adsorption energies for the different charge states is reduced, as the charge is more distributed over a larger volume. Both hybrid functionals B3LYP and PW91 give the same trends, although B3LYP gives lower adsorption energies than PW91 by 39-58 kJ mol^{-1}. However, a similar study by Jiang and Xu[4] using the B3LYP/6-311+G(d)-LANL2DZ functional found that in Au_5CO (neutral charge), CO has a lower energy in a bridging position, denoted as $\mu_{1,1}$ [where μ_n represents a bridging interaction of an adsorbate molecule between n atoms]. As the cluster size increases from n = 5, the difference in adsorption energies for neutral and positively charged clusters becomes negligible; the single positive charge is spread too thinly to be of consequence.

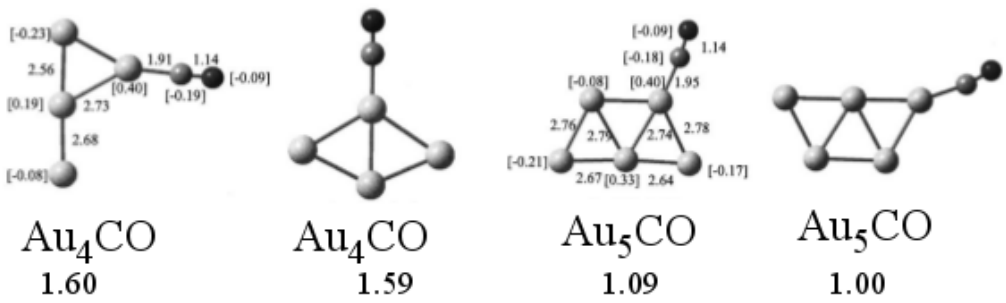

Fig. 6.4 Lowest energy isomers for Au_4CO and Au_5CO as obtained by Wu and co-workers. Adsorption energies are given below the images in eV, with bond lengths for the lowest isomer given in Å and Mulliken charges in square parentheses.

CO adsorption onto small Au_n (n = 1-13) nanoclusters has been studied extensively using density functional theory (DFT) with hybrid functionals to determine the favoured geometry as a consequence of altered strain, arising from the electrostatic interaction between the CO molecule and the adsorption site. Cationic Au_n clusters tend to have a stronger binding energy (E_{ads}) for CO in comparison to neutral and negatively charged clusters until $n \geq 5$, at which point the assigned single positive charge becomes distributed over the whole cluster, diminishing its influence. Molina and Hammer showed that for Au_{34} clusters, decreasing the coordination number of the Au atoms can strengthen E_{ads}, and that edge sites can help CO diffusion.[5] It is suggested in order for CO to adsorb with reasonable cohesion, the coordination number of the gold atoms must not exceed eight and, under reaction conditions, CO is expected to be highly concentrated at the edges, corners and steps of Au nanoparticles.

CO adsorption on Ag nanoclusters has not been explored as extensively at small particle sizes, although it has been suggested that Ag may be an even better catalyst for CO_2 reduction reactions.[6] CO adsorption was found to be more favourable on Au (111) surfaces over Ag surfaces, with the trend reversing when oxygen was co-adsorbed. This finding is not unexpected given the oxidation potential of Ag is smaller than Au (+0.80 and +1.68 eV, respectively[7]), making it more easily oxidised.

The vulnerability of predicting adsorption sites for nanoclusters according to the chosen exchange-correlation functional is well documented: present density functionals tend to overestimate the adsorption energy for sites with high metal coordination in comparison

to those with low metal coordination. The underestimated energy difference between the HOMO (5σ) and LUMO ($2\pi^*$) orbitals contributes to the CO overbinding, and has shown to predict incorrectly CO site energetics on Cu, Rh and Pt.[8] Johnston *et al.*[9] examined the influence of the dispersion correction for the prediction of adsorption sites on differing precious metal nanoparticles: PBE and optPBE functionals favoured a (100) bridge site in truncated octahedral 38-atom Au nanoparticles, but D3 and D2 functionals favoured the (111) face and (111)/(100) bridge site, respectively. The 55-atom Ih Au nanoparticle also favoured differing adsorption sites with different functionals, observing a significant distortion in the nanoparticle geometry. The capability of CO adsorption to change the nanoparticle shape can affect the CO stretching frequency, and thus calculated and measured vibrational frequencies should be treated with caution, as they provide catalyst information not in its initial state, but following its interaction with CO.

We have performed theoretical calculations on small Au_xCO ($x \leq 5$) clusters to support the experimental work of Scott Rogers, a PhD student at the UK Catalysis Hub. Through the use of density functional theory (DFT), we aim to determine whether the unusual IR frequencies obtained experimentally (occurring at ~1900 and ~1875 cm^{-1}) may be attributed to very small gold clusters bonded to carbonyl groups; sub-nanometre particles have previously been shown to exhibit very high catalytic activity and greater durability in comparison to larger nanoparticles. The stretching frequencies are then also compared with those obtained for Au_{147}, Ag_{147}, $Au_{55}@Ag_{92}$ and $Ag_{55}@Au_{92}$ nanoclusters and Au / Ag surfaces. These calculations also prompted us to investigate whether it would be possible to study experimentally the structural evolution of core@shell nanoclusters to an alloy under heating, using CO as a probe molecule to determine changes in the nanocluster surface composition, which would be monitored through the combined extended x-ray absorption fine structure / diffuse reflectance infrared spectroscopy (EXAFS/DRIFTS) facility that is available at Diamond Light Source/ UK Catalysis Hub, complementing our simulations.

6.2 Computational Methods

DFT calculations were performed as implemented by the projector-augmented wave method (PAW) (Ch. 2).[10] Grid-based PAW (GPAW) uses a real-space grid, transforming the wavefunctions at the core to a smooth pseudo-wavefunction.[11] Converged grid spacings of h = 0.18 were used to represent wavefunctions numerically, and convergence achieved when the forces on all atoms were found to be < 0.01 eV $Å^{-1}$.

Geometry optimisations were carried out on the following clusters: Au_5CO, Au_4CO, Au_3CO, Au_2CO, $Au_2(CO)_2$, $Au(CO)_2$, and AuCO, with initial geometries obtained from the work of Jiang and Xu.[4] As there is a differing number of electrons for these structures, both spin-polarized and spin-paired calculations have been performed, using the generalized gradient approximation (GGA) of Perdew, Burke and Ernzerhof (PBE) exchange–correlation functional,[12] with the residual minimisation method, direct inversion in iterative subspace (RMM-DIIS). Spin-polarized calculations are used to determine the influence of changing spin-state (μ) on the energetics of odd-electron structures [Au_5CO, Au_3CO, $Au(CO)_2$ and AuCO], as the influence of spin is unclear. For even-electron structures, (Au_4CO, Au_2CO, $Au_2(CO)_2$), spin-paired calculations have been performed.

Theoretical representation of surfaces is performed using a 'slab', an infinite 2-D thin film oriented to expose the facet of interest, with a vacuum region above the slab to separate periodic images, as shown in Fig. 6.5. For comparison to isolated nanoclusters, we calculate the IR frequencies for CO adsorption corresponding to 1 monolayer (ML) at varying surface sites on the (100) and (111) faces, using a 5-layer thick slab of Au and vacuum spacing of 10 Å and 1 k-point per 0.024 $Å^{-1}$. Periodic boundary conditions were set to be 'true' in the x and y directions and 'false' in the z-direction to prevent periodic interactions between the models of the slab surfaces.

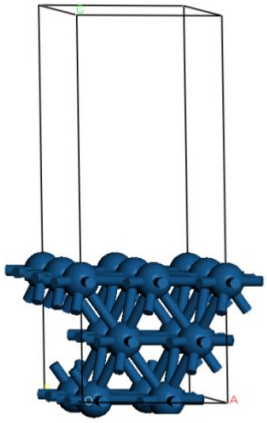

Fig. 6.5 Example of a periodic slab model of a surface. The model illustrated for the representation of a surface was obtained using a Pt p(2x2) unit cell for the (111) surface containing 3 atomic layers and a vacuum region.[13]

DFT Energetic Analysis

In surface simulations, the slab has two surfaces, one at the top and one at the bottom, and should be sufficiently thick enough such that the surfaces do not interact. Therefore, when calculating surface energies for a symmetrical slab, these can be calculated as half the formation energies:

$$\gamma = \frac{1}{2A}(E_{slab} - NE_{bulk}) \qquad \textbf{(6-1)}$$

where A is the surface area of the slab, E_{slab} is the energy of the slab, E_{bulk} is the bulk energy per atom and N is the number of atoms in the surface slab. The ½ prefactor accounts for the two surfaces in the slab model. Comparison of the binding strength of different adsorption sites for the CO molecule is performed by calculating the adsorption energy, E_{ads} for a given configuration, σ:

$$E_{ads}(\sigma) = \frac{1}{N_{CO}} E_{\sigma+CO}^{DFT} - E_{clean}^{DFT} - E_{CO(g)}^{DFT} \qquad \textbf{(6-2)}$$

where N_{CO} is the number of adsorbed CO molecules, $E_{\sigma+CO}^{DFT}$ is the energy of the system with N CO molecules adsorbed, E_{clean}^{DFT} is the energy of the clean system with no adsorbates, and $E_{CO(g)}^{DFT}$ is the DFT energy of the free CO molecule in the gas phase. A

more negative E_{ads} represents a more strongly bound CO molecule. This formula is applicable to both nanoparticles and bulk surfaces.

6.3 Experimental Methods

6.3.1 Sol-immobilisation for bimetallic AuAg nanoparticle synthesis

Pure gold nanoclusters may be synthesised via a number of differing methods. The most well-known is the Turkevich method,[14-15] introduced in 1951, using citrate reduction of $HAuCl_4$ in water (also referred to as colloidal gold). This originally produced nanoclusters ca. 20 nm, leading to the trialling of varying amounts of reducing and stabilizing agents to produce smaller nanoclusters.[16] Kimling *et al*. also revisited this in 2006, determining a correlation between the gold to reducing agent ratio and final particle size.[17] The role of reducing agent was found to be important, with $NaBH_4$ determined as the best reducing agent trialled, provided that by-product borate salts could be removed by washing. In sol technology, the stability of a colloid is a function of the particle interaction energy. The stabilising agent prevents coagulation through electrostatic or steric repulsion. For the polyvinylalcohol (PVA) – stabilized sol, a PVA/Au ratio of 0.65 was found to be optimal, with higher activity on a TiO_2 support in comparison to activated carbon.

An extension of the Turkevich method is the synthesis of Ag nanoclusters, using $AgNO_3$ as the metal source, known as the Lee-Meisel method.[18] However, the size distribution of nanoclusters is widespread, and hence $NaBH_4$ is commonly used as the reducing agent, routinely yielding ~10 nm diameter sized particles with small deviations.[19]

Alloy and core@shell catalysts immobilised on TiO_2 were prepared using sol-immobilisation.[20-21] For the alloy catalyst, an equal molar amount of Au and Ag was incorporated. PVA (4.8 mL, 0.01 g/mL) was added to H_2O (515 mL), followed by $HAuCl_4$ (2.588 mL, 9.297 mg/mL) and $AgNO_3$ (1.409 mL, 10.05 mg/mL). $NaBH_4$ (13.12 mL, 0.1 M) was added immediately in a dropwise fashion to prevent the formation of silver chloride. A colour change to dark purple/black was observed, and the solution left to stir for 30 minutes. TiO_2 (0.96 g) was added, causing a colour change to light mauve, followed by H_2SO_4 (10 drops, 50 %) and the solution left to stir for 1 h.

The solution was then filtered and washed, leaving overnight to dry. The product was then dried at 120 °C for 8 h. The alloy was prepared by S. M. Rogers.

The core@shell structure was prepared using a sequential deposition/reduction method. For experimental ease, we synthesised the Au@Ag arrangement: For a 2 wt. % Au@ 2 wt. % Ag / TiO_2 catalyst, PVA (3.6 mL, 0.1 M) and $HAuCl_4$ (2.003 mL, 9.985 mg/mL) were added to H_2O (1541 mL), with stirring. Dropwise addition of $NaBH_4$ (5.075 mL, 0.1 M) resulted in a colour change from pale yellow to red, and the mixture left to stir for 30 minutes. $AgNO_3$ (1.990 mL, 10.05 mg/mL) was added followed by immediate dropwise addition of $NaBH_4$ (9.327 mL, 0.1 M), and stirred for a further 30 minutes. TiO_2 (1.96 g) was added, causing a colour change to light mauve, followed by H_2SO_4 (14 drops, 50 % M). The solution was left to stir for 1 h. The solution was then filtered and washed and left overnight to dry. The product was dried for 8 h at 120°C.

6.3.2 *In situ* EXAFS/DRIFTS

One of the major aims of current catalytic science is to obtain an understanding of catalytic processes at an atomic level. X-ray absorption spectroscopy (XAS), as discussed in Ch. 2, is a highly useful technique, more so than traditional X-ray diffraction (XRD): due to its independency from long-range order. Progress in spatiotemporal techniques using synchrotron radiation has seen a movement towards combinatorial approaches. One such technique, that is available to us, is the UK Catalysis Hub's X-ray absorption fine structure / diffuse reflectance infrared Fourier transform spectroscopy (XAFS/DRIFTS) facility, where IR spectra can be monitored in real-time alongside XAS data. The mechanical arm extends the optical path of the spectrometer, allowing rapid scanning to be performed.

Our aim was to utilise the XAFS/DRIFTS facility at Diamond Light Source, whilst heating the sample in a CO-rich environment. Changes in DRIFTS frequencies for CO with temperature would be able to reveal changes in the surface composition, and *in situ* XAFS data would also be obtained for correlation. As Au is expected to preferentially adsorb CO over Ag, it was decided that the Ag K-edge would be followed with XAFS and the DRIFTS spectra could follow changes in occurring for Au species, allowing us

to track both metallic elements simultaneously. However, during experiment, it became clear that the core@shell arrangement did not have sufficient metal loading to produce a good X-ray signal. The alloy arrangement was tested, but given the (as expected) stability of the alloy, no change was observed either for the surface as observed from the DRIFTS studies or of the local environment of the Ag atoms as determined from *in situ* XAFS measurements. Below we present the results of the DRIFTS tests that were performed prior to beam-time for the core@shell arrangement, which do show features of restructuring as the Au@Ag nanocluster is heated.

In order to remove any surface species, such as oxygen adsorbates, the Au@Ag sample is first held at room temperature (RT) in air, followed by He at 30 ml/min. 10% H_2 in He is flowed over the system at 325°C for 1 hour to reduce the sample, and then it is re-cooled under He.

Once the surface of the Au@Ag sample was clean, the CO flow is turned on (10% CO in He). Once the CO level in the IR spectra was steady, the sample was heated to 450°C, with a ramp rate of 5°C/min. Fig. 6.6 shows the mass spectrometer results from the ramp. Fig. 6.7 and Fig. 6.8 below show the IR spectra obtained during heating, in 3D and 2D, respectively. As the sample is heated, an additional peak is observed near those usually found for CO_2, at ~2100 cm^{-1}. Once at 450°C, the CO was turned off, to see if any species remained on the surface under He, but it was found to be clean.

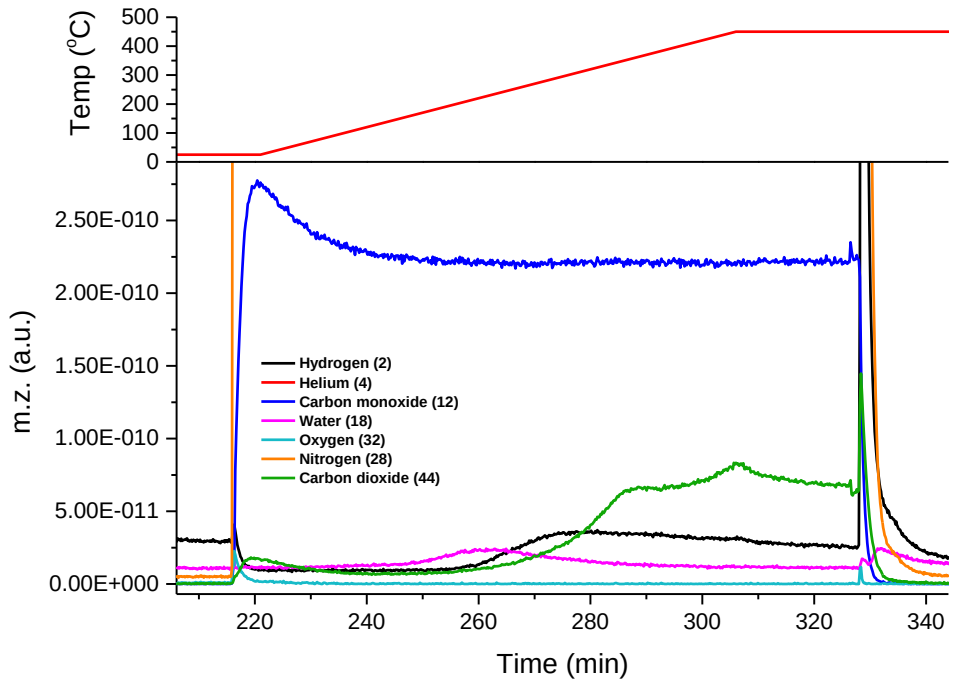

Fig. 6.6 Mass spectrometer results showing the formation of H_2, H_2O and CO_2 during CO adsorption.

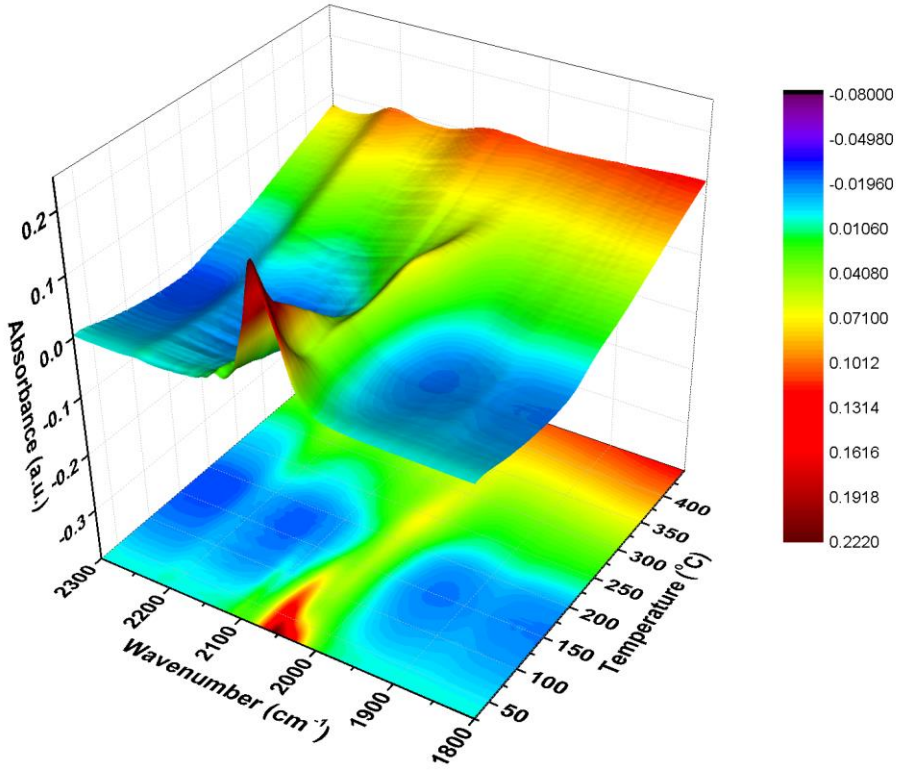

Fig. 6.7 DRIFTS spectra during CO adsorption during ramp from RT to 450°C

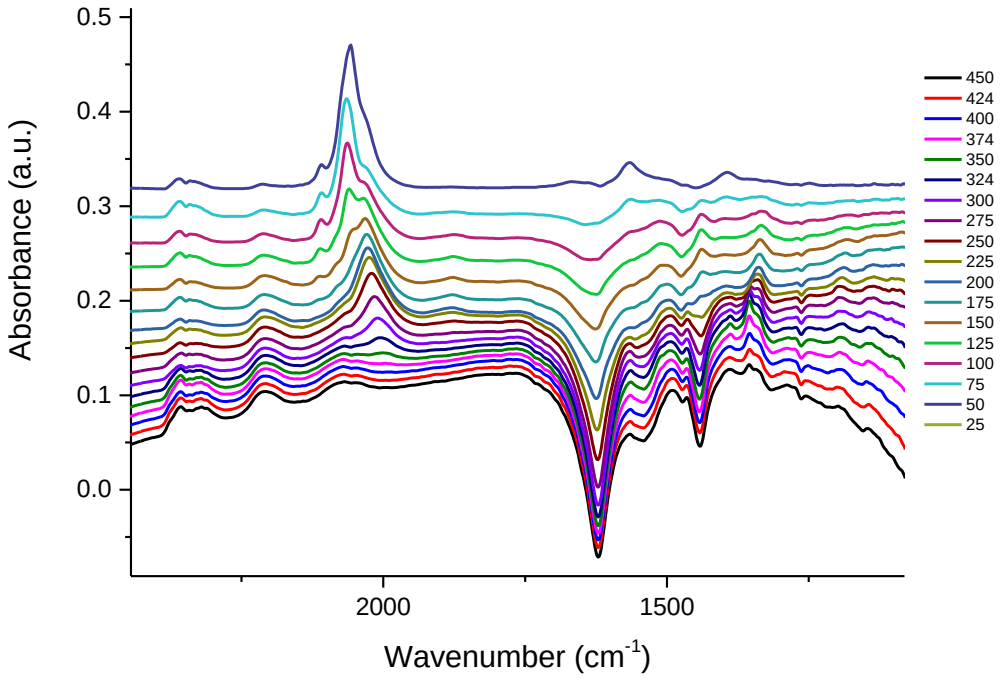

Fig. 6.8 Selected spectra during the ramp to 450°C under CO.

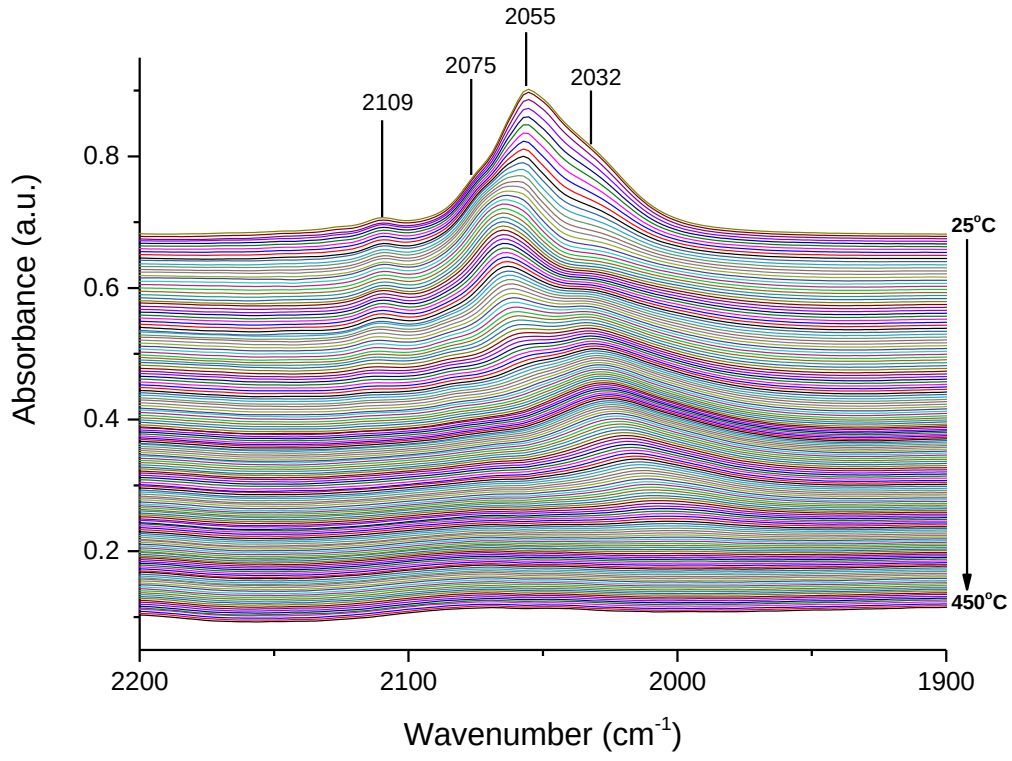

Fig. 6.9 DRIFTS spectra during CO adsorption during ramp from RT to 450°C

Fig. 6.9 shows the transformed DRIFTS spectra during CO adsorption during the ramp from RT to 450°C; the sample under He, at RT, spectra has been subtracted. Four main peaks are identified at 25°C, at 2109, 2075, 2055 and 2032 cm^{-1}, respectively.

CO adsorption on Ag/TiO_2 was performed by Klissurski *et al.*, with CO stretching frequencies (ν_{C-O}) at 2158 and 2165 cm^{-1} assigned to $Ag^{+}-CO$ complexes.[22] However, no carbonyls are formed on Ag following reduction – surface carbonyls with zero-valent Ag atoms do not exist at room temperature.[23] Therefore, we can assume that as we reduce the above sample before introduction of CO, the observed frequencies are not due to Ag−CO stretches. Adsorption of CO on Au/TiO_2 is expected to produce bands at 2130 and 2115 cm^{-1}, assigned to CO adsorbed on both positively charged and neutral Au nanoparticles, respectively. Reduced Au/TiO_2 result in ν_{C-O} at 2109, 2101 cm^{-1}, 2055 and 1990 cm^{-1}, the last of which is attributed to bridging CO adsorbed on small, negatively charged nanoparticles.

Therefore, based on the above, we can assume that given the sample reduction before CO is introduced, there are no Ag−CO complexes present. We suggest that the initial bands in the sample present at 2109, 2055 and 2032 cm^{-1} are CO adsorbed on reduced Au/TiO_2 species, with the latter due to $Au^{(\delta-)}$ species. As the temperature is increased, there is a blue shift to higher wavenumbers for the peak at 2055 cm^{-1}, and the peak at 2109 cm^{-1} is lost, suggesting that the nanoparticles have coagulated. The peak at 2055 cm^{-1} increases in intensity (perhaps best observed in the red regions of Fig. 6.7), with increasing temperature, suggesting that there is a greater concentration of Au now present at the surface. Therefore we suggest that we begin with an Au@AgAu sample, which evolves into an AuAg alloy upon heating. Once at 450°C and the CO is turned off, no CO peaks are identifiable, and therefore we can determine that the peaks are representative of the available CO adsorption sites and do not occur as a result of anything else. CO adsorption was subsequently studied using DFT on small nanoclusters ($\leq$ 5 atoms) and 147-atom nanoparticles, pure monometallics and core@shell arrangements: it would be of interest whether a greater concentration of Au at the surface results in a shift in the CO stretching frequency.

6.4 Theoretical results and discussion

We have calculated $E_{ads,}$ as defined in 6.2, and vibrational frequencies for small Au_xCO nanoclusters, performing geometry optimisations based on previous work by Jiang and Xu. The energetics for both odd and even-electron structures have been given in Table 6.1. For odd-electron structures, the influence of spin state on the energetics has also been considered; the lowest energy states for these clusters occurs when μ=1, and thus we can assume that this is the correct electron configuration (Table 6.2). E_{ads} (per CO molecule) show that CO adsorption is favourable for all nanoclusters, with the highest E_{ads} for Au_3CO, indicating CO is most strongly bound for this carbonyl complex. The two Au atoms not directly bonded to the CO molecule in Au_3CO contribute charge transfer to the Au atom that is connected *directly* to CO, forming a stronger σ bond. Au_5CO has a reduced E_{ads} as the increased number of Au atoms also allows for charge delocalisation over the whole nanocluster. Fig. 6.10 shows the obtained geometries for these small nanoclusters.

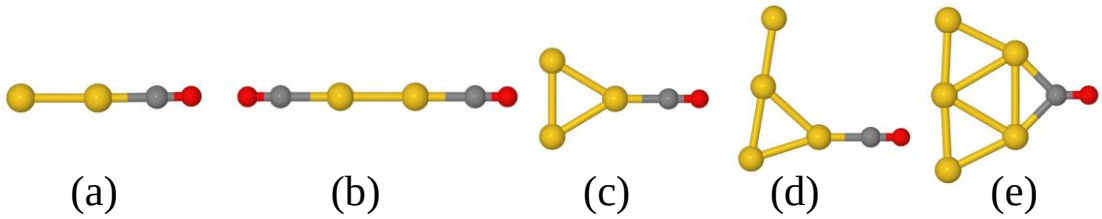

Fig. 6.10 CO adsorption on small Au_xCO nanoclusters (x=1-5 atoms), initial geometries (subsequently optimised) taken from Jiang and Xu. Yellow spheres represent Au, grey spheres represent carbon, and red spheres represent oxygen.

Table 6.1 E_{ads} for small Au_xCO nanoclusters (per CO molecule).

Structure	Spin state (μ)	E_{ads} / eV (per CO molecule)
Au_5CO	1	−1.200
Au_4CO	0	−1.746
Au_3CO	1	−1.808
Au_2CO	0	−1.673
$Au_2(CO)_2$	0	−1.322
$Au(CO)_2$	1	−1.030
Au(CO)	1	−0.909

Table 6.2 Influence of spin state on the energetics of Au_5CO, Au_3CO, $Au(CO)_2$ and AuCO.

Structure	Spin state (μ)	E / eV	ΔE / eV
Au_5CO	3	−23.644	2.02
Au_5CO	2	−24.693	0.97
Au_5CO	1	−25.663	0.00
Au_5CO	0	−25.643	0.02
Au_3CO	3	−18.497	2.63
Au_3CO	2	−19.709	1.42
Au_3CO	1	−21.132	0.00
Au_3CO	0	−21.114	0.02
$Au(CO)_2$	1	−32.650	0.00
$Au(CO)_2$	0	−32.644	0.01
Au(CO)	1	−16.301	0.00
Au(CO)	0	−16.296	0.00

Vibrational analysis

To calculate the infrared peak positions of the above structures, vibrational analysis has been performed using finite difference calculations to determine the second derivative of the energy. We have compared ν_{C-O} obtained for the whole structure, as well as when just the C, O and directly bonded Au atom(s) were sampled. For reference, we also calculate the vibrational frequency of the gas-phase CO molecule. Table 6.3 shows that the ν_{C-O} obtained from both the full degrees of vibrational freedom and from the reduced sampling (Au-C=O) are very similar to those from experiment (column III), which is highly encouraging in regards to the validity. Our obtained frequencies are closer to that of experiment than the hybrid functionals used by Jiang and Xu, demonstrating that the PBE functionals are sufficient for our study. However, these hybrid functionals have better agreement with experiment for CO adsorption on single Au atoms.

As the M-C bond increases in strength due to interaction between the C and the entire metal nanocluster, the C-O bond lengthens and weakens. Therefore, the nanoclusters with larger E_{ads} values are expected to produce the lowest ν_{C-O}: Au_3CO should ideally have the lowest ν_{C-O}. However, Au_1CO and Au_5CO have the lowest ν_{C-O}, at ~1870 cm^{-1} and ~1999 cm^{-1}. The coordination to the CO molecule in Au_5CO results in a red shift to lower wavenumbers – bridged species can often be observed at much lower frequencies. Au_1CO, however, has an experimental ν_{C-O} at ~2039 cm^{-1}, disagreeing with our results,

which suggests that for extremely small nanoclusters, calculation of ν_{C-O} must be performed at a higher level of theory. However, when $n > 2$, we have better agreement with experiment for IR stretching frequency than the B3LYP/6-311+G(d)-LANL2DZ.[4]

Au_5CO produces IR peaks that are very similar to those obtained experimentally by Rogers *et al.* in their complementary experimental work, suggesting that the unusual vibrational frequencies that they observe may be attributed to very small nanoclusters. This was later confirmed by aberration-corrected high angle annular dark field scanning transmission electron microscopy (HAADF-STEM), which identified the presence of isolated Au clusters (1-5 atoms) in the most active catalyst. The identification of these highly active small isolated clusters, as prepared through the use of a modified colloidal preparation method is novel, demonstrating that Au nanocluster characteristics can be tuned according to choice of solvent and synthesis temperature.

We can simulate the effect of charge donating substrates through the addition of a negative charge, and thus this is performed for Au_5CO, resulting in Au_5CO^-. The addition of the extra electron resulted in a large shift in ν_{C-O} to lower frequencies (~100 cm^{-1}, as is expected from theory), but this frequency is not observed experimentally.

Table 6.3 ν_{C-O} as calculated for the full structure, and the reduced system of CO and directly bonded Au atoms [labelled ν_{C-O}(full) and ν_{C-O}(reduced), respectively]. Comparative experimental and B3LYP/6-311+G(d)-LANL2DZ [labelled as B3LYP] calculated frequencies are obtained from Jiang and Xu.[4] All values are in cm^{-1}.

Structure	ν_{C-O}(full)	ν_{C-O}(reduced)	Experiment	B3LYP
Au_5CO (μ=1)	**1869.9**, 468.3, 438.5, 397.5, 231.6, 177.9, 156.7, 125.7, 112.4, 102.6, 101.1, 100.2	**1868.0**, 467.1, 434.3, 395.4, 231.4, 124.1, 110.4, 90.5, 38.6, 31.4, 28.9	1852.9	1923.7
Au_4CO	**2096.1**, 431.2, 374.6, 348.8, 202.3, 191.6, 157.0, 115.4, 103.9, 100.8, 96.6, 78.0, 61.7	**2095.7**, 427.9	2115.9	2198.0
Au_3CO (μ=1)	**2084.3**, 471.4, 315.6, 308.8, 174.3, 125.7, 106.8, 99.0, 97.2, 62.7, 58.3	**2083.3**, 471.1	2075.4	2169.2
Au_2CO	**2108.3**, 454.9, 417.8, 405.8, 261.6, 191.9, 167.4, 101.8, 92.8, 71.7	**2108.5**, 458.4, 417.3, 47.8	2131.9	2192.8
$Au_2(CO)_2$	**2113.5, 2092.5**	-	2110.2	2186.7
$Au(CO)_2$ (μ=1)	**2066.5**	-	1916.3	2103.4
Au(CO) (μ=1)	**1998.7**, 449.0, 340.3, 226.4, 99.7, 96.7, 74.1, 72.3, 49.4	-	2039.3	2065.9
CO	**2134.6**			
Au_5CO^-	**1767.2,** 543.1, 419.3, 395.9, 197.4, 160.5, 132.6, 100.4, 94.7, 88.2, 76.9, 43.4			

6.4.1 Ag_yCO nanoclusters

Throughout this thesis, the focus of work is on AuAg bimetallic nanoclusters, and therefore it is also of interest to compare Ag_yCO nanoclusters, where the subscript *y* denotes the number of Ag atoms (*y*=1-5). Using the same geometries as for the small Au_xCO nanoclusters, we perform the same geometry optimisations and frequency calculations. As seen in Ch. 3 and 4, the electronic properties of the nanocluster can heavily influence the properties: Ag is much less electronegative than Au, and thus it is expected to form weaker M−C bonds than Au_xCO nanoclusters.

Ag_4CO has the most negative E_{ads}, and therefore the strongest bonding to the CO molecule, which is surprising as we expect Au and Ag systems to behave in a similar manner. As mentioned in the introduction, the inclusion of dispersion effects can have a large influence on the optimised geometry when adsorbing CO molecules on small nanoclusters. Therefore, it would be of interest to see whether this behavioural difference between Au and Ag nanoclusters (*n*=1-5) still occurs when dispersion effects are included in the chosen functional, as the next most energetically favourable arrangement is Ag_3CO.

The vibrational frequencies for adsorption of CO on the Ag nanoclusters are given Table 6.5 and again show good agreement between the full and reduced calculation of vibration modes. Therefore, as we move to larger nanoclusters and surfaces, we can apply the technique of only sampling the atomic contributions from atoms local to the CO adsorption site for calculating the vibrational frequencies. As expected, Ag_5CO has the lowest ν_{C-O}, at ~1858 cm^{-1}, due to the bridged nature of the CO binding molecule. From E_{ads}, we expect the next lowest ν_{C-O} to occur for Ag_4CO – however, the stretching frequencies are lower for all clusters where *n* =1-3. We do not have experimental data to compare this to, but we suggest that the agreement for small Ag nanoclusters is not as good as seen for Au nanoclusters, resulting in the discrepancies between E_{ads} and ν_{C-O}. This could be due to the fact that these optimised geometries are obtained specifically for Au nanoclusters, and thus may not be entirely appropriate for Ag nanoclusters.

Table 6.4 E_{ads} for small Ag nanoclusters (per CO molecule).

Structure	Spin state (μ)	E_{ads} / eV (per CO molecule)
Ag_5CO	1	−0.404
Ag_4CO	0	−1.111
Ag_3CO	1	−0.861
Ag_2CO	0	−0.534
$Ag_2(CO)_2$	0	−0.456
$Ag(CO)_2$	1	−0.514
Ag(CO)	1	−0.326

Table 6.5 Vibrational frequencies as calculated for the full structure and just C=O and directly bonded Ag atoms.

Structure	ν_{C-O} (full relaxation) / cm^{-1}	ν_{C-O} (Ag-C=O vibration only) / cm^{-1}
Ag_5CO (μ=1)	**1858.6**, 334.0, 315.0, 310.2, 289.3, 129.6, 127.7, 125.0	**1857.6**, 333.3, 315.9, 311.3, 289.1, 198.1, 170.7, 142.0
Ag_4CO	**2067.8**, 340.4	**2067.8**, 340.4
Ag_3CO (μ=1)	**2038.5**,387.2, 325.2, 319.3, 201.4, 197.6, 155.4	**2039.3**, 388.9
Ag_2CO	**2130.4**, 351.7, 288.2	**2130.4**, 351.7, 288.2
$Ag_2(CO)_2$	**2127.8**, 2117.4, 328.3, 315.8, 272.5, 272.2, 250.8, 250.5	**2127.8**, 2117.4, 328.3, 315.8, 272.5, 272.2, 250.8, 250.5
$Ag(CO)_2$ (μ=1)	**2038.3**, 1950.5, 405.3, 354.9, 303.5, 259.4, 225.8, 177.4	**2038.3**, 1950.5, 405.3, 354.9, 303.5, 259.4, 225.8, 177.4
Ag(CO) (μ=1)	**1982.4**, 338.7, 273.5, 143.2, 127.5	**1982.4**, 338.7, 273.5, 143.2, 127.5

6.4.2 147-atom nanoparticles

Spin-polarised calculations were performed for CO adsorption on Ag_{147}, Au_{147}, $Ag_{55}@Au_{92}$ and $Au_{55}@Ag_{92}$ on four different adsorption sites: vertex, edge, face(100) and face(111), as depicted in Fig. 6.11. The adsorption energies (E_{ads}) are given in Table 6.6 and the ν_{C-O} in Table 6.8. Based on the work on the small nanoclusters, the stretching frequencies are only calculated based on the M-CO atoms, where M is representative of the metal atom the CO molecule binds to, and the rest of the nanocluster is frozen. However, face(111) adsorption sites were not able to converge for 147-atom nanoparticles, and thus these are not reported in the following results.

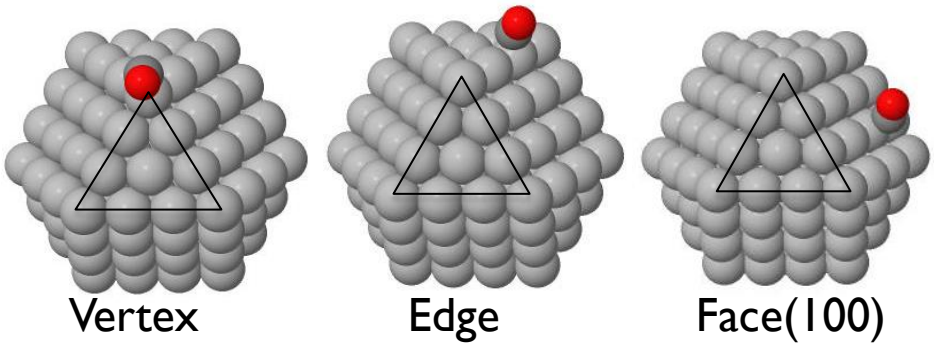

Fig. 6.11 Adsorption sites for 147-atom nanoparticles, as demonstrated for Ag_{147} (light grey spheres).

Table 6.6 Adsorption energies for 147-atom nanoparticles.

	Vertex / eV	Edge / eV	Face(100) / eV
Ag_{147}	−0.319	−0.295	−0.124
Au_{147}	−0.757	−0.498	−0.323
$Ag_{55}@Au_{92}$	−0.826	−0.493	−0.324
$Au_{55}@Ag_{92}$	−0.543	−0.418	−0.337

E_{ads} is negative for all adsorption sites, suggesting that CO adsorption is favourable for all nanocluster chemical orderings and positions considered. The most negative adsorption energies are obtained for vertex sites, where M has the lowest coordination number, resulting in a stronger M−CO bond. The low coordinated atoms have higher lying metal *d* states than for atoms with a high coordination number, making them better at interacting with the valence state of the CO molecule.

CO adsorption is most favourable for nanoclusters with an Au shell, with $Ag_{55}@Au_{92}$ and Au_{147} exhibiting the most negative E_{ads}, at −0.826 and −0.757 eV for the vertex position, respectively. The other adsorption sites for these two particular nanoclusters are very similar, suggesting that the influence of the 55-atom Ag core is most strongly felt at the vertex. However, E_{ads} is not similar for Ag_{147} and $Au_{55}@Ag_{92}$, irrespective of the shell species – the effect of an Au core is much more pronounced, with $Au_{55}@Ag_{92}$ exhibiting more favourable E_{ads}. These differences in the effects of the core species indicate that charge transfer is important for CO adsorption. We also note the degeneracy of E_{ads} for (100) face sites for all nanoclusters, with the exception of Ag_{147}: $Au_{55}@Ag_{92}$ has a greater E_{ads} than expected. In Ch. 2, we found $Ag_{55}@Au_{92}$ to be the most energetically favourable chemical ordering at the DFT level, attributed to the ease of charge transfer to Au, suggesting it is also important

for CO adsorption, and thus we refer back to the results obtained from Ch. 3 regarding charge transfer.

Table 6.7 shows the measured M−C and C−O bond distances for these nanoclusters, as well as their partial charges, reiterated from Ch. 3. E_{ads} is greatest for vertex sites on Au_{147} and $Ag_{55}@Au_{92}$ – these nanoclusters have the shortest M-C bond distances (1.99 and 2.00 Å, respectively) as well as the greatest electron accumulation at the vertex sites (Δq = 0.089 and 0.110 *e*, respectively). Therefore, a greater amount of charge transfer from the metal to the CO bond occurs, making the CO molecule most tightly bound. The vertex sites of Ag_{147} and $Au_{55}@Ag_{92}$ are not similar: Ag_{147} has the lowest E_{ads}(vertex), despite its greater Δq_{vertex} (0.072 and 0.046 for Ag_{147} and $Au_{55}@Ag_{92}$, respectively), although it has the longest M-C bond (2.14 and 2.12 Å for Ag_{147} and $Au_{55}@Ag_{92}$, respectively).

Au_{147} and $Ag_{55}@Au_{92}$ have the shortest M-C distances for edge sites, as well as the largest positive Δq values, indicating charge accumulation at the surface. However, $d_{M\text{-}C}$ is shorter for Au_{147}, whereas $Ag_{55}@Au_{92}$ has the greater Δq_{vertex} value. We can see that E_{ads} is almost identical for these two systems, thus demonstrating the dominant roles of $d_{M\text{-}C}$ and Δq in determining favourable adsorption sites. $d_{M\text{-}C}$ is very similar for Ag_{147} and $Au_{55}@Ag_{92}$, with the edge site of $Au_{55}@Ag_{92}$ being charge depleted. In theory, as the M-C bond strengthens, the C-O bond weakens, and becomes longer. However $d_{C\text{-}O}$ is constant for all nanocluster edge sites, at 1.15 Å.

For the (100) face sites, Au_{147} has the shortest $d_{M\text{-}C}$ value (2.05 Å), whereas all other nanoclusters have $d_{M\text{-}C} \geq 2.13$ Å. E_{ads} is ~ −0.3 eV for all nanoclusters, with the exception of Ag_{147}, which has the smallest E_{ads} at −0.124 eV. $d_{M–C}$ is greatest for Ag_{147}, and as expected, it has a low E_{ads}. Nonetheless, Au_{147} has a similar E_{ads} to both $Au_{55}@Ag_{92}$ and $Ag_{55}@Au_{92}$. Therefore, it would be of interest to perform Bader analysis post-CO adsorption to improve the understanding behind this. We suggest that for $Au_{55}@Ag_{92}$, the electron deleted Ag shell draws greater electron density from the CO molecule. However, rather than completing π-back donation to the fullest extent of the metal, some of this electron density is lost to the Au-core, resulting in both a longer C−O bond (1.15 Å) and shorter M−C bond (2.16 Å) in comparison to Ag_{147}. E_{ads} is more favourable for $Au_{55}@Ag_{92}$ than Ag_{147}, and therefore we suggest that the fact that the face sites are charge *depleted*, it can

actually *draw* electron density from the CO molecule, resulting in a stronger M−C bond.

Table 6.7 Bond distances and partial charges according to adsorption site and nanocluster. $d_{M\text{-}C}$ and $d_{C\text{-}O}$ represent the metal-carbon and carbon-oxygen bond distances, respectively. Δq is taken from Ch. 3.

Site	System	$d_{M\text{-}C}$ / Å	$d_{C\text{-}O}$ / Å	Δq / e
Vertex	Au_{147}	1.99	1.15	0.089
	$Ag_{55}@Au_{92}$	2.00	1.15	0.110
	Ag_{147}	2.14	1.14	0.072
	$Au_{55}@Ag_{92}$	2.12	1.14	0.046
Edge	Au_{147}	2.02	1.15	0.022
	$Ag_{55}@Au_{92}$	2.06	1.15	0.079
	Ag_{147}	2.15	1.15	0.007
	$Au_{55}@Ag_{92}$	2.14	1.15	−0.055
Face(100)	Au_{147}	2.05	1.14	0.017
	$Ag_{55}@Au_{92}$	2.13	1.14	0.062
	Ag_{147}	2.19	1.14	0.014
	$Au_{55}@Ag_{92}$	2.16	1.15	−0.07

The main CO stretching frequencies (i.e. those not in the experimental fingerprint region, <500 cm^{-1}) of the 147-atom nanoclusters are visually represented in Fig. 6.12. We can see that ν_{C-O} generally reflects whether Au or Ag is at the surface, as ν_{C-O} of $Ag_{55}@Au_{92}$ is close to that of Au_{147}, and similarly $Au_{55}@Ag_{92}$ with respect to Ag_{147}.

As the M−CO interaction is strengthened, the C−O bond is weakened, resulting in a red shift in ν_{C-O} to lower wavenumbers. The energetic ordering of E_{ads} being favourably exothermic, for all nanoclusters is vertex > edge > face (100) and therefore we also expect a linear trend in ν_{C-O} to higher wavenumbers as the C−O bond increases in strength. However, Fig. 6.12 shows that there is a shift to higher ν_{C-O} for the edge positions of all other nanoclusters, despite their increased coordination and more positive E_{ads} in comparison to vertex sites. The vertex positions have the strongest M−C bonds, and therefore weakest C−O bonds, which should prompt them to have the lowest ν_{C-O}, theoretically. Nonetheless, Fig. 6.12 shows that the 147-atom nanoparticles do not behave as expected in terms of predicting ν_{C-O}. Further Bader analyses post-adsorption will be a topic for future work, as CO adsorption would cause a re-organisation of electron density

distribution in the nanoparticle,[24] and this may shed some light in regards to this unusual behaviour.

Table 6.8 Vibrational frequencies for 147-atom nanoclusters, based on the CO molecule and atoms directly bonded.

	ν_{C-O} / cm^{-1}		
	Vertex	**Edge**	**Face(100)**
Ag_{147}	**2083.8**, 516.3, 497.1, 430.6, 318.7, 306.5, 170.0, 137.5, 118.1	**2083.6**, 465.4, 449.0, 400.7	**2081.9**
Au_{147}	**2096.5**	**2114.2**	**2105.4**, 519.3, 460.1, 431.3, 343.6, 316.6, 103.5
$Ag_{55}@Au_{92}$	**2097.3**, 534.0	**2096.5**	**2099.9**
$Au_{55}@Ag_{92}$	**2082.5**, 509.6, 473.3, 398.6, 331.7, 249.5, 185.9	**2088.9**	**2074.8**

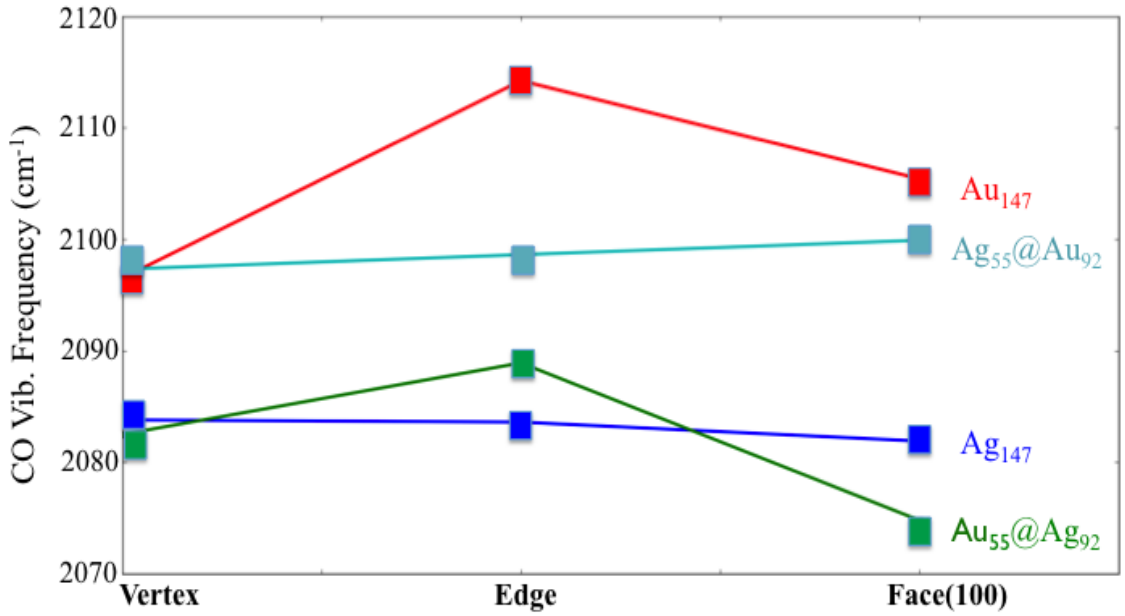

Fig. 6.12 CO stretching frequency as a function of adsorption site.

6.4.3 Slab energies and frequencies

E_{ads} and vibrational frequencies were also calculated and compared, in Table 6.9, for 1 monolayer (1 ML) coverage on Au and Ag surfaces. This coverage is comparable to experiment, given that it would be very difficult to direct adsorption site at lower coverages. E_{ads} is most favourable for an atop position on Au(100), at −1.60 eV, but the majority of positions on other surfaces are energetically unfavourable. Reference energies are also provided in column IV of Table 6.9, from the works of Hussain *et al.* and Mehmood *et al.* – the work of Mehmood *et al.* is more comparable to our own investigation, as both concern a 1 ML coverage, whereas the Hussain and co-workers examined a 0.25 ML coverage.

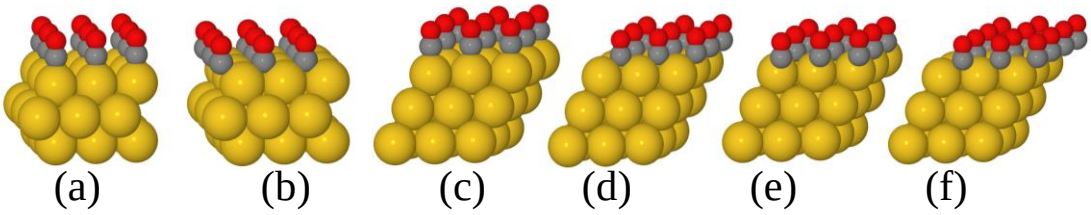

Fig. 6.13 Different adsorption sites for CO (1 ML) on different Au surfaces: (a) (100) face, atop, (b) (100) face, bridge. (c) (111) face, atop, (d) (111) face, bridge, (e) (111) face, fcc hollow, (f) (111) face, hcp hollow. Colours are the same as in Fig. 6.10.

We find E_{ads} is most favourable for atop adsorption, with exothermic values of −0.160 and −0.083 eV for Au and Ag (100) surfaces, respectively. Atop is also the most favourable for the (111) surfaces, although these values are endothermic, at 0.077 and 0.035 eV for Au and Ag, respectively. Despite this disagreement with previous theory regarding increased coordination, experiment has shown CO preferentially adsorbs CO in an atop fashion for Au surfaces, which is in line with our results, as well as those for 147-atom nanoparticles. CO adsorption is not stable for (100) hollow sites and is almost degenerate for (111) fcc and hcp hollow sites; Ag is more favourable in this instance, although E_{ads} is still endothermic for both Au and Ag surfaces.

From theory, it should follow that with increased coordination, the greater the back donation from the metal, resulting in a more strongly bound CO molecule. Therefore, as we progress from atop → bridge → hollow adsorption sites, the coordination number increases, and we expect a corresponding increase in E_{ads}. This has been

observed by Hafner *et al.*[8] for 0.25 ML CO adsorption using the PW91 functional; however, Pascucci *et al.* found that when using the PBE-vdW functional, Ag followed the same energetic ordering, but for Au surfaces, E_{ads} was most favourable for bridge sites, followed by atop and hollow sites. Pascucci and co-workers also performed the same study using the PW91 functional, determining E_{ads} = 0.0 eV for all adsorption sites on both Au and Ag. The difference between these functionals highlights the importance of including dispersion effects: given that PBE and PW91 functionals provide almost the same properties for Cu, Au and Ag metals, in best agreement with experimental data. We can also safely presume that the inclusion of dispersion effects would alter the calculated adsorption energies.

Table 6.9 Adsorption energies for different surfaces and adsorption sites

Surface	**Adsorption site**	E_{ads} **/ eV**	**Reference / eV**
Au (100)	atop	−0.160	−0.46[f] −0.1[g]
	bridge	−0.112	−0.55[f]
	hollow	N/A	
Au (111)	atop	0.077	−0.16[f]
	bridge	0.396	−0.15[f]
	hcp	0.508	−0.16[f]
	fcc	0.520	−0.12[f]
Ag (100)	atop	−0.083	0.19[h]
	bridge	0.055	0.13[h]
	hollow	N/A	0.14[h]
Ag (111)	atop	0.035	0.07[i]
	bridge	0.315	0.32[i]
	hcp	0.345	0.36[i]
	fcc	0.358	0.36[i]

[f] 0.25 ML coverage, 5 layer slab and 7 layers vacuum; no clear preference for adsorption site. Have a value for hollow site on Au(100) despite also stating that this is not stable.[25]

[g] 1 ML on 4 layer slab.[26]

[h] Single CO molecule on cluster model of Ag(100)[27]

[i] 0.25 ML on 4 layer slab, RPBE. [28]

To match our previous work, only directly bonded Au atoms are included in the finite difference calculations, for determining ν_{C-O}, summarised in Table 6.10. For bridged adsorption sites, Au and Ag surfaces can be easily distinguished, with vibrational frequencies occurring at ~1999 and ~1977 cm^{-1} for Au and ~2030 cm^{-1} for Ag. Atop adsorption is similar between Au and Ag surfaces, though we can generally surmise that higher wavenumbers will correspond to an Ag surface. The

calculated ν_{C-O} are in agreement with coordination number theory, in that as coordination to the metal surface is increased, there is a red shift to lower wavenumbers, as seen in the shifts from atop → bridge → hollow adsorption sites. Furthermore, if we expect Au to bind more strongly to CO (as in experiment), then Au surfaces will have a lower ν_{C-O} in comparison to Ag surfaces, which is line with our results.

Table 6.10 Summarised vibrational frequencies for CO adsorbed on different surfaces and adsorption sites.

Surface	Atop / cm^{-1}	Bridge / cm^{-1}	FCC Hollow / cm^{-1}	HCP Hollow / cm^{-1}
Ag (100)	**2094.2**	**2030.5**	N/A	N/A
Ag (111)	**2109.0**	**2031.4**	**2013.9**	**2018.7**
Au (100)	**2085.4**, 342.1, 200.4, 199.3, 111.6, 95.0, 94.6	**1976.7**, 404.9, 345.2, 257.6	N/A	N/A
Au (111)	**2082.6**, 323.4, 245.0, 219.6, 121.9, 16.1	**1998.7**, 387.5, 356.3, 349.8, 212.1, 185.7, 87.7	**1941.1**, 333.4, 328.4, 261.4, 175.9, 142.8, 115.4, 60.4	**1944.9**, 333.2, 332.2, 224.4, 132.8, 119.5, 102.9, 43.8

6.5 Conclusions

It has been shown that the CO vibrational stretching frequency can be used for surface composition analysis, with the shell component heavily influencing the ν_{C-O}. *Ex situ* DRIFTS studies were performed on Au@Ag/TiO_2 nanoparticles, in a CO environment. None of the ν_{C-O} frequencies were identified as Ag−CO species, only Au−CO adsorption was observed. An increase in the intensity of the Au−CO peaks was observed as a result of increasing temperature, suggesting the (irreversible) evolution of an AuAg alloy.

We also performed theoretical calculations to determine whether CO could be used as a probe molecule for detecting changes in surface composition. For very small nanoclusters (n = 1-5), ν_{C-O} could be directly correlated to the strength of E_{ads}, although agreement for ν_{C-O} between theory and experiment was best for $n \geq 3$. Larger 147-atom nanoparticles showed a strong energetic preference for CO adsorption at a vertex position, followed by edge and face sites. Charge accumulation at the vertex sites results in a more strongly bound CO molecule, but additionally, we also observe stronger bonding for Ag charge depleted sites, which can also draw

electron density from the CO molecule. However, ν_{C-O} cannot be directly correlated to E_{ads}, nor increased coordination, as the edge positions had the highest calculated wavenumbers. Finally, we also performed CO adsorption on Au and Ag surfaces (111) and (100), for a 1 monolayer coverage. CO adsorption was found to be energetically favourable only on (100) surfaces, for atop and bridge positions for Au (100) and only atop for Ag (100). For bulk surfaces, ν_{C-O} behaves as one would expect, shifting to lower wavenumbers as a result of increased metal coordination. Therefore (in future work), it would be of interest to perform further Bader analyses following CO adsorption, to determine if the redistribution of electron density affects ν_{C-O}, this may provide insight into the correlation between E_{ads} and ν_{C-O}. Additionally, future work should also consider the inclusion of dispersion effects, as a higher level of theory may alter the energetic ordering of different adsorption sites. Baletto *et al*. showed that the inclusion of dispersion effects on Au nanoparticles (n = 38, 55) can have large effects on the underlying nanoparticle structure, but this is dependent on the initial geometry.[29] Furthermore, due to the size of nanoparticle studied by Baletto *et al.*, the influence of dispersion is likely to be more pronounced. The influence of dispersion effects on Ag nanoparticles is unknown, however, and thus it would be of interest to see its role in AuAg nanoparticles, and whether any observed trends remain true at larger atomic sizes.

The 147-atom nanoclusters showed a higher wavenumber for Au-shell species – however, bulk surfaces showed the opposite trend, with Ag surfaces exhibiting a higher wavenumber than Au surfaces. Therefore we can also determine that this is not only influenced by size, but the extent of CO coverage – we only adsorb a single CO molecule for the nanoclusters, whereas we have a full monolayer for surfaces, thus warranting further investigation of CO saturation for the nanoparticle surfaces.

Relating the theoretical calculations to the experimental work performed, there is an agreement that an evolution of a greater concentration of Au at the surface will result in a shift in ν_{C-O} to higher wavenumbers. However, the blue shift that is observed experimentally is also a possible indication of nanoparticle oxidation and/or an increase in nanoparticle size. However, DFT also shows that as the bulk limit is approached, the same generalisations cannot be made, as Ag surfaces actually have a higher wavenumber. Whilst vibrational frequencies cannot be relied upon in terms of compositional analysis, should restructuring of the chemical arrangement of the

nanocluster from Ag@Au (or Au@Ag) to an alloy occur, a shift in the vibrational frequencies would indicate a change in the surface composition. Therefore, future experimental studies of AuAg chemical arrangement evolution should strongly consider the importance of nanoparticle size, with TEM measurements performed both before and after the XAS study, as well as CO coverage.

6.6 References

1. Haruta, M., Size-and Support-Dependency in the Catalysis of Gold. *Catalysis Today* **1997**, *36*, 153-166.
2. Valden, M.; Lai, X.; Goodman, D. W., Onset of Catalytic Activity of Gold Clusters on Titania with the Appearance of Nonmetallic Properties. *science* **1998**, *281*, 1647-1650.
3. Wu, X.; Senapati, L.; Nayak, S.; Selloni, A.; Hajaligol, M., A Density Functional Study of Carbon Monoxide Adsorption on Small Cationic, Neutral, and Anionic Gold Clusters. *The Journal of chemical physics* **2002**, *117*, 4010-4015.
4. Jiang, L.; Xu, Q., Reactions of Gold Atoms and Small Clusters with Co: Infrared Spectroscopic and Theoretical Characterization of Au N Co (N= 1-5) and Au N (Co) 2 (N= 1, 2) in Solid Argon. *The Journal of Physical Chemistry A* **2005**, *109*, 1026-1032.
5. Molina, L.; Hammer, B., Some Recent Theoretical Advances in the Understanding of the Catalytic Activity of Au. *Applied Catalysis A: General* **2005**, *291*, 21-31.
6. Back, S.; Yeom, M. S.; Jung, Y., Active Sites of Au and Ag Nanoparticle Catalysts for Co2 Electroreduction to Co. *ACS Catalysis* **2015**, *5*, 5089-5096.
7. Ebbing, D. D., *General Chemistry*, 3rd ed.; Houghton Mifflin, 1990.
8. Gajdoš, M.; Eichler, A.; Hafner, J., Co Adsorption on Close-Packed Transition and Noble Metal Surfaces: Trends from Ab Initio Calculations. *Journal of Physics: Condensed Matter* **2004**, *16*, 1141.
9. Paz-Borbon, L. O.; Johnston, R.; Barcaro, G.; Fortunelli, A., Chemisorption of Co and H on Pd, Pt and Au Nanoclusters: A Dft Approach. *The European Physical Journal D* **2009**, *52*, 131-134.
10. Blöchl, P. E., Projector Augmented-Wave Method. *Physical Review B* **1994**, *50*, 17953.
11. Mortensen, J. J.; Hansen, L. B.; Jacobsen, K. W., Real-Space Grid Implementation of the Projector Augmented Wave Method. *Physical Review B* **2005**, *71*, 035109.
12. Perdew, J. P.; Burke, K.; Ernzerhof, M., Generalized Gradient Approximation Made Simple. *Physical review letters* **1996**, *77*, 3865.
13. Gomes, J. R.; Fajín, J. L.; Cordeiro, D.; Natalia, M.; Teixeira, C.; Gomes, P.; Pillai, R. S.; Novell-Leruth, G.; Toda, J.; Jorge, M., Density Functional Treatment of Interactions and Chemical Reactions at Surfaces. **2013**.
14. Turkevich, J.; Stevenson, P. C.; Hillier, J., A Study of the Nucleation and Growth Processes in the Synthesis of Colloidal Gold. *Discussions of the Faraday Society* **1951**, *11*, 55-75.
15. Turkevich, J., Colloidal Gold. Part Ii. *Gold bulletin* **1985**, *18*, 125-131.
16. Frens, G., Controlled Nucleation for the Regulation of the Particle Size in Monodisperse Gold Suspensions. *Nature* **1973**, *241*, 20-22.
17. Kimling, J.; Maier, M.; Okenve, B.; Kotaidis, V.; Ballot, H.; Plech, A., Turkevich Method for Gold Nanoparticle Synthesis Revisited. *The Journal of Physical Chemistry B* **2006**, *110*, 15700-15707.
18. Lee, P.; Meisel, D., Adsorption and Surface-Enhanced Raman of Dyes on Silver and Gold Sols. *The Journal of Physical Chemistry* **1982**, *86*, 3391-3395.
19. Evanoff, D. D.; Chumanov, G., Synthesis and Optical Properties of Silver Nanoparticles and Arrays. *ChemPhysChem* **2005**, *6*, 1221-1231.

20. Dimitratos, N.; Lopez-Sanchez, J. A.; Anthonykutty, J. M.; Brett, G.; Carley, A. F.; Tiruvalam, R. C.; Herzing, A. A.; Kiely, C. J.; Knight, D. W.; Hutchings, G. J., Oxidation of Glycerol Using Gold–Palladium Alloy-Supported Nanocrystals. *Physical Chemistry Chemical Physics* **2009**, *11*, 4952-4961.
21. Pritchard, J.; Kesavan, L.; Piccinini, M.; He, Q.; Tiruvalam, R.; Dimitratos, N.; Lopez-Sanchez, J. A.; Carley, A. F.; Edwards, J. K.; Kiely, C. J., Direct Synthesis of Hydrogen Peroxide and Benzyl Alcohol Oxidation Using Au− Pd Catalysts Prepared by Sol Immobilization†. *Langmuir* **2010**, *26*, 16568-16577.
22. Hadjiivanov, K.; Vasileva, E.; Kantcheva, M.; Klissurski, D., Ir Spectroscopy Study of Silver Ions Adsorbed on Titania (Anatase). *Materials Chemistry and Physics* **1991**, *28*, 367-377.
23. Hadjiivanov, K. I.; Vayssilov, G. N., Characterization of Oxide Surfaces and Zeolites by Carbon Monoxide as an Ir Probe Molecule. *Advances in Catalysis* **2002**, *47*, 307-511.
24. Boronat, M.; Concepción, P.; Corma, A., Unravelling the Nature of Gold Surface Sites by Combining Ir Spectroscopy and Dft Calculations. Implications in Catalysis. *The Journal of Physical Chemistry C* **2009**, *113*, 16772-16784.
25. Hussain, A.; Ferré, D. C.; Gracia, J.; Nieuwenhuys, B.; Niemantsverdriet, J., Dft Study of Co and No Adsorption on Low Index and Stepped Surfaces of Gold. *Surface Science* **2009**, *603*, 2734-2741.
26. Mehmood, F.; Kara, A.; Rahman, T. S.; Henry, C. R., Comparative Study of Co Adsorption on Flat, Stepped, and Kinked Au Surfaces Using Density Functional Theory. *Physical Review B* **2009**, *79*, 075422.
27. Qin, C.; Sremaniak, L. S.; Whitten, J. L., Co Adsorption on Ag (100) and Ag/Mgo (100). *The Journal of Physical Chemistry B* **2006**, *110*, 11272-11276.
28. Abild-Pedersen, F.; Andersson, M., Co Adsorption Energies on Metals with Correction for High Coordination Adsorption Sites–a Density Functional Study. *Surface Science* **2007**, *601*, 1747-1753.
29. Davis, J. B.; Baletto, F.; Johnston, R. L., The Effect of Dispersion Correction on the Adsorption of Co on Metallic Nanoparticles. *The Journal of Physical Chemistry A* **2015**, *119*, 9703-9709.

7. Concluding Remarks

In this research, bimetallic AuAg nanoparticles have been evaluated in terms of their thermodynamic and kinetic stability for use in photocatalytic applications, using a variety of computational methods. The calculations focus primarily on 147-atom nanoparticles, so that any theoretical observations may be extrapolated to experimental sizes, and where possible, experimental comparisons have been provided.

In Ch. 3, we performed a thorough investigation into the optimal chemical orderings for 147-atom AuAg nanoparticles, with respect to their ability to act as co-catalysts in the photocatalytic water splitting reaction. As a large number of homotops are possible, both interatomic potentials and density functional theory (DFT) are used to explore the potential energy landscape. At the Gupta level, chemical arrangements that maximise Au-Ag interactions are more thermodynamically stable, i.e. alloys. However, once charge transfer effects are taken into account at the DFT level, core@shell arrangements become more energetically favourable; in particular, $Ag_{55}@Au_{92}$. This may be attributed to the ease at which Au atoms can attract electron density from Ag, as electrons will naturally migrate to the surface: charge transfer between core@shell arrangements is of an interfacial nature, and thus influences from the core are more pronounced for thin shells. Analysis of the electronic properties showed a lack of unoccupied *d*-orbitals, suggesting that the experimentally observed favourable influence of AuAg nanoparticles may also be dependent on other kinetic processes/surface reactions that are taking place simultaneously.

Understanding the kinetic phenomena that occurs in bimetallic nanoclusters is essential in relating simulations with wet chemistry. The kinetic stability of AuAg nanoparticles is explored in Ch. 4; the protecting agent frequently employed in colloidal synthesis for uniform particle distribution requires a subsequent heat treatment for catalyst activation. However, the high temperatures that are often employed can lead to destabilisation of the chemical ordering, and thus it is necessary to be able to relate kinetic influences to the chemical arrangement evolution. Using the chemical orderings as obtained in Ch. 3, these nanoparticles

were subjected to a heat treatment to 900 K using molecular dynamics (MD). The majority of nanoparticles underwent a martensitic transformation (MT) from the CO geometry to the Ih geometry, maintaining the integrity of the chemical ordering until close to the melting point (T_m). However, Ag@Au nanoparticles were found to undergo low temperature diffusion, at temperatures as low as 190 K and 30 K, where migration of core atoms to the surface is observed. These Ag atoms that migrate to the surface form 5-, 6-, and 7-membered rings, termed a rosette-Ih. $Ag_{55}@Au_{92}$ is particularly susceptible to the formation of the rosette-Ih as a consequence of the thin outer shell; the same is observed for $Ag_{13}@Au_{134}$ but to a lesser extent, and therefore it is suggested that the experimental difficulty in forming Ag@Au nanoparticles using sol-immobilisation techniques arises due to the energetic preference of the pseudo-spherical rosette-Ih.

The MT occurs via a diamond-square-diamond (DSD) mechanism, a straightforward transition for most AuAg nanoparticles. However, given the unexpected low temperature diffusion exhibited by Ag@Au nanoparticles, the transition pathways between CO and Ih geometries were further explored using both doubly nudged elastic band calculations and metadynamics. We have found that the addition of a single dopant atom can have a large influence on the transition pathway, depending on its positioning. Close to the surface, a single Ag atom in an Au-rich nanoparticle does not alter the DSD mechanism. However, a centrally placed Ag atom, $Ag_1@Au_{146}$, results in an alternative pathway, which goes through a variety of truncated octahedra (TO) and rosette-Ih motifs. The Ag atom maintains its central position, and the Au atoms rearrange to expose a subsurface atom, along which several low-lying minima are rosette-Ih geometry. The rate of transformation is determined by the size of the Ag core: at low Ag concentration, deformation of the CO is the most time-consuming process, with the crossover point between CO- and Ih-like structures higher in energy than for the starting structures, whereas at higher Ag concentration, the transition between CO- and Ih-like motifs is via motifs that are lower in energy than the starting structures, and thus r-Ih deformation becomes rate-limiting.

The work presented in this thesis has shown that the transition barrier between high symmetry geometric motifs is strongly dependent on chemical arrangements, as are reactivity and stability. Furthermore, potential is shown favourably for specific

geometric features, such as decorated surface facets and vertices, which are a viable route for improving structural stability within bespoke nanocatalyst design. These nanoparticles can be further stabilised by an interactive semiconducting matrix, although the reactivity of the nanoparticles must remain a consideration.

Due to the small cluster sizes examined in this study, it would be interesting to see whether the same energetic preferences and melting trends occur at larger sizes; there may be a point at which the CO geometry is more favourable for Ag-rich nanoclusters, and we no longer observe an MT. Additionally, this would also allow us to make experimental comparison on the same scale.

Ag nanoparticles are often employed to improve the light-trapping performance of thin film a-Si solar cells, and thus the stability of Ag nanoparticles in a-Si is also an important consideration. In Ch. 5, MD simulations of an embedded Ag nanoparticle in a-Si, subject to extended heating, were performed in parallel to experimental work. Particular regions of the Ag nanoparticles preferentially dissolved, whereas others were stabilised as a result of the interdiffusion of Si into the nanoparticle. Defects were also seen to enhance interdiffusion, lowering the temperature at which diffusion is first observed. This work highlights the different degrees of stability of a composite system under duress, in turn influencing the overall properties of the system.

The reactive properties of nanoparticles can also be influenced by atmospheric species, either through the facilitation of charge transfer or by blocking active sites. In the penultimate chapter, this is investigated with regards to CO adsorption, which is both a σ-donor and π-acceptor binding ligand. Furthermore, CO has the additional capability to be used as a probe molecule for determining changes in surface composition. Both *ex situ* diffuse reflectance infrared Fourier transform spectroscopy and theoretical DFT calculations were performed to determine the suitability of CO in determining surface composition. In experiment, only Au−CO peaks were identifiable, suggesting the irreversible evolution of an AuAg alloy. 147-atom nanoparticles do not behave as expected in terms of predicting ν_{C-O}. It would profitable to re-perform the Bader analysis following CO adsorption as future work, as CO adsorption would cause a re-organisation of electron density distribution in the nanoparticle, and this may shed some light in regards to this unusual behaviour.

Finally, we also performed CO adsorption on Au and Ag surfaces (111) and (100), for a 1 monolayer coverage. CO adsorption was found to be energetically favourable only on (100) surfaces, for atop and bridge sites for Au (100) and only atop sites for Ag (100). For the 147-atom nanoparticles, and bulk surfaces, we find that there is not a good correlation between E_{ads} and ν_{C-O}; in future, repetition of these calculations using a higher level of theory would be of interest, such as the inclusion of dispersion effects.

Finally, the onion-like arrangement for bimetallic alloys is one recurrent theme in the work presented here; with Au favoured in a subsurface position. The propensity towards this arrangement is not currently known, but our previous work has shown interatomic potentials to prefer gold atoms positioned subsurface. As the resultant alloy presented here may be due to the initial starting arrangements, it would beneficial to examine how chemical arrangements from interatomic potentials are altered when charge transfer is included in the model in the future. Previous DFT studies show gold to energetically favour surface positions, due to greater ease of charge transfer – the degrees of freedom are increased at the surface sites. Thus, if we can include charge transfer in our potential model this may provide an insight into the energetic favouring of Ag@Au@Ag. However, performing quantum mechanical (QM) MD has not yet been attempted.